

1 SEARCH FOR PRODUCTION OF A HIGGS BOSON AND A SINGLE TOP  
2 QUARK IN MULTILEPTON FINAL STATES IN  $pp$  COLLISIONS AT  $\sqrt{s} = 13$   
3 TeV.

4 by

5 Jose Andres Monroy Montañez

# A DISSERTATION

7 Presented to the Faculty of

8 The Graduate College at the University of Nebraska

In Partial Fulfilment of Requirements

10 For the Degree of Doctor of Philosophy

11 Major: Physics and Astronomy

12 Under the Supervision of Kenneth Bloom and Aaron Dominguez

13 Lincoln, Nebraska

14 July, 2018

15 SEARCH FOR PRODUCTION OF A HIGGS BOSON AND A SINGLE TOP  
16 QUARK IN MULTILEPTON FINAL STATES IN pp COLLISIONS AT  $\sqrt{s} = 13$   
17 TeV.

18 Jose Andres Monroy Montañez, Ph.D.

19 University of Nebraska, 2018

20 Adviser: Kenneth Bloom and Aaron Dominguez

# <sup>21</sup> Table of Contents

<sup>22</sup>	<b>Table of Contents</b>	<b>iii</b>
<sup>23</sup>	<b>List of Figures</b>	<b>vii</b>
<sup>24</sup>	<b>List of Tables</b>	<b>xi</b>
<sup>25</sup>	<b>1 Theoretical approach</b>	<b>1</b>
<sup>26</sup>	1.1 Introduction . . . . .	1
<sup>27</sup>	1.2 Standard model of particle physics . . . . .	2
<sup>28</sup>	1.2.1 Fermions . . . . .	4
<sup>29</sup>	1.2.1.1 Leptons . . . . .	5
<sup>30</sup>	1.2.1.2 Quarks . . . . .	7
<sup>31</sup>	1.2.2 Fundamental interactions . . . . .	11
<sup>32</sup>	1.2.3 Gauge invariance. . . . .	15
<sup>33</sup>	1.2.4 Gauge bosons . . . . .	17
<sup>34</sup>	1.3 Electroweak unification and the Higgs mechanism . . . . .	18
<sup>35</sup>	1.3.1 Spontaneous symmetry breaking (SSB) . . . . .	26
<sup>36</sup>	1.3.2 Higgs mechanism . . . . .	30
<sup>37</sup>	1.3.3 Masses of the gauge bosons . . . . .	33
<sup>38</sup>	1.3.4 Masses of the fermions . . . . .	34

39	1.3.5	The Higgs field . . . . .	35
40	1.3.6	Production of Higgs bosons at LHC . . . . .	36
41	1.3.7	Higgs boson decay channels . . . . .	40
42	1.4	Experimental status of the anomalous Higgs-fermion coupling . . . .	42
43	1.5	Associated production of a Higgs boson and a single top quark . . . .	44
44	1.6	CP-mixing in $tH$ processes . . . . .	49
45	<b>2</b>	<b>The CMS experiment at the LHC</b>	<b>54</b>
46	2.1	Introduction . . . . .	54
47	2.2	The LHC . . . . .	55
48	2.3	The CMS experiment . . . . .	65
49	2.3.1	CMS coordinate system . . . . .	68
50	2.3.2	Tracking system . . . . .	70
51	2.3.3	Silicon strip tracker . . . . .	73
52	2.3.4	Electromagnetic calorimeter . . . . .	74
53	2.3.5	Hadronic calorimeter . . . . .	76
54	2.3.6	Superconducting solenoid magnet . . . . .	77
55	2.3.7	Muon system . . . . .	79
56	2.3.8	CMS trigger system . . . . .	80
57	2.3.9	CMS computing . . . . .	81
58	<b>3</b>	<b>Event generation, simulation and reconstruction</b>	<b>86</b>
59	3.1	Event generation . . . . .	87
60	3.2	Monte Carlo Event Generators. . . . .	90
61	3.3	CMS detector simulation. . . . .	92
62	3.4	Event reconstruction. . . . .	94
63	3.4.1	Particle-Flow Algorithm. . . . .	94

64	3.4.1.1	Missing transverse energy.	108
65	3.4.2	Event reconstruction examples	109
66	<b>5</b>	<b>Statistical methods</b>	<b>112</b>
67	5.1	Multivariate analysis	112
68	5.1.1	Decision trees	116
69	5.1.2	Boosted decision trees (BDT)	119
70	5.1.3	Overtraining	121
71	5.1.4	Variable ranking	122
72	5.1.5	BDT output example	122
73	5.2	Statistical inference	123
74	5.2.1	Nuisance parameters	124
75	5.2.2	Maximum likelihood estimation method	125
76	5.3	Upper limits	126
77	5.4	Asymptotic limits	130
78	<b>6</b>	<b>Search for production of a Higgs boson and a single top quark in multilepton final states in pp collisions at <math>\sqrt{s} = 13</math> TeV</b>	<b>132</b>
80	6.1	Introduction	132
81	6.2	<i>tHq</i> signature	135
82	6.3	Background processes	137
83	6.4	Data and MC Samples	139
84	6.4.1	Full 2016 data set	139
85	6.4.2	Triggers	140
86	6.4.3	Signal modeling and MC samples	143
87	6.5	Object Identification	145
88	6.5.1	Lepton reconstruction and identification	146

89	6.5.2 Lepton selection efficiency . . . . .	152
90	6.5.3 Jets and $b$ -jet tagging . . . . .	156
91	6.5.4 Missing Energy MET . . . . .	157
92	6.6 Event selection . . . . .	158
93	6.7 Background modeling and predictions . . . . .	160
94	6.7.1 Diboson backgrounds . . . . .	160
95	6.8 Signal discrimination . . . . .	166
96	6.8.1 MVA classifiers evaluation . . . . .	166
97	6.8.2 Discriminating variables . . . . .	167
98	6.8.3 BDTG classifiers response . . . . .	172
99	6.8.4 Additional discriminating variables . . . . .	174
100	6.8.5 Signal extraction procedure . . . . .	175
101	6.8.6 Binning and selection optimization . . . . .	177
102	6.8.7 Other binning strategies . . . . .	179
103	6.8.8 Signal model . . . . .	181
104	<b>A Datasets and triggers</b>	<b>185</b>
105	<b>B BDTG aditional plots</b>	<b>189</b>
106	B.1 BDTG input variables distributions for $2lss$ channel . . . . .	189
107	B.2 Input variables distributions from BDTG classifiers . . . . .	191
108	<b>Bibliography</b>	<b>191</b>
109	<b>References</b>	<b>195</b>

# <sup>110</sup> List of Figures

111	1.1	Standard Model of particle physics.	3
112	1.2	Transformations between quarks	11
113	1.3	Fundamental interactions in nature.	12
114	1.4	SM interactions diagrams	13
115	1.5	Neutral current processes	19
116	1.6	Spontaneous symmetry breaking mechanism	27
117	1.7	SSB Potential form	28
118	1.8	Potential for complex scalar field	29
119	1.9	SSB mechanism for complex scalar field	30
120	1.10	Proton-Proton collision	36
121	1.11	Proton PDFs	37
122	1.12	Higgs boson production mechanism Feynman diagrams	38
123	1.13	Higgs boson production cross section and decay branching ratios	39
124	1.14	$\kappa_t$ - $\kappa_V$ plot of the coupling modifiers. ATLAS and CMS combination.	42
125	1.15	Higgs boson production in association with a top quark	45
126	1.16	Cross section for $tHq$ process as a function of $\kappa_t$	48
127	1.17	Cross section for $tHW$ process as a function of $\kappa_{Htt}$	48
128	1.18	NLO cross section for $tX_0$ and $t\bar{t}X_0$ .	52

129	1.19 NLO cross section for $tWX_0, t\bar{t}X_0$ . . . . .	53
130	2.1 CERN accelerator complex . . . . .	55
131	2.2 LHC protons source. First acceleration stage. . . . .	56
132	2.3 The LINAC2 accelerating system at CERN. . . . .	57
133	2.4 LHC layout and RF cavities module. . . . .	58
134	2.5 LHC dipole magnet. . . . .	60
135	2.6 Integrated luminosity delivered by LHC and recorded by CMS during 2016	62
136	2.7 LHC interaction points . . . . .	63
137	2.8 Multiple $pp$ collision bunch crossing at CMS. . . . .	65
138	2.9 Layout of the CMS detector . . . . .	66
139	2.10 CMS detector transverse slice . . . . .	67
140	2.11 CMS detector coordinate system . . . . .	69
141	2.12 CMS tracking system schematic view. . . . .	70
142	2.13 CMS pixel detector . . . . .	71
143	2.14 SST Schematic view. . . . .	73
144	2.15 CMS ECAL schematic view . . . . .	75
145	2.16 CMS HCAL schematic view . . . . .	77
146	2.17 CMS solenoid magnet . . . . .	78
147	2.18 CMS Muon system schematic view . . . . .	79
148	2.19 CMS Level-1 trigger architecture . . . . .	81
149	2.20 WLCG structure . . . . .	82
150	2.21 Data flow from CMS detector through hardware Tiers . . . . .	84
151	3.1 Event generation process. . . . .	87
152	3.2 Particle flow algorithm. . . . .	95
153	3.3 Stable cones identification . . . . .	102

154	3.4	Jet reconstruction.	104
155	3.5	Jet energy corrections.	106
156	3.6	Secondary vertex in a b-hadron decay.	107
157	3.7	HIG-13-004 Event 1 reconstruction.	109
158	3.8	$e\mu$ event reconstruction.	110
159	3.9	Recorded event reconstruction.	111
160	5.1	Scatter plots-MVA event classification.	114
161	5.2	Scalar test statistical.	115
162	5.3	Decision tree.	116
163	5.4	Decision tree output example.	119
164	5.5	BDT output example.	122
165	5.6	$t_r$ p.d.f. assuming each $H_0$ and $H_1$	128
166	5.7	Illustration of the $CL_s$ limit.	129
167	5.8	Example of Brazilian flag plot	130
168	6.1	Analysis strategy workflow	135
169	6.2	$tHq$ event signature	136
170	6.3	$t\bar{t}$ and $t\bar{t}W$ events signature	139
171	6.4	Trigger efficiency for the same-sign $\mu\mu$ category	141
172	6.5	Trigger efficiency for the $e\mu$ category	142
173	6.6	Trigger efficiency for the $3l$ category	143
174	6.7	$tHq$ and $tHW$ cross section in the $\kappa_t$ - $\kappa_V$ phase space	144
175	6.8	Tight vs loose lepton selection efficiencies in the $2lss$ channel.	154
176	6.9	Tight vs loose lepton selection efficiencies in the $3l$ channel.	155
177	6.10	Kinematic distributions in the diboson control region.	162
178	6.11	Input variables to the BDT for signal discrimination normalized.	164

179	6.12 MVA classifiers performance. . . . .	167
180	6.13 BDTG classifier Input variables distributions. . . . .	169
181	6.14 BDT input variables. Discrimination against $t\bar{t}$ and $t\bar{t}V$ in $3l$ channel. . .	170
182	6.15 Correlation matrices for the BDT input variables. . . . .	171
183	6.16 BDTG classifier response. Default parameters. . . . .	172
184	6.17 BDTG classifier output. . . . .	173
185	6.18 Additional discriminating variables distributions. . . . .	174
186	6.20 Binning overlaid on the S/B ratio map on the plane of classifier outputs. .	176
187	6.21 Binning combination scheme. . . . .	178
188	6.22 Binning by S/B regions for same-sign dilepton (left) and three leptons (right). . . . .	180
190	6.23 Final bins (corresponding to S/B regions in the 2D plane) for same-sign dilepton (left) and three leptons (right). . . . .	180
192	6.24 Binning into geometric regions using a $k$ -means algorithm for same-sign dilepton (left) and three leptons (right). . . . .	181
194	6.25 Final bins using a $k$ -means algorithm for same-sign dilepton (left) and three leptons (right). Note that the bin numbering here is such that signal- like bins are lower. . . . .	182
197	B.1 Distributions of input variables to the BDT for signal discrimination, two lepton same sign channel. . . . .	190
199	B.2 BDT input variables. Discrimination against $t\bar{t}$ in $2lss$ channel. . . . .	191
200	B.3 BDT input variables. Discrimination against $t\bar{t}V$ in $2lss$ channel. . . . .	192
201	B.4 BDT input variables. Discrimination against $t\bar{t}$ in $3l$ channel. . . . .	193
202	B.5 BDT input variables. Discrimination against $t\bar{t}V$ in $3l$ channel. . . . .	194

## <sup>203</sup> List of Tables

204	1.1	Fermions of the SM. . . . .	4
205	1.2	Fermion masses. . . . .	5
206	1.3	Lepton properties. . . . .	7
207	1.4	Quark properties. . . . .	8
208	1.5	Fermion weak isospin and weak hypercharge multiplets. . . . .	9
209	1.6	Fundamental interactions features. . . . .	14
210	1.7	SM gauge bosons. . . . .	18
211	1.8	Higgs boson properties. . . . .	36
212	1.9	Predicted branching ratios for a SM Higgs boson with $m_H = 125 \text{ GeV}/c^2$ . . . . .	41
213	1.10	Predicted SM cross sections for $tH$ production at $\sqrt{s} = 13 \text{ TeV}$ . . . . .	46
214	1.11	Predicted enhancement of the $tHq$ and $tHW$ cross sections at LHC . . . . .	49
215	6.1	Trigger efficiency scale factors and associated uncertainties. . . . .	142
216	6.2	MC signal samples. . . . .	144
217	6.3	Effective areas, for electrons and muons. . . . .	150
218	6.4	Requirements on each of the three muon selections. . . . .	152
219	6.5	Criteria for each of the three electron selections. . . . .	153
220	6.6	Summary of event selection. . . . .	158
221	6.7	BDTG input variables. . . . .	168

222	6.8 Configuration used in the final BDTG training. . . . .	172
223	6.9 Input variables ranking for BDTG classifiers . . . . .	173
224	6.10 ROC-integral for all the testing cases. . . . .	175
225	6.11 Limit variation as a function of tighter cuts. The baseline selection cor-	
226	responds to a looser selection as the one reported in Tab. ?? (which is	
227	the optimal selection determined here (last line)), where only a CSV-loose	
228	-tagged jet is required, and the veto is loosened to $\pm 10$ . . . . .	177
229	6.12 Limit variation as a function of bin size in the three lepton channel. (In	
230	bold: the final bin borders used in the analysis.) . . . . .	179
231	6.13 Limit variation as a function of bin size in the same-sign dimuon channel.	
232	(In bold: the final bin borders used in the analysis.) . . . . .	179
233	6.14 The 33 distinct values of $\kappa_t/\kappa_V$ and $f_t$ as mapped by the 51 $\kappa_t$ and $\kappa_V$	
234	points. . . . .	184
235	A.1 Full 2016 dataset. . . . .	185
236	A.2 HLT . . . . .	186
237	A.3 $\kappa_V$ and $\kappa_t$ combinations. . . . .	187
238	A.4 List of background samples used in this analysis (CMSSW 80X). . . . .	188

<sup>239</sup> **Chapter 1**

<sup>240</sup> **Theoretical approach**

<sup>241</sup> **1.1 Introduction**

<sup>242</sup> The physical description of the universe is a challenge that physicists have faced by  
<sup>243</sup> making theories that refine existing principles and proposing new ones in an attempt  
<sup>244</sup> to embrace emerging facts and phenomena.

<sup>245</sup> At the end of 1940s Julian Schwinger [1] and Richard P. Feynman [2], based on  
<sup>246</sup> the work of Sin-Itiro Tomonaga [3], developed an electromagnetic theory consistent  
<sup>247</sup> with special relativity and quantum mechanics that describes how matter and light  
<sup>248</sup> interact; the so-called *quantum electrodynamics* (QED) was born.

<sup>249</sup> QED has become the blueprint for developing theories that describe the universe.  
<sup>250</sup> It was the first example of a quantum field theory (QFT), which is the theoretical  
<sup>251</sup> framework for building quantum mechanical models that describes particles and their  
<sup>252</sup> interactions. QFT is composed of a set of mathematical tools that combines classical  
<sup>253</sup> fields, special relativity and quantum mechanics, while keeping the quantum point  
<sup>254</sup> particles and locality ideas.

<sup>255</sup> This chapter gives an overview of the standard model of particle physics, starting

256 with a description of the particles and their interactions, followed by a description of  
 257 the electroweak interaction, the Higgs boson and the associated production of Higgs  
 258 boson and a single top quark ( $tH$ ). The description contained in this chapter is based  
 259 on References [4–6].

## 260 1.2 Standard model of particle physics

261 The *standard model of particle physics (SM)* describes particle physics at the funda-  
 262 mental level in terms of a collection of interacting particles and fields. The full picture  
 263 of the SM is composed of three fields<sup>1</sup> whose excitations are interpreted as particles  
 264 called mediators or force-carriers, a set of fields whose excitations are interpreted as  
 265 elementary particles interacting through the exchange of those mediators, and a field  
 266 that gives the mass to elementary particles. Figure 1.1 shows a scheme of the SM  
 267 particles’ organization. In addition, for each of the particles in the scheme there exists  
 268 an antiparticle with the same mass and opposite quantum numbers. The existence of  
 269 antiparticles is a prediction of the relativistic quantum mechanics from the solution  
 270 of the Dirac equation for which a negative energy solution is also possible. In some  
 271 cases a particle is its own anti-particle, like photon or Higgs boson.

272 The mathematical formulation of the SM is based on group theory and the use of  
 273 Noether’s theorem [8] which states that for a physical system modeled by a Lagrangian  
 274 that is invariant under a group of transformations a conservation law is expected. For  
 275 instance, a system described by a time-independent Lagrangian is invariant (symmet-  
 276 ric) under time changes (transformations) with the total energy conservation law as  
 277 the expected conservation law. In QED, the charge operator ( $Q$ ) is the generator of

---

<sup>1</sup> The formal and complete treatment of the SM is out of the scope of this document, however a plenty of textbooks describing it at several levels are available in the literature. The treatment in References [5, 6] is quite comprehensive and detailed. Note that gravitational field is not included in the standard model formulation

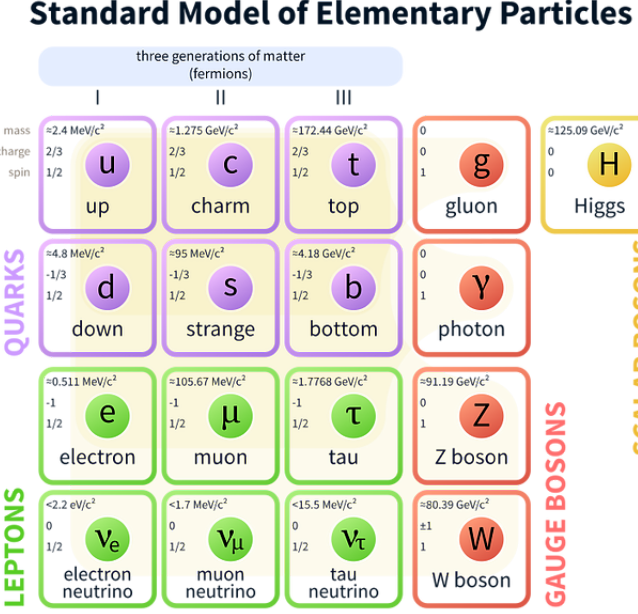


**Figure 1.1:** Schematic representation of the Standard Model of particle physics. The SM is a theoretical model intended to describe three of the four fundamental forces of the universe in terms of a set of particles and their interactions. [7].

278 the  $U(1)$  symmetry which according to the Noether's theorem means that there is a  
 279 conserved quantity; this conserved quantity is the electric charge and thus the law  
 280 conservation of electric charge is established.

281 In the SM, the symmetry group  $SU(3)_C \otimes SU(2)_L \otimes U(1)_Y$  describes three of the  
 282 four fundamental interactions in nature (see Section 1.2.2): strong interaction (SI),  
 283 weak interaction (WI) and electromagnetic interactions (EI) in terms of symmetries  
 284 associated to physical quantities:

- 285     • Strong:  $SU(3)_C$  associated to color charge
  - 286     • Weak:  $SU(2)_L$  associated to weak isospin and chirality
  - 287     • Electromagnetic:  $U(1)_Y$  associated to weak hypercharge and electric charge
- 288 It will be shown that the electromagnetic and weak interactions are combined in

289 the so-called electroweak interaction where chirality, hypercharge, weak isospin and  
 290 electric charge are the central concepts.

291 **1.2.1 Fermions**

292 The basic constituents of the ordinary matter at the lowest level, which form the set  
 293 of elementary particles in the SM formulation, are quarks and leptons. All of them  
 294 have spin 1/2, therefore they are classified as fermions since they obey Fermi-Dirac  
 295 statistics. There are six *flavors* of quarks and three of leptons organized in three  
 296 generations, or families, as shown in Table 1.1.

		Generation		
		1st	2nd	3rd
Leptons	Type	Charged	Electron (e)	Moun( $\mu$ )
	Neutral	Neutral	Electron neutrino ( $\nu_e$ )	Muon neutrino ( $\nu_\mu$ )
Quarks	Up-type	Up (u)	Charm (c)	Top (t)
	Down-type	Down (d)	Strange (s)	Bottom (b)

**Table 1.1:** Fermions of the SM. There are six flavors of quarks and three of leptons, organized in three generations, or families, composed of two pairs of closely related particles. The close relationship is motivated by the fact that each pair of particles is a member of an  $SU(2)_L$  doublet that has an associated invariance under isospin transformations. WI between leptons is limited to the members of the same generation; WI between quarks is not limited but greatly favored, to same generation members.

297

298 There is a mass hierarchy between generations (see Table 1.2), where the higher  
 299 generation particles decays to the lower one, which can explain why the ordinary  
 300 matter is made of particles from the first generation. In the SM, neutrinos are modeled  
 301 as massless particles so they are not subject to this mass hierarchy; however, today it  
 302 is known that neutrinos are massive so the hierarchy could be restated. The reason  
 303 behind this mass hierarchy is one of the most important open questions in particle  
 304 physics, and it becomes more puzzling when noticing that the mass difference between

305 first and second generation fermions is small compared to the mass difference with  
 306 respect to the third generation.

Lepton	Mass (MeV/c <sup>2</sup> )	Quark	Mass (MeV/c <sup>2</sup> )
e	0.51	u	2.2
$\mu$	105.65	c	$1.28 \times 10^3$
$\tau$	1776.86	t	$173.1 \times 10^3$
$\nu_e$	Unknown	d	4.7
$\nu_\mu$	Unknown	s	96
$\tau_\mu$	Unknown	b	$4.18 \times 10^3$

**Table 1.2:** Fermion masses [9]. Generations differ by mass in a way that has been interpreted as a mass hierarchy. Approximate values with no uncertainties are used, for comparison purpose.

307

308        Usually, the second and third generation fermions are produced in high energy  
 309 processes, like the ones recreated in particle accelerators.

310 **1.2.1.1 Leptons**

311 A lepton is an elementary particle that is not subject to the SI. As seen in Table 1.1,  
 312 there are two types of leptons, the charged ones (electron, muon and tau) and the  
 313 neutral ones (the three neutrinos). The electric charge (Q) is the property that gives  
 314 leptons the ability to participate in the EI. From the classical point of view, Q plays  
 315 a central role determining, among others, the strength of the electric field through  
 316 which the electromagnetic force is exerted. It is clear that neutrinos are not affected  
 317 by EI because they don't carry electric charge.

318        Another feature of the leptons that is fundamental in the mathematical description  
 319 of the SM is the chirality, which is closely related to spin and helicity. Helicity  
 320 defines the handedness of a particle by relating its spin and momentum such that  
 321 if they are parallel then the particle is right-handed; if spin and momentum are

322 antiparallel the particle is said to be left-handed. The study of parity conservation  
 323 (or violation) in  $\beta$ -decay has shown that only left-handed electrons/neutrinos or right-  
 324 handed positrons/anti-neutrinos are created [10]; the inclusion of that feature in the  
 325 theory was achieved by using projection operators for helicity, however, helicity is  
 326 frame dependent for massive particles which makes it not Lorentz invariant and then  
 327 another related attribute has to be used: *chirality*.

328 Chirality is a purely quantum attribute which makes it not so easy to describe in  
 329 graphical terms but it defines how the wave function of a particle transforms under  
 330 certain rotations. As with helicity, there are two chiral states, left-handed chiral (L)  
 331 and right-handed chiral (R). In the highly relativistic limit where  $E \approx p \gg m$  helicity  
 332 and chirality converge, becoming exactly the same for massless particles.

333 In the following, when referring to left-handed (right-handed) it will mean left-  
 334 handed chiral (right-handed chiral). The fundamental fact about chirality is that  
 335 while EI and SI are not sensitive to chirality, in WI left-handed and right-handed  
 336 fermions are treated asymmetrically, such that only left-handed fermions and right-  
 337 handed anti-fermions are allowed to couple to WI mediators, which is a violation of  
 338 parity. The way to translate this statement in a formal mathematical formulation is  
 339 based on the isospin symmetry group  $SU(2)_L$ .

340 Each generation of leptons is seen as a weak isospin doublet.<sup>2</sup> The left-handed  
 341 charged lepton and its associated left-handed neutrino are arranged in doublets of  
 342 weak isospin  $T=1/2$  while their right-handed partners are singlets:

$$\begin{pmatrix} \nu_l \\ l \end{pmatrix}_L, l_R := \begin{pmatrix} \nu_e \\ e \end{pmatrix}_L, \begin{pmatrix} \nu_\mu \\ \mu \end{pmatrix}_L, \begin{pmatrix} \nu_\tau \\ \tau \end{pmatrix}_L, e_R, \mu_R, \tau_R, \nu_{eR}, \nu_{\mu R}, \nu_{\tau R} \quad (1.1)$$

343 The isospin third component refers to the eigenvalues of the weak isospin operator

---

<sup>2</sup> The weak isospin is an analogy of the isospin symmetry in strong interaction where neutron and proton are affected equally by strong force but differ in their charge.

344 which for doublets is  $T_3 = \pm 1/2$ , while for singlets it is  $T_3 = 0$ . The physical meaning  
 345 of this doublet-singlet arrangement falls in that the WI couples the two particles in  
 346 the doublet by exchanging the interaction mediator while the singlet member is not  
 347 involved in WI. The main properties of the leptons are summarized in Table 1.3.

348 Although all three flavor neutrinos have been observed, their masses remain un-  
 349 known and only some estimations have been made [11]. The main reason is that  
 350 the flavor eigenstates are not the same as the mass eigenstates which implies that  
 351 when a neutrino is created its mass state is a linear combination of the three mass  
 352 eigenstates and experiments can only probe the squared difference of the masses. The  
 353 Pontecorvo-Maki-Nakagawa-Sakata (PMNS) mixing matrix encodes the relationship  
 354 between flavor and mass eigenstates.

Lepton	$Q(e)$	$T_3$	$L_e$	$L_\mu$	$L_\tau$	Lifetime (s)
Electron (e)	-1	-1/2	1	0	0	Stable
Electron neutrino( $\nu_e$ )	0	1/2	1	0	0	Unknown
Muon ( $\mu$ )	-1	-1/2	0	1	0	$2.19 \times 10^{-6}$
Muon neutrino ( $\nu_\mu$ )	0	1/2	0	1	0	Unknown
Tau ( $\tau$ )	-1	-1/2	0	0	1	$290.3 \times 10^{-15}$
Tau neutrino ( $\nu_\tau$ )	0	1/2	0	0	1	Unknown

**Table 1.3:** Lepton properties [9]. Q: electric charge,  $T_3$ : weak isospin. Only left-handed leptons and right-handed anti-leptons participate in the WI. Anti-particles with inverted  $T_3$ , Q and lepton number complete the leptons set but are not listed. Right-handed leptons and left-handed anti-leptons, neither listed, form weak isospin singlets with  $T_3 = 0$  and do not take part in the weak interaction.

355

### 356 1.2.1.2 Quarks

357 Quarks are the basic constituents of protons and neutrons. The way quarks join to  
 358 form bound states, called *hadrons*, is through the SI. Quarks are affected by all the  
 359 fundamental interactions which means that they carry all the four types of charges:  
 360 color, electric charge, weak isospin and mass.

Flavor	$Q(e)$	$I_3$	$T_3$	B	C	S	T	$B'$	Y	Color
Up (u)	2/3	1/2	1/2	1/3	0	0	0	0	1/3	r,b,g
Charm (c)	2/3	0	1/2	1/3	1	0	0	0	4/3	r,b,g
Top(t)	2/3	0	1/2	1/3	0	0	1	0	4/3	r,b,g
Down(d)	-1/3	-1/2	-1/2	1/3	0	0	0	0	1/3	r,b,g
Strange(s)	-1/3	0	-1/2	1/3	0	-1	0	0	-2/3	r,b,g
Bottom(b)	-1/3	0	-1/2	1/3	0	0	0	-1	-2/3	r,b,g

**Table 1.4:** Quark properties [9]. Q: electric charge,  $I_3$ : isospin,  $T_3$ : weak isospin, B: baryon number, C: charmness, S: strangeness, T: topness,  $B'$ : bottomness, Y: hypercharge. Anti-quarks posses the same mass and spin as quarks but all charges (color, flavor numbers) have opposite sign.

361

362     Table 1.4 summarizes the features of quarks, among which the most remarkable  
 363    is their fractional electric charge. Note that fractional charge is not a problem, given  
 364    that quarks are not found isolated, but serves to explain how composed particles are  
 365    formed out of two or more valence quarks<sup>3</sup>.

366     Color charge is responsible for the SI between quarks and is the symmetry ( $SU(3)_C$ )  
 367    that defines the formalism to describe SI. There are three colors: red (r), blue (b)  
 368    and green (g) and their corresponding three anti-colors; thus each quark carries one  
 369    color unit while anti-quarks carries one anti-color unit. As explained in Section 1.2.2,  
 370    quarks are not allowed to be isolated due to the color confinement effect, hence, their  
 371    features have been studied indirectly by observing their bound states created when

- 372       • one quark with a color charge is attracted by an anti-quark with the correspond-  
 373       ing anti-color charge forming a colorless particle called a *meson*.  
  
 374       • three quarks (anti-quarks) with different color (anti-color) charges are attracted  
 375       among them forming a colorless particle called a *baryon (anti-baryon)*.

<sup>3</sup> Hadrons can contain an indefinite number of virtual quarks and gluons, known as the quark and gluon sea, but only the valence quarks determine hadrons' quantum numbers.

376 In practice, when a quark is left alone isolated a process called *hadronization* occurs  
 377 where the quark emits gluons (see Section 1.2.4) which eventually will generate new  
 378 quark-antiquark pairs and so on; those quarks will recombine to form hadrons that  
 379 will decay into leptons. This proliferation of particles looks like a *jet* coming from  
 380 the isolated quark. More details about the hadronization process and jet structure  
 381 will be given in chapter3.

382 In the first version of the quark model (1964), M. Gell-Mann [12] and G. Zweig  
 383 [13, 14] developed a consistent way to classify hadrons according to their properties.  
 384 Only three quarks (u, d, s) were involved in a scheme in which all baryons have baryon  
 385 number  $B=1$  and therefore quarks have  $B=1/3$ ; non-baryons have  $B=0$ . Baryon  
 386 number is conserved in SI and EI which means that single quarks cannot be created  
 387 but in pairs  $q - \bar{q}$ .

388 The scheme organizes baryons in a two-dimensional space ( $I_3$  - Y); Y (hyper-  
 389 charge) and  $I_3$  (isospin) are quantum numbers related by the Gell-Mann-Nishijima  
 390 formula [15, 16]:

$$Q = I_3 + \frac{Y}{2} \quad (1.2)$$

391 where  $Y = B + S + C + T + B'$  are the quantum numbers listed in Table 1.4.

392 There are six quark flavors organized in three generations (see Table 1.1) fol-  
 393 lowing a mass hierarchy which, again, implies that higher generations decay to first  
 394 generation quarks.

	Quarks			$T_3$	$Y_W$	Leptons			$T_3$	$Y_W$
Doublets	$(\frac{u}{d'})_L$	$(\frac{c}{s'})_L$	$(\frac{t}{b'})_L$	$(\frac{1/2}{-1/2})$	$1/3$	$(\nu_e)_L$	$(\nu_\mu)_L$	$(\nu_\tau)_L$	$(\frac{1/2}{-1/2})$	-1
Singlets	$u_R$	$c_R$	$t_R$	0	$4/3$	$\nu_{eR}$	$\nu_{\mu R}$	$\nu_{\tau R}$		
	$d'_R$	$s'_R$	$b'_R$	0	$-2/3$	$e_R$	$\mu_R$	$\tau_R$	0	-2

**Table 1.5:** Fermion weak isospin and weak hypercharge multiplets. Weak hypercharge is calculated through the Gell-Mann-Nishijima formula 1.2 but using the weak isospin and charge for quarks.

395

396 Isospin doublets of quarks are also defined (see Table 1.5), and same as for neutrinos,  
 397 the WI eigenstates are not the same as the mass eigenstates which means that  
 398 members of different quark generations are connected by the WI mediator; thus, up-  
 399 type quarks are coupled not to down-type quarks (the mass eigenstates) directly but  
 400 to a superposition of down-type quarks ( $q'_d$ ; *the weak eigenstates*) via WI according  
 401 to:

$$402 \quad q'_d = V_{CKM} q_d$$

$$\begin{pmatrix} d' \\ s' \\ b' \end{pmatrix} = \begin{pmatrix} V_{ud} & V_{us} & V_{ub} \\ V_{cd} & V_{cs} & V_{cb} \\ V_{td} & V_{ts} & V_{tb} \end{pmatrix} \begin{pmatrix} d \\ s \\ b \end{pmatrix} \quad (1.3)$$

403 where  $V_{CKM}$  is known as Cabibbo-Kobayashi-Maskawa (CKM) mixing matrix [17,18]  
 404 given by

$$\begin{pmatrix} |V_{ud}| & |V_{us}| & |V_{ub}| \\ |V_{cd}| & |V_{cs}| & |V_{cb}| \\ |V_{td}| & |V_{ts}| & |V_{tb}| \end{pmatrix} = \begin{pmatrix} 0.97427 \pm 0.00015 & 0.22534 \pm 0.00065 & 0.00351^{+0.00015}_{-0.00014} \\ 0.22520 \pm 0.00065 & 0.97344 \pm 0.00016 & 0.0412^{+0.0011}_{-0.0005} \\ 0.00867^{+0.00029}_{-0.00031} & 0.0404^{+0.0011}_{-0.0005} & 0.999146^{+0.000021}_{-0.000046} \end{pmatrix}. \quad (1.4)$$

405 The weak decays of quarks are represented in the diagram of Figure 1.2; again  
 406 the CKM matrix plays a central role since it contains the probabilities for the differ-  
 407 ent quark decay channels, in particular, note that quark decays are greatly favored  
 408 between generation members.

409 CKM matrix is a  $3 \times 3$  unitary matrix parametrized by three mixing angles and  
 410 the *CP-mixing phase*; the latter is the parameter responsible for the Charge-Parity

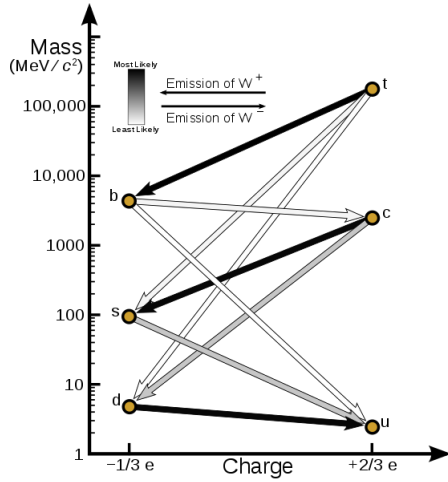


**Figure 1.2:** Transformations between quarks through the exchange of a WI. Higher generations quarks decay to first generation quarks by emitting a W boson. The arrow color indicates the likelihood of the transition according to the grey scale in the top left side which represent the CKM matrix parameters [19].

411 symmetry violation (CP-violation) in the SM. The fact that the top quark decays  
 412 almost all the time to a bottom quark is exploited in this thesis when making the  
 413 selection of the signal events by requiring the presence of a jet tagged as a jet coming  
 414 from a  $b$  quark in the final state.

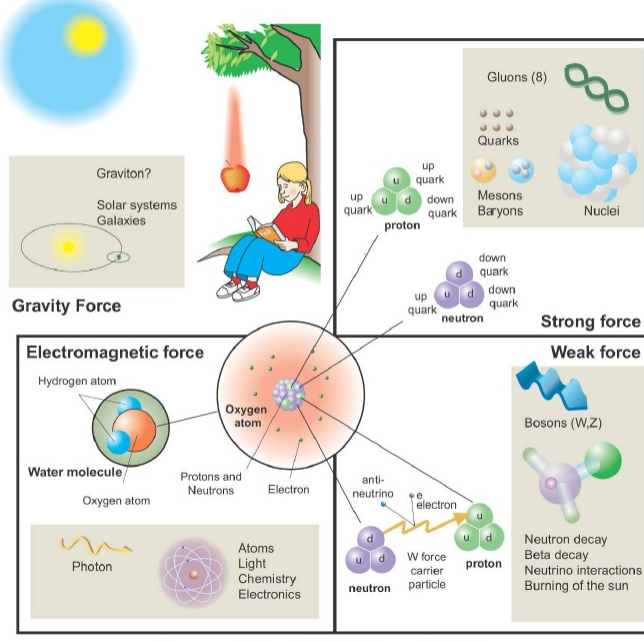
### 415 1.2.2 Fundamental interactions

416 Even though there are many manifestations of force in nature, like the ones repre-  
 417 sented in Figure 1.3, we can classify all of them in four fundamental interactions:

- 418 • *Electromagnetic interaction (EI)* affects particles that are *electrically charged*,  
 419 like electrons and protons. Figure 1.4a. shows a graphical representation, known  
 420 as *Feynman diagram*, of electron-electron scattering.
- 421 • *Strong interaction (SI)* described by Quantum Chromodynamics (QCD). Hadrons  
 422 like the proton and the neutron have internal structure given that they are com-

## Fundamental interactions.

Illustration: Typoform



Summer School KPI 15 August 2009

**Figure 1.3:** Fundamental interactions in nature. Despite the many manifestations of forces in nature, we can track all of them back to one of the fundamental interactions. The most common forces are gravity and electromagnetic given that all of us are subject and experience them in everyday life.

423        posed of two or more valence quarks<sup>4</sup>. Quarks have fractional electric charge  
 424        which means that they are subject to electromagnetic interaction and in the case  
 425        of the proton they should break apart due to electrostatic repulsion; however,  
 426        quarks are held together inside the hadrons against their electrostatic repulsion  
 427        by the *Strong Force* through the exchange of *gluons*. The analog to the electric  
 428        charge is the *color charge*. Electrons and photons are elementary particles as  
 429        quarks but they don't carry color charge, therefore they are not subject to SI. A  
 430        Feynman diagram for gluon exchange between quarks is shown in Figure 1.4b.  
  
 431        • *Weak interaction (WI)* described by the weak theory (WT), is responsible, for  
 432        instance, for the radioactive decay in atoms and the deuterium production

<sup>4</sup> Particles made of four and five quarks are exotic states not so common.

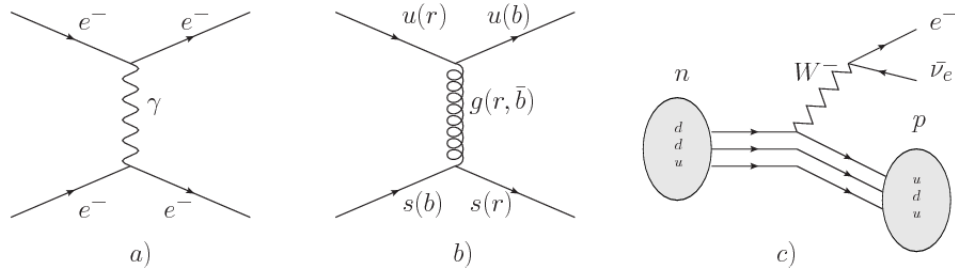


**Figure 1.4:** Feynman diagrams representing the interactions in SM; a) EI:  $e$ - $e$  scattering; b) SI: gluon exchange between quarks ; c) WI:  $\beta$ -decay

within the sun. Quarks and leptons are the particles affected by the weak interaction; they possess a property called *flavor charge* (see 1.2.1) which can be changed by emitting or absorbing one weak force mediator. There are three mediators of the *weak force* known as  $Z$  boson in the case of electrically neutral flavor changes and  $W^\pm$  bosons in the case of electrically charged flavor changes. The *weak isospin* is the WI analog to electric charge in EI, and color charge in SI, and defines how quarks and leptons are affected by the weak force. Figure 1.4c. shows the Feynman diagram of  $\beta$ -decay where a neutron ( $n$ ) is transformed in a proton ( $p$ ) by emitting a  $W^-$  particle.

- *Gravitational interaction (GI)* described by General Theory of Relativity (GR). It is responsible for the structure of galaxies and black holes as well as the expansion of the universe. As a classical theory, in the sense that it can be formulated without even appeal to the concept of quantization, it implies that the space-time is a continuum and predictions can be made without limitation to the precision of the measurement tools. The latter represents a direct contradiction of the quantum mechanics principles. Gravity is deterministic while quantum mechanics is probabilistic; despite that, efforts to develop a quantum theory of gravity have predicted the *graviton* as mediator of the gravitational

451 force<sup>5</sup>.

Interaction	Acts on	Relative strength	Range (m)	Mediators
Electromagnetic (QED)	Electrically charged particles	$10^{-2}$	Infinite	Photon
Strong (QCD)	Quarks and gluons	1	$10^{-15}$	Gluon
Weak (WI)	Leptons and quarks	$10^{-6}$	$10^{-18}$	$W^\pm, Z$
Gravitational (GI)	Massive particles	$10^{-39}$	Infinite	Graviton

Table 1.6: Fundamental interactions features [20].

452

453 Table 1.6 summarizes the main features of the fundamental interactions. The  
 454 strength of the interactions is represented by the coupling constants which depend  
 455 on the energy scale at which the interaction is evaluated, therefore, it is the relative  
 456 strength of the fundamental forces that reveals the meaning of strong and weak; in  
 457 a context where the relative strength of the SI is 1, the EI is about hundred times  
 458 weaker and WI is about million times weaker than the SI. A good description on how  
 459 the relative strength and range of the fundamental interactions are calculated can  
 460 be found in References [20, 21]. In the everyday life, only EI and GI are explicitly  
 461 experienced due to the range of these interactions; i.e., at the human scale distances  
 462 only EI and GI have appreciable effects, in contrast to SI which at distances greater  
 463 than  $10^{-15}$ m become negligible. Is it important to clarify that the weakness of the  
 464 WI is attributed to the fact that its mediators are highly massive which affects the  
 465 propagators of the interaction, as a result, the effect of the coupling constant is  
 466 reduced.

---

<sup>5</sup> Actually a wide variety of theories have been developed in an attempt to describe gravity; some famous examples are string theory and supergravity.

467 **1.2.3 Gauge invariance.**

468 QED was built successfully on the basis of the classical electrodynamics theory (CED)  
 469 of Maxwell and Lorentz, following theoretical and experimental requirements imposed  
 470 by

- 471     • Lorentz invariance: independence on the reference frame.
- 472     • Locality: interacting fields are evaluated at the same space-time point to avoid  
     473       action at a distance.
- 474     • Renormalizability: physical predictions are finite and well defined.
- 475     • Particle spectrum, symmetries and conservation laws already known must emerge  
     476       from the theory.
- 477     • Local gauge invariance.

478 The gauge invariance requirement reflects the fact that the fundamental fields  
 479 cannot be directly measured but associated fields which are the observables. Electric  
 480 (**E**) and magnetic (**B**) fields in CED are associated with the electric scalar potential  
 481  $V$  and the vector potential **A**. In particular, **E** can be obtained by measuring the  
 482 change in the space of the scalar potential ( $\Delta V$ ); however, two scalar potentials  
 483 differing by a constant  $f$  correspond to the same electric field. The same happens  
 484 in the case of the vector potential **A**; thus, different configurations of the associated  
 485 fields result in the same set of values of the observables. The freedom in choosing one  
 486 particular configuration is known as *gauge freedom*; the transformation law connecting  
 487 two configurations is known as *gauge transformation* and the fact that the observables  
 488 are not affected by a gauge transformation is called *gauge invariance*.

489 When the gauge transformation:

$$\begin{aligned} \mathbf{A} &\rightarrow \mathbf{A} - \Delta f \\ V &\rightarrow V - \frac{\partial f}{\partial t} \end{aligned} \tag{1.5}$$

490 is applied to Maxwell equations, they are still satisfied and the fields remain invariant.  
 491 Thus, CED is invariant under gauge transformations and is called a *gauge theory*.  
 492 The set of all gauge transformations form the *symmetry group* of the theory, which  
 493 according to the group theory, has a set of *group generators*. The number of group  
 494 generators determine the number of *gauge fields* of the theory.

495 As mentioned in the first lines of Section 1.2, QED has one symmetry group ( $U(1)$ )  
 496 with one group generator (the  $Q$  operator) and one gauge field (the electromagnetic  
 497 field  $A^\mu$ ). In CED there is not a clear definition, beyond the historical convention,  
 498 of which fields are the fundamental and which are the associated, but in QED the  
 499 fundamental field is  $A^\mu$ . When a gauge theory is quantized, the gauge fields are  
 500 quantized and their quanta are called *gauge bosons*. The word boson characterizes  
 501 particles with integer spin which obey Bose-Einstein statistics.

502 As will be detailed in Section 1.3, interactions between particles in a system can  
 503 be obtained by considering first the Lagrangian density of free particles in the sys-  
 504 tem, which of course is incomplete because the interaction terms have been left out,  
 505 and demanding global phase transformation invariance. Global phase transforma-  
 506 tion means that a gauge transformation is performed identically to every point  
 507 in the space<sup>6</sup> and the Lagrangian remains invariant. Then, the global transforma-  
 508 tion is promoted to a local phase transformation (this time the gauge transformation  
 509 depends on the position in space) and again invariance is required.

---

<sup>6</sup> Here space corresponds to the 4-dimensional space i.e. space-time.

510 Due to the space dependence of the local transformation, the Lagrangian density is  
 511 not invariant anymore. In order to reinstate the gauge invariance, the gauge covariant  
 512 derivative is introduced in the Lagrangian and with it the gauge field responsible for  
 513 the interaction between particles in the system. The new Lagrangian density is gauge  
 514 invariant, includes the interaction terms needed to account for the interactions and  
 515 provides a way to explain the interaction between particles through the exchange of  
 516 the gauge boson.

517 This recipe was used to build QED and the theories that aim to explain the  
 518 fundamental interactions.

### 519 1.2.4 Gauge bosons

520 The importance of the gauge bosons comes from the fact that they are the force  
 521 mediators or force carriers. The features of the gauge bosons reflect those of the fields  
 522 they represent and they are extracted from the Lagrangian density used to describe  
 523 the interactions. In Section 1.3, it will be shown how the gauge bosons of the EI and  
 524 WI emerge from the electroweak Lagrangian. The SI gauge bosons features are also  
 525 extracted from the SI Lagrangian but it is not detailed in this document. The main  
 526 features of the SM gauge bosons will be briefly presented below and summarized in  
 527 Table 1.7.

- 528     • **Photon.** EI occurs when the photon couples to (is exchanged between) parti-  
 529       cles carrying electric charge; however, The photon itself does not carry electric  
 530       charge, therefore, there is no coupling between photons. Given that the photon  
 531       is massless the EI is of infinite range, i.e., electrically charged particles interact  
 532       even if they are located far away one from each other; this also implies that  
 533       photons always move with the speed of light.

- 534     • **Gluon.** SI is mediated by gluons which just as photons are massless. They  
 535       carry one unit of color charge and one unit of anticolor charge, hence, gluons  
 536       can couple to other gluons. As a result, the range of the SI is not infinite  
 537       but very short due to the attraction between gluons, giving rise to the *color*  
 538       *confinement* which explains why color charged particles cannot be isolated but  
 539       live within composite particles, like quarks inside protons.
- 540     • **W, Z.**  $W^\pm$  and Z, are massive which explains their short-range. Given that  
 541       the WI is the only interaction that can change the flavor of the interacting  
 542       particles, the W boson is the responsible for the nuclear transmutation where  
 543       a neutron is converted into a proton or vice versa with the involvement of an  
 544       electron and a neutrino (see Figure 1.4c). The Z boson is the responsible for the  
 545       neutral weak processes like neutrino elastic scattering where no electric charge  
 546       but momentum transference is involved. WI gauge bosons carry isospin charge  
 547       which makes interaction between them possible.

Interaction	Mediator	Electric charge (e)	Color charge	Weak Isospin	mass (GeV/c <sup>2</sup> )
Electromagnetic	Photon ( $\gamma$ )	0	No	0	0
Strong	Gluon (g)	0	Yes -octet	No	0
Weak	$W^\pm$	$\pm 1$	No	$\pm 1$	$80.385 \pm 0.015$
	Z	0	No	0	$91.188 \pm 0.002$

**Table 1.7:** SM gauge bosons main features [9].

548

### 549    1.3 Electroweak unification and the Higgs 550       mechanism

551    Physicists dream of building a theory that contains all the interactions in one single  
 552    interaction, i.e., showing that at some scale in energy all the four fundamental inter-

actions are unified and only one interaction emerges in a *Theory of everything*. The first sign of the feasibility of such unification came from success in the construction of the CED. Einstein spent years trying to reach that full unification, which by 1920 only involved electromagnetism and gravity, with no success; however, a new partial unification was achieved in the 1960's, when S.Glashow [22], A.Salam [23] and S.Weinberg [24] independently proposed that electromagnetic and weak interactions are two manifestations of a more general interaction called *electroweak interaction* (EWI). EWI was developed by following the useful prescription provided by QED and the gauge invariance principles.

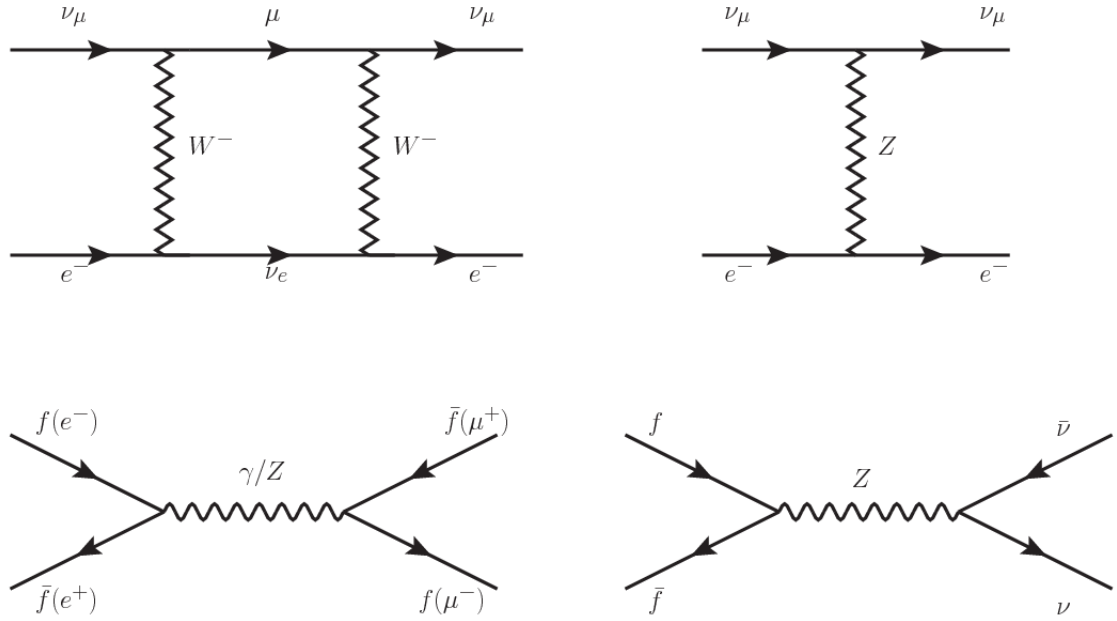


**Figure 1.5:** Top:  $\nu_\mu - e^-$  scattering going through charged currents (left) and neutral currents (right). Bottom: neutral current processes for charged fermions (left) and involving neutrinos (right). While neutral current processes involving only charged fermions can proceed through EI or WI, those involving neutrinos can only proceed via WI.

The *classic* weak theory developed by Fermi, did not have the concept of the W boson but instead it was treated as a point interaction with the dimensionful constant  $G_F$  associated with it. It works really well at low energies very far off the W mass

565 shell. When going up in energy, the theory of weak interactions involving the W  
 566 boson is capable of explaining the  $\beta$ -decay and in general the processes mediated by  
 567  $W^\pm$  bosons. However, there were some processes like the  $\nu_\mu - e$  scattering which  
 568 would require the exchange of two W bosons (see Figure 1.5 top diagrams) giving  
 569 rise to divergent loop integrals and then non-finite predictions. The EWI theory, by  
 570 including neutral currents involving fermions via the exchange of a neutral bosons Z,  
 571 overcomes those divergences and the predictions become realistic.

572 Neutral weak interaction vertices conserve flavor in the same way as the electro-  
 573 magnetic vertices do, but additionally, the Z boson can couple to neutrinos which  
 574 implies that processes involving charged fermions can proceed through EI or WI but  
 575 processes involving neutrinos can proceed only through WI.

576 The prescription to build a gauge theory of the WI consists of proposing a free  
 577 field Lagrangian density that includes the particles involved; next, by requesting  
 578 invariance under global phase transformations first and generalizing to local phase  
 579 transformations invariance later, the conserved currents are identified and interactions  
 580 are generated by introducing gauge fields. Given that the goal is to include the EI  
 581 and WI in a single theory, the group symmetry considered should be a combination of  
 582  $SU(2)_L$  and  $U(1)_{em}$ , however the latter cannot be used directly because the EI treats  
 583 left and right-handed particles indistinctly in contrast to the former. Fortunately, the  
 584 weak hypercharge, which is a combination of the weak isospin and the electric charge  
 585 (Eqn. 1.2) is suitable to be used since it is conserved by the EI and WI. Thus, the  
 586 symmetry group to be considered is

$$G \equiv SU(2)_L \otimes U(1)_Y \quad (1.6)$$

587 The following treatment applies to any of the fermion generations, but for sim-

588 plicity the first generation of leptons will be considered [5, 6, 25, 26].

589 Given the first generation of leptons

$$\psi_1 = \begin{pmatrix} \nu_e \\ e^- \end{pmatrix}_L, \quad \psi_2 = \nu_{eR}, \quad \psi_3 = e_R^- \quad (1.7)$$

590 the charged fermionic currents are given by

$$J_\mu \equiv J_\mu^+ = \bar{\nu}_{eL} \gamma_\mu e_L, \quad J_\mu^\dagger \equiv J_\mu^- = \bar{e}_L \gamma_\mu \nu_{eL} \quad (1.8)$$

591 and the free Lagrangian is given by

$$\mathcal{L}_0 = \sum_{j=1}^3 i\bar{\psi}_j(x) \gamma^\mu \partial_\mu \psi_j(x). \quad (1.9)$$

592 Mass terms are included directly in the QED free Lagrangians since they preserve  
 593 the invariance under the symmetry transformations involved which treat left and right  
 594 handed particles similarly, however mass terms of the form

$$m_W^2 W_\mu^\dagger(x) W^\mu(x) + \frac{1}{2} m_Z^2 Z_\mu(x) Z^\mu(x) - m_e \bar{\psi}_e(x) \psi_e(x) \quad (1.10)$$

595 which represent the mass of  $W^\pm$ , Z and electrons, are not invariant under G trans-  
 596 formations, therefore the gauge fields described by the EWI are in principle massless.

597 Experiments have shown that the EWI gauge fields are not massless [27–30];  
 598 however, they have to acquire mass through a mechanism compatible with the gauge  
 599 invariance; that mechanism is known as the *Higgs mechanism* and will be considered  
 600 later in this Section. The global transformations in the combined symmetry group G  
 601 can be written as

$$\begin{aligned}
\psi_1(x) &\xrightarrow{G} \psi'_1(x) \equiv U_Y U_L \psi_1(x), \\
\psi_2(x) &\xrightarrow{G} \psi'_2(x) \equiv U_Y \psi_2(x), \\
\psi_3(x) &\xrightarrow{G} \psi'_3(x) \equiv U_Y \psi_3(x)
\end{aligned} \tag{1.11}$$

602 where  $U_L$  represent the  $SU(2)_L$  transformation acting only on the weak isospin dou-  
 603 blet and  $U_Y$  represent the  $U(1)_Y$  transformation acting on all the weak isospin mul-  
 604 tiplets. Explicitly

$$U_L \equiv \exp\left(i \frac{\sigma_i}{2} \alpha^i\right), \quad U_Y \equiv \exp(i y_i \beta) \quad (i = 1, 2, 3) \tag{1.12}$$

605 with  $\sigma_i$  the Pauli matrices and  $y_i$  the weak hypercharges. In order to promote the  
 606 transformations from global to local while keeping the invariance, it is required that  
 607  $\alpha^i = \alpha^i(x)$ ,  $\beta = \beta(x)$  and the replacement of the ordinary derivatives by the covariant  
 608 derivatives

$$\begin{aligned}
D_\mu \psi_1(x) &\equiv \left[ \partial_\mu + ig\sigma_i W_\mu^i(x)/2 + ig'y_1 B_\mu(x) \right] \psi_1(x) \\
D_\mu \psi_2(x) &\equiv \left[ \partial_\mu + ig'y_2 B_\mu(x) \right] \psi_2(x) \\
D_\mu \psi_3(x) &\equiv \left[ \partial_\mu + ig'y_3 B_\mu(x) \right] \psi_3(x)
\end{aligned} \tag{1.13}$$

609 introducing in this way four gauge fields,  $W_\mu^i(x)$  and  $B_\mu(x)$ , in the process. The  
 610 covariant derivatives (Eqn. 1.13) are required to transform in the same way as fermion  
 611 fields  $\psi_i(x)$  themselves, therefore, the gauge fields transform as:

$$\begin{aligned} B_\mu(x) &\xrightarrow{G} B'_\mu(x) \equiv B_\mu(x) - \frac{1}{g'} \partial_\mu \beta(x) \\ W_\mu^i(x) &\xrightarrow{G} W_\mu^{i\prime}(x) \equiv W_\mu^i(x) - \frac{i}{g} \partial_\mu \alpha_i(x) - \varepsilon_{ijk} \alpha_i(x) W_\mu^j(x). \end{aligned} \quad (1.14)$$

612 The G invariant version of the Lagrangian density 1.9 can be written as

$$\mathcal{L}_0 = \sum_{j=1}^3 i \bar{\psi}_j(x) \gamma^\mu D_\mu \psi_j(x) \quad (1.15)$$

613 where free massless fermion and gauge fields and fermion-gauge boson interactions  
 614 are included. The EWI Lagrangian density must additionally include kinetic terms  
 615 for the gauge fields ( $\mathcal{L}_G$ ) which are built from the field strengths, according to

$$B_{\mu\nu}(x) \equiv \partial_\mu B_\nu - \partial_\nu B_\mu \quad (1.16)$$

$$W_{\mu\nu}^i(x) \equiv \partial_\mu W_\nu^i(x) - \partial_\nu W_\mu^i(x) - g \varepsilon^{ijk} W_\mu^j W_\nu^k \quad (1.17)$$

616 the last term in Eqn. 1.17 is added in order to hold the gauge invariance; therefore,

$$\mathcal{L}_G = -\frac{1}{4} B_{\mu\nu}(x) B^{\mu\nu}(x) - \frac{1}{4} W_{\mu\nu}^i(x) W_i^{\mu\nu}(x) \quad (1.18)$$

617 which contains not only the free gauge fields contributions, but also the gauge fields  
 618 self-interactions and interactions among them.

619 The three weak isospin conserved currents resulting from the  $SU(2)_L$  symmetry  
 620 are given by

$$J_\mu^i(x) = \frac{1}{2} \bar{\psi}_1(x) \gamma_\mu \sigma^i \psi_1(x) \quad (1.19)$$

621 while the weak hypercharge conserved current resulting from the  $U(1)_Y$  symmetry is  
 622 given by

$$J_\mu^Y = \sum_{j=1}^3 \bar{\psi}_j(x) \gamma_\mu y_j \psi_j(x) \quad (1.20)$$

623 In order to evaluate the electroweak interactions modeled by an isos triplet field  
 624  $W_\mu^i$  that couples to isospin currents  $J_\mu^i$  with strength  $g$  and additionally the singlet  
 625 field  $B_\mu$  which couples to the weak hypercharge current  $J_\mu^Y$  with strength  $g'/2$ . The  
 626 interaction Lagrangian density to be considered is

$$\mathcal{L}_I = -g J^{i\mu}(x) W_\mu^i(x) - \frac{g'}{2} J^{Y\mu}(x) B_\mu(x) \quad (1.21)$$

627 Note that the weak isospin currents are not the same as the charged fermionic cur-  
 628 rents that were used to describe the WI (Eqn. 1.8), since the weak isospin eigenstates  
 629 are not the same as the mass eigenstates, but they are closely related

$$J_\mu = \frac{1}{2}(J_\mu^1 + iJ_\mu^2), \quad J_\mu^\dagger = \frac{1}{2}(J_\mu^1 - iJ_\mu^2). \quad (1.22)$$

630 The same happens with the gauge fields  $W_\mu^i$  which are related to the mass eigen-  
 631 states  $W^\pm$  by

$$W_\mu^+ = \frac{1}{\sqrt{2}}(W_\mu^1 - iW_\mu^2), \quad W_\mu^- = \frac{1}{\sqrt{2}}(W_\mu^1 + iW_\mu^2). \quad (1.23)$$

632 The fact that there are three weak isospin conserved currents is an indication that  
 633 in addition to the charged fermionic currents, which couple charged to neutral leptons,  
 634 there should be a neutral fermionic current that does not involve electric charge  
 635 exchange; therefore, it couples neutral fermions or fermions of the same electric charge.  
 636 The third weak isospin current contains a term that is similar to the electromagnetic

637 current ( $j_\mu^{em}$ ), indicating that there is a relation between them and resembling the  
 638 Gell-Mann-Nishijima formula 1.2 adapted to electroweak interactions

$$Q = T_3 + \frac{Y_W}{2}. \quad (1.24)$$

639 Just as  $Q$  generates the  $U(1)_{em}$  symmetry, the weak hypercharge generates the  
 640  $U(1)_Y$  symmetry as said before. It is possible to write the relationship in terms of  
 641 the currents as

$$j_\mu^{em} = J_\mu^3 + \frac{1}{2} J_\mu^Y. \quad (1.25)$$

642 The neutral gauge fields  $W_\mu^3$  and  $B_\mu$  cannot be directly identified with the  $Z$   
 643 and the photon fields since the photon interacts similarly with left and right-handed  
 644 fermions; however, they are related through a linear combination given by

$$\begin{aligned} A_\mu &= B_\mu \cos \theta_W + W_\mu^3 \sin \theta_W \\ Z_\mu &= -B_\mu \sin \theta_W + W_\mu^3 \cos \theta_W \end{aligned} \quad (1.26)$$

where  $\theta_W$  is known as the *Weinberg angle*. The interaction Lagrangian is now given by

$$\begin{aligned} \mathcal{L}_I = -\frac{g}{\sqrt{2}}(J^\mu W_\mu^+ + J^{\mu\dagger} W_\mu^-) - &\left(g \sin \theta_W J_\mu^3 + g' \cos \theta_W \frac{J_\mu^Y}{2}\right) A^\mu \\ &- \left(g \cos \theta_W J_\mu^3 - g' \sin \theta_W \frac{J_\mu^Y}{2}\right) Z^\mu \end{aligned} \quad (1.27)$$

645 the first term is the weak charged current interaction, while the second term is the

646 electromagnetic interaction under the condition

$$g \sin \theta_W = g' \cos \theta_W = e, \quad \frac{g'}{g} = \tan \theta_W \quad (1.28)$$

647 contained in the Eqn.1.25; the third term is the neutral weak current.

648

649 Note that the neutral fields transformation given by the Eqn. 1.26 can be written  
 650 in terms of the coupling constants  $g$  and  $g'$  as:

$$A_\mu = \frac{g' W_\mu^3 + g B_\mu}{\sqrt{g^2 + g'^2}}, \quad Z_\mu = \frac{g W_\mu^3 - g' B_\mu}{\sqrt{g^2 + g'^2}}. \quad (1.29)$$

651 So far, the Lagrangian density describing the non-massive EWI is:

$$\mathcal{L}_{nmEWI} = \mathcal{L}_0 + \mathcal{L}_G \quad (1.30)$$

652 where fermion and gauge fields have been considered massless because their regular  
 653 mass terms are manifestly non invariant under  $G$  transformations; therefore, masses  
 654 have to be generated in a gauge invariant way. The mechanism by which this goal is  
 655 achieved is known as the *Higgs mechanism* and is closely connected to the concept of  
 656 *spontaneous symmetry breaking*.

### 657 1.3.1 Spontaneous symmetry breaking (SSB)

658 Figure 1.6 left shows a steel nail (top) which is subject to an external force; the form  
 659 of the potential energy is also shown (bottom).

660 Before reaching the critical force value, the system has rotational symmetry with  
 661 respect to the nail axis; however, after the critical force value is reached the nail buck-

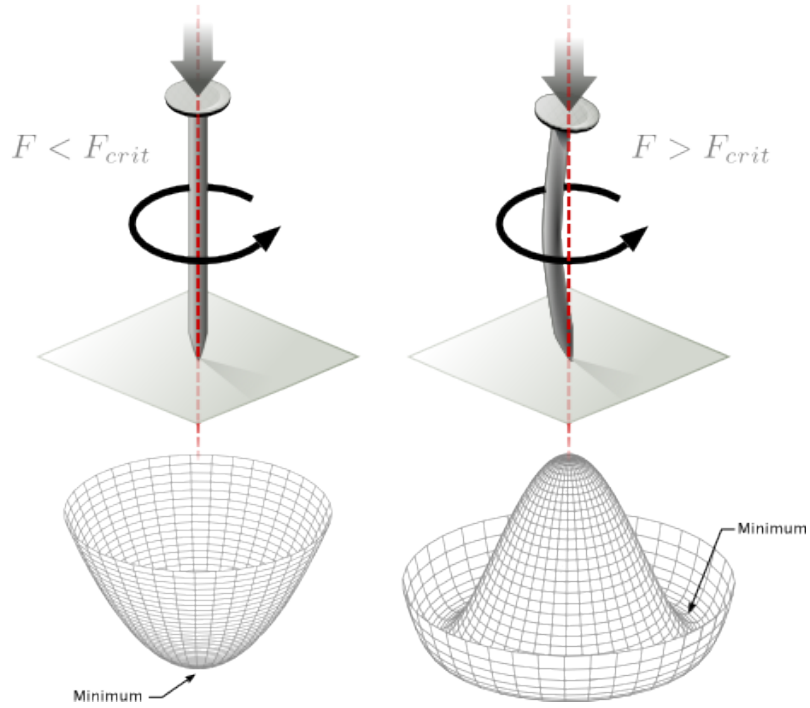


**Figure 1.6:** Spontaneous symmetry breaking mechanism. The steel nail, subject to an external force (top left), has rotational symmetry with respect to its axis. When the external force overcomes a critical value the nail buckles (top right) choosing a minimal energy state (ground state) and thus *breaking spontaneously the rotational symmetry*. The potential energy (bottom) changes but holds the rotational symmetry; however, an infinite number of asymmetric ground states are generated and circularly distributed in the bottom of the potential [31].

662 les (top right). The form of the potential energy (bottom right) changes appearing a  
 663 set of infinity minima but preserving its rotational symmetry. Right before the nail  
 664 buckles there is no indication of the direction the nail will bend because any of the  
 665 directions are equivalent, but once the nail bends, choosing a direction, an arbitrary  
 666 minimal energy state (ground state) is selected and it does not share the system's  
 667 rotational symmetry. This mechanism for reaching an asymmetric ground state is  
 668 known as *spontaneous symmetry breaking*.

669 The lesson from this analysis is that the way to introduce the SSB mechanism  
 670 into a system is by adding the appropriate potential to it.

671 Figure 1.7 shows a plot of the potential  $V(\phi)$  in the case of a scalar field  $\phi$

$$V(\phi) = \mu^2 \phi^\dagger \phi + \lambda (\phi^\dagger \phi)^2 \quad (1.31)$$

672 If  $\mu^2 > 0$  the potential has only one minimum at  $\phi = 0$  and describes a scalar field  
 673 with mass  $\mu$ . If  $\mu^2 < 0$  the potential has a local maximum at  $\phi = 0$  and two minima  
 674 at  $\phi = \pm\sqrt{-\mu^2/\lambda}$  which enables the SSB mechanism to work.

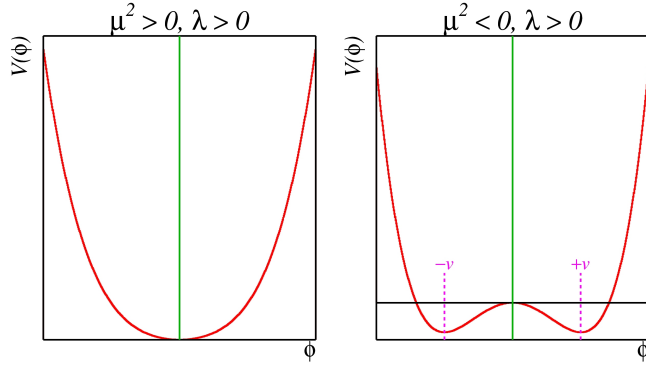


**Figure 1.7:** Shape of the potential  $V(\phi)$  for  $\lambda > 0$  and:  $\mu^2 > 0$  (left) and  $\mu^2 < 0$  (right). The case  $\mu^2 < 0$  corresponds to the potential suitable for introducing the SSB mechanism by choosing one of the two ground states which are connected via reflection symmetry. [31].

675 In the case of a complex scalar field  $\phi(x)$

$$\phi(x) = \frac{1}{\sqrt{2}}(\phi_1 + i\phi_2) \quad (1.32)$$

676 the Lagrangian (invariant under global  $U(1)$  transformations) is given by

$$\mathcal{L} = (\partial_\mu \phi)^\dagger (\partial^\mu \phi) - V(\phi), \quad V(\phi) = \mu^2 \phi^\dagger \phi + \lambda (\phi^\dagger \phi)^2 \quad (1.33)$$

677 where an appropriate potential has been added in order to introduce the SSB.

678 As seen in Figure 1.8, the potential has now an infinite number of minima circularly  
 679 distributed along the  $\xi$ -direction which makes possible the occurrence of the SSB by  
 680 choosing an arbitrary ground state; for instance,  $\xi = 0$ , i.e.  $\phi_1 = v, \phi_2 = 0$

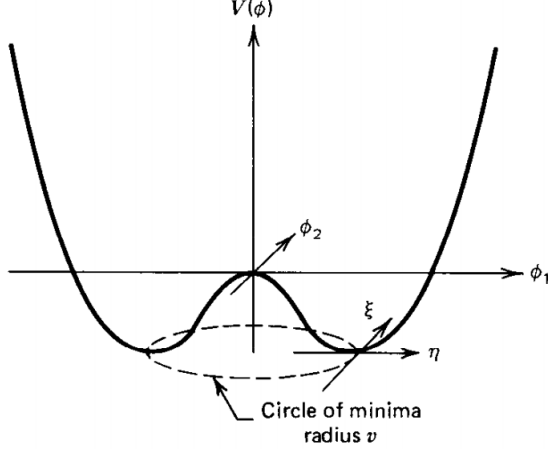


**Figure 1.8:** Potential for complex scalar field. There is a circle of minima of radius  $v$  along the  $\xi$ -direction [6].

$$\phi_0 = \frac{v}{\sqrt{2}} \exp(i\xi) \xrightarrow{\text{SSB}} \phi_0 = \frac{v}{\sqrt{2}} \quad (1.34)$$

681 As usual, excitations over the ground state are studied by making an expansion  
682 about it; thus, the excitations can be parametrized as:

$$\phi(x) = \frac{1}{\sqrt{2}}(v + \eta(x) + i\xi(x)) \quad (1.35)$$

683 which when substituted into Eqn. 1.33 produces a Lagrangian in terms of the new  
684 fields  $\eta$  and  $\xi$

$$\mathcal{L}' = \frac{1}{2}(\partial_\mu \xi)^2 + \frac{1}{2}(\partial_\mu \eta)^2 + \mu^2 \eta^2 - V(\phi_0) - \lambda v \eta (\eta^2 + \xi^2) - \frac{\lambda}{4}(\eta^2 + \xi^2)^2 \quad (1.36)$$

685 where the last two terms represent the interactions and self-interaction between the  
686 two fields  $\eta$  and  $\xi$ . The particular feature of the SSB mechanism is revealed when  
687 looking to the first three terms of  $\mathcal{L}'$ . Before the SSB, only the massless  $\phi$  field is

688 present in the system; after the SSB there are two fields of which the  $\eta$ -field has  
 689 acquired mass  $m_\eta = \sqrt{-2\mu^2}$  while the  $\xi$ -field is still massless (see Figure 1.9).

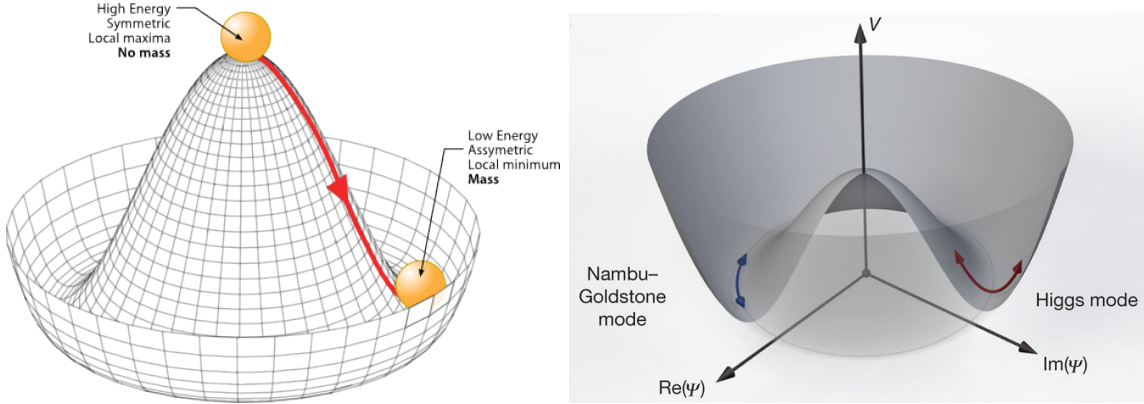


**Figure 1.9:** SSB mechanism for a complex scalar field [31, 32].

690 Thus, the SSB mechanism serves as a method to generate mass but as a side ef-  
 691 fect a massless field is introduced in the system. This fact is known as the Goldstone  
 692 theorem and states that a massless scalar field appears in the system for each con-  
 693 tinuous symmetry spontaneously broken. Another version of the Goldstone theorem  
 694 states that “if a Lagrangian is invariant under a continuous symmetry group  $G$ , but  
 695 the vacuum is only invariant under a subgroup  $H \subset G$ , then there must exist as many  
 696 massless spin-0 particles (Nambu-Goldstone bosons) as broken generators.” [26] The  
 697 Nambu-Goldstone boson can be understood considering that the potential in the  $\xi$ -  
 698 direction is flat so excitations in that direction are not energy consuming and thus  
 699 represent a massless state.

### 700 1.3.2 Higgs mechanism

701 When the SSB mechanism is introduced in the formulation of the EWI in an attempt  
 702 to generate the mass of the so far massless gauge bosons and fermions, an interesting  
 703 effect is revealed. In order to keep the  $G$  symmetry group invariance and generate

704 the mass of the EW gauge bosons, a G invariant Lagrangian density ( $\mathcal{L}_S$ ) has to be  
 705 added to the non massive EWI Lagrangian (Eqn. 1.30)

$$\mathcal{L}_S = (D_\mu \phi)^\dagger (D^\mu \phi) - \mu^2 \phi^\dagger \phi - \lambda (\phi^\dagger \phi)^2, \quad \lambda > 0, \mu^2 < 0 \quad (1.37)$$

$$D_\mu \phi = \left( i\partial_\mu - g \frac{\sigma_i}{2} W_\mu^i - g' \frac{Y}{2} B_\mu \right) \phi \quad (1.38)$$

706  $\phi$  has to be an isospin doublet of complex scalar fields so it preserves the G invariance;  
 707 thus  $\phi$  can be defined as:

$$\phi = \begin{pmatrix} \phi^+ \\ \phi^0 \end{pmatrix} \equiv \frac{1}{\sqrt{2}} \begin{pmatrix} \phi_1 + i\phi_2 \\ \phi_3 + i\phi_4 \end{pmatrix}. \quad (1.39)$$

708 The minima of the potential are defined by

$$\phi^\dagger \phi = \frac{1}{2} (\phi_1^2 + \phi_2^2 + \phi_3^2 + \phi_4^2) = -\frac{\mu^2}{2\lambda}. \quad (1.40)$$

709 The choice of the ground state is critical. By choosing a ground state, invariant  
 710 under  $U(1)_{em}$  gauge symmetry, the photon will remain massless and the  $W^\pm$  and  $Z$   
 711 bosons masses will be generated which is exactly what is needed. In that sense, the  
 712 best choice corresponds to a weak isospin doublet with  $T_3 = -1/2$ ,  $Y_W = 1$  and  $Q = 0$   
 713 which defines a ground state with  $\phi_1 = \phi_2 = \phi_4$  and  $\phi_3 = v$ :

$$\phi_0 \equiv \frac{1}{\sqrt{2}} \begin{pmatrix} 0 \\ v \end{pmatrix}, \quad v^2 \equiv -\frac{\mu^2}{\lambda}. \quad (1.41)$$

714 where the vacuum expectation value  $v$  is fixed by the Fermi coupling  $G_F$  according  
 715 to  $v = (\sqrt{2}G_F)^{1/2} \approx 246$  GeV.

716 The G symmetry has been broken and three Nambu-Goldstone bosons will appear.

717 The next step is to expand  $\phi$  about the chosen ground state as:

$$\phi(x) = \frac{1}{\sqrt{2}} \exp\left(\frac{i}{v} \sigma_i \theta^i(x)\right) \begin{pmatrix} 0 \\ v + H(x) \end{pmatrix} \approx \frac{1}{\sqrt{2}} \begin{pmatrix} \theta_1(x) + i\theta_2(x) \\ v + H(x) - i\theta_3(x) \end{pmatrix} \quad (1.42)$$

718 to describe fluctuations from the ground state  $\phi_0$ . The fields  $\theta_i(x)$  represent the  
 719 Nambu-Goldstone bosons while  $H(x)$  is known as *Higgs field*. The fundamental fea-  
 720 ture of the parametrization used is that the dependence on the  $\theta_i(x)$  fields is factored  
 721 out in a global phase that can be eliminated by taking the physical *unitary gauge*  
 722  $\theta_i(x) = 0$ . Therefore the expansion about the ground state is given by:

$$\phi(x) \frac{1}{\sqrt{2}} \begin{pmatrix} 0 \\ v + H(x) \end{pmatrix} \quad (1.43)$$

723 which when substituted into  $\mathcal{L}_S$  (Eqn. 1.37) results in a Lagrangian containing the  
 724 now massive three gauge bosons  $W^\pm, Z$ , one massless gauge boson (photon) and  
 725 the new Higgs field ( $H$ ). The three degrees of freedom corresponding to the Nambu-  
 726 Goldstone bosons are now integrated into the massive gauge bosons as their lon-  
 727 gitudinal polarizations which were not available when they were massless particles.  
 728 The effect by which vector boson fields acquire mass after an spontaneous symmetry  
 729 breaking, but without an explicit gauge invariance breaking is known as the *Higgs*  
 730 *mechanism*.

731 The mechanism was proposed by three independent groups: F.Englert and R.Brout  
 732 in August 1964 [33], P.Higgs in October 1964 [34] and G.Guralnik, C.Hagen and  
 733 T.Kibble in November 1964 [35]; however, its importance was not realized until  
 734 S.Glashow [22], A.Salam [23] and S.Weinberg [24], independently, proposed that elec-  
 735 tromagnetic and weak interactions are two manifestations of a more general interac-  
 736 tion called *electroweak interaction* in 1967.

<sup>737</sup> **1.3.3 Masses of the gauge bosons**

<sup>738</sup> The masses of the gauge bosons are extracted by evaluating the kinetic part of La-  
<sup>739</sup> grangian  $\mathcal{L}_S$  in the ground state (known also as the vacuum expectation value), i.e.,

$$\left| \left( \partial_\mu - ig \frac{\sigma_i}{2} W_\mu^i - i \frac{g'}{2} B_\mu \right) \phi_0 \right|^2 = \left( \frac{1}{2} v g \right)^2 W_\mu^+ W^{-\mu} + \frac{1}{8} v^2 (W_\mu^3, B_\mu) \begin{pmatrix} g^2 & -gg' \\ -gg' & g'^2 \end{pmatrix} \begin{pmatrix} W^{3\mu} \\ B^\mu \end{pmatrix} \quad (1.44)$$

<sup>740</sup> comparing with the typical mass term for a charged boson  $M_W^2 W^+ W^-$

$$M_W = \frac{1}{2} v g. \quad (1.45)$$

The second term in the right side of the Eqn.1.44 comprises the masses of the neutral bosons, but it needs to be written in terms of the gauge fields  $Z_\mu$  and  $A_\mu$  in order to be compared to the typical mass terms for neutral bosons, therefore using Eqn. 1.29

$$\begin{aligned} \frac{1}{8} v^2 [g^2 (W_\mu^3)^2 - 2gg' W_\mu^3 B^\mu + g'^2 B_\mu^2] &= \frac{1}{8} v^2 [g W_\mu^3 - g' B_\mu]^2 + 0[g' W_\mu^3 + g B_\mu]^2 \quad (1.46) \\ &= \frac{1}{8} v^2 [\sqrt{g^2 + g'^2} Z_\mu]^2 + 0[\sqrt{g^2 + g'^2} A_\mu]^2 \end{aligned}$$

<sup>741</sup> and then

$$M_Z = \frac{1}{2} v \sqrt{g^2 + g'^2}, \quad M_A = 0 \quad (1.47)$$

742 **1.3.4 Masses of the fermions**

743 The lepton mass terms can be generated by introducing a gauge invariant Lagrangian  
 744 term describing the Yukawa coupling between the lepton field and the Higgs field

$$\mathcal{L}_{Yl} = -G_l \left[ (\bar{\nu}_l, \bar{l})_L \begin{pmatrix} \phi^+ \\ \phi^0 \end{pmatrix} l_R + \bar{l}_R (\phi^-, \bar{\phi}^0) \begin{pmatrix} \nu_l \\ l \end{pmatrix} \right], \quad l = e, \mu, \tau. \quad (1.48)$$

745 After the SSB and replacing the usual field expansion about the ground state  
 746 (Eqn.1.41) into  $\mathcal{L}_{Yl}$ , the mass term arises

$$\mathcal{L}_{Yl} = -m_l (\bar{l}_L l_R + \bar{l}_R l_L) - \frac{m_l}{v} (\bar{l}_L l_R + \bar{l}_R l_L) H = -m_l \bar{l} \left( 1 + \frac{H}{v} \right) \quad (1.49)$$

747

$$m_l = \frac{G_l}{\sqrt{2}} v \quad (1.50)$$

748 where the additional term represents the lepton-Higgs interaction. The quark masses  
 749 are generated in a similar way as lepton masses but for the upper member of the  
 750 quark doublet a different Higgs doublet is needed:

$$\phi_c = -i\sigma_2 \phi^* = \begin{pmatrix} -\bar{\phi}^0 \\ \phi^- \end{pmatrix}. \quad (1.51)$$

751 Additionally, given that the quark isospin doublets are not constructed in terms  
 752 of the mass eigenstates but in terms of the flavor eigenstates, as shown in Table 1.5,  
 753 the coupling parameters will be related to the CKM matrix elements; thus, the quark  
 754 Lagrangian is given by:

$$\mathcal{L}_{Yq} = -G_d^{i,j} (\bar{u}_i, \bar{d}'_i)_L \begin{pmatrix} \phi^+ \\ \phi^0 \end{pmatrix} d_{jR} - G_u^{i,j} (\bar{u}_i, \bar{d}'_i)_L \begin{pmatrix} -\bar{\phi}^0 \\ \phi^- \end{pmatrix} u_{jR} + h.c. \quad (1.52)$$

755 with  $i, j = 1, 2, 3$ . After SSB and expansion about the ground state, the diagonal form

756 of  $\mathcal{L}_{Yq}$  is:

$$\mathcal{L}_{Yq} = -m_d^i \bar{d}_i d_i \left(1 + \frac{H}{v}\right) - m_u^i \bar{u}_i u_i \left(1 + \frac{H}{v}\right) \quad (1.53)$$

757 Fermion masses depend on arbitrary couplings  $G_l$  and  $G_{u,d}$  and are not predicted  
758 by the theory.

### 759 1.3.5 The Higgs field

760 After the characterization of the fermions and gauge bosons as well as their interac-  
761 tions, it is necessary to characterize the Higgs field itself. The Lagrangian  $\mathcal{L}_S$  in Eqn.  
762 1.37 written in terms of the gauge bosons is given by

$$\mathcal{L}_S = \frac{1}{4} \lambda v^4 + \mathcal{L}_H + \mathcal{L}_{HV} \quad (1.54)$$

763

$$\mathcal{L}_H = \frac{1}{2} \partial_\mu H \partial^\mu H - \frac{1}{2} m_H^2 H^2 - \frac{1}{2v} m_H^2 H^3 - \frac{1}{8v^2} m_H^2 H^4 \quad (1.55)$$

764

$$\mathcal{L}_{HV} = m_H^2 W_\mu^+ W^{\mu-} \left(1 + \frac{2}{v} H + \frac{2}{v^2} H^2\right) + \frac{1}{2} m_Z^2 Z_\mu Z^\mu \left(1 + \frac{2}{v} H + \frac{2}{v^2} H^2\right) \quad (1.56)$$

765 The mass of the Higgs boson is deduced as usual from the mass term in the Lagrangian  
766 resulting in:

$$m_H = \sqrt{-2\mu^2} = \sqrt{2\lambda}v \quad (1.57)$$

767 however, it is not predicted by the theory either. The experimental measurement of  
768 the Higgs boson mass have been performed by the *Compact Muon Solenoid (CMS)*  
769 experiment and the *A Toroidal LHC Appartus (ATLAS)* experiments at the *Large  
770 Hadron Collider (LHC)*, [36–38], and is presented in Table 1.8.

771

Property	Value
Electric charge	0
Color charge	0
Spin	0
Weak isospin	-1/2
Weak hypercharge	1
Parity	1
Mass (GeV/c <sup>2</sup> )	125.09±0.21 (stat.)±0.11 (syst.)

**Table 1.8:** Higgs boson properties. Higgs mass is not predicted by the theory and the value here corresponds to the experimental measurement.

### **1.3.6 Production of Higgs bosons at LHC**

773 At the LHC, Higgs bosons are produced as a result of the collision of two counter-  
774 rotating protons beams. A detailed description of the LHC machine will be presented  
in chapter 2.

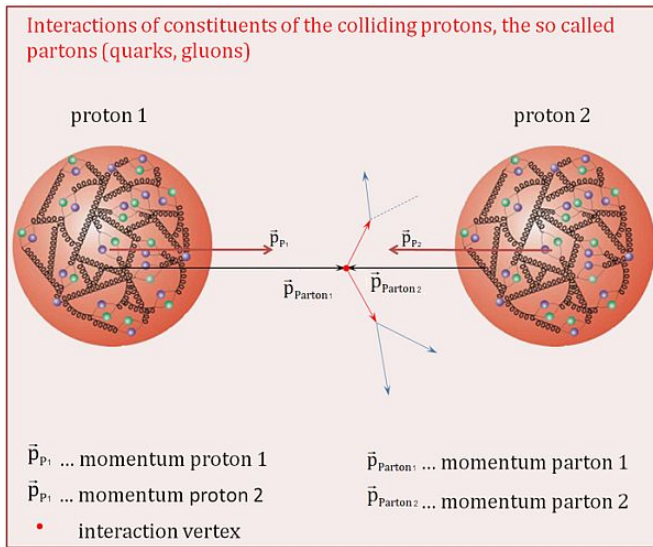


**Figure 1.10:** Proton-proton collision. Protons are composed of 3 valence quarks, a sea of quarks and gluons; therefore in a proton-proton collision, quarks and gluons are those who collide. [39].

775

776 Protons are composed of quarks and these quarks are bound by gluons; however,  
777 what is commonly called the quark content of the proton makes reference to the  
778 valence quarks. In fact, a proton is not just a rigid entity with three balls in it all  
779 tied up with springs, but the gluons exchanged by the valence quarks tend to split

780 spontaneously into quark-antiquark pairs or more gluons, creating *sea of quarks and*  
 781 *gluons* as represented in Figure 1.10.

782 In a proton-proton ( $pp$ ) collision, the proton's constituents, quarks and gluons, are  
 783 those that collide. The  $pp$  cross section depends on the momentum of the colliding  
 784 particles, reason for which it is needed to know how the momentum is distributed  
 785 inside the proton. Quarks and gluons are known as partons, hence, the functions  
 786 that describe how the proton momentum is distributed among partons inside it are  
 787 called *parton distribution functions (PDFs)*; PDFs are determined from experimental  
 788 data obtained in experiments where the internal structure of hadrons is tested, and  
 789 depend on the momentum transfer  $Q$  and the fraction of momentum  $x$  carried by an  
 790 specific parton. Figure 1.11 shows the proton PDFs ( $xf(x, Q^2)$ ) for two values of  $Q$ .

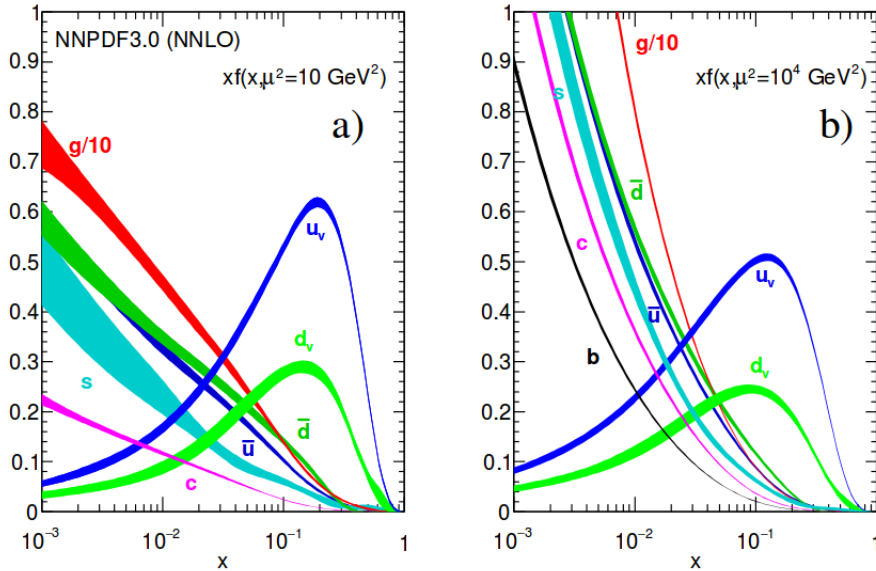


**Figure 1.11:** Proton PDFs for two values of  $Q^2$ : left.  $\mu^2 = Q^2 = 10 \text{ GeV}^2$ , right.  $\mu^2 = Q^2 = 10^4 \text{ GeV}^2$ .  $u_v$  and  $d_v$  correspond to the  $u$  and  $d$  valence quarks,  $s, c, b, \bar{u}, \bar{d}$  correspond to sea quarks, and  $g$  corresponds to gluons. Note that gluons carry a high fraction of the proton's momentum. [9]

791 In physics, a common approach to study complex systems consists of starting  
 792 with a simpler version of them, for which a well known description is available, and

adding an additional *perturbation* which represents a small deviation from the known behavior. If the perturbation is small enough, the physical quantities associated with the perturbed system are expressed as a series of corrections to those of the simpler system. The perturbation series corresponds to an expansion in power series of a small parameter, therefore, the more terms are considered in the series (the higher order in the perturbation series), the more precise is the description of the complex system. If the perturbation does not get progressively smaller, the strategy cannot be applied and new methods have to be employed.

High energy systems, like the Higgs production at LHC explored in this thesis, usually can be treated perturbatively with the expansion made in terms of the coupling constants. The overview presented here will be oriented specifically to the Higgs boson production mechanisms in  $pp$  collisions at LHC.

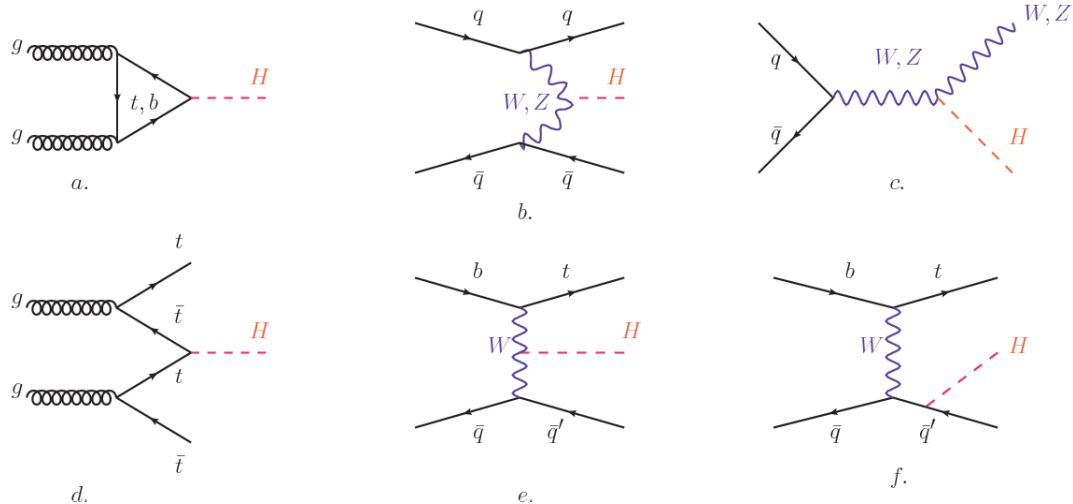


**Figure 1.12:** Main Higgs boson production mechanism Feynman diagrams. a. gluon-gluon fusion, b. vector boson fusion (VBF), c. Higgs-strahlung, d. Associated production with a top or bottom quark pair, e-f. associated production with a single top quark.

Figure 1.12 shows the Feynman diagrams for the leading order (first order) Higgs production processes at LHC; note that in these diagrams the incoming particles are not the protons themselves but the partons from the protons that actually participate

in the interaction, hence, theorists typically calculate the cross section for the parton interaction, and then convolute that cross section with the information from the PDFs to get a production cross section that is actually measured in experiments. The cross section for Higgs production as a function of the center of mass-energy ( $\sqrt{s}$ ) for  $pp$  collisions is showed in Figure 1.13 left. The tags NLO (next to leading order), NNLO (next to next to leading order) and N3LO (next to next to next to leading order) make reference to the order at which the perturbation series have been considered while the tags QCD and EW correspond to the strong and electroweak coupling constants respectively.

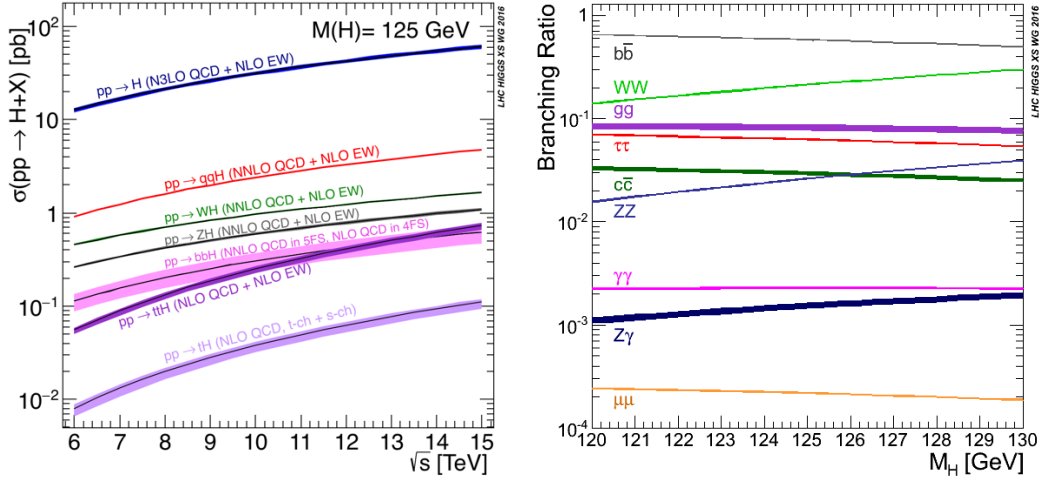


**Figure 1.13:** Higgs boson production cross sections (left) and decay branching ratios (right) for the main mechanisms. The VBF is indicated as  $qqH$  [40].

The main production mechanism is the gluon fusion (Figure 1.12a and  $pp \rightarrow H$  in Figure 1.13) given that gluons carry the highest fraction of momentum of the protons in  $pp$  colliders (as shown in Figure ??). Since the Higgs boson does not couple to gluons, the mechanism proceeds through the exchange of a virtual top-quark loop. Note that in this process the Higgs boson is produced alone, turning out to be problematic for some Higgs decays, because such absence of anything produced in

823 association with the Higgs represent a trouble for triggering, however, this mechanism  
 824 is experimentally clean when combined with the two-photon or the four-lepton decay  
 825 channels (see Section 1.3.7).

826 Vector boson fusion (Figure 1.12b and  $pp \rightarrow qqH$  in Figure 1.13) has the second  
 827 largest production cross section. The scattering of two fermions is mediated by a weak  
 828 gauge boson which later emits a Higgs boson. In the final state, the two fermions tend  
 829 to be located in the central region of the detector; this kind of features are generally  
 830 used as a signature when analyzing the datasets provided by the experiments<sup>7</sup>.

831 In the Higgs-strahlung mechanism (Figure 1.12c and  $pp \rightarrow WH, pp \rightarrow ZH$  in  
 832 Figure 1.13) two fermions annihilate to form a weak gauge boson. If the initial  
 833 fermions have enough energy, the emergent boson might emit a Higgs boson.

834 The associated production with a top or bottom quark pair and the associated  
 835 production with a single top quark (Figure 1.12d-f and  $pp \rightarrow bbH, pp \rightarrow t\bar{t}H, pp \rightarrow tH$   
 836 in Figure 1.13) have a smaller cross section than the main three mechanisms above,  
 837 but they provide a good opportunity to test the Higgs-top coupling. The analysis  
 838 reported in this thesis is developed using these production mechanisms. A detailed  
 839 description of the  $tH$  mechanism will be given in Section 1.5.

### 840 1.3.7 Higgs boson decay channels

841 When a particle can decay through several modes, also known as channels, the prob-  
 842 ability of decaying through a given channel is quantified by the *branching ratio (BR)*  
 843 of the decay channel; thus, the BR is defined as the ratio of number of decays go-  
 844 ing through that given channel to the total number of decays. In regard to the  
 845 Higgs boson decay, the BR can be predicted with accuracy once the Higgs mass is  
 846 known [41, 42]. In Figure 1.13 right, a plot of the BR as a function of the Higgs mass

---

<sup>7</sup> More details about how to identify events of interest in this analysis will be given in chapter 6.

847 is presented; the largest predicted BR corresponds to the  $b\bar{b}$  pair decay channel (see  
 848 Table 1.9) given that it is the heaviest particle pair whose on-shell<sup>8</sup> production is  
 849 kinematically allowed in the decay.

Decay channel	Branching ratio	Rel. uncertainty
$H \rightarrow b\bar{b}$	$5.84 \times 10^{-1}$	+3.2% – 3.3%
$H \rightarrow W^+W^-$	$2.14 \times 10^{-1}$	+4.3% – 4.2%
$H \rightarrow \tau^+\tau^-$	$6.27 \times 10^{-2}$	+5.7% – 5.7%
$H \rightarrow ZZ$	$2.62 \times 10^{-2}$	+4.3% – 4.1%
$H \rightarrow \gamma\gamma$	$2.27 \times 10^{-3}$	+5.0% – 4.9%
$H \rightarrow Z\gamma$	$1.53 \times 10^{-3}$	+9.0% – 8.9%
$H \rightarrow \mu^+\mu^-$	$2.18 \times 10^{-4}$	+6.0% – 5.9%

**Table 1.9:** Predicted branching ratios and the relative uncertainty for some decay channels of a SM Higgs boson with  $m_H = 125\text{GeV}/c^2$  [9]; the uncertainties are driven by theoretical uncertainties for the different Higgs boson partial widths and by parametric uncertainties associated to the strong coupling and the masses of the quarks which are the input parameters. Further details on these calculations can be found in Reference [43]

850

851 Decays to other lepton and quark pairs, like electron, strange, up, and down  
 852 quark pairs not listed in the table, are also possible but their likelihood is too small  
 853 to measure since they are very lightweight, hence, their interaction with the Higgs  
 854 boson is very weak. On other hand, the decay to top quark pairs is heavily suppressed  
 855 due to the top quark mass ( $\approx 173\text{ GeV}/c^2$ ).

856 Decays to gluons proceed indirectly through a virtual top quark loop while the  
 857 decays to photons proceed through a virtual W boson loop, therefore, their branching  
 858 ratio is smaller compared to direct interaction decays. Same is true for the decay to  
 859 a photon and a Z boson.

---

<sup>8</sup> In general, on-shell or real particles are those which satisfy the energy-momentum relation ( $E^2 - |\vec{p}|^2 c^2 = m^2 c^4$ ); off-shell or virtual particles does not satisfy it which is possible under the uncertainty principle of quantum mechanics. Usually, virtual particles correspond to internal propagators in Feynman diagrams.

860 In the case of decays to pairs of W and Z bosons, the decay proceed with one of  
 861 the bosons being on-shell and the other being off-shell. The likelihood of the process  
 862 diminish depending on how far off-shell are the virtual particles involved, hence, the  
 863 branching ratio for W boson pairs is bigger than for Z boson pairs since Z boson mass  
 864 is bigger than W boson mass.

865 Note that the decay to a pair of virtual top quarks is possible, but the probability  
 866 is way too small.

867 **1.4 Experimental status of the anomalous  
 868 Higgs-fermion coupling**

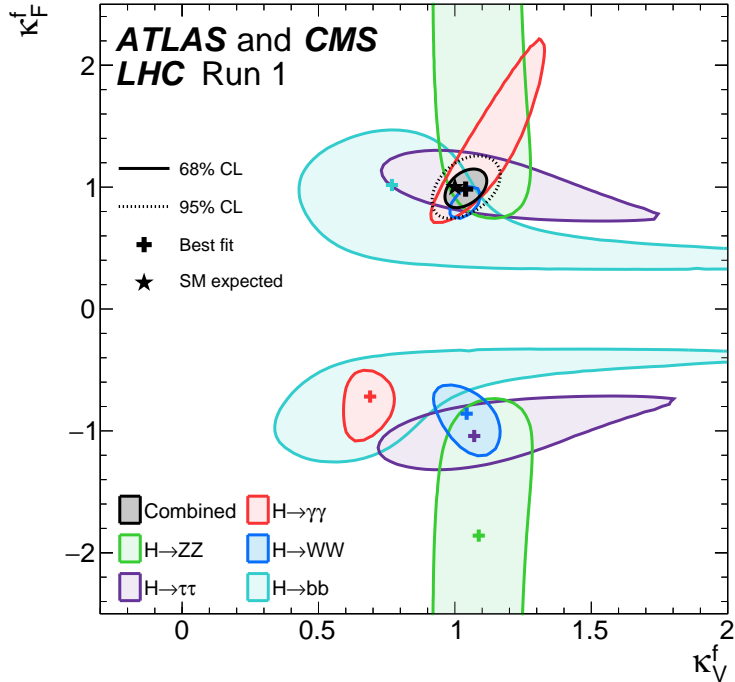


**Figure 1.14:** Combination of the ATLAS and CMS fits for coupling modifiers  $\kappa_t - \kappa_V$ ; also shown the individual decay channels combination and their global combination. No assumptions have been made on the sign of the coupling modifiers [44].

869       ATLAS and CMS have performed analyses of the anomalous Higgs-fermion cou-  
 870       pling by making likelihood scans for the two coupling modifiers,  $\kappa_f$  and  $\kappa_V$ , under  
 871       the assumption that  $\kappa_Z = \kappa_W \equiv \kappa_V$  and  $\kappa_t = \kappa_\tau = \kappa_b \equiv \kappa_f$ . Figure 1.14 shows the  
 872       result of the combination of ATLAS and CMS fits; also the individual decay channels  
 873       combination and the global combination results are shown. Note that from this plot  
 874       there is limited information on the sign of the coupling since the only information  
 875       available about the sign of the coupling comes from decays rather than production.

876       While all the channels are compatible for positive values of the modifiers, for  
 877       negative values of  $\kappa_f$  there is no compatibility. The best fit for individual channels  
 878       is compatible with negative values of  $\kappa_f$  except for the  $H \rightarrow bb$  channel. The best  
 879       fit for the combination yields  $\kappa_f \geq 0$ , in contrast to the yields from the individual  
 880       channels; the reason of this yield resides in the  $H \rightarrow \gamma\gamma$  coupling.  $H \rightarrow \gamma\gamma$  decay  
 881       proceeds through a loop of either top quarks or W bosons, hence, this channel is  
 882       sensitive to  $\kappa_t$  thanks to the interference of these two amplitude contributions; under  
 883       the assumption that no beyond SM particles take part in the loops, a flipped sign  
 884       of  $\kappa_t$  will increase the  $H \rightarrow \gamma\gamma$  branching fraction by a factor of  $\sim 2.4$  which is not  
 885       supported by measurements; thus, this large asymmetry between the positive and  
 886       negative coupling ratios in the  $H \rightarrow \gamma\gamma$  channel drives the yield of the global fit and  
 887       would mean that the anomalous H-t coupling is excluded as stated in Reference [44],  
 888       but there is a caveat, this exclusion holds only if no new particles contribute to the  
 889       loop in the main diagram for that decay.

890       Although the  $H \rightarrow bb$  channel is expected to be the most sensitive channel and  
 891       its best fit value of  $\kappa_t$  is positive, and then the global fit yield is still supported,  
 892       the contributions from all the other decay channels, small compared to the  $H \rightarrow bb$ ,  
 893       indicate that the anomalous H-t coupling cannot be excluded completely, motivating  
 894       to look at  $tH$  processes which can help with both, the limited information on the sign

895 of the H-t coupling and the access to information from the Higgs boson production  
 896 rather than from its decays.

897 It will be shown in Section 1.5 that the same interference effect enhance the  
 898  $tH$  production rate and could reveal evidence of direct production of heavy new par-  
 899 ticles as predicted in composite and little Higgs models [45], or new physics related  
 900 to Higgs boson mediated flavor changing neutral currents [46] as well as probes the  
 901 CP-violating phase of the H-t coupling [47, 48].

## 902 **1.5 Associated production of a Higgs boson and a 903 single top quark**

904 The production of Higgs boson in association with a top quark has been extensively  
 905 studied [47, 49–52]. While measurements of the main Higgs production mechanisms  
 906 rates are sensitive to the strength of the Higgs coupling to W boson or top quark,  
 907 they are not sensitive to the relative sign between the two couplings. In this thesis,  
 908 the Higgs boson production mechanism explored is the associated production with a  
 909 single top quark ( $tH$ ) which offers sensitivity to the relative sign of the Higgs couplings  
 910 to W boson and to top quark. The description given here is based on Reference [51]

A process where two incoming particles interact and produce a final state with two  
 particles can proceed in three called channels (see, for instance, Figure 1.15 omitting  
 the red line). The t-channel represents processes where an intermediate particle is  
 emitted by one of the incoming particles and absorbed by the other. The s-channel  
 represents processes where the two incoming particles merge into an intermediate par-  
 ticle which eventually will split into the particles in the final state. The third channel,  
 u-channel, is similar to the t-channel but the two outgoing particles interchange their

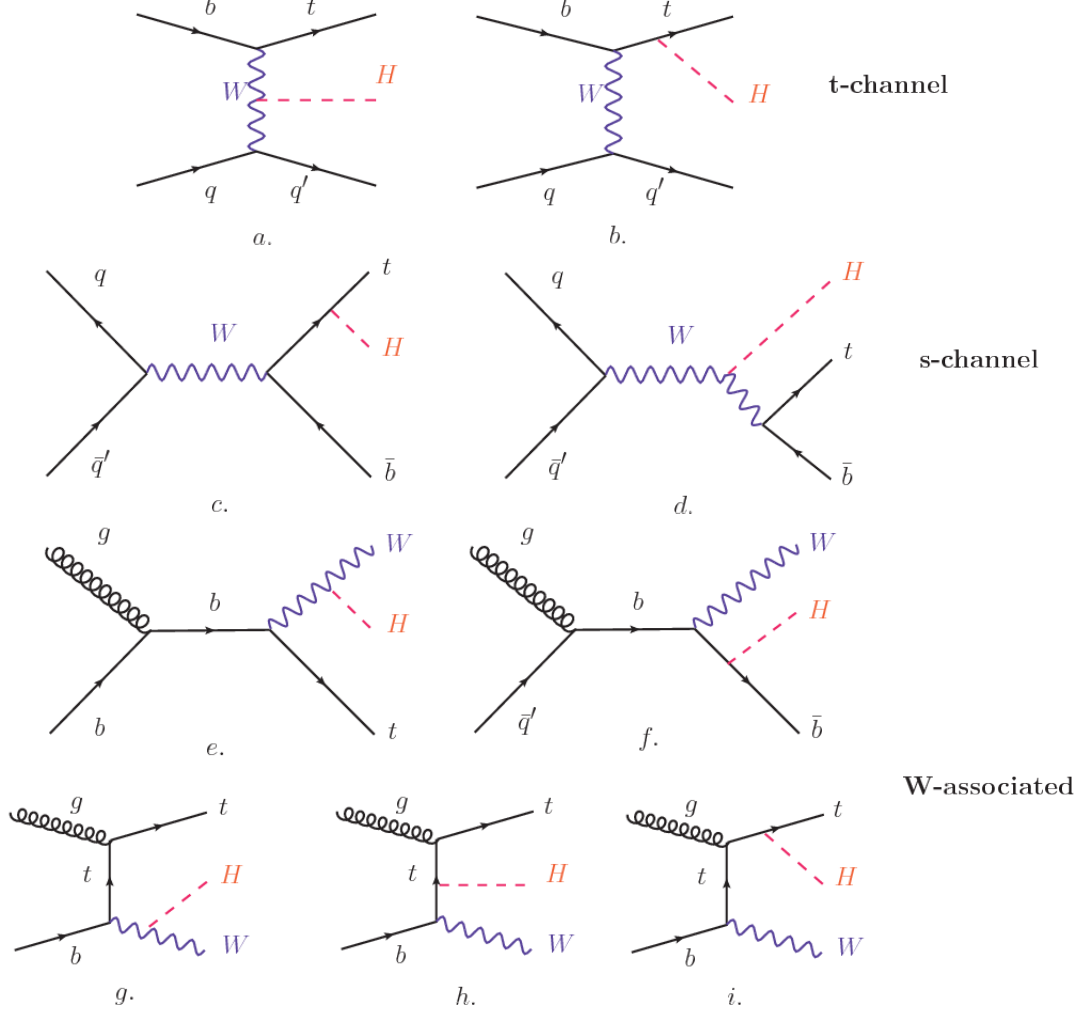


**Figure 1.15:** Associated Higgs boson production with a top quark mechanism Feynman diagrams. a.,b. t-channel ( $tHq$ ), c.,d. s-channel ( $tHb$ ), e-i. W-associated.

roles. These three channels are connected to the so-called Mandelstam variables

$$s = (p_1 + p_2)^2 = (p'_1 + p'_2)^2 \rightarrow \text{square of the center mass-energy.} \quad (1.58)$$

$$t = (p_1 - p'_1)^2 = (p'_2 - p_2)^2 \rightarrow \text{square of the four-momentum transfer.} \quad (1.59)$$

$$u = (p_1 - p'_2)^2 = (p'_1 - p_2)^2 \rightarrow \text{square of the crossed four-momentum transfer.} \quad (1.60)$$

$$s + t + u = m_1^2 + m_2^2 + m'_1{}^2 + m'_2{}^2 \quad (1.61)$$

which relate the momentum, energy and the angles of the incoming and outgoing particles in an scattering process of two particles to two particles. The importance of the Mandelstam variables reside in that they form a minimum set of variables needed to describe the kinematics of this scattering process; they are Lorentz invariant which makes them very useful when doing calculations.

The  $tH$  production, where Higgs boson can be radiated either from the top quark or from the W boson, is represented by the leading order Feynman diagrams in Figure 1.15. The cross section for the  $tH$  process is calculated, as usual, summing over the contributions from the different Feynman diagrams; therefore it depends on the interference between the contributions. In the SM, the interference for t-channel ( $tHq$  process) and W-associated ( $tHW$  process) production is destructive [49] resulting in the small cross sections presented in Table 1.10.

$tH$ production channel	Cross section (fb)
t-channel ( $pp \rightarrow tHq$ )	$70.79^{+2.99}_{-4.80}$
W-associated ( $pp \rightarrow tHW$ )	$15.61^{+0.83}_{-1.04}$
s-channel( $pp \rightarrow tHb$ )	$2.87^{+0.09}_{-0.08}$

**Table 1.10:** Predicted SM cross sections for  $tH$  production at  $\sqrt{s} = 13$  TeV [53, 54].

923

The s-channel contribution can be neglected. It will be shown that a deviation from the SM destructive interference would result in an enhancement of the  $tH$  cross section compared to that in SM, which could be used to get information about the sign of the Higgs-top coupling [51, 52]. In order to describe  $tH$  production processes, Feynman diagram 1.15b will be considered; there, the W boson is radiated by a quark in the proton and eventually it will interact with the b quark. In the high energy regime, the effective W approximation [55] is used to describe the process as the

931 emission of an approximately on-shell W and its hard scattering with the b quark;  
 932 i.e.  $Wb \rightarrow th$ . The scattering amplitude for the process is given by

$$\mathcal{A} = \frac{g}{\sqrt{2}} \left[ (\kappa_t - \kappa_V) \frac{m_t \sqrt{s}}{m_W v} A \left( \frac{t}{s}, \varphi; \xi_t, \xi_b \right) + \left( \kappa_V \frac{2m_W s}{v t} + (2\kappa_t - \kappa_V) \frac{m_t^2}{m_W v} \right) B \left( \frac{t}{s}, \varphi; \xi_t, \xi_b \right) \right], \quad (1.62)$$

933 where  $\kappa_V \equiv g_{HVV}/g_{HVV}^{SM}$  and  $\kappa_t \equiv g_{Ht}/g_{Ht}^{SM} = y_t/y_t^{SM}$  are scaling factors that quantify  
 934 possible deviations of the couplings from the SM values, Higgs-Vector boson (H-  
 935 W) and Higgs-top (H-t) respectively, from the SM couplings;  $s = (p_W + p_b)^2$ ,  $t =$   
 936  $(p_W - p_H)^2$ ,  $\varphi$  is the Higgs azimuthal angle around the  $z$  axis taken parallel to the  
 937 direction of motion of the incoming W; A and B are functions describing the weak  
 938 interaction in terms of the chiral states  $(\xi_t, \xi_b)$  of the quarks  $b$  and  $t$ . Terms that  
 939 vanish in the high energy limit have been neglected as well as the Higgs and  $b$  quark  
 940 masses<sup>9</sup>.

941 The scattering amplitude grows with energy like  $\sqrt{s}$  for  $\kappa_V \neq \kappa_t$ , in contrast to  
 942 the SM ( $\kappa_t = \kappa_V = 1$ ), where the first term in 1.62 cancels out and the amplitude  
 943 is constant for large  $s$ ; therefore, a deviation from the SM predictions represents an  
 944 enhancement in the  $tHq$  cross section. In particular, for a SM H-W coupling and a  
 945 H-t coupling of inverted sign with respect to the SM ( $\kappa_V = -\kappa_t = 1$ ) the  $tHq$  cross  
 946 section is enhanced by a factor greater 10 as seen in the Figure 1.16 taken from  
 947 Reference [51]; Reference [56] has reported similar enhancement results.

948 A similar analysis is valid for the W-associated channel but, in that case, the in-  
 949 terference is more complicated since there are more than two contributions and an ad-  
 950 ditional interference with the production of Higgs boson and a top pair process( $t\bar{t}H$ ).  
 951 The calculations are made using the so-called Diagram Removal (DR) technique where

---

<sup>9</sup> A detailed explanation of the structure and approximations used to derive  $\mathcal{A}$  can be found in Reference [51]

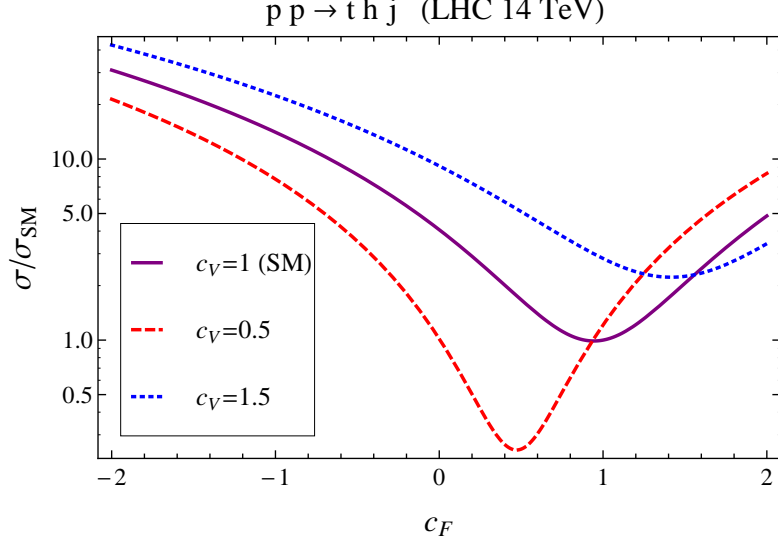


**Figure 1.16:** Cross section for  $tHq$  process as a function of  $\kappa_t$ , normalized to the SM, for three values of  $\kappa_V$ . In the plot  $c_f$  refers to the Higgs-fermion coupling which is dominated by the H-t coupling and represented here by  $\kappa_t$ . Solid, dashed and dotted lines correspond to  $c_V \rightarrow \kappa_V = 1, 0.5, 1.5$  respectively. Note that for the SM ( $\kappa_V = \kappa_t = 1$ ), the destructive effect of the interference is maximal.

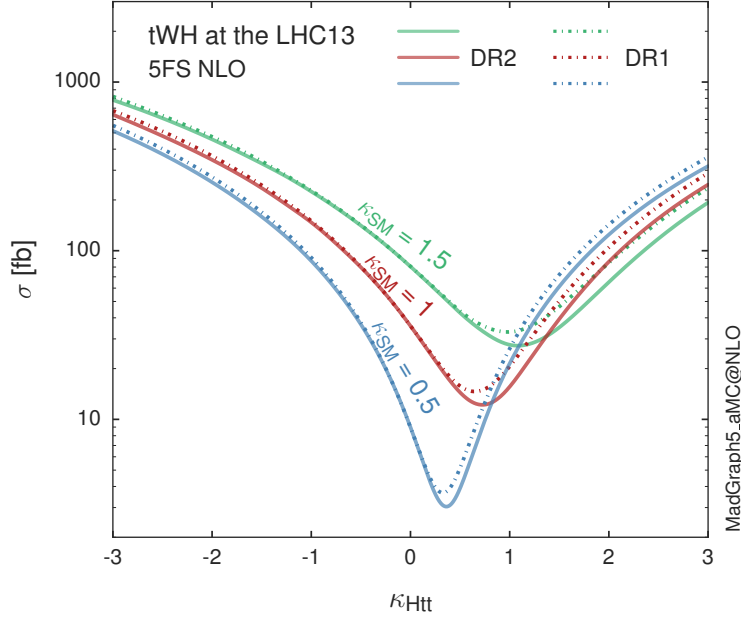


**Figure 1.17:** Cross section for  $tHW$  process as a function of  $\kappa_{Htt}$ , for three values of  $\kappa_{SM}$  at  $\sqrt{s} = 13$  TeV.  $\kappa_{Htt}^2 = \sigma_{Htt}/\sigma_{Htt}^{SM}$  is a simple re-scaling of the SM Higgs interactions.

interfering diagrams are removed (or added) from the calculations in order to evaluate the impact of the removed contributions. DR1 was defined to neglect  $t\bar{t}H$  interference while DR2 was defined to take  $t\bar{t}H$  interference into account [48]. As shown in Figure 1.17, the  $tHW$  cross section is enhanced from about 15 fb (SM:  $\kappa_{Htt} = 1$ ) to about 150 fb ( $\kappa_{Htt} = -1$ ). Differences between curves for DR1 and DR2 help to gauge the impact of the interference with  $t\bar{t}H$ . Results of the calculations of the  $tHq$  and  $tHW$  cross sections at  $\sqrt{s} = 13$  TeV can be found in Reference [57] and a summary of the results is presented in Table 1.11.

	$\sqrt{s}$ TeV	$\kappa_t = 1$	$\kappa_t = -1$
$\sigma^{LO}(tHq)(fb)$ [51]	8	$\approx 17.4$	$\approx 252.7$
	14	$\approx 80.4$	$\approx 1042$
$\sigma^{NLO}(tHq)(fb)$ [51]	8	$18.28^{+0.42}_{-0.38}$	$233.8^{+4.6}_{-0.0}$
	14	$88.2^{+1.7}_{-0.0}$	$982.8^{+28}_{-0.0}$
$\sigma^{LO}(tHq)(fb)$ [56]	14	$\approx 71.8$	$\approx 893$
$\sigma^{LO}(tHW)(fb)$ [56]	14	$\approx 16.0$	$\approx 139$
$\sigma^{NLO}(tHq)(fb)$ [57]	8	$18.69^{+8.62\%}_{-17.13\%}$	-
	13	$74.25^{+7.48\%}_{-15.35\%}$	$848^{+7.37\%}_{-13.70\%}$
	14	$90.10^{+7.34\%}_{-15.13\%}$	$1011^{+7.24\%}_{-13.39\%}$
$\sigma^{LO}(tHW)(fb)$ [48]	13	$15.77^{+15.91\%}_{-15.76\%}$	-
$\sigma^{NLO}DR1(tHW)(fb)$ [48]	13	$21.72^{+6.52\%}_{-5.24\%}$	$\approx 150$
$\sigma^{NLO}DR2(tHW)(fb)$ [48]	13	$16.28^{+7.34\%}_{-15.13\%}$	$\approx 150$

**Table 1.11:** Predicted enhancement of the  $tHq$  and  $tHW$  cross sections at LHC for  $\kappa_V = 1$  and  $\kappa_t = \pm 1$  at LO and NLO; the cross section enhancement of more than a factor of 10 is due to the flipping in the sign of the H-t coupling with respect to the SM one.

960

## 1.6 CP-mixing in $tH$ processes

In addition to the sensitivity to sign of the H-t coupling, the  $tHq$  and  $tHW$  processes have been proposed as a tool to investigate the possibility of a H-t coupling that does

964 not conserve CP [47, 48, 58].

965 In this thesis, the sensitivity of  $tH$ processes to CP-mixing is also studied on the  
 966 basis of References [47, 48] using the effective field theory framework where a generic  
 967 particle ( $X_0$ ) of spin-0 and a general CP violating interaction with the top quark  
 968 ( $Htt$  coupling), can couple to scalar and pseudo-scalar fermionic densities. The H-W  
 969 interaction is assumed to be SM-like. The Lagrangian modeling the H-t interaction  
 970 is given by

$$\mathcal{L}_0^t = -\bar{\psi}_t (c_\alpha \kappa_{Htt} g_{Htt} + i s_\alpha \kappa_{Att} g_{Att} \gamma_5) \psi_t X_0, \quad (1.63)$$

971 where  $\alpha$  is the CP-mixing phase,  $c_\alpha \equiv \cos \alpha$  and  $s_\alpha \equiv \sin \alpha$ ,  $\kappa_{Htt}$  and  $\kappa_{Att}$  are real  
 972 dimensionless re-scaling parameters<sup>10</sup> used to parametrize the magnitude of the CP-  
 973 violating and CP-conserving parts of the amplitude. The model defines  $g_{Htt} =$   
 974  $g_{Att} = m_t/v = y_t/\sqrt{2}$  with  $v \sim 246$  GeV the Higgs vacuum expectation value. In  
 975 this parametrization, three special cases can be recovered

976 • CP-even coupling  $\rightarrow \alpha = 0^\circ$

977 • CP-odd coupling  $\rightarrow \alpha = 90^\circ$

978 • SM coupling  $\rightarrow \alpha = 0^\circ$  and  $\kappa_{Htt} = 1$

979 The loop induced  $X_0$  coupling to gluons can also be described in terms of the  
 980 parametrization above, according to

$$\mathcal{L}_0^g = -\frac{1}{4} \left( c_\alpha \kappa_{Hgg} g_{Hgg} G_{\mu\nu}^a G^{a,\mu\nu} + s_\alpha \kappa_{Agg} g_{Agg} G_{\mu\nu}^a \tilde{G}^{a,\mu\nu} \right) X_0. \quad (1.64)$$

981 where  $g_{Hgg} = -\alpha_s/3\pi v$  and  $g_{Agg} = \alpha_s/2\pi v$  and  $G_{\mu\nu}$  is the gluon field strength tensors.

982 Under the assumption that the top quark dominates the gluon-fusion process at LHC

---

<sup>10</sup> analog to  $\kappa_t$  and  $\kappa_V$

983 energies,  $\kappa_{Hgg} \rightarrow \kappa_{Htt}$  and  $\kappa_{Agg} \rightarrow \kappa_{Att}$ , so that the ratio between the gluon-gluon  
 984 fusion cross section for  $X_0$  and for the SM Higgs prediction can be written as

$$\frac{\sigma_{NLO}^{gg \rightarrow X_0}}{\sigma_{NLO,SM}^{gg \rightarrow H}} = c_\alpha^2 \kappa_{Htt}^2 + s_\alpha^2 \left( \kappa_{Att} \frac{g_{Agg}}{g_{Hgg}} \right)^2. \quad (1.65)$$

985 If the re-scaling parameters are set to

$$\kappa_{Htt} = 1, \quad \kappa_{Att} = \left| \frac{g_{Hgg}}{g_{Agg}} \right| = \frac{2}{3}. \quad (1.66)$$

986 the gluon-fusion SM cross section is reproduced for every value of the CP-mixing  
 987 angle  $\alpha$ ; therefore, by imposing that condition to the Lagrangian density 1.63, the  
 988 CP-mixing angle is not constrained by current data. Figure 1.18 shows the NLO cross  
 989 sections for t-channel  $tX_0$ (blue) and  $t\bar{t}X_0$  (red) associated production processes as a  
 990 function of the CP-mixing angle  $\alpha$ .  $X_0$  is a generic spin-0 particle with top quark  
 991 CP-violating coupling. Re-scaling factors  $\kappa_{Htt}$  and  $\kappa_{Att}$  have been set to reproduce  
 992 the SM gluon-fusion cross sections.

993 It is interesting to notice that the  $tX_0$  cross section is enhanced, by a factor of  
 994 about 10, when a continuous rotation in the scalar-pseudoscalar plane is applied; this  
 995 enhancement is similar to the enhancement produced when the H-t coupling is flipped  
 996 in sign with respect to the SM ( $y_t = -y_{t,SM}$  in the plot), as showed in Section 1.5. In  
 997 contrast, the degeneracy in the  $t\bar{t}X_0$  cross section is still present given that it depends  
 998 quadratically on the H-t coupling, but more interesting is to notice that  $t\bar{t}X_0$  cross  
 999 section is exceeded by  $tX_0$  cross section after  $\alpha \sim 60^\circ$ .

1000 A similar parametrization can be used to investigate the  $tHW$  process sensitivity  
 1001 to CP-violating H-t coupling. As said in 1.5, the interference in the W-associated  
 1002 channel is more complicated because there are more than two contributions and also  
 1003 there is interference with the  $t\bar{t}H$  production process.

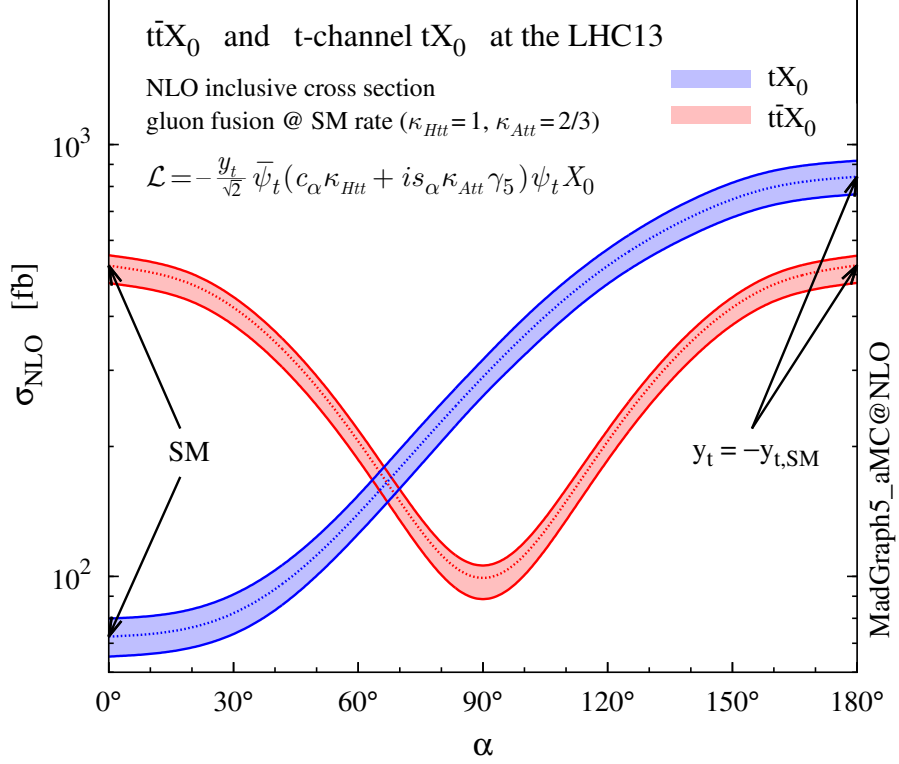


**Figure 1.18:** NLO cross sections for t-channel  $tX_0$ (blue) and  $t\bar{t}X_0$  (red) associated production processes as a function of the CP-mixing angle  $\alpha$ .  $X_0$  is a generic spin-0 particle with top quark CP-violating coupling [47].

1004     Figure 1.19 shows the NLO cross sections for t-channel  $tX_0$ (blue),  $t\bar{t}X_0$  (red)  
 1005     associated production and for the combined  $tWX_0+t\bar{t}X_0+interference$  (orange) as  
 1006     a function of the CP-mixing angle. It is clear that the effect of the interference in the  
 1007     combined case is the lifting of the degeneracy present in the  $t\bar{t}X_0$  production. The  
 1008     constructive interference enhances the cross section from about 500 fb at SM ( $\alpha = 0$ )  
 1009     to about 600 fb ( $\alpha = 180^\circ \rightarrow y_t = -y_{t,SM}$ ).

1010     An analysis combining  $tHq$  and  $tHW$ processes will be made in this thesis taking  
 1011     advantage of the sensitivity improvement.

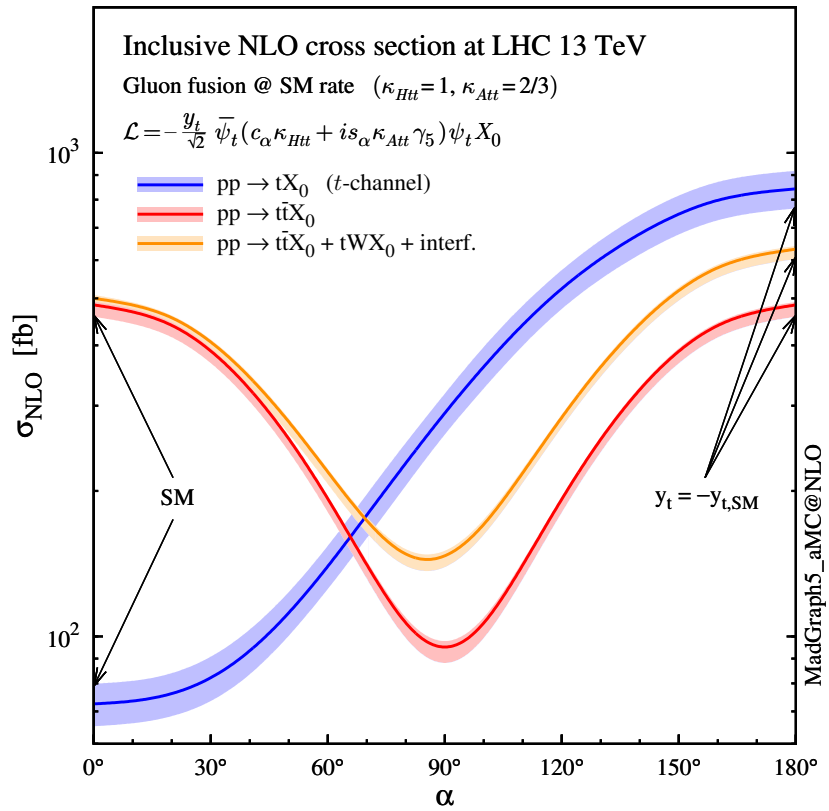


**Figure 1.19:** NLO cross sections for t-channel  $tX_0$ (blue),  $t\bar{t}X_0$  (red) associated production processes and combined  $tWX_0 + t\bar{t}X_0$  (including interference) production as a function of the CP-mixing angle  $\alpha$  [47].

<sub>1012</sub> **Chapter 2**

<sub>1013</sub> **The CMS experiment at the LHC**

<sub>1014</sub> **2.1 Introduction**

<sub>1015</sub> Located on the Swiss-French border, the European Council for Nuclear Research  
<sub>1016</sub> (CERN) is the largest scientific organization leading particle physics research. About  
<sub>1017</sub> 13000 people in a broad range of roles including users, students, scientists, engineers,  
<sub>1018</sub> among others, contribute to the data taking and analysis, with the goal of unveiling  
<sub>1019</sub> the secrets of nature and revealing the fundamental structure of the universe. CERN  
<sub>1020</sub> is also the home of the Large Hadron Collider (LHC), the largest particle accelerator  
<sub>1021</sub> around the world, where protons (or heavy ions) traveling close to the speed of light,  
<sub>1022</sub> are made to collide. These collisions open a window to investigate how particles (and  
<sub>1023</sub> their constituents if they are composite) interact with each other, providing clues  
<sub>1024</sub> about the laws of nature. This chapter presents an overview of the LHC structure  
<sub>1025</sub> and operation. A detailed description of the CMS detector is offered, given that the  
<sub>1026</sub> data used in this thesis have been taken with this detector.

## 1027 2.2 The LHC

1028 With 27 km of circumference, the LHC is currently the most powerful circular accelerator  
 1029 in the world. It is installed in the same tunnel where the Large Electron-Positron  
 1030 (LEP) collider was located, taking advantage of the existing infrastructure. The LHC  
 1031 is part of the CERN's accelerator complex composed of several successive accelerat-  
 1032 ing stages before the particles are injected into the LHC ring where they reach their  
 1033 maximum energy (see Figure 2.1).

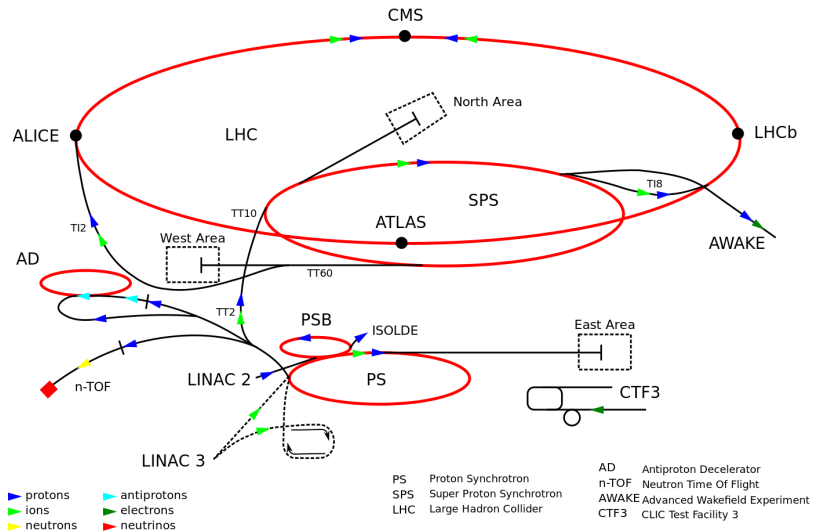


**Figure 2.1:** CERN accelerator complex. Blue arrows show the path followed by protons along the acceleration process [61].

1034 The LHC runs in three collision modes depending on the particles being acceler-  
 1035 ated

1036 • Proton-Proton collisions ( $pp$ ) for multiple physics experiments.

1037 • Lead-Lead collisions ( $Pb-Pb$ ) for heavy ion experiments.

1038 • Proton-Lead collisions ( $p-Pb$ ) for quark-gluon plasma experiments.

1039 In this thesis only  $pp$  collisions will be considered.

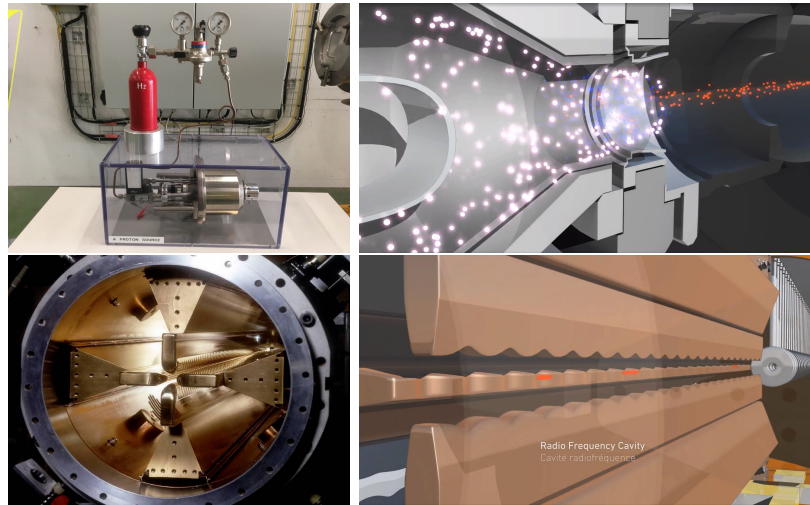


**Figure 2.2:** LHC protons source and the first acceleration stage. Top: the bottle contains hydrogen gas which is injected into the metal cylinder (white dots) to be broken down into electrons (blue dots) and protons (red dots); Bottom: the obtained protons are directed towards the radio frequency quadrupole which perform the first acceleration, focus the beam and create the bunches of protons. Left images are real pictures while right images are drawings [65, 66].

1040      Collection of protons starts with hydrogen atoms taken from a bottle, containing  
 1041     hydrogen gas, and injecting them in a metal cylinder; hydrogen atoms are broken  
 1042     down into electrons and protons by an intense electric field (see Figure 2.2 top).  
 1043     The resulting protons leave the metal cylinder towards a radio frequency quadrupole  
 1044     (RFQ) that focus the beam, accelerates the protons and creates the packets of protons  
 1045     called bunches. In the RFQ, an electric field is generated by a RF wave at a frequency  
 1046     that matches the resonance frequency of the cavity where the electrodes are contained.  
 1047     The beam of protons traveling on the RFQ axis experiences an alternating electric  
 1048     field gradient that generates the focusing forces.

1049     In order to accelerate the protons, a longitudinal time-varying electric field com-  
 1050     ponent is added to the system; it is done by giving the electrodes a sine-like profile as  
 1051     shown in Figure 2.2 bottom. By matching the speed and phase of the protons with  
 1052     the longitudinal electric field the bunching is performed; protons synchronized with

1053 the RFQ (synchronous protons) do not feel an accelerating force, but those protons in  
 1054 the beam that have more (or less) energy than the synchronous proton (asynchronous  
 1055 protons) will feel a decelerating (accelerating) force; therefore, asynchronous protons  
 1056 will oscillate around the synchronous ones forming bunches of protons [63]. From the  
 1057 RFQ protons emerge with energy 750 keV in bunches of about  $1.15 \times 10^{11}$  protons [64].

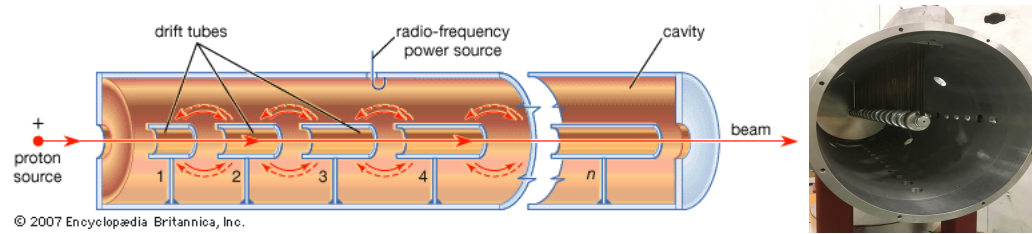


**Figure 2.3:** Left: drawing of the LINAC2 accelerating system at CERN. Electric fields generated by radio frequency (RF) create acceleration and deceleration zones inside the cavity; deceleration zones are blocked by drift tubes where quadrupole magnets focus the proton beam. Right: picture of a real RF cavity [67].

1058 Proton bunches coming from the RFQ go to the linear accelerator 2 (LINAC2)  
 1059 where they are accelerated to reach 50 MeV energy. In the LINAC2 stage, acceleration  
 1060 is performed using electric fields generated by radio frequency which create zones  
 1061 of acceleration and deceleration as shown in Figure 2.3. In the deceleration zones,  
 1062 the electric field is blocked using drift tubes where protons are free to drift while  
 1063 quadrupole magnets focus the beam.

1064 The beam coming from LINAC2 is injected into the proton synchrotron booster  
 1065 (PSB) to reach 1.4 GeV in energy. The next acceleration is provided at the proton  
 1066 synchrotron (PS) up to 26 GeV, followed by the injection into the super proton  
 1067 synchrotron (SPS) where protons are accelerated to 450 GeV. Finally, protons are  
 1068 injected into the LHC where they are accelerated to the target energy of 6.5 TeV.

1069 PSB, PS, SPS and LHC accelerate protons using the same RF acceleration tech-  
 1070 nique described before.

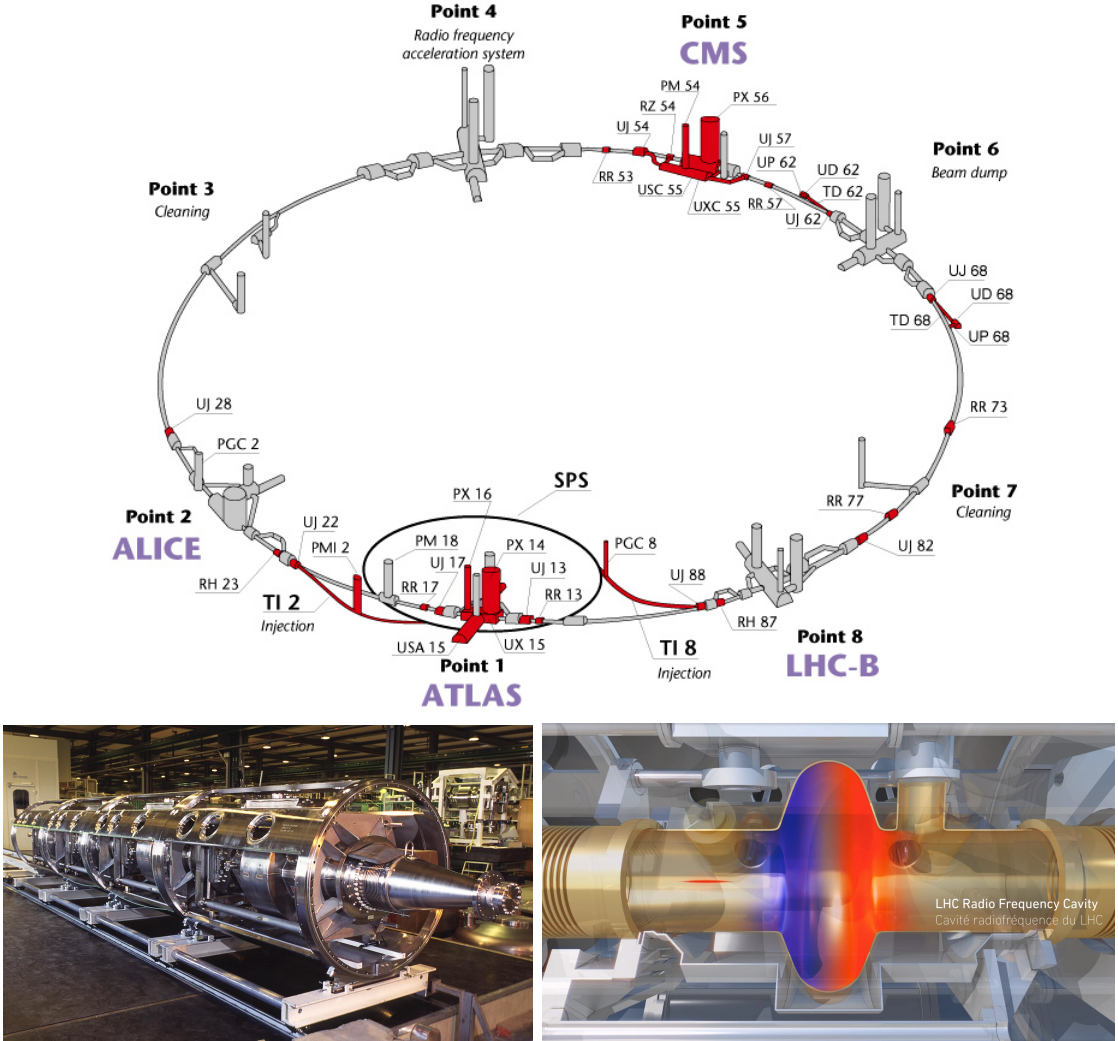


**Figure 2.4:** Top: LHC layout. The red zones indicate the infrastructure additions to the LEP installations, built to accommodate the ATLAS and CMS experiments which exceed the size of the former experiments located there [62]. Bottom: LHC RF cavities. A module (left picture) accommodates 4 cavities, each like the one in the right drawing, that accelerate protons and preserve the bunch structure of the beam. The color gradient pattern represents the strength of the electric field inside the cavity; red zone corresponds to the maximum of the oscillation electric field while the blue zone corresponds to the minimum. [66, 68]

1071        The LHC has a system of 16 RF cavities located in the so-called point 4, as  
 1072 shown in Figure 2.4 top, tuned at a frequency of 400 MHz. The bottom side of  
 1073 Figure 2.4 shows a picture of a RF module composed of 4 RF cavities working in a  
 1074 superconducting state at 4.5 K; also, a representation of the accelerating electric field

that accelerates the protons in the bunch is shown. The maximum of the oscillating electric field (red region) picks the proton bunches at the entrance of the cavity and keeps accelerating them through the whole cavity. The protons are carefully timed so that in addition to the acceleration effect the bunch structure of the beam is preserved.

While protons are accelerated in one section of the LHC ring, where the RF cavities are located, in the rest of their path they have to be kept in the curved trajectory defined by the LHC ring. Technically, LHC is not a perfect circle; RF, injection, beam dumping, beam cleaning and sections before and after the experimental points where protons collide are all straight sections. In total, there are 8 arcs 2.45 km long each and 8 straight sections 545 m long each. In order to curve the proton's trajectory in the arc sections, superconducting dipole magnets are used.

Inside the LHC ring, there are two proton beams traveling in opposite directions in two separated beam pipes; the beam pipes are kept at ultra-high vacuum ( $\sim 10^{-9}$  Pa) to ensure that there are no particles that interact with the proton beams. The superconducting dipole magnets used in LHC are made of a NbTi alloy, capable of transporting currents of about 12000 A when cooled at a temperature below 2K using liquid helium (see Figure 2.5).

Protons in the arc sections of LHC feel a centripetal force exerted by the dipole magnets; the magnitude of magnetic field needed to keep the protons in the LHC curved trayectomy can be found assuming that protons travel at  $v \approx c$ , using the standard values for proton mass and charge and the LHC radius, as

$$F_m = \frac{mv^2}{r} = qBv \rightarrow B = 8.33T \quad (2.1)$$

which is about 100000 times the Earth's magnetic field. A representation of the

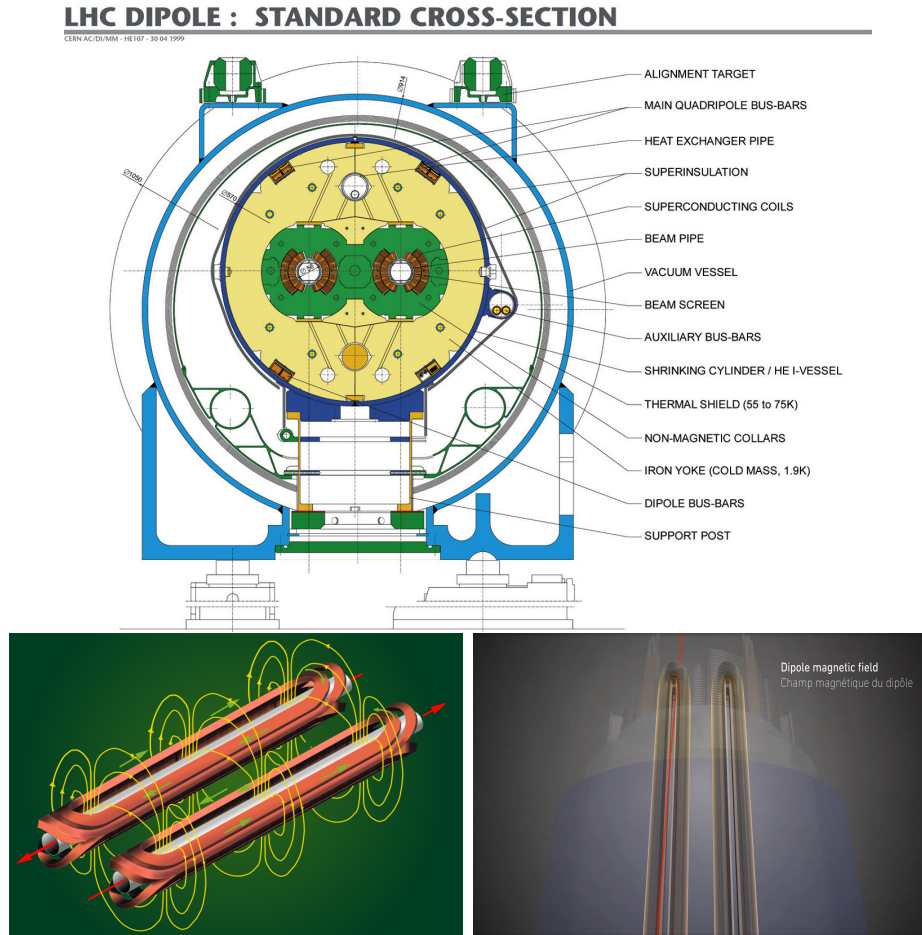


**Figure 2.5:** Top: LHC dipole magnet transverse view; cooling, shielding and mechanical support are indicated. Bottom left: Magnetic field generated by the dipole magnets; note that the direction of the field inside one beam pipe is opposite with respect to the other beam pipe which guarantee that both proton beams are curved in the same direction towards the center of the ring. The effect of the dipole magnetic field on the proton beam is represented on the bottom right side [66, 69, 70].

1098 magnetic field generated by the dipole magnets is shown on the bottom left side of  
 1099 Figure 2.5. The bending effect of the magnetic field on the proton beam is shown on  
 1100 the bottom right side of Figure 2.5. Note that the dipole magnets are not curved;  
 1101 the arc section of the LHC ring is composed of straight dipole magnets of about 15  
 1102 m. In total there are 1232 dipole magnets along the LHC ring.  
 1103 In addition to the bending of the beam trajectory, the beam has to be focused. The

focusing is performed by quadrupole magnets installed in a different straight section; in total 858 quadrupole magnets are installed along the LHC ring. Other effects like electromagnetic interaction among bunches, interaction with electron clouds from the beam pipe, the gravitational force on the protons, differences in energy among protons in the same bunch, among others, are corrected using sextupole and other magnetic multipoles.

The two proton beams inside the LHC ring are made of bunches with a cylindrical shape of about 7.5 cm long and about 1 mm in diameter; when bunches are close to the interaction point (IP), the beam is focused up to a diameter of about 16  $\mu\text{m}$  in order to maximize the probability of collisions between protons. The number of collisions per second is proportional to the cross section of the bunches with the *luminosity* ( $L$ ) as the proportionality factor, thus, the luminosity can be calculated using

$$L = fn \frac{N_1 N_2}{4\pi\sigma_x\sigma_y} \quad (2.2)$$

where  $f$  is the revolution frequency,  $n$  is the number of bunches per beam,  $N_1$  and  $N_2$  are the numbers of protons per bunch,  $\sigma_x$  and  $\sigma_y$  are the gaussian transverse sizes of the bunches. With the expected parameters, the LHC expected luminosity is about

$$f = \frac{v}{2\pi r_{LHC}} \approx \frac{3 \times 10^8 \text{ m/s}}{27 \text{ km}} \approx 11.1 \text{ kHz},$$

$$n = 2808$$

$$N_1 = N_2 \sim 1.5 \times 10^{11}$$

$$\sigma_x = \sigma_y = 16 \mu\text{m}$$

1119

$$L = 1.28 \times 10^{34} \text{ cm}^{-2} \text{ s}^{-1} = 1.28 \times 10^{-5} \text{ fb}^{-1} \text{ s}^{-1} \quad (2.3)$$

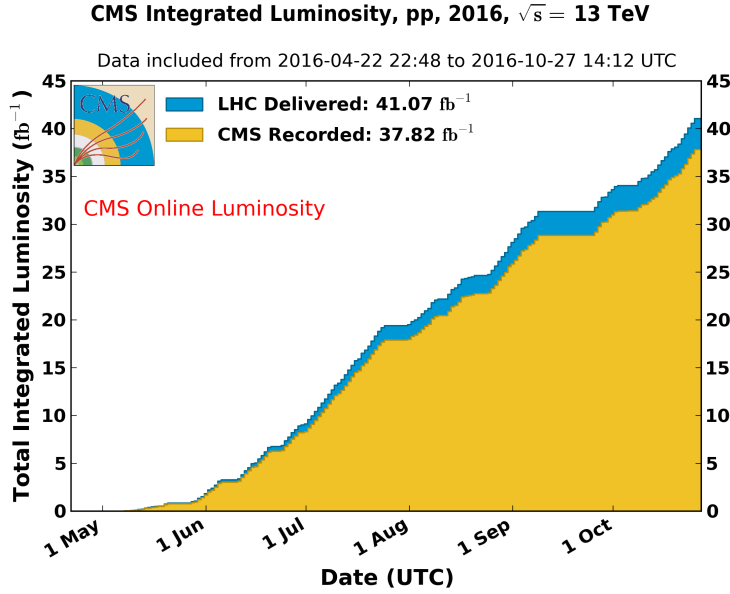


**Figure 2.6:** Integrated luminosity delivered by LHC and recorded by CMS during 2016. The difference between the delivered and the recorded luminosity is due to fails and issues occurred during the data taking in the CMS experiment [71].

1120        Luminosity is a fundamental aspect of LHC given that the bigger luminosity the  
 1121        bigger number of collisions, which means that for processes with a very small cross  
 1122        section the number of expected occurrences is increased and so the chances of being  
 1123        detected. The integrated luminosity, collected by the CMS experiment during 2016  
 1124        is shown in Figure 2.6; the data analyzed in this thesis corresponds to an integrated  
 1125        luminosity of  $35.9 \text{ fb}^{-1}$  at a center of mass-energy  $\sqrt{s} = 13 \text{ TeV}$ .

1126        One way to increase  $L$  is increasing the number of bunches in the beam. Cur-  
 1127        rently, the separation between two consecutive bunches in the beam is 7.5 m which  
 1128        corresponds to a time separation of 25 ns. In the full LHC ring the allowed number  
 1129        of bunches is  $n = 27\text{km}/7.5\text{m} = 3600$ ; however, there are some gaps in the bunch pat-  
 1130        tern intended for preparing the dumping and injection of the beam, thus, the proton  
 1131        beams are composed of 2808 bunches.

1132        Once the proton beams reach the desired energy, they are brought to cross each

other producing  $pp$  collisions. The bunch crossing happens in precise places where the four LHC experiments are located, as seen in the top of Figure 2.7. In 2008  $pp$  collisions of  $\sqrt{s} = 7$  TeV were performed; the energy was increased to 8 TeV in 2012 and to 13 TeV in 2015.

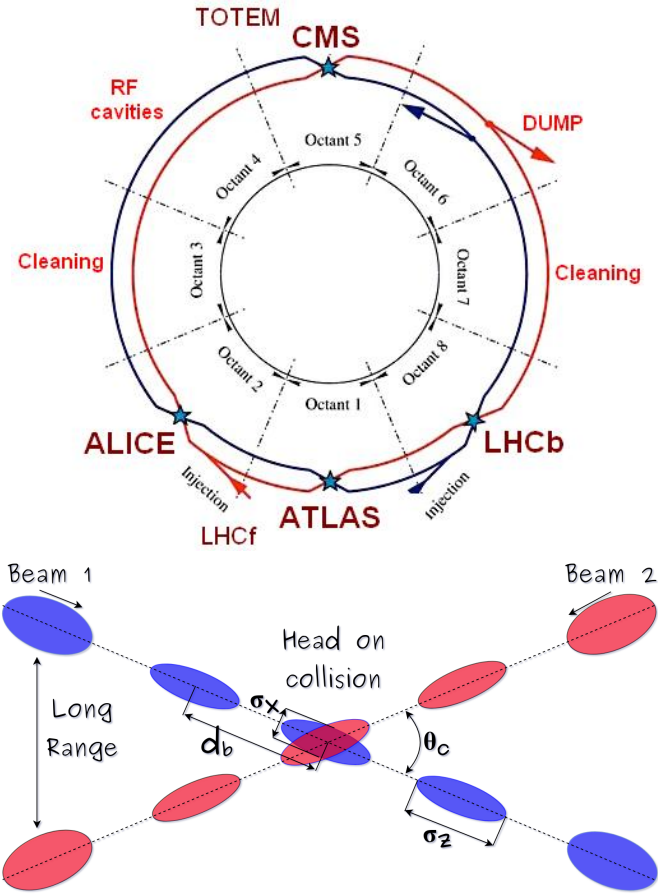


**Figure 2.7:** Top: LHC interaction points. Bunch crossing occurs where the LHC experiments are located [72]. Sections indicated as cleaning are dedicated to collimate the beam in order to protect the LHC ring from collisions with protons in very spreaded bunches. Bottom: bunch crossing scheme. Since the bunch crossing is not perfectly head-on, the luminosity is reduced in a factor of 17%; adapted from Reference [86].

The CMS and ATLAS experiments are multi-purpose experiments, hence, they are enabled to explore physics in any of the LHC collision modes. LHCb experiment is optimized to explore bottom quark physics, while ALICE is optimized for heavy

1140 ion collisions searches; TOTEM and LHCf are dedicated to forward physics studies;  
 1141 MoEDAL (not indicated in the Figure) is intended for monopole or massive pseudo  
 1142 stable particles searches.

1143 At the IP there are two interesting details that need to be addressed. The first  
 1144 one is that the bunch crossing does not occur head-on but at a small crossing angle  $\theta_c$   
 1145 (280  $\mu$ rad in CMS and ATLAS) as shown in the bottom side of Figure 2.7, affecting  
 1146 the overlapping between bunches; the consequence is a reduction of about 17% in  
 1147 the luminosity (represented by a factor not included in eqn. 2.2). The second one  
 1148 is the occurrence of multiple  $pp$  collisions in the same bunch crossing; this effect is  
 1149 called *pileup* (PU). A fairly simple estimation of the PU follows from estimating the  
 1150 probability of collision between two protons, one from each of the bunches in the  
 1151 course of collision; it depends roughly on the ratio of proton size and the cross section  
 1152 of the bunch in the IP, i.e.,

$$P(pp\text{-}collision) \sim \frac{d_{proton}^2}{\sigma_x \sigma_y} = \frac{(1\text{fm})^2}{(16\mu\text{m})^2} \sim 4 \times 10^{-21} \quad (2.4)$$

1153 however, there are  $N = 1.15 \times 10^{11}$  protons in a bunch, thus the estimated number of  
 1154 collisions in a bunch crossing is

$$PU = N^2 * P(pp\text{-}collision) \sim 50pp \text{ collision per bunch crossing}, \quad (2.5)$$

1155 about 20 of which are inelastic. A multiple  $pp$  collision event in a bunch crossing at  
 1156 CMS is shown in Figure 2.8.

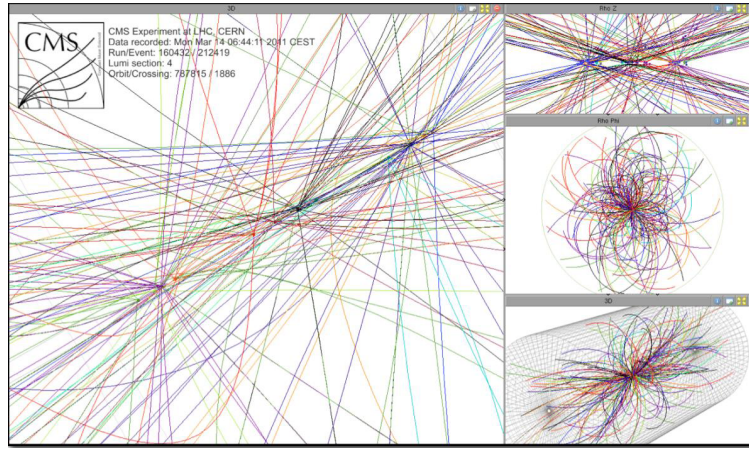


**Figure 2.8:** Multiple  $pp$  collision bunch crossing at CMS. [73].

## 1157 2.3 The CMS experiment

1158 CMS is a general-purpose detector designed to conduct research in a wide range  
 1159 of physics from the standard model to new physics like extra dimensions and dark  
 1160 matter. Located at Point 5 in the LHC layout as shown in Figure 2.4, CMS is  
 1161 composed of several detection systems distributed in a cylindrical structure; in total,  
 1162 CMS weights about 12500 tons in a very compact 21.6 m long and 14.6 m diameter  
 1163 cylinder. It was built in 15 separate sections at the ground level and lowered to the  
 1164 cavern individually to be assembled. A complete and detailed description of the CMS  
 1165 detector and its components is given in Reference [74] on which this section is based.  
 1166 Figure 2.9 shows the layout of the CMS detector. The detection system is composed  
 1167 of (from the innermost to the outermost)

- 1168     • Pixel detector.
- 1169     • Silicon strip tracker.
- 1170     • Preshower detector.
- 1171     • Electromagnetic calorimeter.

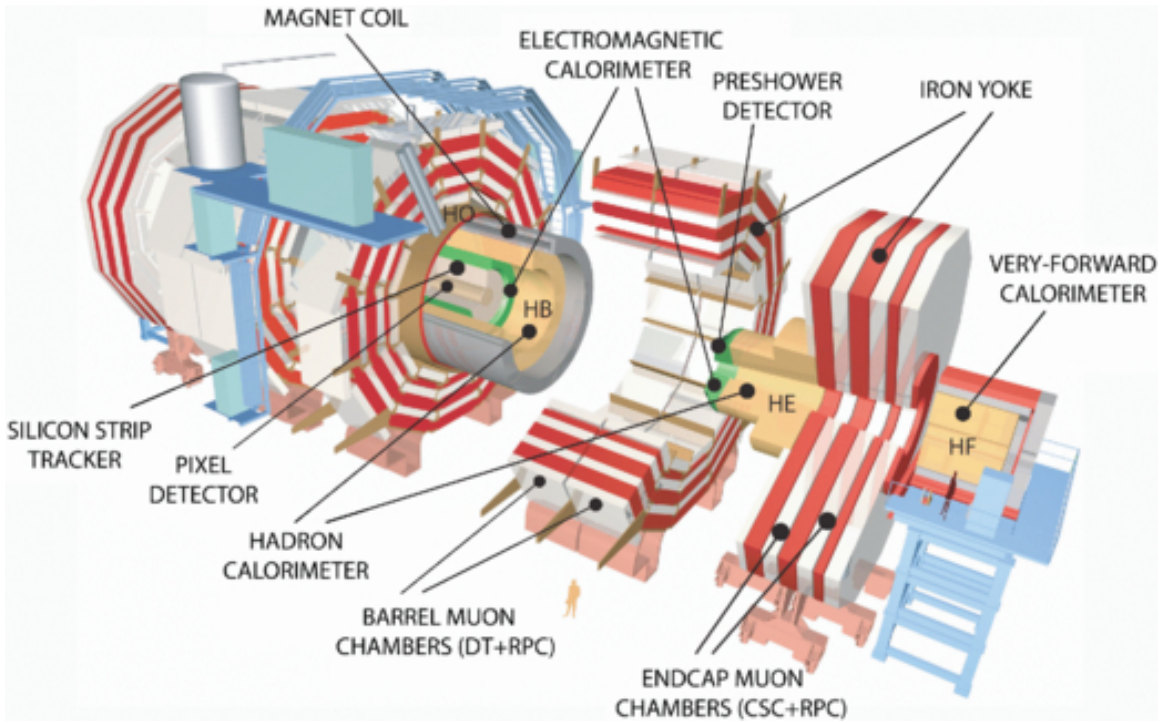


**Figure 2.9:** Layout of the CMS detector. The several subdetectors are indicated. The central region of the detector is referred as the barrel section while the endcaps are referred as the forward sections. [75].

1172 • Hadronic calorimeter.

1173 • Muon chambers (barrel and endcap)

1174 The central region of the detector is commonly referred as the barrel section while  
 1175 the endcaps are referred as the forward sections of the detector; thus, each subdetector  
 1176 is composed of a barrel section and a forward section.

1177 When a  $pp$  collision happens inside the CMS detector, many different particles are  
 1178 produced, but only some of them live long enough to be detected; they are electrons,  
 1179 photons, pions, kaons, protons, neutrons and muons; neutrinos are not detected by  
 1180 the CMS detector. Thus, the CMS detector was designed to detect those particles and  
 1181 measure their properties. Figure 2.10 shows a transverse slice of the CMS detector.  
 1182 The silicon tracker (pixel detector + strip tracker) is capable to register the track of

the charged particles traversing it, while calorimeters (electromagnetic and hadronic) measure the energy of the particles that are absorbed by their materials. Considering the detectable particles, mentioned above, emerging from the IP, a basic description of the detection process is as follows.

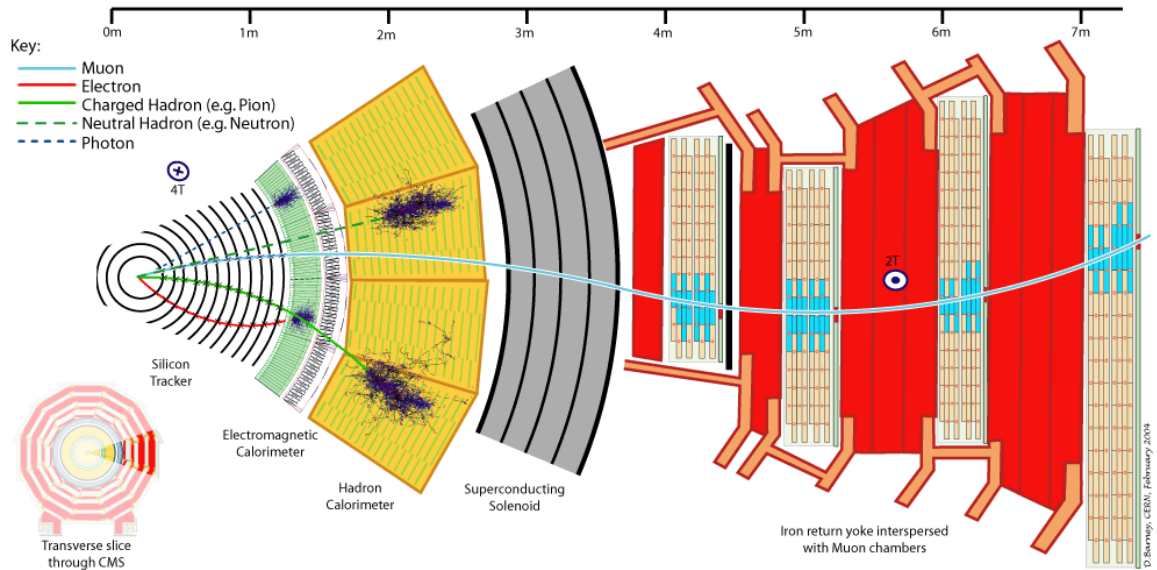


**Figure 2.10:** CMS detector transverse slice [76].

A muon emerging from the IP, will create a track on the silicon tracker and on the muon chambers. The design of the CMS detector is driven by the requirements on the identification, momentum resolution and unambiguous charge determination of the muons; therefore, a large bending power is provided by the solenoid magnet made of superconducting cable capable of generating a 3.8 T magnetic field. The muon track is bent twice since the magnetic field inside the solenoid is directed along the  $z$ -direction but outside its direction is reversed. Muons interact very weakly with the calorimeters, therefore, it is not absorbed but escape away from the detector.

An electron emerging from the IP will create a track along the tracker which will be bent due to the presence of the magnetic field, later, it will be absorbed in the electromagnetic calorimeter where its energy is measured.

1198        A photon will not leave a track because it is neutral, but it will be absorbed in  
 1199        the electromagnetic calorimeter.

1200        A neutral hadron, like the neutron, will not leave a track either but it will lose a  
 1201        small amount of its energy during its passage through the electromagnetic calorimeter  
 1202        and then it will be absorbed in the hadron calorimeter depositing the rest of its energy.

1203        A charged hadron, like the proton or  $\pi^\pm$ , will leave a curved track on the silicon  
 1204        tracker, some of its energy in the electromagnetic calorimeter and finally will be  
 1205        absorbed in the hadronic calorimeter.

1206        A more detailed description of each detection system will be presented in the  
 1207        following sections.

### 1208        2.3.1 CMS coordinate system

1209        The coordinate system used by CMS is centered on the geometrical center of the  
 1210        detector which is the nominal IP as shown in Figure 2.11<sup>1</sup>. The  $z$ -axis is parallel  
 1211        to the beam direction, while the  $Y$ -axis pointing vertically upward, and the  $X$ -axis  
 1212        pointing radially inward toward the center of the LHC.

1213        In addition to the common cartesian and cylindrical coordinate systems, two co-  
 1214        ordinates are of particular utility in particle physics: rapidity ( $y$ ) and pseudorapidity  
 1215        ( $\eta$ ), defined in connection to the polar angle  $\theta$ , energy and longitudinal momentum  
 1216        component (momentum along the  $z$ -axis) according to

$$y = \frac{1}{2} \ln \frac{E + p_z}{E - p_z} \quad \eta = -\ln \left( \tan \frac{\theta}{2} \right) \quad (2.6)$$

1217        Rapidity is related to the angle between the  $XY$ -plane and the direction in which  
 1218        the products of a collision are emitted; it has the nice property that the difference

---

<sup>1</sup> Not all the  $pp$  interaction occur at the nominal IP because of the bunch lenght, therefore, each  $pp$  collision has its own IP location

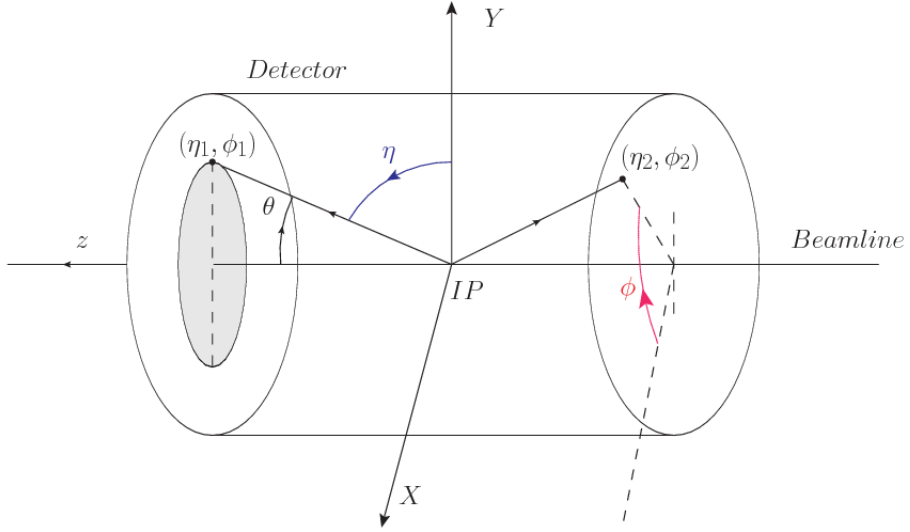


**Figure 2.11:** CMS detector coordinate system.

1219 between the rapidities of two particles is invariant with respect to Lorentz boosts  
 1220 along the  $z$ -axis, hence, data analysis becomes more simple when based on rapid-  
 1221 ity; however, it is not simple to measure the rapidity of highly relativistic particles,  
 1222 as those produced after  $pp$  collisions. Under the highly relativistic motion approxi-  
 1223 mation,  $y$  can be rewritten in terms of the polar angle, concluding that rapidity is  
 1224 approximately equal to the pseudorapidity defined above, i.e.,  $y \approx \eta$ . Note that  $\eta$   
 1225 is easier to measure than  $y$  given the direct relationship between the former and the  
 1226 polar angle.

1227 The angular distance between two objects in the detector ( $\Delta R$ ) is commonly used  
 1228 to judge the isolation of those object; it is defined in terms of their coordinates  $(\eta_1, \phi_1)$ ,  
 1229  $(\eta_2, \phi_2)$  as

$$\Delta R = \sqrt{(\Delta\eta)^2 - (\Delta\phi)^2} \quad (2.7)$$

### 1230 2.3.2 Tracking system

1231 The CMS tracking system is designed to provide a precise measurement of the trajectories (*track*) followed by the charged particles created after the  $pp$  collisions; also, the  
 1232 precise reconstruction of the primary and secondary origins of the tracks (*vertices*) is  
 1233 expected in an environment where, each 25 ns, the bunch crossing produces about 20  
 1234 inelastic collisions and about 1000 particles.  
 1235

1236 Physics requirements guiding the tracking system performance include the precise characterization of events involving gauge bosons, W and Z, and their leptonic  
 1237 decays for which an efficient isolated lepton and photon reconstruction is of capital  
 1238 importance, given that isolation is required to suppress background events to a level  
 1239 that allows observations of interesting processes like Higgs boson decays or beyond  
 1240 SM events.

1242 The ability to identify and reconstruct  $b$ -jets and B-hadrons within these jets is also  
 1243 a fundamental requirement, achieved through the ability to reconstruct accurately  
 1244 displaced vertices, given that  $b$ -jets are part of the signature of top quark physics, like  
 1245 the one treated in this thesis.

1246 An schematic view of the CMS tracking system is shown in Figure 2.12

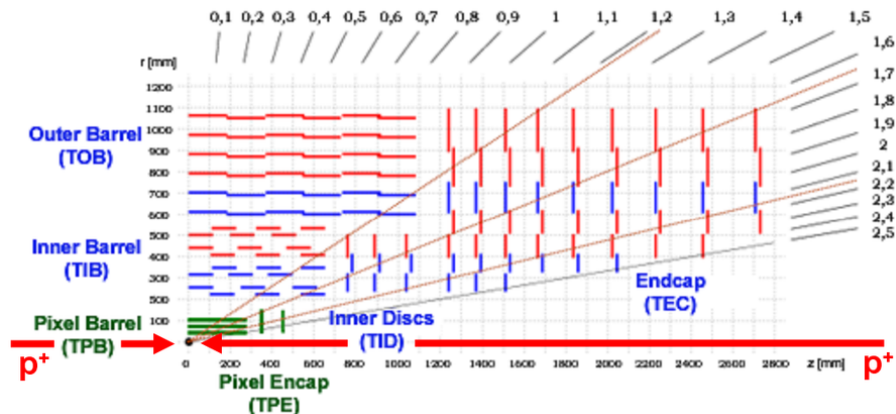


**Figure 2.12:** CMS tracking system schematic view [78].

1247 In order to satisfy these performance requirements, the tracking system uses two  
 1248 different detector subsystems arranged in concentric cylindrical volumes, the pixel  
 1249 detector and the silicon strip tracker; the pixel detector is located in the high particle  
 1250 density region ( $r < 20\text{cm}$ ) while the silicon strip tracker is located in the medium and  
 1251 lower particle density regions  $20\text{cm} < r < 116\text{cm}$ .

1252 **Pixel detector**

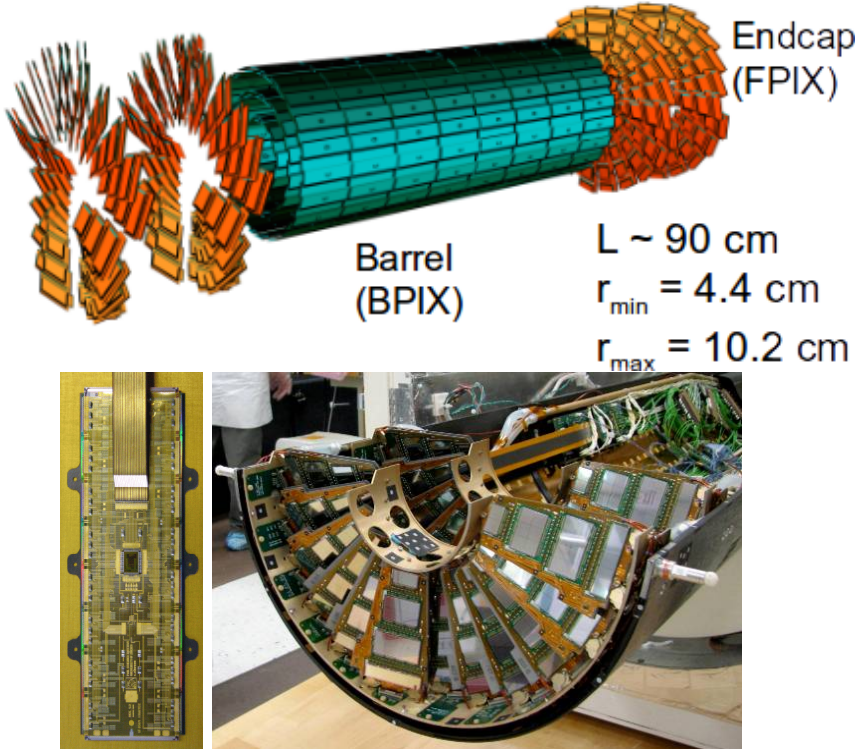


**Figure 2.13:** CMS pixel detector. Top: schematic view; Bottom: pictures of a barrel(BPIX) module(left) and forward modules(right) [74].

1253 The pixel detector was replaced during the 2016-2017 extended year-end technical  
 1254 stop, due to the increasingly challenging operating conditions like the higher particle  
 1255 flux and more radiation harsh environment, among others. The new one is responding  
 1256 as expected, reinforcing its crucial role in the successful way to fulfill the new LHC

physics objectives after the discovery of the Higgs boson. Since the data sets used in this thesis were produced using the previous version of the pixel detector, it will be the subject of the description in this section. The last chapter of this thesis is dedicated to describe my contribution to the *Forward Pixel Phase 1 upgrade*.

The pixel detector was composed of 1440 silicon pixel detector modules organized in three-barrel layers in the central region (BPix) and two disks in the forward region (FPix) as shown in the top side of Figure 2.13; it was designed to record efficiently and with high precision, up to  $20\mu\text{m}$  in the  $XY$ -plane and  $20\mu\text{m}$  in the  $z$ -direction, the first three space-points (*hits*) nearest to the IP region in the range  $|\eta| \leq 2.5$ . The first barrel layer was located at a radius of 44 mm from the beamline, while the third layer was located at a radius of 102 mm, closer to the strip tracker inner barrel layer (see Section 2.3.3) in order to reduce the rate of fake tracks. The high granularity of the detector is represented in its about 66 Mpixels, each of size  $100 \times 150\mu\text{m}^2$ . The transverse momentum resolution of tracks can be measured with a resolution of 1-2% for muons of  $p_T = 100$  GeV.

A charged particle passing through the pixel sensors produce ionization in them, giving energy for electrons to be removed from the silicon atoms, hence, creating electron-hole pairs. The collection of charges in the pixels generates an electrical signal that is read out by an electronic readout chip (ROC); each pixel has its own electronics which amplifies the signal. Combining the signal from the pixels activated by a traversing particle in the several layers of the detector allows one to reconstruct the particle's trajectory in 3D.

Commonly, the charge produced by traversing of a particle is collected by and shared among several pixels; by interpolating between pixels, the spatial resolution is improved. In the barrel section the charge sharing in the  $r\phi$ -plane is due to the Lorentz effect. In the forward pixels the charge sharing is enhanced by arranging the

1283 blades in the turbine-like layout as shown in Figure 2.13 bottom left.

1284 **2.3.3 Silicon strip tracker**

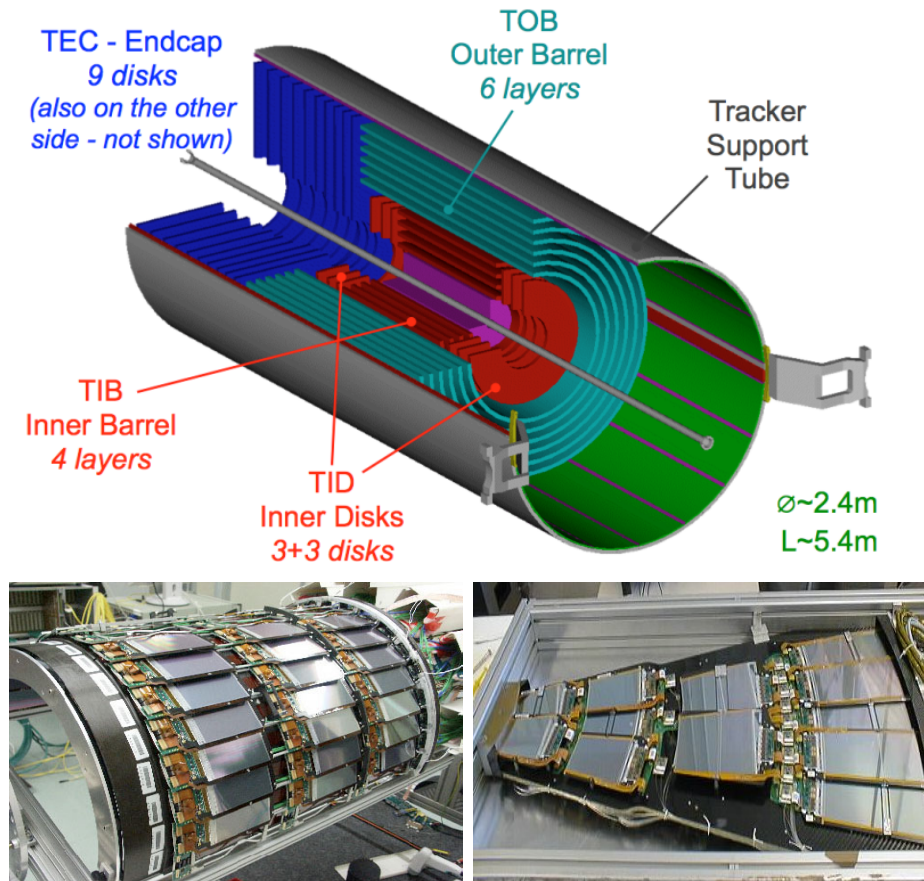


**Figure 2.14:** Top: CMS Silicon Strip Tracker (SST) schematic view. The SST is composed of the tracker inner barrel (TIB), the tracker inner disks (TID), the tracker outer barrel (TOB) and the tracker endcaps (TEC). Each part is made of silicon strip modules; the modules in blue represent two modules mounted back-to-back and rotated in the plane of the module by a stereo angle of 120 mrad in order to provide a 3-D reconstruction of the hit positions. Bottom: pictures of the TIB (left) and TEC (right) modules [80–82].

1285 The silicon strip tracker (SST) is the second stage in the CMS tracking system.

1286 The top side of Figure 2.14 shows a schematic of the SST. The inner tracker region is

1287 composed of the tracker inner barrel (TIB) and the tracker inner disks (TID) covering

1288 the region  $r < 55$  cm and  $|z| < 118$  cm. The TIB is composed of 4 layers while the TID

1289 is composed of 3 disks at each end. The silicon sensors in the inner tracker are 320  
 1290  $\mu\text{m}$  thick, providing a resolution of about 13-38  $\mu\text{m}$  in the  $r\phi$  position measurement.

1291       The modules indicated in blue in the schematic view of Figure 2.14 are two mod-  
 1292       ules mounted back-to-back and rotated in the plane of the module by a *stereo* angle  
 1293       of 100 mrad; the hits from these two modules, known as *stereo hits*, are combined to  
 1294       provide a measurement of the second coordinate ( $z$  in the barrel and  $r$  on the disks)  
 1295       allowing the reconstruction of hit positions in 3-D.

1296       The outer tracker region is composed of the tracker outer barrel (TOB) and the  
 1297       tracker endcaps (TEC). The six layers of the TOB offer coverage in the region  $r > 55$   
 1298       cm and  $|z| < 118$  cm, while the 9 disks of the TEC cover the region  $124 < |z| < 282$   
 1299       cm. The resolution offered by the outer tracker is about 13-38  $\mu\text{m}$  in the  $r\phi$  position  
 1300       measurement. The inner four TEC disks use silicon sensors 320  $\mu\text{m}$  thick; those in  
 1301       the TOB and the outer three TEC disks use silicon sensors of 500  $\mu\text{m}$  thickness. The  
 1302       silicon strips run parallel to the  $z$ -axis and the distance between strips varies from 80  
 1303        $\mu\text{m}$  in the inner TIB layers to 183  $\mu\text{m}$  in the inner TOB layers; in the endcaps the  
 1304       wedge-shaped sensors with radial strips, whose pitch range between 81  $\mu\text{m}$  at small  
 1305       radii and 205  $\mu\text{m}$  at large radii.

1306       The whole SST has 15148 silicon modules, 9.3 million silicon strips and cover a  
 1307       total active area of about 198  $\text{m}^2$ .

### 1308     **2.3.4 Electromagnetic calorimeter**

1309       The CMS electromagnetic calorimeter (ECAL) is designed to measure the energy of  
 1310       electrons and photons. It is composed of 75848 lead tungstate crystals which have a  
 1311       short radiation length (0.89 cm) and fast response, since 80% of the light is emitted  
 1312       within 25 ns; however, they are combined with Avalanche photodiodes (APDs) as

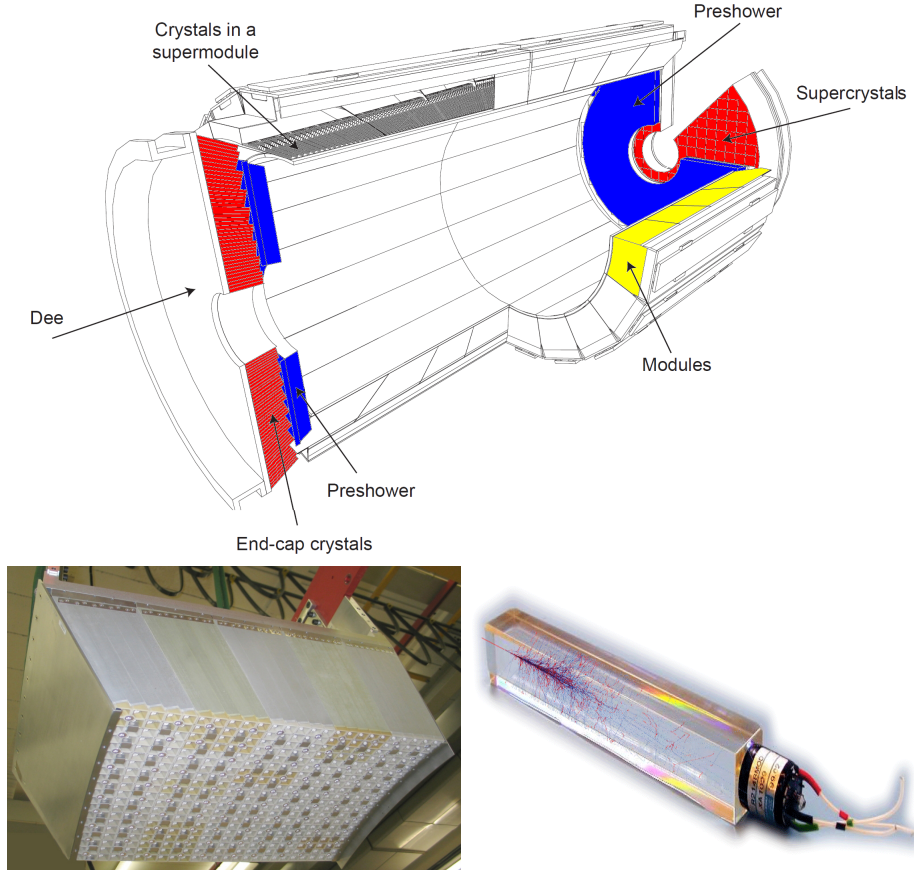


**Figure 2.15:** Top: CMS ECAL schematic view. Bottom: Module equipped with the crystals (left); ECAL crystal(right) with an artistic representation of an electromagnetic shower [74].

1313 photodetectors given that crystals themselves have a low light yield ( $30\gamma/\text{MeV}$ ). A  
 1314 schematic view of the ECAL is shown in Figure 2.15.

1315 Energy is measured when electrons and photons are absorbed by the crystals  
 1316 which generates an electromagnetic *shower*, as seen in bottom right picture of the  
 1317 Figure 2.15; the shower is seen as a *cluster* of energy which depending on the amount  
 1318 of energy deposited can involve several crystals. The ECAL barrel (EB) covers the  
 1319 region  $|\eta| < 1.479$ , using crystals of depth of 23 cm and  $2.2 \times 2.2 \text{ cm}^2$  transverse  
 1320 section; the ECAL endcap (EE) covers the region  $1.479 < |\eta| < 3.0$  using crystals of  
 1321 depth 22 cm and transverse section of  $2.86 \times 2.86 \text{ cm}^2$ ; the photodetectors used are

vacuum phototriodes (VPTs). Each EE is divided in two structures called *Dees*.

The preshower detector (ES) is installed in front of the EE and covers the region  $1.653 < |\eta| < 2.6$ . The ES provides a precise measurement of the position of electromagnetic showers, which allows to distinguish electrons and photon signals from  $\pi^0$  decay signals. The ES is composed of a layer of lead radiators followed by a layer of silicon strip sensors. The lead radiators initiate electromagnetic showers when reached by photons and electrons, then, the strip sensors measure the deposited energy and the transverse shower profiles. The full ES thickness is 20 cm.

### 2.3.5 Hadronic calorimeter

Hadrons are not absorbed by the ECAL<sup>2</sup> but by the hadron calorimeter (HCAL), which is made of a combination of alternating brass absorber layers and silicon photomultiplier(SiPM) layers; therefore, particles passing through the scintillator material produce showers, as in the ECAL, as a result of the inelastic scattering of the hadrons with the detector material. Since the particles are not absorbed in the scintillator, their energy is sampled; therefore the total energy is not measured but estimated from the energy clusters, which reduces the resolution of the detector. Brass was chosen as the absorber material due to its short interaction length ( $\lambda_I = 16.42\text{cm}$ ) and its non-magnetivity. Figure 2.16 shows a schematic view of the CMS HCAL.

The HCAL is divided into four sections; the Hadron Barrel (HB), the Hadron Outer (HO), the Hadron Endcap (HE) and the Hadron Forward (HF) sections. The HB covers the region  $0 < |\eta| < 1.4$ , while the HE covers the region  $1.3 < |\eta| < 3.0$ . The HF, made of quartz fiber scintillator and steel as absorption material, covers the forward region  $3.0 < |\eta| < 5.2$ . Both the HB and HF are located inside the solenoid. The HO is placed outside the magnet as an additional layer of scintillators with the

---

<sup>2</sup> Most hadrons are not absorbed, but few low-energy ones might be.

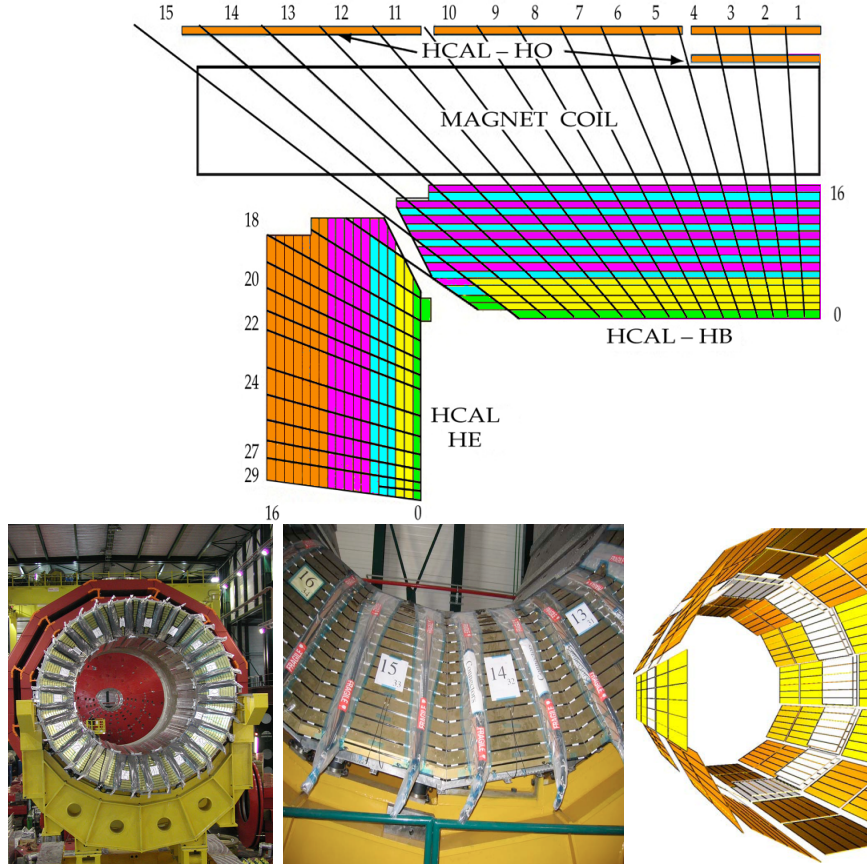


**Figure 2.16:** Top: CMS HCAL schematic view, the colors indicate the layers that are grouped into the same readout channels. Bottom: picture of a section of the HB; the absorber material is the golden region and scintillators are placed in between the absorber material (left and center). Schematic view of the HO (right). [83,84]

1346 purpose of measure the energy tails of particles passing through the HB and the  
 1347 magnet (see Figure 2.16 top and bottom right).

### 1348 **2.3.6 Superconducting solenoid magnet**

1349 The superconducting magnet installed in the CMS detector is designed to provide  
 1350 an intense and highly uniform magnetic field in the central part of the detector.  
 1351 In fact, the tracking system takes advantage of the bending power of the magnetic  
 1352 field to measure with precision the momentum of the particles that traverse it; the

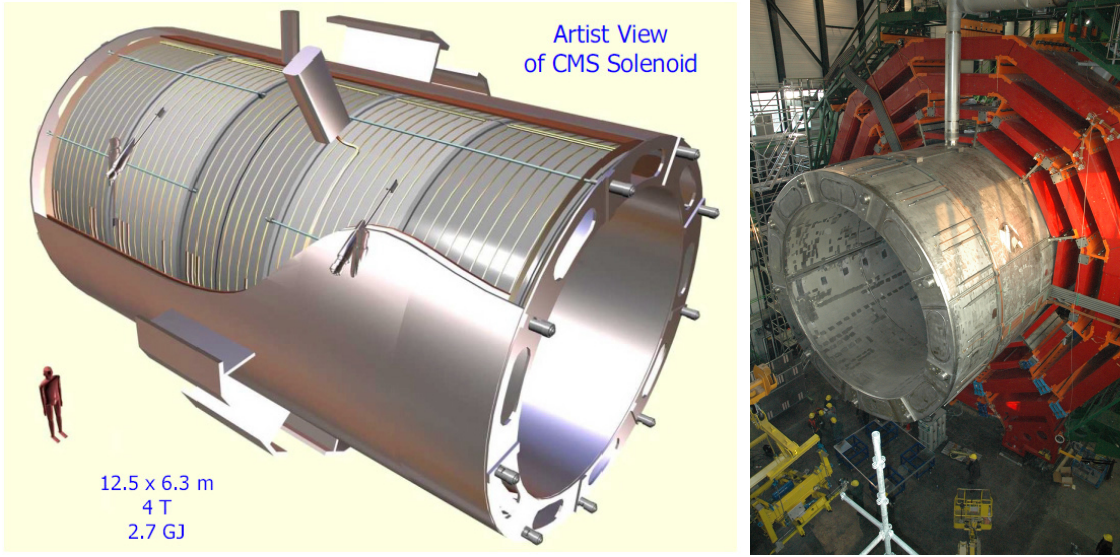


**Figure 2.17:** Artistic representation of the CMS solenoid magnet(left). The magnet is supported on an iron yoke (right) which also serves as the house of the muon detector and as mechanical support for the whole CMS detector [77].

1353 unambiguous determination of the sign for high momentum muons was a driving  
 1354 principle during the design of the magnet. The magnet has a diameter of 6.3 m, a  
 1355 length of 12.5 m and a cold mass of 220 t; the generated magnetic field reaches a  
 1356 strength of 3.8T. Since it is made of Ni-Tb superconducting cable it has to operate at  
 1357 a temperature of 4.7 K by using a helium cryogenic system; the current circulating in  
 1358 the cables reaches 18800 A under normal running conditions. The left side of Figure  
 1359 2.17 shows an artistic view of the CMS magnet, while the right side shows a transverse  
 1360 view of the cold mass where the winding structure is visible.

1361 The yoke (see Figure 2.17), composed of 5 barrel wheels and 6 endcap disks made  
 1362 of iron, serves not only as the media for magnetic flux return but also provides housing  
 1363 for the muon detector system and structural stability to the full detector.

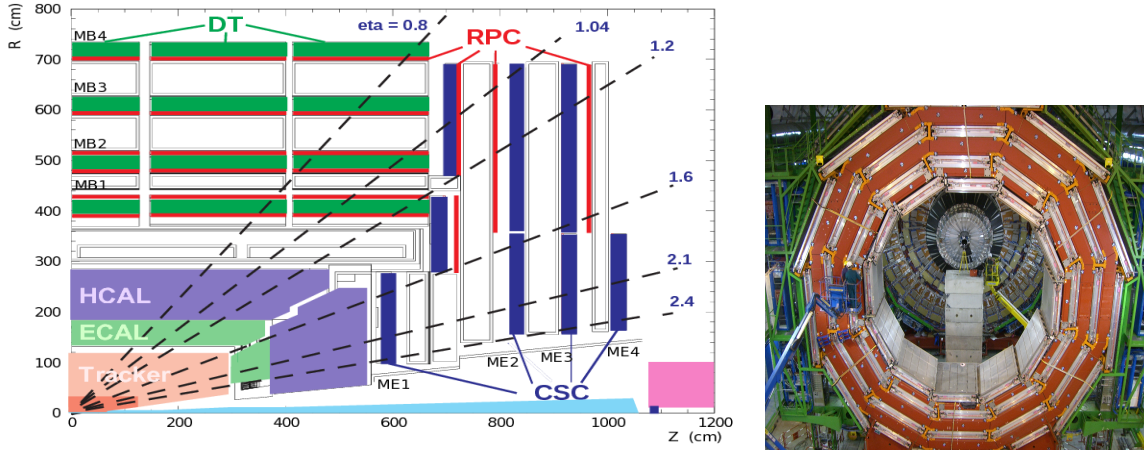


**Figure 2.18:** Left: CMS muon system schematic view; Right: one of the yoke rings with the muon DTs and RPCs installed; in the back it is possible to see the muon endcap [85].

### 1364 2.3.7 Muon system

1365 Muons are the only charged particles able to pass through all the CMS detector due  
 1366 to their low ionization energy loss; thus, muons can be separated easily from the  
 1367 high amount of particles produced in a  $pp$  collision. Also, muons are expected to be  
 1368 produced in the decay of several new particles; therefore, good detection of muons  
 1369 was one of the leading principles when designing the CMS detector.

1370 The CMS muon detection system (muon spectrometer) is embedded in the return  
 1371 yoke as seen in Figure 2.18. It is composed of three different detector types, the drift  
 1372 tube chambers (DT), cathode strip chambers (CSC), and resistive plate chambers  
 1373 (RPC); DT are located in the central region  $\eta < 1.2$  arranged in four layers of drift  
 1374 chambers filled with an Ar/CO<sub>2</sub> gas mixture.

1375 The muon endcaps are made of CSCs covering the region  $\eta < 2.4$  and filled with  
 1376 a mixture of Ar/CO<sub>2</sub>/CF<sub>4</sub>. The reason behind using a different detector type lies on  
 1377 the different conditions in the forward region like the higher muon rate and higher  
 1378 residual magnetic field compared to the central region.

1379 The third type of detector used in the muon system is a set of four disks of RPCs

1380 working in avalanche mode. The RPCs provide good spatial and time resolutions. The  
 1381 track of high- $p_T$  muon candidates is built combining information from the tracking  
 1382 system and the signal from up to six RPCs and four DT chambers.

1383 The muon tracks are reconstructed from the hits in the several layers of the muon  
 1384 system.

### 1385 2.3.8 CMS trigger system

1386 CMS expects  $pp$  collisions every 25 ns, i.e., an interaction rate of 40 MHz for which  
 1387 it is not possible to store the recorded data in full. In order to handle this high event  
 1388 rate data, an online event selection, known as triggering, is performed; triggering  
 1389 reduces the event rate to 100 Hz for storage and further offline analysis.

1390 The trigger system starts with a reduction of the event rate to 100 kHz in the  
 1391 so-called *the level 1 trigger* (L1). L1 is based on dedicated programmable hardware  
 1392 like Field Programmable Gate Arrays (FPGAs) and Application Specific Integrated  
 1393 Circuits (ASICs), partly located in the detector itself; another portion is located in  
 1394 the CMS underground cavern. Hit pattern information from the muon chambers  
 1395 and the energy deposits in the calorimeter are used to decide if an event is accepted  
 1396 or rejected, according to selection requirements previously defined, which reflect the  
 1397 interesting physics processes. Figure 2.19 shows the L1 trigger architecture.

1398 The second stage in the trigger system is called *the high-level trigger* (HLT); events  
 1399 accepted by L1 are passed to HLT in order to make an initial reconstruction of them.  
 1400 HLT is software based and runs on a dedicated server farm, using selection algorithms  
 1401 and high-level object definitions; the event rate at HLT is reduced to 100 Hz. The  
 1402 first HLT stage takes information from the muon detectors and the calorimeters to  
 1403 make the initial object reconstruction; in the next HLT stage, information from the

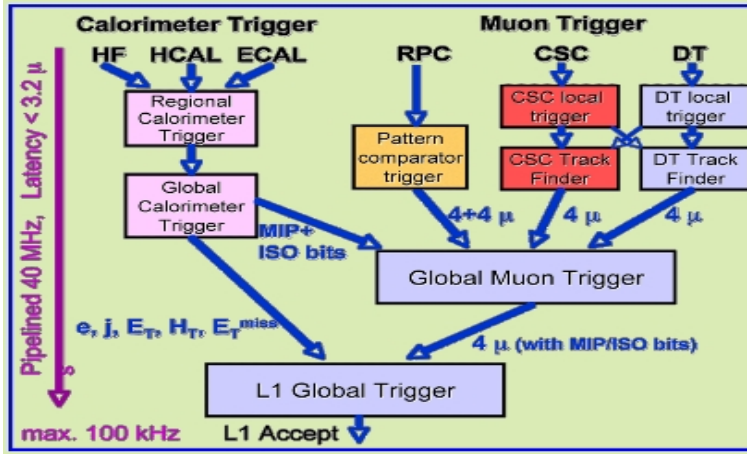


**Figure 2.19:** CMS Level-1 trigger architecture [86].

pixel and strip detectors is used to do first fast tracking and then full tracking online.  
 This initial object reconstruction is used in further steps of the trigger system.

Events and preliminary reconstructed physics objects from HLT are sent to be fully reconstructed at the CERN computing center known also as Tier-0 facility. Again, the pixel detector information provides high-quality seeds for the track reconstruction algorithm offline, primary vertex reconstruction, electron and photon identification, muon reconstruction,  $\tau$  identification, and b-tagging. After full reconstruction, data sets are made available for offline analyses.

### 2.3.9 CMS computing

Data coming from the experiment have to be stored and made available for further analysis; in order to cope with all the tasks implied in the offline data processing, like transfer, simulation, reconstruction and reprocessing, among others, a large computing power is required. The CMS computing system is based on the distributed architecture concept, where users of the system and physical computer centers are distributed worldwide and interconnected by high-speed networks.

The worldwide LHC computing grid (WLCG) is the mechanism used to provide

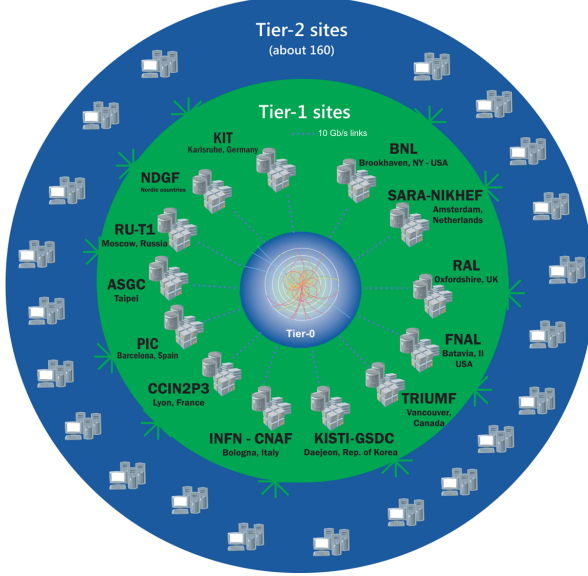


**Figure 2.20:** WLCG structure. The primary computer centers (Tier-0) are located at CERN (data center) and at the Wigner datacenter in Budapest. Tier-1 is composed of 13 centers and Tier-2 is composed of about 160 centers. [87].

1420 that distributed environment. WLCG is a tiered structure connecting computing  
 1421 centers around the world, which provides the necessary storage and computing facil-  
 1422 ities. The primary computing centers of the WLCG are located at the CERN and  
 1423 the Wigner datacenter in Budapest and are known as Tier-0 as shown in Figure 2.20.  
 1424 The main responsibilities for each tier level are [87]

- 1425     • **Tier-0:** initial reconstruction of recorded events and storage of the resulting  
       1426       datasets, the distribution of raw data to the Tier-1 centers.
- 1427     • **Tier-1:** provide storage capacity, support for the Grid, safe-keeping of a pro-  
       1428       portional share of raw and reconstructed data, large-scale reprocessing and safe-  
       1429       keeping of corresponding output, generation of simulated events, distribution  
       1430       of data to Tier 2s, safe-keeping of a share of simulated data produced at these  
       1431       Tier 2s.
- 1432     • **Tier-2:** store sufficient data and provide adequate computing power for spe-

1433       cific analysis tasks and proportional share of simulated event production and  
1434       reconstruction.

1435       Aside from the general computing strategy to manage the huge amount of data  
1436       produced by experiments, CMS uses a software framework to perform a variety of  
1437       processing, selection and analysis tasks. The central concept of the CMS data model  
1438       referred to as *event data model* (EDM) is the *Event*; therefore, an event is the unit  
1439       that contains the information from a single bunch crossing, any data derived from  
1440       that information like the reconstructed objects, and the details of the derivation.

1441       Events are passed as the input to the *physics modules* that obtain information  
1442       from them and create new information; for instance, *event data producers* add new  
1443       data into the events, *analyzers* produce an information summary from an event set,  
1444       *filters* perform selection and triggering.

1445       CMS uses several event formats with different levels of detail and precision

1446       • **Raw format:** events in this format contain the full recorded information from  
1447       the detector as well as trigger decision and other metadata. An extended version  
1448       of raw data is used to store information from the CMS Monte Carlo simulation  
1449       tools (see Chapter 3). Raw data are stored permanently, occupying about  
1450       2MB/event

1451       • **RECO format:** events in this format correspond to raw data that have been  
1452       submitted to reconstruction algorithms like primary and secondary vertex re-  
1453       construction, particle ID, and track finding. RECO events contain physics ob-  
1454       jects and all the information used to reconstruct them; average size is about 0.5  
1455       MB/event.

- 1456     • **AOD format:** Analysis Object Data (AOD) is the data format used in the  
 1457        physics analyses given that it contains the parameters describing the high-level  
 1458        physics objects in addition to enough information to allow a kinematic refitting if  
 1459        needed. AOD events are filtered versions of the RECO events to which skimming  
 1460        or other filtering have been applied, hence AOD events are subsets of RECO  
 1461        events. Requires about 100 kB/event.
- 1462     • **Non-event data** are data needed to interpret and reconstruct events. Some  
 1463        of the non-event data used by CMS contains information about the detector  
 1464        contraction and condition data like calibrations, alignment, and detector status.

1465     Figure 2.21 shows the data flow scheme between CMS detector and tiers.

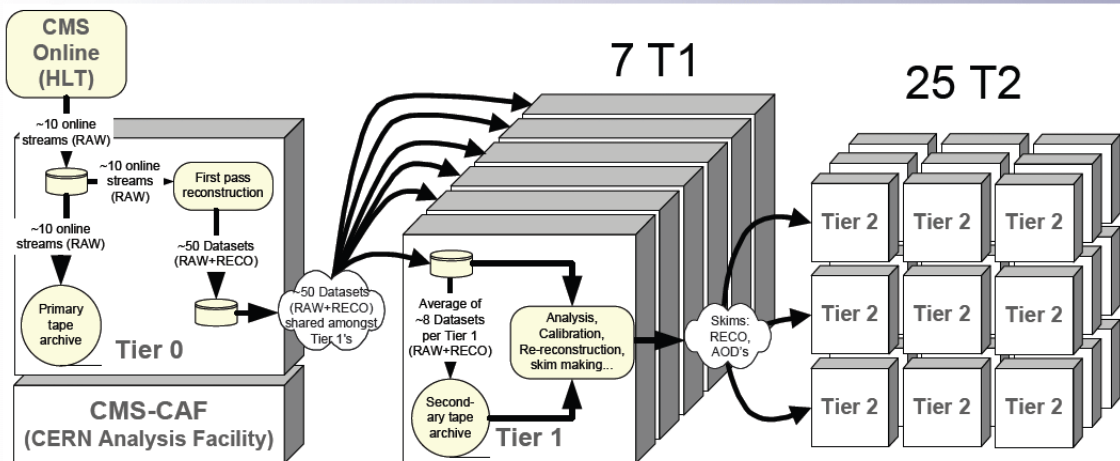


**Figure 2.21:** Data flow from CMS detector through tiers.

1466     The whole collection of software built as a framework is referred to as *CMSSW*. This  
 1467        framework provides the services needed by the simulation, calibration and alignment,  
 1468        and reconstruction modules that process event data, so that physicists can perform  
 1469        analysis. The CMSSW event processing model is composed of one executable, called  
 1470        `cmsRun`, and several plug-in modules which contains all the tools (calibration, recon-

1471 struction algorithms) needed to process an event. The same executable is used for  
1472 both detector data and Monte Carlo simulations [88].

<sup>1473</sup> **Chapter 3**

<sup>1474</sup> **Event generation, simulation and  
<sup>1475</sup> reconstruction**

<sup>1476</sup> The process of analyzing data recorded by the CMS experiment involves several stages  
<sup>1477</sup> where the data are processed in order to interpret the information provided by all  
<sup>1478</sup> the detection systems; in those stages, the particles produced after the  $pp$  collision  
<sup>1479</sup> are identified by reconstructing their trajectories and measuring their features. In  
<sup>1480</sup> addition, the SM provides a set of predictions that have to be compared with the  
<sup>1481</sup> experimental results; however, in most of the cases, theoretical predictions are not  
<sup>1482</sup> directly comparable to experimental results due to the diverse source of uncertainties  
<sup>1483</sup> introduced by the experimental setup and theoretical approximations, among others.

<sup>1484</sup> The strategy to face these conditions consists in using statistical methods imple-  
<sup>1485</sup> mented in computational algorithms to produce numerical results that can be con-  
<sup>1486</sup> trasted with the experimental results. These computational algorithms are commonly  
<sup>1487</sup> known as Monte Carlo (MC) methods and, in the case of particle physics, they are  
<sup>1488</sup> designed to apply the SM rules and produce predictions about the physical observ-  
<sup>1489</sup> ables measured in the experiments. Since particle physics is governed by quantum

mechanics principles, predictions are not allowed from single events; therefore, a high number of events are *generated* and predictions are produced in the form of statistical distributions for the observables. Effects of the detector presence are included in the predictions by introducing simulations of the detector itself.

This chapter presents a description of the event generation strategy and the tools used to perform the detector simulation and physics objects reconstruction. A comprehensive review of event generators for LHC physics can be found in Reference [89] on which this chapter is based.

### 3.1 Event generation

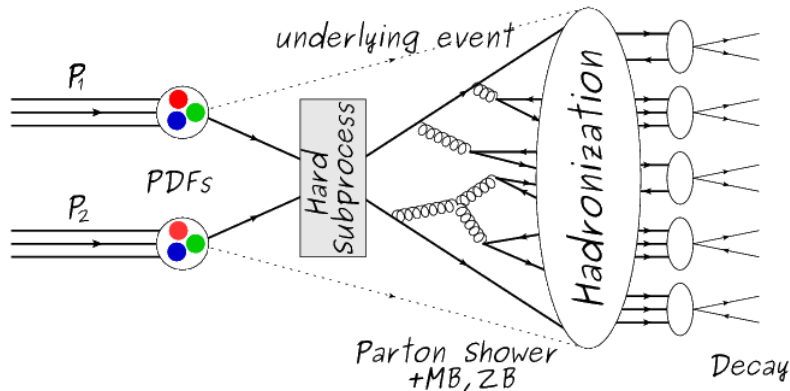


**Figure 3.1:** Event generation process. The actual interaction is generated in the hard subprocess. The parton shower describes the evolution of the partons from the hard subprocess. Modified from Reference [90].

The event generation is intended to create events that mimic the behavior of actual events produced in collisions; they obey a sequence of steps from the particles collision hard process to the decay process into the final state. Figure 3.1 shows a schematic view of the event generation process; the fact that the full process can be treated as several independent steps is motivated by the QCD factorization theorem.

1504        Generation starts by taking into account the PDFs of the incoming particles.  
 1505      Event generators offer the option to chose from several PDF sets depending on the  
 1506      particular process under simulation<sup>1</sup>; in the following,  $pp$  collisions will be consid-  
 1507      ered. The *hard subprocess* describes the actual interaction between partons from the  
 1508      incoming protons; it is represented by the matrix element connecting the initial and  
 1509      final states of the interaction. Normally, the matrix element can be written as a  
 1510      sum over Feynman diagrams and consider interferences between terms in the sum-  
 1511      mation. During the generation of the hard subprocess, the production cross section  
 1512      is calculated.

1513        The order to which the cross section is calculated depends on the order of the Feyn-  
 1514      man diagrams involved in the calculation; therefore, radiative corrections are included  
 1515      by considering a higher order Feynman diagrams where QCD radiation dominates.  
 1516      Currently, cross sections calculated to LO do not offer a satisfactory description of the  
 1517      processes, i.e., the results are only reliable for the shape of distributions; therefore,  
 1518      NLO calculations have to be performed with the implication that the computing time  
 1519      needed is highly increased.

1520        The final parton content of the hard subprocess is subjected to the *parton shower*  
 1521      which generates the gluon radiation. Parton shower evolves the partons, i.e., glouns  
 1522      split into quark-antiquark pairs and quarks with enough energy radiate gluons giv-  
 1523      ing rise to further parton multiplication, following the DGLAP (Dokshitzer-Gribov-  
 1524      Lipatov-Altarelli-Parisi) equations. Showering continues until the energy scale is low  
 1525      enough to reach the non-perturbative limit.

1526        In the simulation of LHC processes that involve  $b$  quarks, like the single top quark  
 1527      or Higgs associated production, it is needed to consider that the  $b$  quark is heavier  
 1528      than the proton; hence, the QCD interaction description is made in two different

---

<sup>1</sup> Tool in Reference [91] allows to plot different PDF sets under customizable conditions.

1529 schemes [95]

- 1530 • four-flavor (4F) scheme.  $b$  quarks appear only in the final state because they  
 1531 are heavier than the proton and therefore they can be produced only from the  
 1532 splitting of a gluon into pairs or singly in association with a  $t$  quark in high  
 1533 energy-scale interactions; furthermore, during the simulation, the  $b$ -PDFs are set  
 1534 to zero. Calculations in this scheme are more complicated due to the presence  
 1535 of the second  $b$  quark but the full kinematics is considered already at LO and  
 1536 therefore the accuracy of the description is better.
- 1537 • five-flavor (5F) scheme.  $b$  quarks are considered massless, therefore they can  
 1538 appear in both initial and final states since they can now be part of the proton;  
 1539 thus, during the simulation  $b$ -PDFs are not set to zero. In this scheme, calcu-  
 1540 lations are simpler than in the 4F scheme and possible logarithmic divergences  
 1541 are absorbed by the PDFs through the DGLAP evolution.

1542 In this thesis, the  $tHq$  events are generated using the 4F scheme in order to reduce  
 1543 uncertainties, while the  $tHW$  events are generated using the 5F scheme to eliminate  
 1544 LO interference with  $t\bar{t}H$  process [48].

1545 Partons involved in the  $pp$  collision are the focus of the simulation, however, the  
 1546 rest of the partons inside the incoming protons are also affected because the remnants  
 1547 are colored objects; also, multiple parton interactions can occur. The hadronization  
 1548 of the remnants and multiple parton interactions are known as *underlying event* and  
 1549 it has to be included in the simulation. In addition, multiple  $pp$  collisions in the same  
 1550 bunch crossing (pile-up mentioned in 2.2) occurs, actually in two forms

- 1551 • *in-time PU* which refers to multiple  $pp$  collision in the bunch crossing but that  
 1552 are not considered as primary vertices.

1553       • *Out-of-time PU* which refers to overlapping  $pp$  collisions from consecutive bunch  
 1554       crossings; this can occur due to the time-delays in the detection systems where  
 1555       information from one bunch crossing is assigned to the next or previous one.

1556       While the underlying event effects are included in generation using generator-  
 1557       specific tools, PU effects are added to the generation by overlaying Minimum-bias (MB)  
 1558       and Zero-bias (ZB) events to the generated events. MB events are inelastic events  
 1559       selected by using a loose trigger with as little bias as possible, therefore accepting a  
 1560       large fraction of the overall inelastic event; ZB events correspond to random events  
 1561       recorded by the detector when collisions are likely. MB models in-time PU and ZB  
 1562       models out-of-time PU.

1563       The next step in the generation process is called *hadronization*. Since particles  
 1564       with a net color charge are not allowed to exits isolated, they have to recombine  
 1565       to form bound states. This is precisely the process by which the partons resulting  
 1566       from the parton shower arrange themselves as color singlets to form hadrons. At  
 1567       this step, the energy-scale is low and the strong coupling constant is large, therefore  
 1568       hadronization process is non-perturbative and the evolution of the partons is described  
 1569       using phenomenological models. Most of the baryons and mesons produced in the  
 1570       hadronization are unstable and hence they will decay in the detector.

1571       The last step in the generation process corresponds to the decay of the unstable  
 1572       particles generated during hadronization; it is also simulated in the hadronization  
 1573       step, based on the known branching ratios.

## 1574       **3.2 Monte Carlo Event Generators.**

1575       The event generation described in the previous section has been implemented in  
 1576       several software packages for which a brief description is given.

- 1577     • **PYTHIA 8.** It is a program designed to perform the generation of high energy  
 1578        physics events which describes the collisions between particles such as electrons  
 1579        and protons. Several theories and models are implemented in it, in order to  
 1580        describe physical aspects like hard and soft interaction, parton distributions,  
 1581        initial and final-state parton showers, multiple parton interactions, beam rem-  
 1582        nants, hadronization<sup>2</sup> and particle decay. Thanks to extensive testing, several  
 1583        optimized parametrizations, known as *tunings*, have been defined in order to  
 1584        improve the description of actual collisions to a high degree of precision; for  
 1585        analysis at  $\sqrt{s} = 13$  TeV, the underline event CUETP8M1 tune is employed [97].  
 1586        The calculation of the matrix element is performed at LO which is not enough  
 1587        for the current required level of precision; therefore, pythia is often used for  
 1588        parton shower, hadronization and decays, while other event generators are used  
 1589        to generate the matrix element at NLO.
- 1590     • **MadGraph5\_aMC@NLO.** MadGraph is a matrix element generator which  
 1591        calculates the amplitudes for all contributing Feynman diagrams of a given  
 1592        process but does not provide a parton shower while MC@NLO incorporates  
 1593        NLO QCD matrix elements consistently into a parton shower framework; thus,  
 1594        MadGraph5\_aMC@NLO, as a merger of the two event generators MadGraph5  
 1595        and aMC@NLO, is an event generator capable to calculate tree-level and NLO  
 1596        cross sections and perform the matching of those with the parton shower. It is  
 1597        one of the most frequently used matrix element generators; however, it has the  
 1598        particular feature of the presence of negative event weights which reduce the  
 1599        number of events used to reproduce the properties of the objects generated [98].
- 1600     • **POWHEG.** It is an NLO matrix element generator where the hardest emis-

---

<sup>2</sup> based in the Lund string model [96]

1601 sion of color charged particles is generated in such a way that the negative event  
 1602 weights issue of MadGraph5\_aMC@NLO is overcome; however, the method re-  
 1603 quires an interface with  $p_T$ -ordered parton shower or a parton shower generator  
 1604 where this highest emission can be vetoed in order to avoid double counting of  
 1605 this highest-energetic emission. PYTHIA is a commonly matched to POWHEG  
 1606 event generator [100].

1607 Events resulting from the whole generation process are known as MC events.

### 1608 **3.3 CMS detector simulation.**

1609 After generation, MC events contain the physics of the collisions but they are not  
 1610 ready to be compared to the events recorded by the experiment since these recorded  
 1611 events correspond to the response of the detection systems to the interaction with  
 1612 the particles traversing them. The simulation of the CMS detector has to be applied  
 1613 on top of the event generation; it is simulated with a MC toolkit for the simulation  
 1614 of particles passing through matter called Geant4 which is also able to simulate the  
 1615 electronic signals that would be measured by all detectors inside CMS.

1616 The simulation takes the generated particles contained in the MC events as input,  
 1617 makes them pass through the simulated geometry, and models physics processes that  
 1618 particles experience during their passage through matter. The full set of results from  
 1619 particle-matter interactions corresponds to the simulated hit which contains informa-  
 1620 tion about the energy loss, momentum and position. Particles of the input event are  
 1621 called *primary*, while the particles originating from GEANT4-modeled interactions of  
 1622 a primary particle with matter are called a *secondary*. Simulated hits are the input  
 1623 of subsequent modules that emulate the response of the detector readout system and

1624 triggers. The output from the emulated detection systems and triggers is known as  
 1625 digitization [101, 102].

1626 The modeling of the CMS detector corresponds to the accurate modeling of the  
 1627 interaction among particles, the detector material, and the magnetic field. This  
 1628 simulation procedure includes the following standard steps

1629 • Modeling of the Interaction Region.

1630 • Modeling of the particle passage through the hierarchy of volumes that compose  
 1631 CMS detector and of the accompanying physics processes.

1632 • Modeling of the effect of multiple interactions per beam crossing and/or the  
 1633 effect of events overlay ( Pile-Up simulation).

1634 • Modeling of the detector's electronics response, signal shape, noise, calibration  
 1635 constants (digitization).

1636 In addition to the full simulation, i.e., a detailed detector simulation, a faster  
 1637 simulation (FastSim) have been developed, that may be used where much larger  
 1638 statistics are required. In FastSim, detector material effects are parametrized and  
 1639 included in the hits; those hits are used as input of the same higher-level algorithms<sup>3</sup>  
 1640 used to analyze the recorded events. In this way, comparisons between fast and full  
 1641 simulations can be performed [104].

1642 After the full detector simulation, the output events can be directly compared  
 1643 to events actually recorded in the CMS detector. The collection of MC events that  
 1644 reproduces the expected physics for a given process is known as MC sample.

---

<sup>3</sup> track fitting, calorimeter clustering, b tagging, electron identification, jet reconstruction and calibration, trigger algorithms which will be considered in the next sections

1645 **3.4 Event reconstruction.**

1646 The CMS experiment use the *particle-flow event reconstruction algorithm (PF)* to do  
1647 the reconstruction of particles produced in  $pp$  collisions. Next sections will present  
1648 a basic description of the *Elements* used by PF (tracker tracks, energy clusters, and  
1649 muon tracks), based in the References [105, 106] where more detailed descriptions can  
1650 be found.

1651 **3.4.1 Particle-Flow Algorithm.**

1652 Each of the several sub detection systems of the CMS detector is dedicated to identify  
1653 an specific type of particles, i.e., photons and electrons are absorbed by the ECAL  
1654 and their reconstruction is based on ECAL information; hadrons are reconstructed  
1655 from clusters in the HCAL while muons are reconstructed from hits in the muon  
1656 chambers. PF is designed to correlate signals from all the detector layers (tracks and  
1657 energy clusters) in order to reconstruct and identify each final state particle and its  
1658 properties as sketched in Figure 3.2.

1659 For instance, a charged hadron is identified by a geometrical connection, known  
1660 as *link*, between one or more calorimeter clusters and a track in the tracker, provided  
1661 there are no hits in the muon system; combining several measurements allows a better  
1662 determination of the energy and charge sign of the charged hadron.

1663 **Charged-particle track reconstruction.**

1664 The strategy used by PF in order to reconstruct tracks is called *Iterative Tracking*  
1665 which occurs in four steps

- 1666 • Seed generation where initial track candidates are found by looking for a combi-  
1667 nation of hits in the pixel detector, strip tracker, and muon chambers. In total

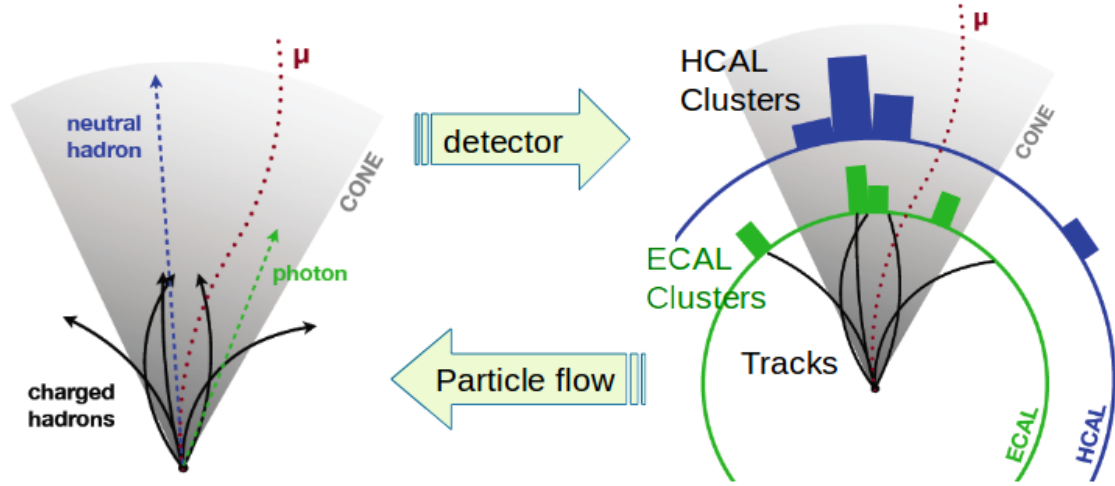


**Figure 3.2:** Particle flow algorithm. Information from the several CMS detection systems is provided as input to the algorithm which then combines it to identify and reconstruct all the particles in the final state and their properties. Reconstruction of simulated events is also performed by providing information from MC samples, detector and trigger simulation [107].

1668 ten iterations are performed, each one with a different seeding requirement.  
 1669 Seeds are used to estimate the trajectory parameters and uncertainties at the  
 1670 time of the full track reconstruction. Seeds are also considered track candidates.

- 1671     • Track finding using a tracking software known as Combinatorial Track Finder  
  1672       (CTF) [108]. The seed trajectories are extrapolated along the expected flight  
  1673       path of a charged particle, in agreement to the trajectory parameters obtained  
  1674       in the first step, in an attempt to find additional hits that can be assigned to  
  1675       the track candidates.
- 1676     • Track-fitting where the found tracks are passed as input to a module which  
  1677       provides the best estimate of the parameters of each trajectory.
- 1678     • Track selection where track candidates are submitted to a selection which dis-  
  1679       cards those that fail a set of defined quality criteria.

1680 Iterations differ in the seeding configuration and the final track selection as elab-

1681 orated in References [105, 106]. In the first iteration, high  $p_T$  tracks and tracks pro-  
 1682 duced near to the interaction region are identified and those hits are masked thereby  
 1683 reducing the combinatorial complexity. Next, iterations search for more complicated  
 1684 tracks, like low  $p_T$  tracks and tracks from b hadron decays, which tend to be displaced  
 1685 from the interaction region.

1686 **Vertex reconstruction.**

1687 During the track reconstruction, an extrapolation toward to the calorimeters is per-  
 1688 formed in order to match energy deposits; that extrapolation is performed also toward  
 1689 the beamline in order to find the origin of the track known as *vertex*. The vertex re-  
 1690 construction is performed by selecting from the available reconstructed tracks, those  
 1691 that are consistent with being originated in the interaction region where  $pp$  collisions  
 1692 are produced. The selection involves a requirement on the number of tracker (pixel  
 1693 and strip) hits and the goodness of the track fit.

1694 Selected tracks are clustered using a *deterministic annealing algorithm* (DA)<sup>4</sup>. A  
 1695 set of candidate vertices and their associated tracks, resulting from the DA, are then  
 1696 fitted with an *adaptive vertex fitter* (AVF) to produce the best estimate of the vertices  
 1697 locations.

1698 The  $p_T$  of the tracks associated to a reconstructed vertex is added, squared and  
 1699 used to organize the vertices; the vertex with the highest squared sum is designated  
 1700 as the *primary vertex* (*PV*) while the rest are designated as PU vertices.

1701 **Calorimeter clustering.**

1702 After traversing the CMS tracker system, electrons, photons and hadrons deposit their  
 1703 energy in the ECAL and HCAL cells. The PF clustering algorithm aims to provide

---

<sup>4</sup> DA algorithm and AVF are described in detail in References [110, 111]

1704 a high detection efficiency even for low-energy particles and an efficient distinction  
 1705 between close energy deposits. The clustering runs independently in the ECAL barrel  
 1706 and endcaps, HCAL barrel and endcaps, and the two preshower layers, following two  
 1707 steps

- 1708     • cells with an energy larger than a given seed threshold and larger than the energy  
     1709        of the neighboring cells are identified as cluster seeds. The neighbor cells are  
     1710        those that either share a side with the cluster seed candidate, or the eight closest  
     1711        cells including cells that only share a corner with the seed candidate.
- 1712     • cells with at least a corner in common with a cell already in the cluster seed  
     1713        and with an energy above a cell threshold are grouped into topological clusters.

1714 Clusters formed in this way are known as *particle-flow clusters*. With this cluster-  
 1715 ing strategy, it is possible to detect and measure the energy and direction of photons  
 1716 and neutral hadrons as well as differentiate these neutral particles from the charged  
 1717 hadron energy deposits. In cases involving charged hadrons for which the track pa-  
 1718 rameters are not determined accurately, for instance, low-quality and high- $p_T$  tracks,  
 1719 clustering helps in the energy measurements.

## 1720 Electron track reconstruction.

1721 Although the charged-particle track reconstruction described above works for elec-  
 1722 trons, they lose a significant fraction of their energy via bremsstrahlung photon radi-  
 1723 ation before reaching the ECAL; thus, the reconstruction performance depends on the  
 1724 ability to measure also the radiated energy. The reconstruction strategy, in this case,  
 1725 requires information from the tracking system and from the ECAL. Bremsstrahlung  
 1726 photons are emitted at similar  $\eta$  values to that of the electron but at different values  
 1727 of  $\phi$ ; therefore, the radiated energy can be recovered by grouping ECAL clusters in a

1728  $\eta$  window over a range of  $\phi$  around the electron direction. The group is called ECAL  
 1729 supercluster.

1730 Electron candidates from the track-seeding and ECAL super clustering are merged  
 1731 into a single collection which is submitted to a full electron tracking fit with a  
 1732 Gaussian-sum filter (GSF) [109]. The electron track and its associated ECAL su-  
 1733 percluster form a *particle-flow electron*.

1734 **Muon track reconstruction.**

1735 Given that the CMS detector is equipped with a muon spectrometer capable to iden-  
 1736 tify and measure the momentum of the muons traversing it, the muon reconstruction  
 1737 is not specific to PF; therefore, three different muon types are defined

- 1738     • *Standalone muon.* A clustering on the DTs or CSCs hits is performed to form  
           1739       track segments; those segments are used as seeds for the reconstruction in the  
           1740       muon spectrometer. All DTs, CSCs, and RPCs hits along the muon trajectory  
           1741       are combined and fitted to form the full track. The fitting output is called a  
           1742       *standalone-muon track*.
- 1743     • *Tracker muon.* Each track in the inner tracker with  $p_T$  larger than 0.5 GeV and  
           1744       a total momentum  $p$  larger than 2.5 GeV is extrapolated to the muon system.  
           1745       A *tracker muon track* corresponds to a extrapolated track that matches at least  
           1746       one muon segment.
- 1747     • *Global muon.* When tracks in the inner tracker (inner tracks) and standalone-  
           1748       muon tracks are matched and turn out being compatibles, their hits are com-  
           1749       bined and fitted to form a *global-muon track*.

1750        Global muons sharing the same inner track with tracker muons are merged into  
 1751      a single candidate. PF muon identification uses the muon energy deposits in ECAL,  
 1752      HCAL, and HO associated with the muon track to improve the muon identification.

1753 **Particle identification and reconstruction.**

1754      PF elements are connected by a linker algorithm that tests the connection between any  
 1755      pair of elements; if they are found to be linked, a geometrical distance that quantifies  
 1756      the quality of the link is assigned. Two elements may be linked indirectly through  
 1757      common elements. Linked elements form *PF blocks* and each PF block may contain  
 1758      elements originating in one or more particles. Links can be established between  
 1759      tracks, between calorimeter clusters, and between tracks and calorimeter clusters.  
 1760      The identification and reconstruction start with a PF block and proceed as follows

- 1761      • Muons. An *isolated global muon* is identified by evaluating the presence of  
                 inner track and energy deposits close to the global muon track in the  $(\eta, \phi)$   
                 plane, i.e., in a particular point of the global muon track, inner tracks and  
                 energy deposits are sought within a radius of  $\Delta R = 0.3$  (see eqn. 2.7) from the  
                 muon track; if they exist and the  $p_T$  of the found track added to the  $E_T$  of the  
                 found energy deposit does not exceed 10% of the muon  $p_T$  then the global muon  
                 is an isolated global muon. This isolation condition is stringent enough to reject  
                 hadrons misidentified as muons.

1769      *Non-isolated global muons* are identified using additional selection requirements  
 1770      on the number of track segments in the muon system and energy deposits along  
 1771      the muon track. Muons inside jets are identified with more stringent criteria  
 1772      in isolation and momentum as described in Reference [112]. The PF elements  
 1773      associated with an identified muon are masked from the PF block.

- 1774     ● Electrons are identified and reconstructed as described above plus some addi-  
 1775       tional requirements on fourteen variables like the amount of energy radiated,  
 1776       the distance between the extrapolated track position at the ECAL and the po-  
 1777       sition of the associated ECAL supercluster, among others, which are combined  
 1778       in an specialized multivariate analysis strategy that improves the electron iden-  
 1779       tification. Tracks and clusters used to identify and reconstruct electrons are  
 1780       masked in the PF block.
  
- 1781     ● Isolated photons are identified from ECAL superclusters with  $E_T$  larger than 10  
 1782       GeV, for which the energy deposited at a distance of 0.15, from the supercluster  
 1783       position on the  $(\eta, \phi)$  plane, does not exceed 10% of the supercluster energy;  
 1784       note that this is an isolation requirement. In addition, there must not be links  
 1785       to tracks. Clusters involved in the identification and reconstruction are masked  
 1786       in the PF block.
  
- 1787     ● Bremsstrahlung photons and prompt photons tend to convert to electron-positron  
 1788       pairs inside the tracker, therefore, a dedicated finder algorithm is used to link  
 1789       tracks that seem to originate from a photon conversion; in case those two tracks  
 1790       are compatible with the direction of a bremsstrahlung photon, they are also  
 1791       linked to the original electron track. Photon conversion tracks are also masked  
 1792       in the PF block.
  
- 1793     ● The remaining elements in the PF block are used to identify hadrons. In the  
 1794       region  $|\eta| \leq 2.5$ , neutral hadrons are identified with HCAL clusters not linked  
 1795       to any track while photons from neutral pion decays are identified with ECAL  
 1796       clusters without links to tracks. In the region  $|\eta| > 2.5$  ECAL clusters linked to  
 1797       HCAL clusters are identified with a charged or neutral hadron shower; ECAL  
 1798       clusters with no links are identified with photons. HCAL clusters not used yet,

1799       are linked to one or more unlinked tracks and to an unlinked ECAL in order to  
 1800       reconstruct charged-hadrons or a combination of photons and neutral hadrons  
 1801       according to certain conditions on the calibrated calorimetric energy.

- 1802       • Charged-particle tracks may be liked together when they converge to a *sec-*  
 1803       *ondary vertex (SV)* displaced from the IP where the PV and PU vertices are  
 1804       reconstructed; at least three tracks are needed in that case, of which at most  
 1805       one has to be an incoming track with hits in tracker region between a PV and  
 1806       the SV.

1807       The linker algorithm, as well as the whole PF algorithm, has been validated and  
 1808       commissioned; results from that validation are presented in the Reference [105].

1809       **Jet reconstruction.**

1810       Quarks and gluons may be produced in the  $pp$  collisions, therefore, their hadronization  
 1811       will be seen in the detector as a shower of hadrons and their decay products in the  
 1812       form of a *jet*. Two classes of clustering algorithms have been developed based in  
 1813       their jet definition [113]:

- 1814       • Iterative cone algorithms (IC). Jets are defined in terms of circles of fixed radius  
 1815        $R$  in the  $\eta\text{-}\phi$  plane, known as *stable cones*, for which the sum of the momenta  
 1816       of all the particles within the cone points in the same direction as the center  
 1817       of the circle. The seed of the iteration is the hardest non-isolated particle in  
 1818       the event, then, the resulting momentum direction is assigned as the new cone  
 1819       direction and a new iteration starts; iteration process stops when the cone if  
 1820       found to be stable.

1821     • Sequential recombination algorithms. The distance between non-isolated par-  
 1822        ticles is calculated; if that distance is below a threshold, these particles are  
 1823        recombined into a new object. The sequence is repeated until the separation  
 1824        between the recombined object and any other particle is above certain thresh-  
 1825        old; the recombined object is called a jet and the algorithm starts again with  
 1826        the remaining particles.

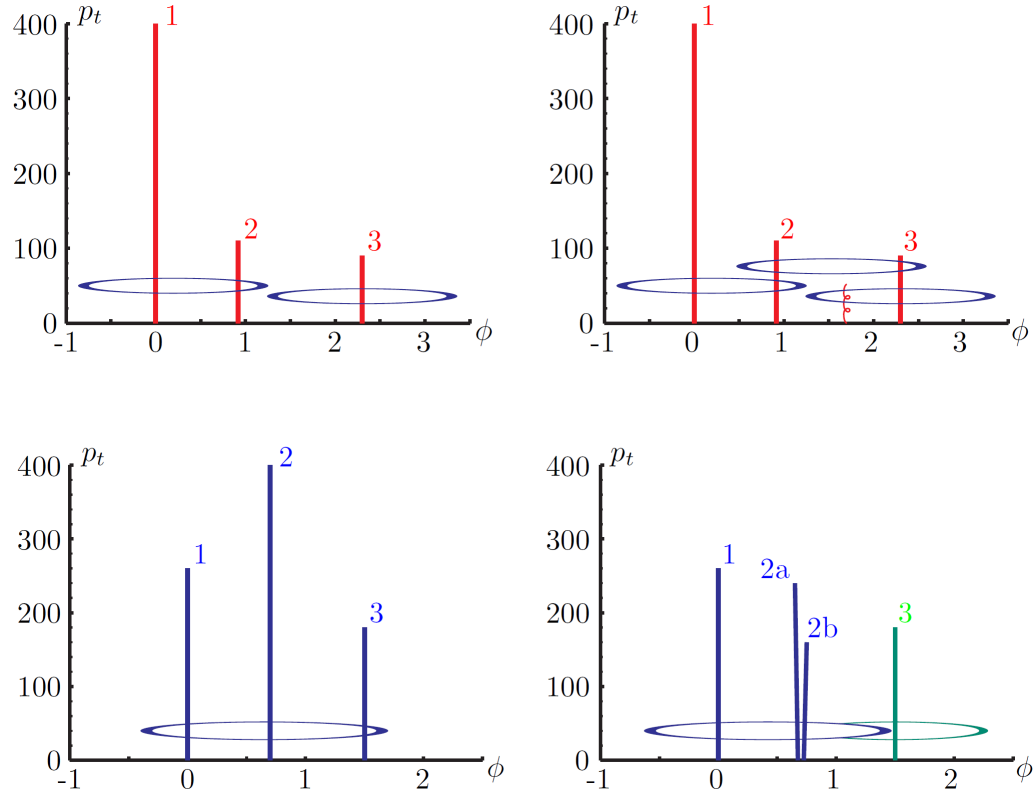


**Figure 3.3:** Stable cones identification using IC algorithms [113].

1827       Two conditions are of particular importance for the clustering algorithms, *infrared*  
 1828       and *collinear (IRC) safety*. In order to explain the concept of infrared (IR) safety,  
 1829       consider an event with three hard particles as shown in the top left side of Figure 3.3,  
 1830       two stable cones are found and then two jets are identified; if a soft gluon is added, as  
 1831       shown in the top right side of Figure 3.3, three stable cones are found and the three

1832 hard particles are now clustered into a single jet. If the addition of soft particles  
 1833 change the outcome of the clustering, then it is said that the algorithm is IR unsafe.  
 1834 Soft radiation is highly likely in perturbative QCD, which dominates the physics of  
 1835 the jets, and then IR unsafe effect leads to divergences [113].

1836 The concept of collinear safety can also be explained considering a three hard  
 1837 particles event, as shown in the bottom left side of Figure 3.3, where one stable cone  
 1838 containing all three particles is found and one jet is identified; if the hardest particle  
 1839 is split into two collinear particles (2a and 2b) in the bottom right side of Figure 3.3,  
 1840 then the clustering results in a different jet identification and the algorithm is said  
 1841 to be collinear unsafe. The collinear unsafe effect leads to divergences in jet cross  
 1842 section calculations [114].

1843 It has been determined that IC algorithms are IRC unsafe, and therefore, they  
 1844 have to be replaced by algorithms that not only provide the finite perturbative results  
 1845 from theoretical computations, but also that are not highly dependent on underlying  
 1846 event and pileup effects which leads to significant corrections [113].

1847 The sequential recombination algorithms arise as the IRC safe alternative used by  
 1848 the CMS experiment; in particular the anti- $k_t$  algorithm which is a generalization of  
 1849 the previously existing  $k_t$  [115] and Cambridge/Aachen [116] jet clustering algorithms.

1850 The anti- $k_t$  algorithm is used to perform the jet reconstruction by clustering those  
 1851 PF particles within a cone (see Figure 3.4); previously, isolated electrons, isolated  
 1852 muons, and charged particles associated with other interaction vertices are excluded  
 1853 from the clustering.

1854 The anti- $k_t$  algorithm proceeds in a sequential recombination of PF particles; the  
 1855 distance between particles  $i$  and  $j$  ( $d_{ij}$ ) and the distance between particles and the  
 1856 beam are defined as

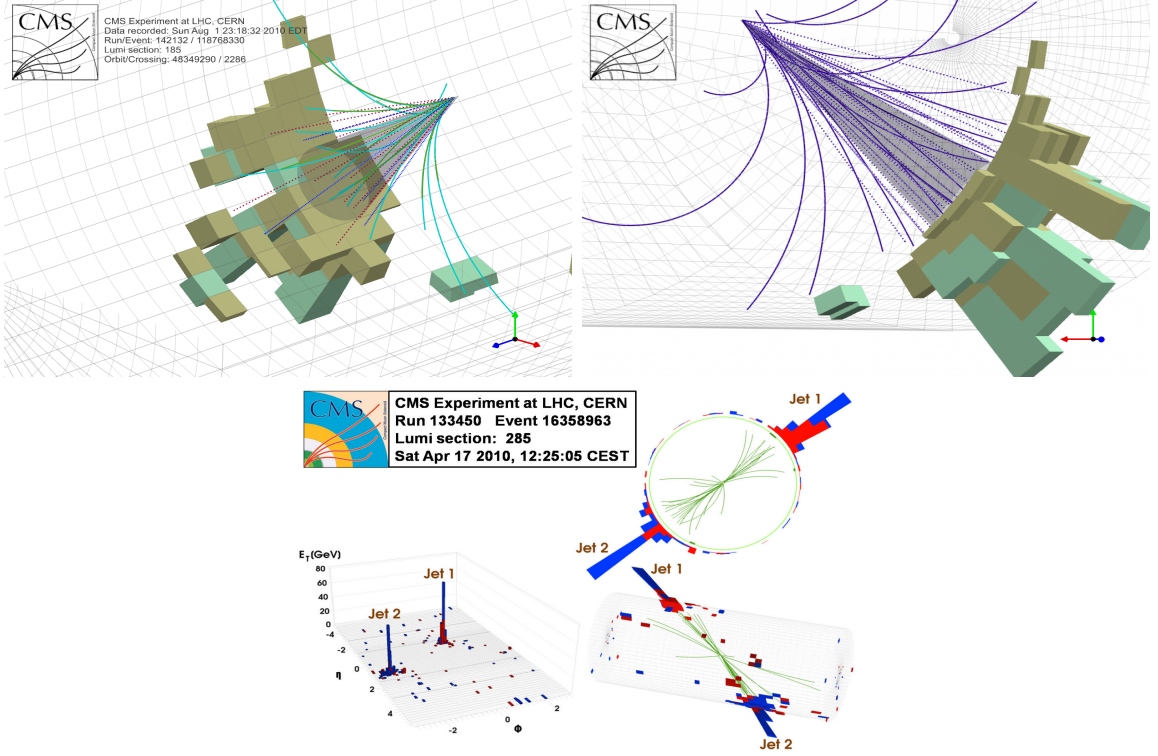


**Figure 3.4:** Jet reconstruction performed by the anti- $k_t$  algorithm. Top: Two different views of a CMS recorded event are presented. Continuous lines correspond to tracks left by charged particles in the tracker while dotted lines are the imaginary paths followed by neutral particles. The green cubes represent the ECAL cells while the blue ones represent the HCAL cells; in both cases, the height of the cube represent the amount of energy deposited in the cells [117]. Bottom: Reconstruction of a recorded event with two jets [118].

$$d_{ij} = \min\left(\frac{1}{k_{ti}^2}, \frac{1}{k_{tj}^2}\right) \frac{\Delta_{ij}^2}{R^2}$$

$$d_{iB} = \frac{1}{k_{ti}^2} \quad (3.1)$$

1857 where  $\Delta_{ij}^2 = (y_i - y_j)^2 + (\phi_i - \phi_j)^2$ ,  $k_{ti}, y_i$  and  $\phi_i$  are the transverse momentum, ra-  
1858 pidity and azimuth of particle  $i$  respectively and  $R$  is the called jet radius. For all  
1859 the remaining PF particles, after removing the isolated ones,  $d_{ij}$  and  $d_{iB}$  are calcu-

lated<sup>5</sup> and the smallest is identified; if it is a  $d_{ij}$ , particles  $i$  and  $j$  are replaced with  
 a new object whose momentum is the vectorial sum of the combined particles. If the  
 smallest distance is a  $d_{iB}$  the clustering process ends, the object  $i$  (which at this stage  
 should be a combination of several PF particles) is declared as a *Particle-flow-jet* (PF  
 jet) and all the associated PF particles are removed from the detector. The clustering  
 process is repeated until no PF particles remain.  $R$  is a free parameter that can be  
 adjusted according to the specific analysis conditions; usually, two values are used,  
 $R=0.4$  and  $R=0.5$ , giving the name to the so-called AK4-jet and AK5-jet respectively.

An advantage of the anti- $k_t$  algorithm over other clustering algorithms is the reg-  
 ularity of the boundaries of the resulting jets. For all known IRC safe algorithms,  
 soft radiation can introduce irregularities in the boundaries of the final jets; however,  
 anti- $k_t$  algorithm is soft-resilient, meaning that jets shape is not affected by soft radi-  
 ation, which is a valuable property considering that knowing the typical shape of jets  
 makes experimental calibration of jets more simple. In addition, that soft-resilience  
 is expected to simplify certain theoretical calculations and reduce the momentum-  
 resolution loss caused by underlying-event (UE) and pileup contamination [114].

The effect of the UE and pileup contamination over a jet identification, can be  
 seen as if soft events are added to the jet; for instance, if a soft event representing UE  
 or pileup is added to an event for which a set of jets  $J$  have been identified, and the  
 clustering is rerun on that new extended event, the outcome will be different in two  
 aspects: jets will contain some additional soft energy and the distribution of particles  
 in jets may have change; that effect is called *back-reaction*. The back-reaction effect in  
 the anti- $k_t$  algorithm is suppressed not by the amount of momentum added to the jet  
 but by the jet transverse momentum  $p_{T,J}$ , which means that this strong suppression  
 leads to a smaller correction due to EU and pileup effect [114].

---

<sup>5</sup> Notice that this is a combinatorial calculation.

## 1885 Jet energy Corrections

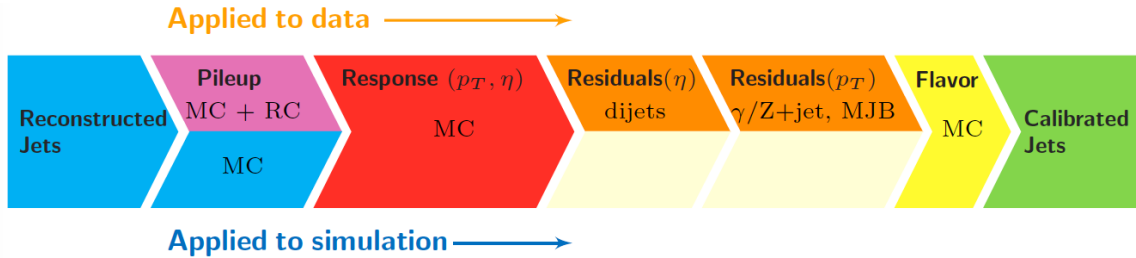


**Figure 3.5:** Jet energy correction diagram. Correction levels are applied sequentially in the indicated fixed order [120].

1886 Even though jets can be reconstructed efficiently, there are some effects that are  
 1887 not included in the reconstruction and that lead to discrepancies between the re-  
 1888 constructed results and the predicted results; in order to overcome these discrep-  
 1889 ancies, a factorized model has been designed in the form of jet energy corrections  
 1890 (JEC) [119, 120] applied sequentially as shown in the diagram of Figure 3.5.

1891 At each level, the jet four-momentum is multiplied by a scaling factor based on  
 1892 jet properties, i.e.,  $\eta$ , flavor, etc.

- 1893 • Level 1 correction removes the energy coming from pile-up. The scale factor is  
 1894 determined using a MC sample of QCD dijet (2 jets) events with and without  
 1895 pileup overlay; it is parametrized in terms of the offset energy density  $\rho$ , jet  
 1896 area  $A$ , jet  $\eta$  and jet  $p_T$ . Different corrections are applied to data and MC due  
 1897 to the detector simulation.
- 1898 • MC-truth correction accounts for differences between the reconstructed jet en-  
 1899 ergy and the MC particle-level energy. The correction is determined on a QCD  
 1900 dijet MC sample and is parametrized in terms of the jet  $p_T$  and  $\eta$ .
- 1901 • Residuals correct remaining small differences within jet response in data and  
 1902 MC. The Residuals  $\eta$ -dependent correction compares jets of similar  $p_T$  in the

1903 barrel reference region. The Residuals  $p_T$ -dependent correct the jet absolute  
 1904 scale (JES vs  $p_T$ ).

- 1905 • Jet-flavor corrections are derived in the same way as MC-truth corrections but  
 1906 using QCD pure flavor samples.

1907 ***b*-tagging of jets.**

1908 A particular feature of the hadrons containing bottom quarks (*b*-hadrons) is that  
 1909 their lifetime is long enough to travel some distance before decaying, but it is not as  
 1910 long as those of light quark hadrons; therefore, when looking at the hadrons produced  
 1911 in  $pp$  collisions, *b*-hadrons decay typically inside the tracker rather than reaching the  
 1912 calorimeters as some light-hadrons do. As a result, a *b*-hadron decay gives rise to a  
 1913 displaced vertex (secondary vertex) with respect to the primary vertex as shown in  
 1914 Figure 3.6; the SV displacement is in the order of a few millimeters. A jet resulting  
 1915 from the decay of a *b*-hadron is called *b* jet; other jets are called light jets.

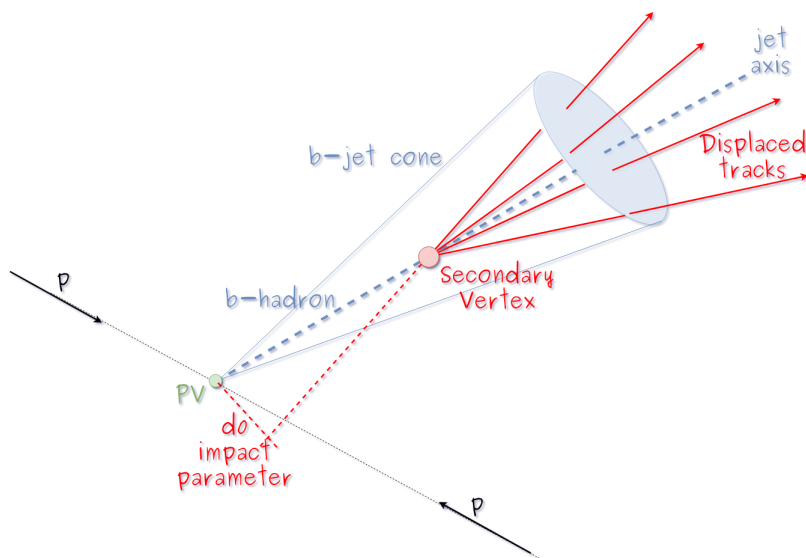


**Figure 3.6:** Secondary vertex in a *b*-hadron decay.

1916 Several methods to identify *b*-jets (*b*-tagging) have been developed; the method

1917 used in this thesis is known as *Combined Secondary Vertex* algorithm in its second  
 1918 version (CSVv2) [121]. By using information of the impact parameter, the recon-  
 1919 structed secondary vertices, and the jet kinematics as input in a multivariate analysis  
 1920 that combines the discrimination power of each variable in one global discrimina-  
 1921 tor variable, three working points (references): loose, medium and tight, are defined  
 1922 which quantify the probabilities of mistag jets from light quarks as jets from  $b$  quarks;  
 1923 10, 1 and 0.1 % respectively. Although the mistagging probability decreases with the  
 1924 working point strength, the efficiency to correctly tag  $b$ -jets also decreases as 83, 69  
 1925 and 49 % for the respective working point; therefore, a balance needs to be achieved  
 1926 according to the specific requirements of the analysis.

### 1927 3.4.1.1 Missing transverse energy.

1928 The fact that proton bunches carry momentum along the  $z$ -axis implies that for  
 1929 each event it is expected that the momentum in the transverse plane is balanced.  
 1930 Imbalances are quantified by the missing transverse energy (MET) and are attributed  
 1931 to several sources including particles escaping undetected through the beam pipe,  
 1932 neutrinos produced in weak interactions processes which do not interact with the  
 1933 detector and thus escaping without leaving a sign, or even undiscovered particles  
 1934 predicted by models beyond the SM.

1935 The PF algorithm assigns the negative sum of the momenta of all reconstructed  
 1936 PF particles to the *particle-flow MET* according to

$$\vec{E}_T = - \sum_i \vec{p}_{T,i} \quad (3.2)$$

1937 JEC are propagated to the calculation of the  $\vec{E}_T$  as described in the Reference [122].

1938 **3.4.2 Event reconstruction examples**

1939 Figures 3.7-3.9 show the results of the reconstruction performed on 3 recorded events.

1940 Descriptions are taken directly from the source.

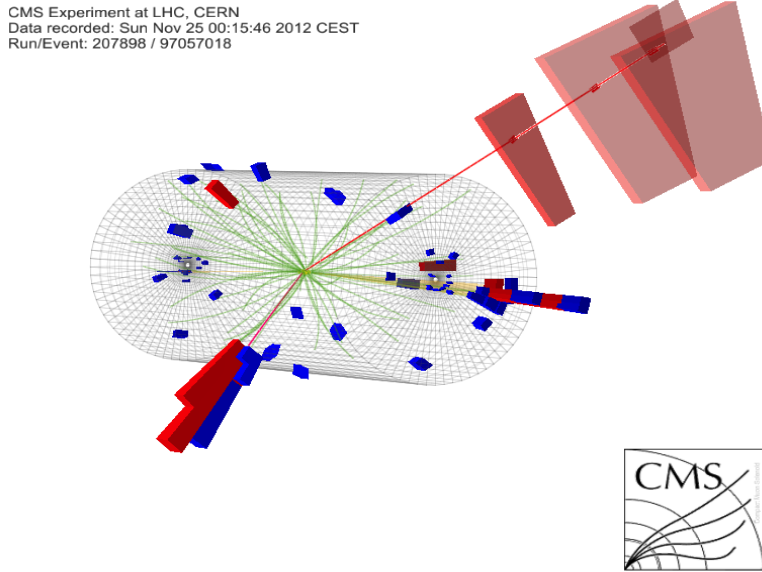


**Figure 3.7:** HIG-13-004 Event 1 reconstruction results; “HIG-13-004 Event 1: Event recorded with the CMS detector in 2012 at a proton-proton center-of-mass energy of 8 TeV. The event shows characteristics expected from the decay of the SM Higgs boson to a pair of  $\tau$  leptons. Such an event is characterized by the production of two forward-going jets, seen here in opposite endcaps. One of the  $\tau$  decays to a muon (red lines on the right) and neutrinos, while the other  $\tau$  decays into a charged hadron and a neutrino.” [123].

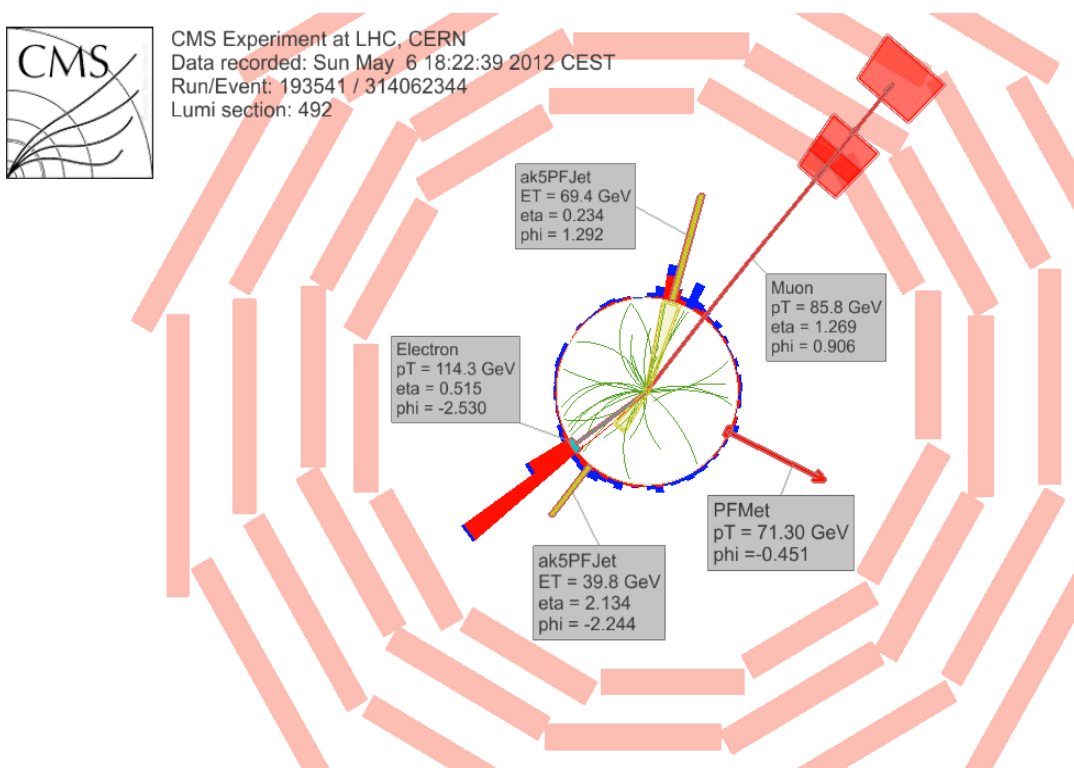


**Figure 3.8:**  $e\mu$  event reconstruction results; “An  $e\mu$  event candidate selected in 8 TeV data, as seen from the direction of the proton beams. The kinematics of the main objects used in the event selection are highlighted: two isolated leptons and two particle-flow jets. The reconstructed missing transverse energy is also displayed for reference” [124].

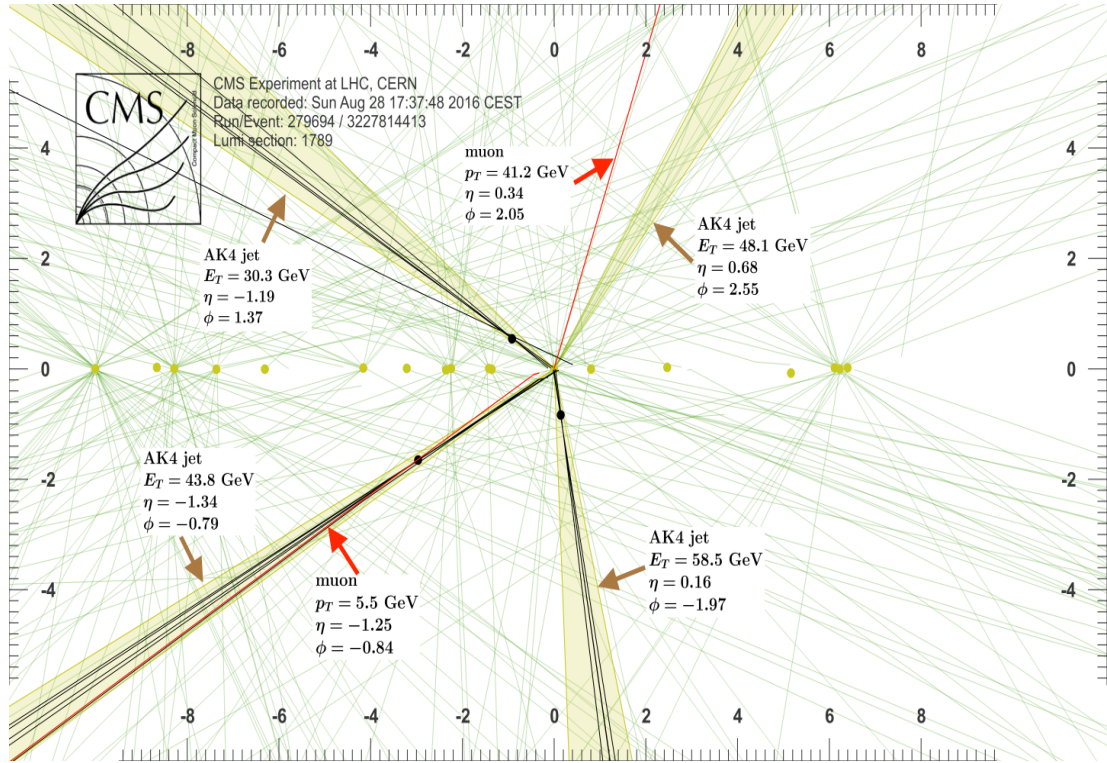


**Figure 3.9:** Recorded event reconstruction results; “Recorded event ( $\rho$ - $z$  projection) with three jets with  $p_T > 30$  GeV with one displaced muon track in 2016 data collected at 13 TeV. Each of the three jets has a displaced reconstructed vertex. The jet with  $p_T(j) = 43.8$  GeV,  $\eta(j) = -1.34$ ,  $\phi(j) = -0.79$  contains muon with  $p_T(\mu) = 5.5$  GeV,  $\eta(\mu) = -1.25$ ,  $\phi(\mu) = -0.84$ . Event contains reconstructed isolated muon with  $p_T(\mu) = 41.2$  GeV,  $\eta(\mu) = 0.34$ ,  $\phi(\mu) = 2.05$  and MET with  $p_T = 72.5$  GeV,  $\phi = -0.32$ . Jet candidates for a  $b$ -jet from top quark leptonic and hadronic decays are tagged by CSVv2T algorithm. One of the other two jets is tagged by CharmT algorithm. Tracks with  $p_T > 0.5$  GeV are shown. The number of reconstructed primary vertices is 18. Reconstructed  $m_T(W)$  is 101.8 GeV. Beam spot position correction is applied. Reconstructed primary vertices are shown in yellow color, while reconstructed displaced vertices and associated tracks are presented in black color. Dimensions are given in cm” [125].

<sub>1941</sub> **Chapter 5**

<sub>1942</sub> **Statistical methods**

<sub>1943</sub> In the course of analyzing the data sets provided by the CMS experiment and used in  
<sub>1944</sub> this thesis, several statistical tools have been employed; in this chapter, a description  
<sub>1945</sub> of these tools will be presented, starting with the general statement of the multivariate  
<sub>1946</sub> analysis methods, followed by the particularities of the Boosted Decision Trees (BDT)  
<sub>1947</sub> method and its application to the classification problem. Statistical inference methods  
<sub>1948</sub> used will also be presented. This chapter is based mainly on References [126–128].

<sub>1949</sub> **5.1 Multivariate analysis**

<sub>1950</sub> Multivariate data analysis (MVA) makes use of the statistical techniques developed to  
<sub>1951</sub> analyze more than one variable at once, taking into account all the correlations among  
<sub>1952</sub> variables. MVA is employed in a variety of fields like consumer and market research,  
<sub>1953</sub> quality control and process optimization. Using MVA it is possible to identify the  
<sub>1954</sub> dominant patterns in a data sample, like groups, outliers and trends, and determine  
<sub>1955</sub> to which group a set of values belong; in the particle physics context, MVA methods  
<sub>1956</sub> are used to perform the selection of certain type of events from a large data set.

1957        Processes with small cross section, such as the  $tHq$  process ( $\sigma_{SM}(\sqrt{s} = 13\text{TeV}) =$   
 1958      70.96 fb), are hard to detect in the presence of the processes with larger cross sections,  
 1959       $\sigma_{SM}^{t\bar{t}}(\sqrt{s} = 13\text{TeV}) = 823.44$  fb for instance; therefore, only a small fraction of the data  
 1960      contains events of interest (signal), the major part is signal-like events, which mimic  
 1961      signal characteristics but belong to different processes, so they are a background to  
 1962      the process of interest. This implies that it is not possible to say with certainty  
 1963      that a given event is a signal or a background and statistical methods should be  
 1964      involved. In that sense, the challenge can be formulated as one where a set of events  
 1965      have to be classified according to certain special features; these features correspond  
 1966      to the measurements of several parameters like energy or momentum, organized in a  
 1967      set of *input variables*. The measurements for each event can be written in a vector  
 1968       $\mathbf{x} = (x_1, \dots, x_n)$  for which

- 1969        •  $f(\mathbf{x}|s)$  is the probability density (*likelihood function*) that  $\mathbf{x}$  is the set of mea-  
 1970        sured values given that the event is a signal event (signal hypothesis).
- 1971        •  $f(\mathbf{x}|b)$  is the probability density (*likelihood function*) that  $\mathbf{x}$  is the set of mea-  
 1972        sured values given that the event is a background event (background hypothe-  
 1973        sis).

1974        Figure 5.1 shows three ways to perform a classification of events for which mea-  
 1975        surements of two properties, i.e., two input variables  $x_1$  and  $x_2$ , have been performed;  
 1976        blue circles represent signal events while red triangles represent background events.  
 1977        The classification on the left is *cut-based* requiring  $x_1 < c_1$  and  $x_2 < c_2$ ; usually the  
 1978        cut values ( $c_1$  and  $c_2$ ) are chosen according to some knowledge about the event pro-  
 1979        cess. In the middle plot, the classification is performed using a linear function of  
 1980        the input variables, hence the boundary is a straight line, while in the right plot the

1981 the relationship between input variables is not linear thus the boundary is not linear  
 1982 either.

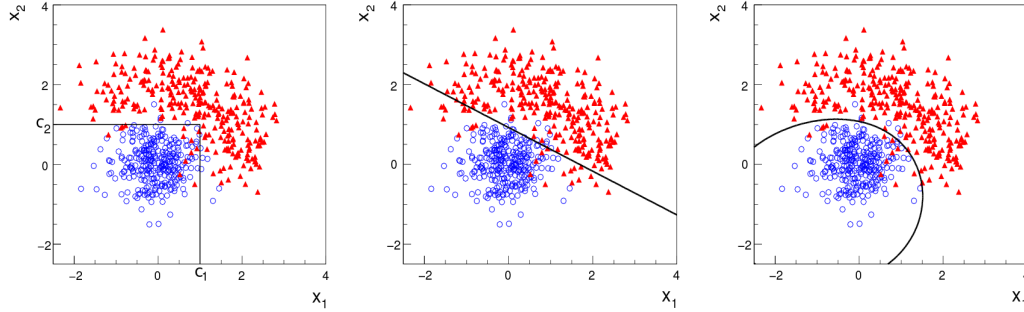


**Figure 5.1:** Scatter plots-MVA event classification. Distribution of two input variables  $x_1$  and  $x_2$  measured for a set of events; blue circles represent signal events and red triangles represent background events. The classification is based on cuts (left), linear boundary (center), and nonlinear boundary (right) [126]

1983 In general, the boundary can be parametrized in terms of the input variables such  
 1984 that the cut is set on the parametrization instead of on the variables, i.e.,  $y(\mathbf{x}) = y_{cut}$   
 1985 with  $y_{cut}$  being a constant; thus, the acceptance or rejection of an event is based on  
 1986 which side of the boundary the event is located. If  $y(\mathbf{x})$ , usually called *test statistic*,  
 1987 has functional form, it can be used to determine the probability distribution functions  
 1988  $p(y|s)$  and  $p(y|b)$  and then perform a test statistic with a single cut on the scalar  
 1989 variable  $y$ .

1990 Figure 5.2 shows an example of what would be the probability distribution func-  
 1991 tions under the signal and background hypotheses for a scalar test statistic with a cut  
 1992 on the classifier  $y$ . Note that the tails of the distributions indicate that some signal  
 1993 events fall in the rejection region and some background events fall on the acceptance  
 1994 region; therefore, it is convenient to define the *efficiency* with which events of a given  
 1995 type are accepted. The signal and background efficiencies are given by

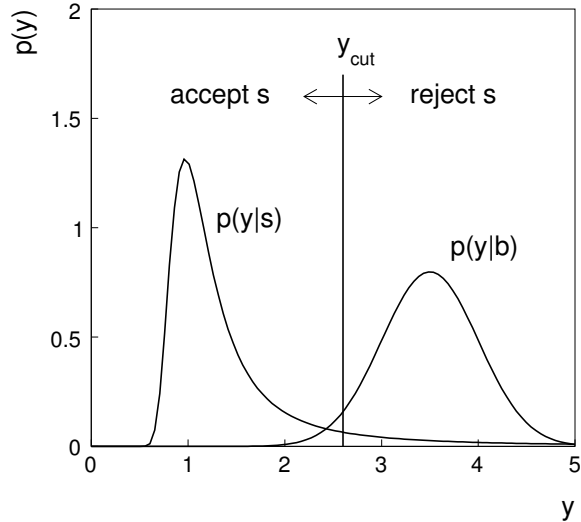


**Figure 5.2:** Distributions of the scalar test statistic  $y(\mathbf{x})$  under the signal and background hypotheses. [126]

$$\varepsilon_s = P(\text{accept event}|s) = \int_A f(\mathbf{x}|s) d\mathbf{x} = \int_{-\infty}^{y_{cut}} p(y|s) dy , \quad (5.1)$$

$$\varepsilon_b = P(\text{accept event}|b) = \int_A f(\mathbf{x}|b) d\mathbf{x} = \int_{-\infty}^{y_{cut}} p(y|b) dy , \quad (5.2)$$

1996 where  $A$  is the acceptance region. If the background hypothesis is the *null hypothesis*  
 1997 ( $H_0$ ), the signal hypothesis would be *alternative hypothesis* ( $H_1$ ); in this context, the  
 1998 background efficiency corresponds to the significance level of the test ( $\alpha$ ) and describes  
 1999 the misidentification probability, while the signal efficiency corresponds to the power  
 2000 of the test ( $1-\beta$ )<sup>1</sup> and describes the probability of rejecting the background hypothesis  
 2001 if the signal hypothesis is true. What is sought in an analysis is to maximize the power  
 2002 of the test relative to the significance level, i.e., set a selection with the largest possible  
 2003 selection efficiency and the smallest possible misidentification probability.

---

<sup>1</sup>  $\beta$  is the fraction of signal events that fall out of the acceptance region

2004 **5.1.1 Decision trees**

2005 For this thesis, the implementation of the MVA strategy, described above, is per-  
 2006 formed through decision trees by using the TMVA software package [127] included  
 2007 in the ROOT analysis framework [129]. In a simple picture, a decision tree classifies  
 2008 events according to their input variables values by setting a cut on each input variable  
 2009 and checking which events are on which side of the cut, just as proposed in the MVA  
 2010 strategy, but in addition, as a machine learning algorithm, decision trees offer the  
 2011 possibility to be trained and then perform the classification efficiently.

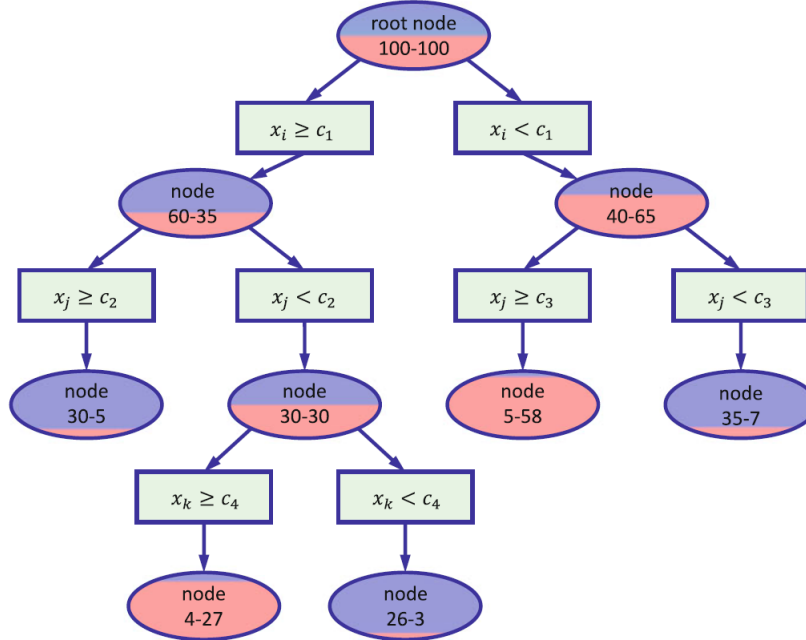


**Figure 5.3:** Example of a decision tree. Each node is fed with a MC sample mixing signal and background events (left-right numbers); nodes colors represent the relative number of signal/background events [128].

2012 The training or growing of a decision tree is the process where the rules for clas-  
 2013 sifying events are defined; this process is represented in Figure 5.3 and consists of  
 2014 several steps:

- 2015 • take MC samples of signal and background events and split them into two parts

2016        each; the first parts will be used in the decision tree training, while the second  
 2017        parts will be used for testing the final classifier obtained from the training.  
 2018        Each event has associated a set of input variables  $\mathbf{x} = (x_1, \dots, x_n)$  which serve  
 2019        to distinguish between signal and background events. The training sample is  
 2020        taken in at the *root node*.

- 2021        • Pick one variable, say  $x_i$ .
- 2022        • Pick one value of  $x_i$ , each event has its own value of  $x_i$ , and split the training  
               sample into two subsamples  $B_1$  and  $B_2$ ;  $B_1$  contains events for which  $x_i < c_1$   
               while  $B_2$  contains the rest of the training events;
- 2025        • scan all possible values of  $x_i$  and find the splitting value that provides the *best*  
               classification<sup>2</sup>, i.e.,  $B_1$  is mostly made of signal events while  $B_2$  is mostly made  
               of background events.
- 2028        • It is possible that variables other than the picked one produce a better classi-  
               fication, hence, all the variables have to be evaluated. Pick the next variable,  
               say  $x_j$ , and repeat the scan over its possible values.
- 2031        • At the end, all the variables and their values will have been scanned, the *best*  
               variable and splitting value will have been identified, say  $x_1, c_1$ , and there will  
               be two nodes fed with the subsamples  $B_1$  and  $B_2$ .

2034        Nodes are further split by repeating the decision process until a given number of  
 2035 final nodes is obtained, nodes are largely dominated by either signal or background  
 2036 events, or nodes have too few events to continue. Final nodes are called *leaves* and  
 2037 they are classified as signal or background leaves according to the class of the majority  
 2038 of events in them. Each *branch* in the tree corresponds to a sequence of cuts.

---

<sup>2</sup> Quality of the classification will be treated in the next paragraph.

2039        The quality of the classification at each node is evaluated through a separation  
 2040 criteria; there are several of them but the *Gini Index* ( $G$ ) is the one used in the  
 2041 decision trees trained for the analysis in this thesis.  $G$  is written in terms of the  
 2042 purity ( $P$ ), i.e., the fraction of signal events in the samples after the separation is  
 2043 made; it is given by

$$G = P(1 - P) \quad (5.3)$$

2044 note that  $P=0.5$  at the root node while  $G=0$  for pure leaves. For a node  $A$  split into  
 2045 two nodes  $B_1$  and  $B_2$  the  $G$  gain is

$$\Delta G = G(A) - G(B_1) - G(B_2). \quad (5.4)$$

2046        The *best* classification corresponds to that for which the gain of  $G$  is maximized;  
 2047 hence, the scanning over all the variables in an event and their values is of great  
 2048 importance.

2049        In order to provide a numerical output for the classification, events in a sig-  
 2050 nal(background) leaf are assigned a score of 1(-1) each, defining in this way the  
 2051 decision tree *classifier/weak learner* as

$$f(\mathbf{x}) = \begin{cases} 1 & \mathbf{x} \text{ in signal region,} \\ -1 & \mathbf{x} \text{ in background region.} \end{cases}$$

2052        Figure 5.4 shows an example of the classification of a sample of events, containing  
 2053 two variables, performed by a decision tree.

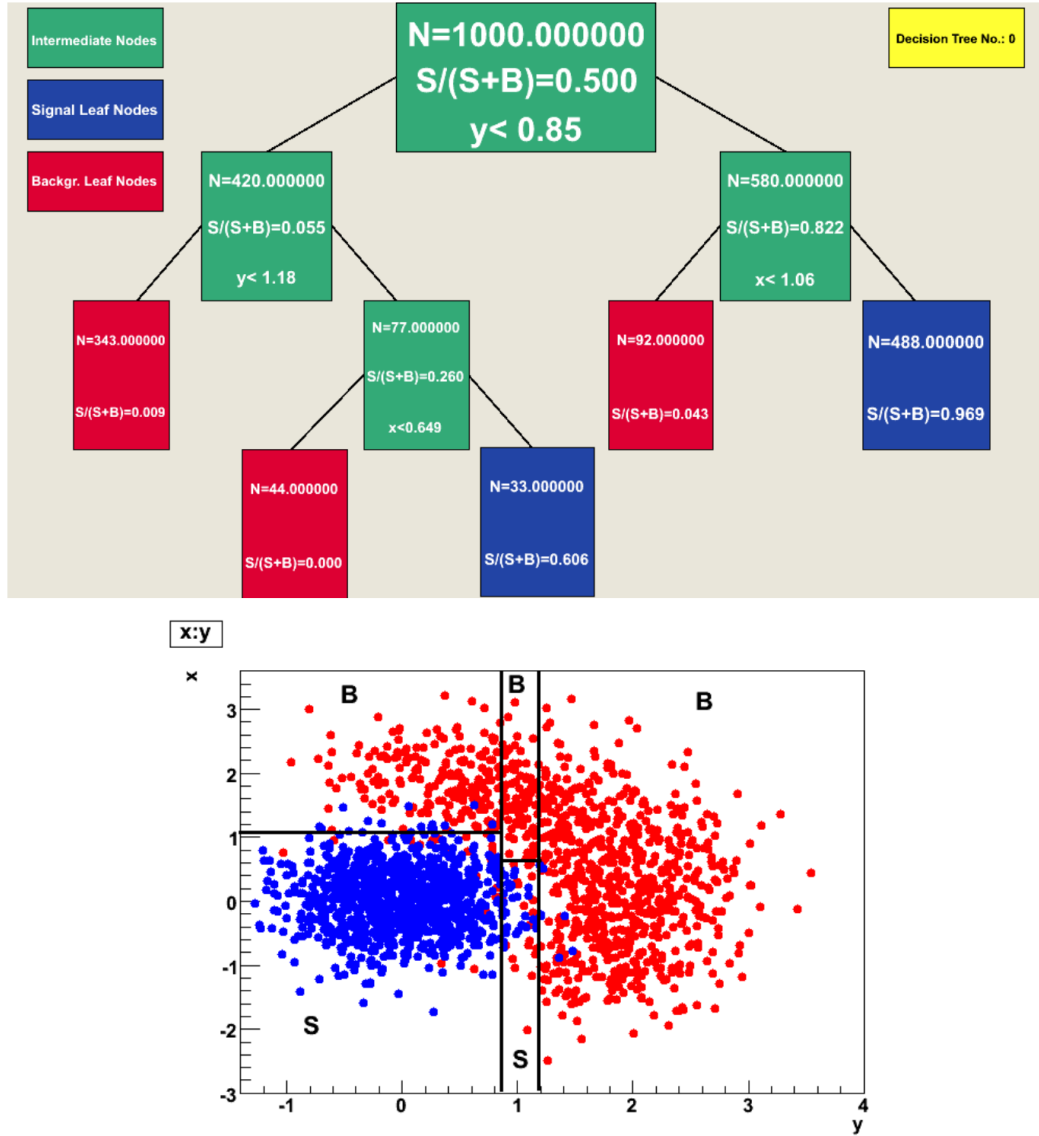


**Figure 5.4:** Example of a decision tree output. Each leaf, blue for signal events and red for background events, is represented by a region in the variables phase space [130].

### 2054 5.1.2 Boosted decision trees (BDT).

2055 Event misclassification occurs when a training event ends up in the wrong leaf, i.e., a  
 2056 signal event ends up in a background leaf or a background event ends up in a signal  
 2057 leaf. A way to correct it is to assign a weight to the misclassified events and train  
 2058 a second tree using the reweighted events; the event reweighting is performed by a

2059 boosting algorithm in such a way that when used in the training of a new decision  
 2060 tree the *boosted events* get correctly classified. The process is repeated iteratively  
 2061 adding a new tree to the forest and creating a set of classifiers, which are combined  
 2062 to create the next classifier; the final classifier offers more stability<sup>3</sup> and has a smaller  
 2063 misclassification rate than any individual ones. The resulting tree collection is known  
 2064 as a *boosted decision tree (BDT)*.

2065 Thus, purity of the sample is generalized to

$$P = \frac{\sum_s w_s}{\sum_s w_s + \sum_b w_b} \quad (5.5)$$

2066 where  $w_s$  and  $w_b$  are the weights of the signal and background events respectively;  
 2067 the Gini index is also generalized

$$G = \left( \sum_i^n w_i \right) P(1 - P) \quad (5.6)$$

2068 with  $n$  the number of events in the node. The final score of an event, after pass-  
 2069 ing through the forest, is calculated as the renormalized sum of all the individual  
 2070 (possibly weighted) scores; thus, high(low) score implies that the event is most likely  
 2071 signal(background).

2072 The boosting procedure, implemented in the *Gradient boosting* algorithm used in  
 2073 this thesis, produces a classifier  $F(\mathbf{x})$  which is the weighted sum of the individual  
 2074 classifiers obtained after each iteration, i.e.,

$$F(\mathbf{x}) = \sum_{m=1}^M \beta_m f(\mathbf{x}; a_m) \quad (5.7)$$

2075 where  $M$  is the number of trees in the forest. The *loss function*  $L(F, y)$  represents the

---

<sup>3</sup> Decision trees suffer from sensitivity to statistical fluctuations in the training sample which may lead to very different results with a small change in the training samples.

2076 deviation between the classifier  $F(\mathbf{x})$  response and the true value  $y$  obtained from the  
 2077 training sample (1 for signal events and -1 for background event), according to

$$L(F, y) = \ln(1 + e^{-2F(\mathbf{x})y}) \quad (5.8)$$

2078 thus, the reweighting is employed to ensure the minimization of the loss function; a  
 2079 more detailed description of the minimization procedure can be found in Reference  
 2080 [131]. The final classifier output is later used as a final discrimination variable, labeled  
 2081 as *BDT output/response*.

### 2082 5.1.3 Overtraining

2083 Decision trees offer the possibility to have as many nodes as desired in order to  
 2084 reduce the misclassification to zero (in theory); however, when a classifier is too much  
 2085 adjusted to a particular training sample, the classifier's response to a slightly different  
 2086 sample may leads to a completely different classification results; this effect is known  
 2087 as *overtraining*.

2088 An alternative to reduce the overtraining in BDTs consists in pruning the tree  
 2089 by removing statistically insignificant nodes after the tree growing is completed but  
 2090 this option is not available for BDTs with gradient boosting in the TMVA-toolkit,  
 2091 therefore, the overtraining has to be reduced by tuning the algorithm, number of  
 2092 nodes, minimum number of events in the leaves, etc. The overtraining can be evaluated  
 2093 by comparing the responses of the classifier when running over the training and  
 2094 test samples.

2095 **5.1.4 Variable ranking**

2096 BDTs have a couple of particular advantages related to the input variables; they are  
 2097 relatively insensitive to the number of input variables used in the vector  $\mathbf{x}$ . The  
 2098 ranking of the BDT input variables is determined by counting the number of times a  
 2099 variable is used to split decision tree nodes; in addition, the separation gain-squared  
 2100 achieved in the splitting and the number of events in the node are accounted by  
 2101 applying a weighting to that number. Thus, those variables with small or no power  
 2102 to separate signal and background events are rarely chosen to split the nodes, i.e., are  
 2103 effectively ignored.

2104 In addition, variables correlations play an important role for some MVA methods  
 2105 like the Fisher discriminant algorithm in which the first step consist of performing a  
 2106 linear transformation to a phase space where the correlations between variables are  
 2107 removed; in the case of BDT algorithm, correlations do not affect the performance.

2108 **5.1.5 BDT output example**

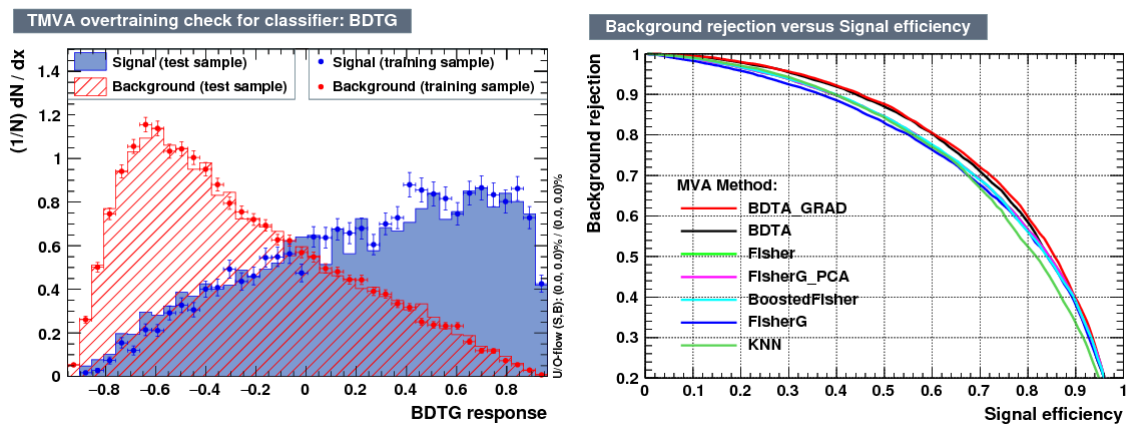


**Figure 5.5:** Left: Output distributions for the gradient boosted decision tree (BDTG) classifier using a sample of signal ( $pp \rightarrow tHq$ ) and background ( $pp \rightarrow tt$ ) events. Right: Background rejection vs signal efficiency (ROC curves) for various MVA classifiers running over the same sample used to produce the plot on the left.

2109        The left side of figure 5.5 shows the BDT output distributions for signal ( $pp \rightarrow$   
 2110  $tHq$ ) and background ( $pp \rightarrow t\bar{t}$ ) events; this plot is the equivalent to the one showed  
 2111 in Figure 5.2. A forest with 800 trees, maximum depth per tree = 3, and gradient  
 2112 boosting have been used as training parameters. The BDTG classifier offers a good  
 2113 separation power. There is a small overtraining in the signal distribution, while the  
 2114 background distribution is very well predicted which might indicate that the sample  
 2115 is composed of more background than signal events.

2116        The right side of figure 5.5 shows the background rejection vs signal efficiency  
 2117 curves for several combinations of MVA classifiers-boosting algorithms running over  
 2118 the same MC sample; these curves are known as ROC curves and give an indication  
 2119 of the performance of the classifier. In this particular example, the best performance  
 2120 is achieved with the BDTG classifier (BDTA\_GRAD), which motivate its use in this  
 2121 thesis.

## 2122        5.2 Statistical inference

2123        Once events are classified, the next step consists of finding the parameters that define  
 2124 the likelihood functions  $f(\mathbf{x}|s)$ ,  $f(\mathbf{x}|b)$  for signal and background events respectively.  
 2125 In general, likelihood functions depend not only on the measurements but also on  
 2126 parameters ( $\theta_m$ ) that define their shapes; the process of estimating these *unknown*  
 2127 *parameters* and their uncertainties from the experimental data is called *inference*.

2128        The statistical inference tools used in this analysis are implemented in the RooFit  
 2129 toolkit [132] and COMBINE package [133] included in the CMSSW software frame-  
 2130 work.

2131 **5.2.1 Nuisance parameters**

2132 The unknown parameter vector  $\theta$  is made of two types of parameters: those pa-  
 2133 rameters that provide information about the physical observables of interest for the  
 2134 experiment or *parameters of interest*, and the *nuisance parameters* that are not of  
 2135 direct interest for the experiment but that need to be included in the analysis in  
 2136 order to achieve a satisfactory description of the data; they represent effects of the  
 2137 detector response like the finite resolutions of the detection systems, miscalibrations,  
 2138 and in general any source of uncertainty introduced in the analysis.

2139 Nuisance parameters can be estimated from experimental data; for instance, data  
 2140 samples from a test beam are usually employed for calibration purposes. In cases  
 2141 where experimental samples are not availables, the estimation of nuisance parameters  
 2142 makes use of dedicated simulation programs to provide the required samples.

2143 The estimation of the unknown parameters involves certain deviations from their  
 2144 true values, hence, the measurement of the nuisance parameter is written in terms  
 2145 of an estimated value, also called central value,  $\hat{\theta}$  and its uncertainty  $\delta\theta$  using the  
 2146 notation

$$\theta = \hat{\theta} \pm \delta\theta \quad (5.9)$$

2147 where the interval  $[\hat{\theta} - \delta\theta, \hat{\theta} + \delta\theta]$  is called *confidence interval*; it is usually interpreted,  
 2148 in the limit of infinite number of experiments, as the interval where the true value  
 2149 of the unknown parameter  $\theta$  is contained with a probability of 0.6827 (if no other  
 2150 convention is stated); this interval represents the area under a Gaussian distribution  
 2151 in the interval  $\pm 1\sigma$ .

2152 The uncertainties associated with nuisance parameters produce *systematic uncer-*  
 2153 *tainties* in the final measurement, while the uncertainties related only to fluctuations

2154 in data and that affect the determination of parameters of interest produce *statistical*  
 2155 *uncertainties*.

2156 **5.2.2 Maximum likelihood estimation method**

2157 The estimation of the unknown parameters that are in best agreement with the ob-  
 2158 served data is performed through a function of the data sample that returns the  
 2159 estimate of those parameters; that function is called an *estimator*. Estimators are  
 2160 usually constructed using mathematical expressions encoded in algorithms.

2161 In this thesis, the estimator used is the likelihood function  $f(\mathbf{x}|\boldsymbol{\theta})$ <sup>4</sup> which depends  
 2162 on a set of measured variables  $\mathbf{x}$  and a set of unknown parameters  $\boldsymbol{\theta}$ . The likelihood  
 2163 function for N events in a sample is the combination of all the individual likelihood  
 2164 functions, i.e.,

$$L(\boldsymbol{\theta}) = \prod_{i=1}^N f(\mathbf{x}^i|\boldsymbol{\theta}) = \prod_{i=1}^N f(x_1^i, \dots, x_n^i; \theta_1, \dots, \theta_m) \quad (5.10)$$

2165 and the estimation method used is the *Maximum Likelihood Estimation* method  
 2166 (MLE); it is based on the combined likelihood function defined by eqn. 5.10 and  
 2167 the procedure seeks for the parameter set that corresponds to the maximum value of  
 2168 the combined likelihood function, i.e., the *maximum likelihood estimator* of the un-  
 2169 known parameter vector  $\boldsymbol{\theta}$  is the function that produces the vector of *best estimators*  
 2170  $\hat{\boldsymbol{\theta}}$  for which the likelihood function  $L(\boldsymbol{\theta})$  evaluated at the measured  $\mathbf{x}$  is maximum.

2171 Usually, the logarithm of the likelihood function is used in numerical algorithm  
 2172 implementations in order to avoid underflow the numerical precision of the computers  
 2173 due to the product of low likelihoods. In addition, it is common to minimize the  
 2174 negative logarithm of the likelihood function, therefore, the negative log-likelihood

---

<sup>4</sup> analogue to the likelihood functions described in previous sections

2175 function is

$$F(\boldsymbol{\theta}) = -\ln L(\boldsymbol{\theta}) = -\sum_{i=1}^N f(\mathbf{x}^i | \boldsymbol{\theta}). \quad (5.11)$$

2176 The minimization process is performed by the software MINUIT [134] implemented in the ROOT analysis framework. In case of data samples with large number 2177 of measurements, the computational resources necessary to calculate the likelihood 2178 function are too big; therefore, the parameter estimation is performed using binned 2179 distributions of the variables of interest for which the *binned likelihood function* is 2180 given by

$$L(\mathbf{x}|r, \boldsymbol{\theta}) = \prod_{i=1} \frac{(r \cdot s_i(\boldsymbol{\theta}) + b_i(\boldsymbol{\theta}))^{n_i}}{n_i!} e^{-r \cdot s_i(\boldsymbol{\theta}) - b_i(\boldsymbol{\theta})} \prod_{j=1} \frac{1}{\sqrt{2\pi}\sigma_{\theta_j}^2} e^{-(\theta_j - \theta_{0,j})^2/2\sigma_{\theta_j}^2}, \quad (5.12)$$

2182 with  $s_i$  and  $b_i$  the expected number of signal and background yields for the bin  $i$ ,  $n_i$   
 2183 is the observed number of events in the bin  $i$  and  $r = \sigma/\sigma_{SM}$  is the signal strength.  
 2184 Note that the number of entries per bin follows a Poisson distribution. The effect  
 2185 of the nuisance parameters have been included in the likelihood function through  
 2186 the multiplication by a Gaussian distribution that models the nuisance. The three  
 2187 parameters,  $r$ ,  $s_i$  and  $b_i$  are jointly fitted to estimate the value of  $r$ .

## 2188 5.3 Upper limits

2189 In this analysis, two hypotheses are considered; the background only hypothesis  
 2190 ( $H_0(b)$ ) and the signal plus background hypothesis ( $H_1(s+b)$ ), i.e., the sample of  
 2191 events is composed of background only events ( $r=0$ ) or it is a mixture of signal plus  
 2192 background events ( $r=1$ ). The exclusion of one hypothesis against the other means  
 2193 that the observed data sample better agrees with  $H_0$  or rather with  $H_1$ . In order  
 2194 to discriminate these hypotheses, a test statistic is constructed on the basis of the

2195 likelihood function evaluated for each of the hypothesis.

2196 The *Neyman-Pearson* lemma [135] states that the test statistic that provides the  
 2197 maximum power for  $H_1$  for a given significance level (background misidentification  
 2198 probability  $\alpha$ ), is given by the ratio of the likelihood functions  $L(\mathbf{x}|H_1)$  and  $L(\mathbf{x}|H_0)$ ;  
 2199 however, in order to use that definition it is necessary to know the true likelihood  
 2200 functions, which in practice is not always possible. Approximate functions obtained  
 2201 by numerical methods, like the BDT method described above, have to be used, so  
 2202 that the *profile likelihood* test statistic is defined by

$$\lambda(\mathbf{r}) = \frac{L(\mathbf{x}|r, \hat{\boldsymbol{\theta}}(r))}{L(\mathbf{x}|\hat{r}, \hat{\boldsymbol{\theta}})}, \quad (5.13)$$

2203 where,  $\hat{r}$  and  $\hat{\boldsymbol{\theta}}$  maximize the likelihood function, and  $\hat{\boldsymbol{\theta}}$  maximizes the likelihood  
 2204 function for a given value of the signal strength modifier  $r$ . In practice, the test  
 2205 statistic  $t_r$

$$t_r = -2\ln\lambda(r) \quad (5.14)$$

2206 is used to evaluate the presence of signal in the sample, since the minimum of  $t_r$  at  
 2207  $r = \hat{r}$  suggests the presence of signal with signal strength  $\hat{r}$ . The uncertainty interval  
 2208 for  $r$  is determined by the values of  $r$  for which  $t_r = +1$ .

2209 The expected probability density function (p.d.f)  $f(t_r|r, \boldsymbol{\theta})$  of the test statistic  $t_r$   
 2210 can be obtained numerically by generating MC samples where one hypothesis,  $H_0(b)$   
 2211 or  $H_1(s+b)$ , is assumed; thus, MC samples contain the possible values of  $t_r$  obtained  
 2212 from *pseudo-experiments* as shown in Figure 5.6. The probability that  $t_r$  takes a value  
 2213 equal or greater than the observed value ( $t_{r,obs}$ ) when a signal with a signal modifier  
 2214  $r$  is present in the data sample, is called the *p-value* of the observation; it can be  
 2215 calculated using

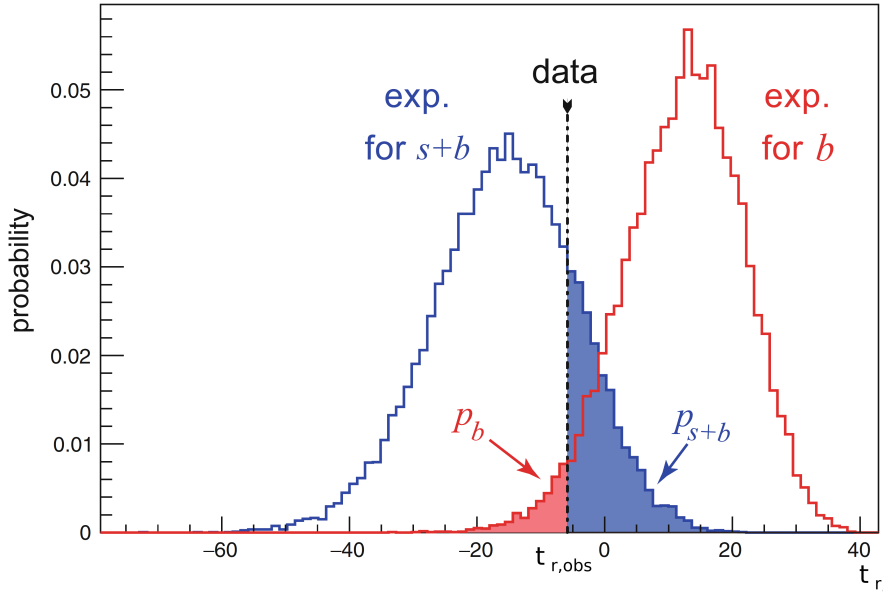


**Figure 5.6:**  $t_r$  p.d.f. from MC pseudo experiments assuming  $H_0$  (red) and  $H_1$  (blue). The black dashed line shows the value of the test statistic as measured from data. Adapted from Reference [128].

$$p_r = \int_{t_{r,obs}}^{\infty} f(t'_r | r, \boldsymbol{\theta}) dt'_r, \quad (5.15)$$

thus,  $p_r < 0.05$  means that, for that particular value of  $r$ ,  $H_1$  could be excluded at 95% Confidence Level (CL). The corresponding background-only p-value is given by

$$1 - p_b = \int_{t_{r,obs}}^{\infty} f(t'_r | 0, \boldsymbol{\theta}) dt'_r, \quad (5.16)$$

If the  $t_r$  p.d.f.s for both hypotheses are well separated, as shown in the top side of Figure 5.7, the experiment is sensitive to the presence of signal in the sample. If the signal presence is small, both p.d.f.s will be largely overlapped (bottom of Figure ??) and either the signal hypothesis could be rejected with not enough justification because the experiment is not sensitive to the signal or a fluctuation of the background could be misinterpreted as presence of signal with the corresponding rejection of the

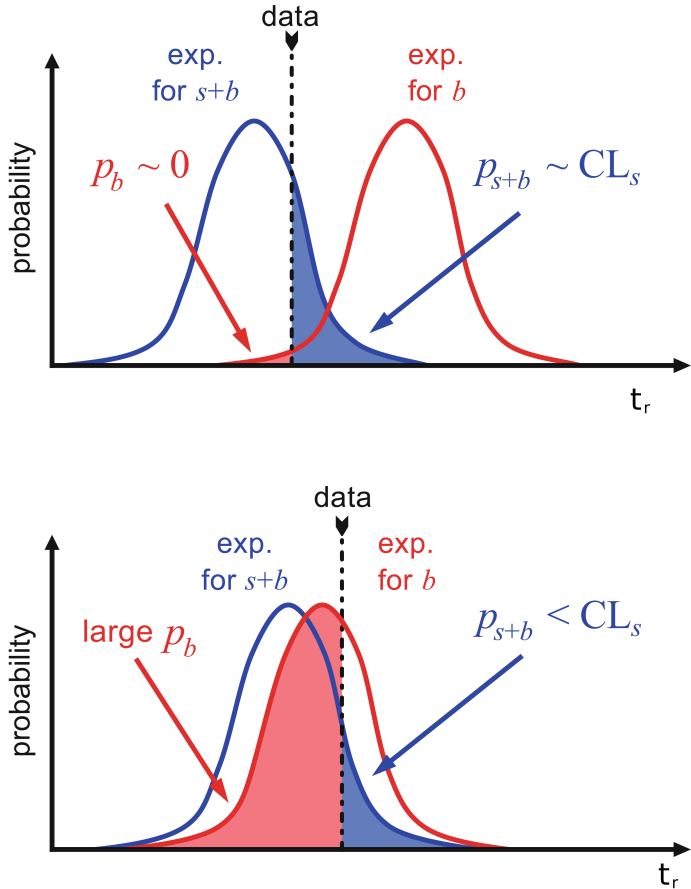


**Figure 5.7:**  $CL_s$  limit illustration. When the test statistic p.d.f. for the two hypotheses  $H_0$  and  $H_1$  are well separated (top) and when they are largely overlapped (bottom). Adapted from Reference [128].

2224 background-only hypothesis. These issues are corrected by using the modified p-  
2225 value [136]

$$p'_r = \frac{p_r}{1 - p_b} \equiv CL_s. \quad (5.17)$$

2226 If  $H_1$  is true, then  $p_b$  is small,  $CL_s \simeq p_r$  and  $H_0$  is rejected; if there is large  
2227 overlap and an statistical fluctuation cause that  $p_b$  is large, then both numerator and  
2228 denominator in Eqn. 5.17 become small but  $CL_s$  would allow the rejection of  $H_1$   
2229 even if there is poor sensitivity to signal.

2230        The upper limit of the parameter of interest  $r^{up}$  is determined by excluding the  
 2231   range of values of  $r$  for which  $CL_s(r, \theta)$  is lower than the confidence level desired,  
 2232   normally 90% or 95%, e.g, scanning over  $r$  and finding the value for which  $p_r'^{up} =$   
 2233   0.05. The expected upper limit can be calculated using pseudo-experiments based on  
 2234   the background-only hypothesis and obtaining a distribution for  $r_{ps}^{up}$ ; the median of  
 2235   that distribution corresponds to the expected upper limit, while the  $\pm 1\sigma$  and  $\pm 2\sigma$   
 2236   deviations correspond to the values of the distribution that defines the 68% and 95%  
 2237   of the area under the distribution centered in the median. It is usual to present all  
 2238   the information about the expected and observed limits in the so-called *Brazilian-flag*  
 2239   *plot* as the one showed in Figure 5.8. The solid line represent the observed  $CL_s$

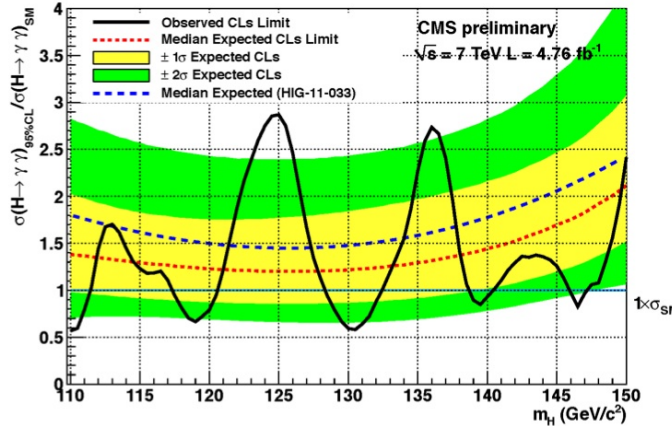


**Figure 5.8:** Brazilian flag plot of CMS experiment limits for Higgs boson decaying to photons [137].

## 2240        5.4 Asymptotic limits

2241   As said before, the complexity of the likelihood functions, the construction of test  
 2242   statistics, and the calculation of the limits and their uncertainties is not always man-  
 2243   ageable and requires extensive computational resources; in order to overcome those  
 2244   issues, asymptotic approximations for likelihood-based test statistics, like the ones

described in previous sections, have been developed [138, 139] using Wilks' theorem.  
Asymptotic approximations replace the construction of the test statistics p.d.f.s using  
MC pseudo-experiments, with the approximate calculation of the test statistics p.d.f.s  
by employing the so-called *Asimov dataset*.

The Asimov dataset is defined as the dataset that produce the true values of the  
nuisance parameters when it is used to evaluate the estimators for all the parameters;  
it is obtained by setting the values of the variables in the dataset to their expected  
values [139].

Limits calculated by using the asymptotic approximation and the Asimov dataset  
are know as *asymptotic limits*.

2255 **Chapter 6**

2256 **Search for production of a Higgs**

2257 **boson and a single top quark in**

2258 **multilepton final states in pp**

2259 **collisions at  $\sqrt{s} = 13$  TeV**

2260 **6.1 Introduction**

2261 The Higgs boson discovery, supported on experimental observations and theoretical  
2262 predictions made about the SM, gives the clue of the way in that elementary particles  
2263 acquire mass through the Higgs mechanism; therefore, knowing the Higgs mass, the  
2264 Higgs-vector boson and Higgs-fermion couplings can be determined. In order to test  
2265 the Higgs-top coupling, several measurements have been performed, as stated in the  
2266 chapter 1, but they are limited in sensitivity to measure the square of the coupling.  
2267 The production of a Higgs boson in association with a single top quark ( $tH$ ) not  
2268 only offers access to the sign of the coupling, but also, to the CP phase of the Higgs

2269 couplings.

2270 This chapter presents the search for the associated production of a Higgs boson  
 2271 and a single top quark ( $tHq$ ) events, focusing on leptonic signatures provided by the  
 2272 Higgs decay modes to  $WW$ ,  $ZZ$ , and  $\tau\tau$ ; the 13 TeV dataset produced in 2016, which  
 2273 corresponds to an integrated luminosity of  $35.9\text{fb}^{-1}$ , is used.

2274 As shown in Section 1.5, the SM cross section of  $tHq$  process is driven by a  
 2275 destructive interference between two contributions (see Figure 1.15), where the Higgs  
 2276 couples to either the W boson or the top quark; however, if the sign of the Higgs-  
 2277 top coupling is flipped with respect to the SM prediction, a large enhancement of  
 2278 the cross section occurs, making this analysis sensitive to such deviation. A second  
 2279 process, where the Higgs boson and top quark are accompanied by a W boson ( $tHW$ )  
 2280 has similar behavior, albeit with a weaker interference pattern and lower contribution  
 2281 to the cross section, therefore, a combination of both processes would increase the  
 2282 sensitivity to the sign of the coupling; in this analysis both contributions are combined  
 2283 and referred as  $tH$ channel. A third contribution comes from  $t\bar{t}H$  process. The purpose  
 2284 of this analysis is to investigate the exclusion of the presence of the  $tH + t\bar{t}H$  processes  
 2285 under the assumption of the anomalous Higgs-top coupling modifier ( $\kappa_t = -1$ ). The  
 2286 analysis exploits signatures with two leptons of the same sign ( $2lss$ ) channel and three  
 2287 leptons ( $3l$ ) channel in the final state.

2288 Constraints on the sign of the Higgs-top coupling ( $y_t$ ) have been derived from the  
 2289 decay rate of Higgs boson to photon pairs [50] and from the cross section for associated  
 2290 production of Higgs and Z bosons via gluon fusion [141], with recent results disfavoring  
 2291 negative signs of the coupling [44, 59, 142], although the negative sign coupling have  
 2292 not been completely excluded.

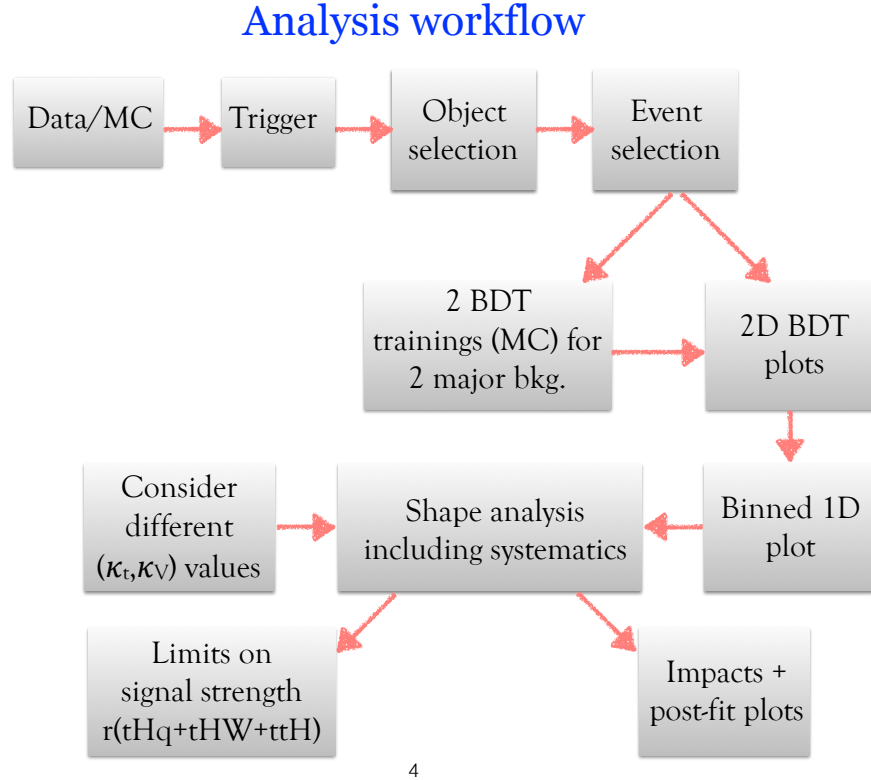
2293 The analysis presented here, expands previous analyses performed at 8 TeV [143,  
 2294 144] and searches for associated production of  $t\bar{t}$  pair and a Higgs boson in the multi-

lepton final state channel [145]; it also complements searches in other decay channels targeting  $H \rightarrow b\bar{b}$  [146].

The first sections present the characteristic  $tHq$  signature as well as the expected backgrounds. The MC samples, data sets, and the physics object definitions are then defined. Following, the background predictions, the signal extraction, and the statistical treatment of the selected events as well as the systematic uncertainties are described. The final section present the results for the exclusion limits as a function of the ratio of  $\kappa_t$  and the dimensionless modifier of the Higgs-vector boson coupling  $\kappa_V$ .

The analysis is designed to efficiently identify and select prompt leptons from on-shell W and Z boson decays and to reject non-prompt leptons from  $b$  quark decays and spurious lepton signatures from hadronic jets. Events are then selected in the  $2lss$  and  $3l$  channels, and are required to contain hadronic jets, some of which must be consistent with  $b$  quark hadronization. Finally, the signal yield is extracted by simultaneously fitting the output of two dedicated multivariate discriminants, trained to separate the  $tHq$  signal from the two dominant backgrounds, in all categories. The fit result is then used to set an upper limit on the combined  $t\bar{t}H + tH$  production cross section, as a function of the relative coupling strengths of Higgs-top quark and Higgs-Vector boson. Figure 6.1 shows an schematic overview of the analysis strategy workflow.

With respect to the 8 TeV analysis, the object selections have been adjusted for the updated LHC running conditions at 13 TeV, the lepton identification has been improved, and more powerful multivariate analysis techniques are used for the signal extraction.



4

**Figure 6.1:** A schematic overview of the analysis workflow. Based on sets of optimized physics object definitions and selection criteria, signal and background events in a data sample are discriminated. The discrimination is performed by a BDT, previously trained using MC samples of the dominant backgrounds, using discriminant variables based on the  $b$ -jet multiplicity, the activity in the forward region of the detector, and the kinematic properties of leptons. The  $CL_s$  limits on the combined  $t\bar{t}H + tH$  production cross section, as a function of the relative coupling strengths are calculated.

## 2319 6.2 $tHq$ signature

2320 In order to select events of  $tHq$  process, its features are translated into a set of  
 2321 selection rules; Figure 6.2 shows the Feynman diagram and an schematic view of the  
 2322  $tHq$  process from the  $pp$  collision to the final state configuration. A single top quark  
 2323 is produced accompanied by a light quark, denoted as  $q$ ; this light quark is produced  
 2324 predominantly in the forward region of the detector. The Higgs boson can be either  
 2325 emitted by the exchanged  $W$  boson or directly by the singly produced top quark.

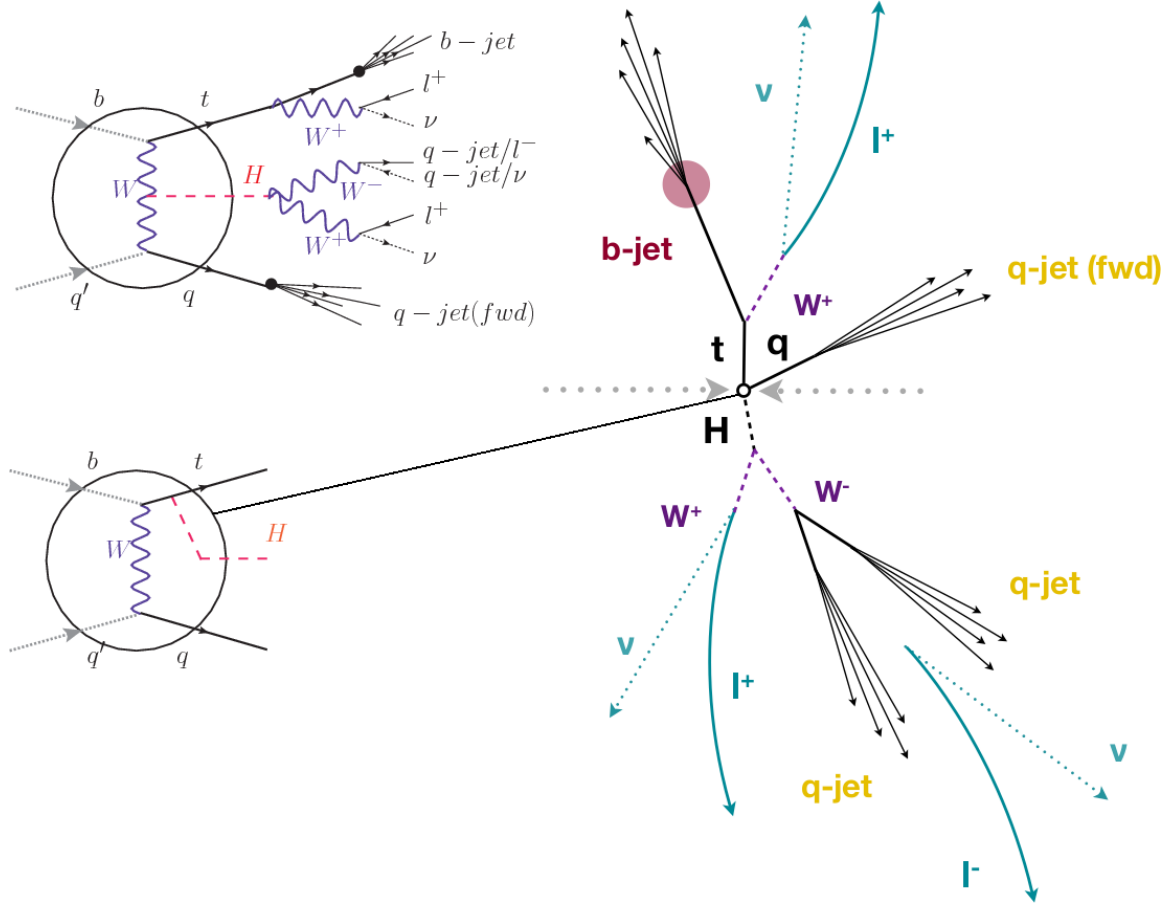


**Figure 6.2:**  $tHq$  event signature. Left: Feynman diagram including the whole evolution up to the final state for the case of the Higgs boson emitted by the  $W$  boson (top); Feynman diagram for the case where the Higgs boson is emitted by the top quark. Right: Schematic view as it would be seen in the detector; the circle in the Feynman diagrams on the left corresponds to the circle in the center of the schematic view as indicated by the line connecting them. In the  $2lss$  channel, one of the  $W$  bosons from the Higgs boson decays to two light-quark jets while in the  $3l$  channel both  $W$  bosons decay to leptons.

2326 Due to their high masses/short lifetimes, top quark and Higgs boson decay after  
 2327 their production within the detector. The Higgs boson is required to decay into a  $W$   
 2328 boson pair<sup>1</sup>. The top quark almost always decays into a bottom quark and a  $W$  boson,  
 2329 as encoded in the CMK matrix. The  $W$  bosons are required to decay leptonically  
 2330 either all the three in the  $3l$  channel or the pair with equal electrical charge in the

<sup>1</sup> ZZ and  $\tau\tau$  decays are also included in the analysis but they are not separately reconstructed

2331     $2lss$  channel case;  $\tau$  leptons are not reconstructed separately and only their leptonic  
 2332    decays into either electrons or muons are considered in this analysis.

2333       In summary, the signal process is characterized by a the final state with

2334       • one light-flavored forward jet,

2335       • one central b-jet,

2336       •  $2lss$  channel  $\rightarrow$  two leptons of the same sign, two neutrinos and two light (often  
 2337       soft) jets,

2338       •  $3l$  channel  $\rightarrow$  three leptons, three neutrinos and no central light-flavored jets,

2339       The presence of neutrinos is inferred from the presence of MET. The analysis has  
 2340    been made public by CMS as a Physics Analysis Summary [147] combining the result  
 2341    for the three lepton and two lepton same-sign channels. Currently, an effort to turn  
 2342    the analysis into a paper is ongoing.

## 2343    6.3 Background processes

2344    The background processes are those that can mimic the signal signature or at least  
 2345    can be reconstructed as that as a result of certain circumstances. The backgrounds  
 2346    can be classified as

2347       • irreducible backgrounds: where genuine prompt leptons are produced in on-  
 2348       shell W and Z boson decays; they can be reliably estimated directly from MC  
 2349       simulated events, using higher-order cross sections or data control regions for  
 2350       the overall normalization.

2351     • reducible backgrounds: where at least one of the leptons is *non-prompt*, i.e.,  
 2352       produced within a hadronic jet; genuine leptons from heavy flavor decays and  
 2353       misreconstructed jets, also known as *mis-ID leptons* or *fake leptons*, are consid-  
 2354       ered non-prompt leptons. These non-prompt leptons leave tracks and hits in  
 2355       the detection systems as would a prompt lepton, but correlating those hits with  
 2356       nearby jets could be a way of removing them. The misassignment of electron  
 2357       charge in processes like  $t\bar{t}$  or Drell-Yan, represent an additional source of back-  
 2358       ground, but it is relevant only for the  $2lss$  channel. Reducible backgrounds are  
 2359       not well predicted by simulation, hence, they are estimated using data-driven  
 2360       methods.

2361       The main sources of background events for  $tHq$  process are  $t\bar{t}$  process and  $t\bar{t} +$   
 2362        $X$  ( $X = W, Z, \gamma$ ) processes, the latter regarded together as  $t\bar{t}V$  process. Figure 6.3  
 2363       shows the signature for  $t\bar{t}$  and  $t\bar{t}W$  processes.

2364       The largest contribution to irreducible backgrounds comes from  $t\bar{t}W$  and  $t\bar{t}Z$  processes  
 2365       for which the number of ( $b$ -)jets (( $b$ -)jet multiplicity) is higher than that of the sig-  
 2366       nal events, while for other contributing background events,  $WZ$ ,  $ZZ$ , and rare SM  
 2367       processes like  $W^\pm W^\pm qq$ ,  $t\bar{t}t\bar{t}$ ,  $tZq$ ,  $tZW$ ,  $WWW$ ,  $WWZ$ ,  $WZZ$ ,  $ZZZ$ , the ( $b$ -)jet  
 2368       multiplicity is lower compared to that of the signal events. None of the irreducible  
 2369       backgrounds present activity in the forward region of the detector.

2370       On the side of the reducible backgrounds, the largest contribution comes from the  
 2371        $t\bar{t}$  events which have a very similar signature to the signal events but does no present  
 2372       activity in the forward region of the detector either; A particular feature of the  $t\bar{t}$   
 2373       events is their charge-symmetry, which is also a difference with respect to the signal  
 2374       events.

2375       The charge misidentification plays an important role in the the  $2lss$  channel since

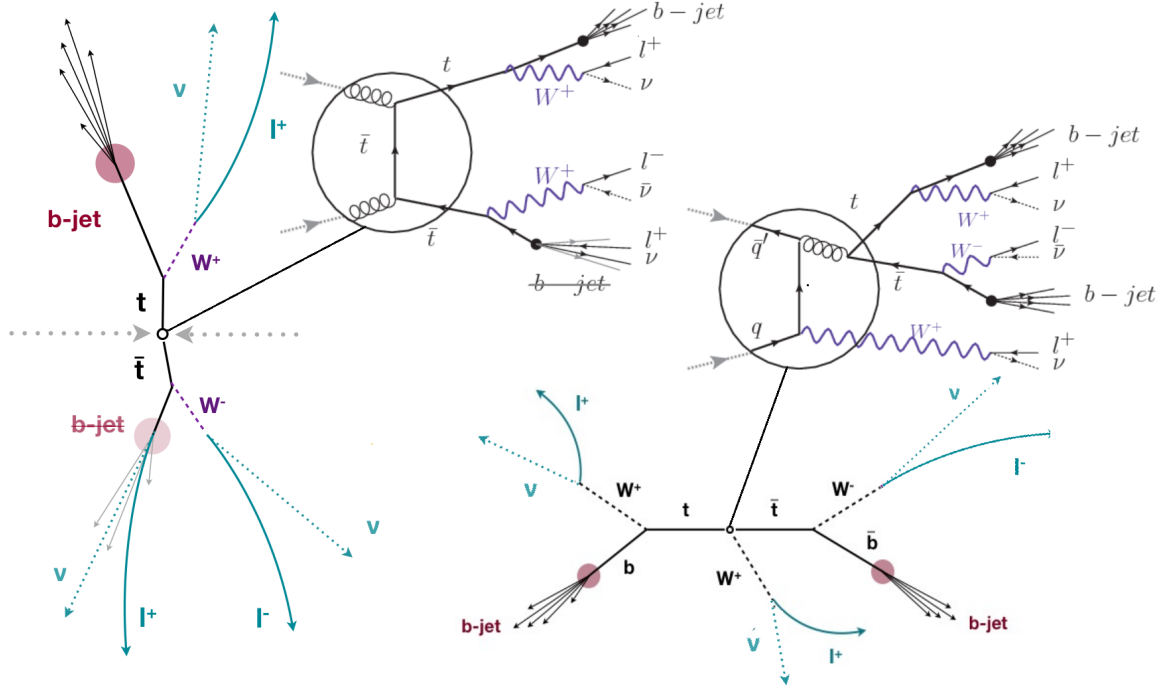


**Figure 6.3:**  $t\bar{t}$  (left) and  $t\bar{t}W$  (right) events signature as they would be seen in the detector; the Feynman diagrams including the whole evolution up to the final state are also showed. The  $t\bar{t}$  process signature is very similar to that of the signal process with one fake lepton and no forward activity. The  $t\bar{t}W$  process present a higher  $b$ -jet multiplicity compared to the signal process, a prompt lepton and no forward activity.

2376 leptons in processes like  $t\bar{t} + \text{jets}$  or  $Z + \text{jets}$  can be charge misidentified, leading to  
 2377 backgrounds increments. An identification variable have been designed in order to  
 2378 reject this type of background events.

## 2379 6.4 Data and MC Samples

### 2380 6.4.1 Full 2016 data set

2381 The data set used in this analysis was collected by the CMS experiment during 2016  
 2382 at while running at  $\sqrt{s} = 13\text{TeV}$  and corresponds to a total integrated luminosity  
 2383 of  $35.9\text{fb}^{-1}$ . Only periods when the CMS magnet was on were considered when

2384 selecting the data samples; that corresponds to the 23Sep2016 (Run B to G) and  
 2385 **PromptReco** (Run H) versions of the datasets.

2386 Multilepton final states with either two same-sign leptons or three leptons tar-  
 2387 get the case where the Higgs boson decays to a pair of W bosons,  $\tau$  leptons, or Z  
 2388 bosons, and where the top quark decays leptonically, hence, the **SingleElectron**,  
 2389 **SingleMuon**, **DoubleEG**, **MuonEG**, **DoubleMuon** dataset (see Table A.1) compose the  
 2390 full dataset. The certified luminosity sections are selected using the golden JSON file  
 2391 defined by the CMS experiment [148].

## 2392 6.4.2 Triggers

2393 The events considered are those online-reconstructed events triggered by one, two, or  
 2394 three leptons. Single-lepton triggers are included in order to boost the acceptance  
 2395 of events where the  $p_T$  of the sub-leading lepton falls below the threshold of the  
 2396 double-lepton triggers. The trigger efficiency is increased by including double-lepton  
 2397 triggers in the  $3l$  category, and single-lepton triggers in all categories; it is possible  
 2398 given the logical “or” of the trigger decisions of all the individual triggers in a given  
 2399 category. Table A.2 shows the lowest-threshold non-prescaled triggers present in the  
 2400 High-Level Trigger (HLT) menus for both Monte-Carlo and data in 2016.

### 2401 Trigger efficiency scale factors

2402 Trigger efficiency describes the ability of events to pass the trigger requirements. It  
 2403 is measured in simulated events using generator information given that there is no  
 2404 trigger bias with the MC sample. Measuring the trigger efficiency in data requires a  
 2405 more elaborated procedure; first, select a set of events collected by a trigger that is  
 2406 uncorrelated with the lepton triggers such that the selected events form an unbiased

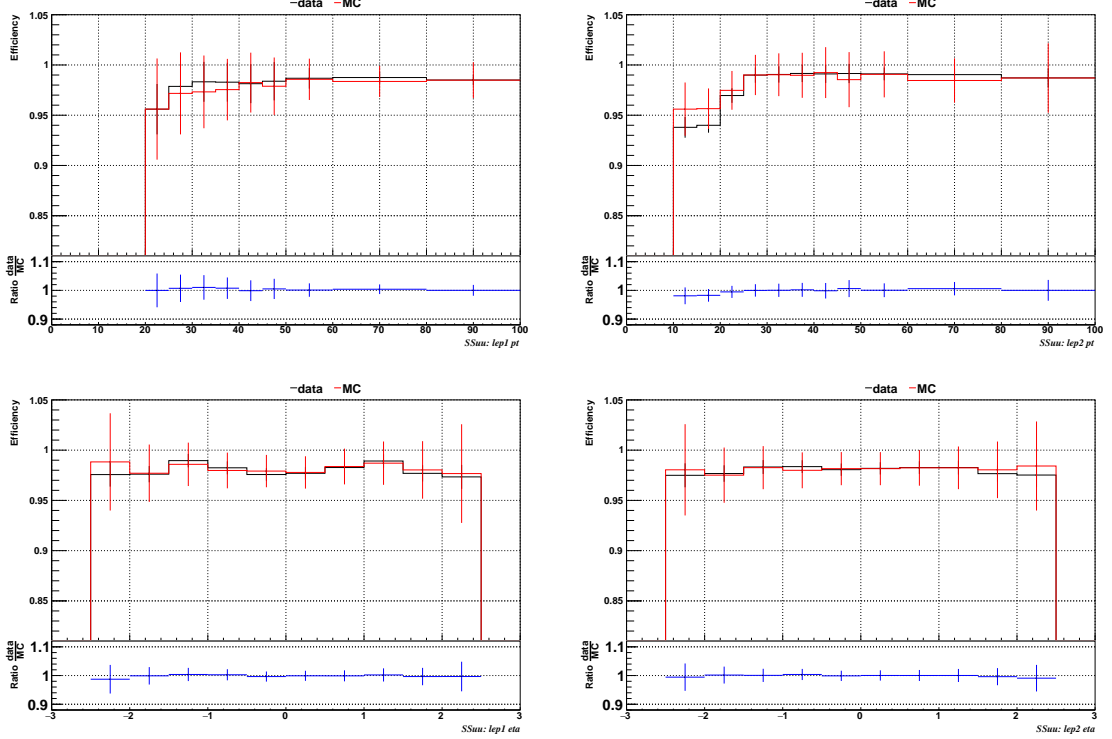


**Figure 6.4:** Comparison between data and MC trigger efficiencies in the same-sign  $\mu\mu$  category, as a function of the  $p_T$  and  $\eta$  of the leading lepton (left) and the sub-leading lepton (right) [149].

sample. In this analysis, that uncorrelated trigger is a MET trigger. Second step is looking for candidate events with exactly two good leptons (exactly three good leptons for the  $3l$  channel). Finally, measure the efficiency for the candidate events to pass the logical “or” of triggers being considered in a given event category as defined in Table A.2.

Comparisons between the data and MC efficiencies for each category, showed in Figures 6.4, 6.5, and 6.6, reveal that they are in good agreement; the difference is corrected by applying scale factors derived from the ratio between both efficiencies.

Applied flat scale factors in each category are shown in Tab. 6.1; they have been inherited from Reference [149].

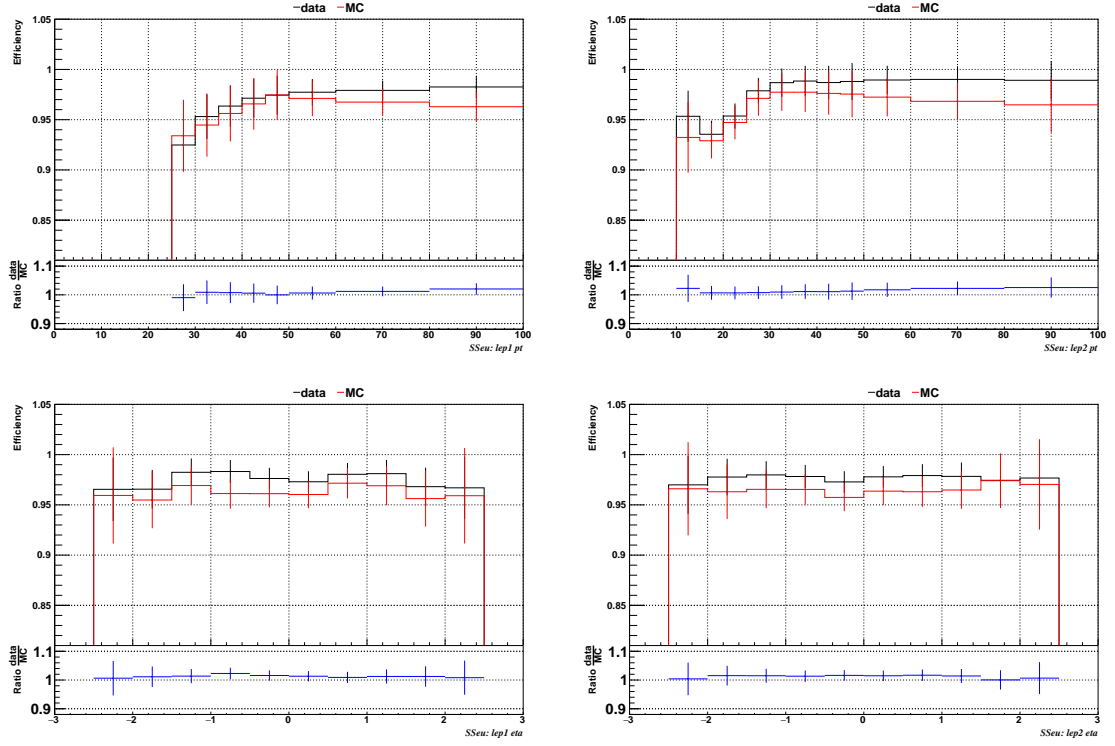


**Figure 6.5:** Comparison between data and MC trigger efficiencies in the same-sign  $e\mu$  category as a function of the  $p_T$  and  $\eta$  of the leading lepton (left) and the sub-leading lepton (right) [149].

Category	Scale Factor
ee	$1.01 \pm 0.02$
$e\mu$	$1.01 \pm 0.01$
$\mu\mu$	$1.00 \pm 0.01$
3l	$1.00 \pm 0.03$

**Table 6.1:** Trigger efficiency scale factors and associated uncertainties, shown here rounded to the nearest percent.

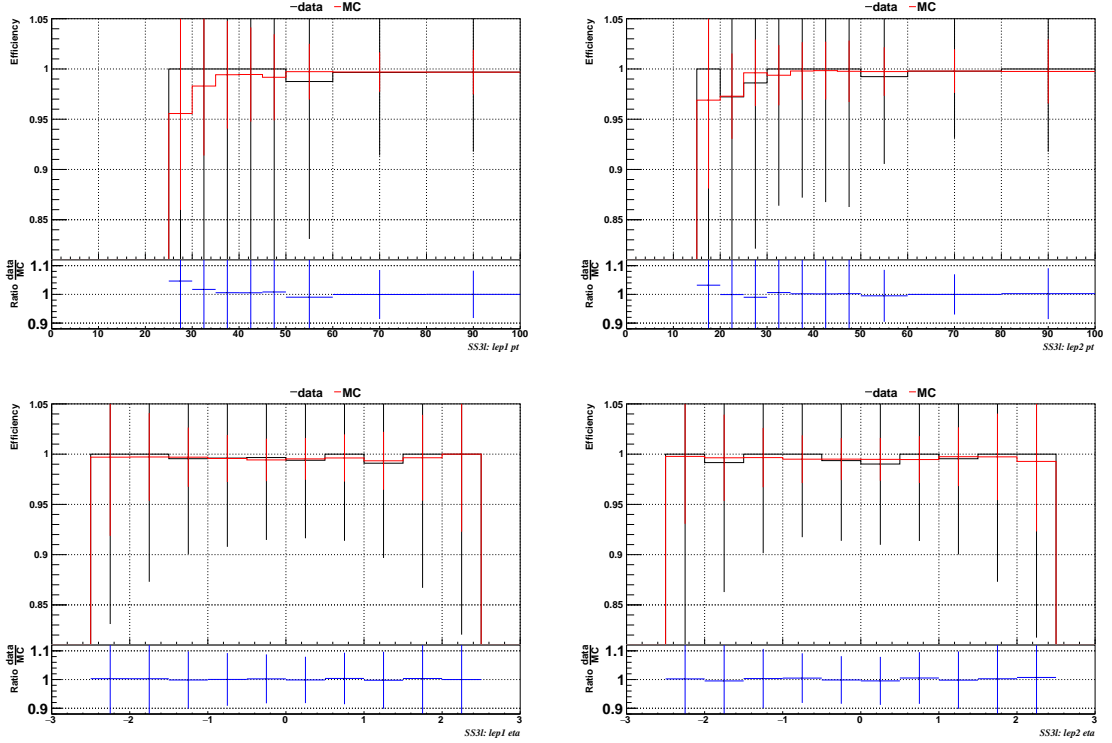


**Figure 6.6:** Comparison between data and MC trigger efficiencies in the  $3l$  category, as a function of the  $p_T$  and  $\eta$  of the leading lepton (left) and the sub-leading lepton (right) [149].

### 2417 6.4.3 Signal modeling and MC samples

2418 Current event generators allow for adjusting the kinematics of the generated events,  
 2419 based on an event-wise reweighting; in this way, several generation parameters phase  
 2420 spaces can be explored according to the experimental interests. The signal samples  
 2421 used in this analysis were generated in such a way that not only the case  $\kappa_t = -1$ , but  
 2422 an extended range of  $\kappa_t$  and  $\kappa_V$  values may be investigated.

2423  $tHq$  and  $tHW$  cross section in the  $\kappa_t$ - $\kappa_V$  phase space are shown in Figure 6.7. As  
 2424 said in section 3.1, the  $tHq$  sample was generated using the 4F scheme which provides  
 2425 a better description of the additional  $b$  quark from the initial gluon splitting, while the  
 2426  $tHW$  sample was generated using the 5F scheme in order to remove its the interference  
 2427 with  $t\bar{t}H$  at LO.

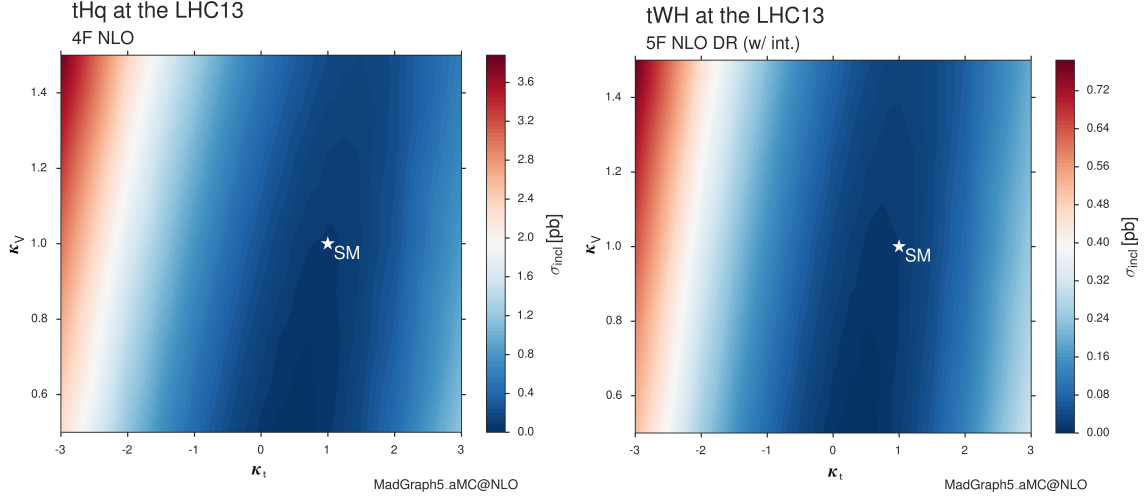


**Figure 6.7:**  $tHq$  and  $tHW$  cross section in the  $\kappa_t$ - $\kappa_V$  phase space [150].

## 2428 MC signal samples

2429 The two signal samples,  $tHq$  and  $tHW$ , correspond to the `RunIISummer16MiniAODv2`  
 2430 campaign produced with `CMSSW_80X`; they were produced with `MG5_aMC@NLO`  
 2431 (version 5.2.2.3), in LO order mode at  $\sqrt{s} = 13$  TeV, and are normalized to NLO cross  
 2432 sections (see Table 6.2). The Higgs boson is assumed to be SM-like except for the  
 2433 values of its couplings to the top quark and W boson. Each sample was generated  
 2434 with a set of event weights corresponding to 51 different values of  $(\kappa_t, \kappa_V)$  couplings,  
 2435 accessible in terms of LHE event weights as shown in Table A.3; however, the main  
 2436 interest is the  $(\kappa_t = -1, \kappa_V = 1)$  case.

Sample	$\sigma$ [pb]	BF
<code>/THQ_Hincl_13TeV-madgraph-pythia8_TuneCUETP8M1/</code>	0.7927	0.324
<code>/THW_Hincl_13TeV-madgraph-pythia8_TuneCUETP8M1/</code>	0.1472	1.0
<code>/tthJetToNonbb_M125_13TeV_amcatnloFXFX_madspin_pythia8_mWCutfix/</code>	0.2151	1.0

**Table 6.2:** MC signal samples used in this analysis; cross section and branching fraction are also listed [150].

2437 The  $t\bar{t}H$  sample was produced using `AMC@NLO` interfaced to `PYTHIA 8` for  
 2438 the parton shower, and is scaled to NLO cross sections. The  $t\bar{t}H$  cross section depends

2439 quadratically on  $\kappa_t$ ; however, in contrast to the  $tHq$  and tHW samples, the scaling  
 2440 is not performed during the sample generation process but in the analysis code since  
 2441 it was decided to include the  $t\bar{t}H$  process as part of the signal in the course of the  
 2442 analysis.

2443 **MC background samples**

2444 Several MC generators were used to generate the samples of the background processes.  
 2445 The dominant background sources ( $t\bar{t}$ ,  $t\bar{t}W$ ,  $t\bar{t}Z$ ) were produced using AMC@NLO  
 2446 interfaced to PYTHIA8, and are scaled to NLO cross sections. Other minor back-  
 2447 ground processes are simulated using POWHEG interfaced to PYTHIA, or bare  
 2448 PYTHIA as stated in the sample names in Table A.4. Pileup interactions are in-  
 2449 cluded in the simulation in order to reflect the observed multiplicity in data; the  
 2450 simulated events are weighted according to the actual pileup in data, estimated from  
 2451 the measured bunch-to-bunch instantaneous luminosity and the total inelastic cross  
 2452 section, 69.2 mb. All events are finally passed through a full simulation of the CMS  
 2453 detector based on GEANT4, and reconstructed using the same algorithms as used for  
 2454 the data.

2455 **6.5 Object Identification**

2456 In this section, the specific definitions of the physical objects in terms of the numerical  
 2457 values assigned to the reconstruction parameters are presented; thus, the provided  
 2458 details summarize and complement the descriptions presented in previous chapters.  
 2459 The object reconstruction and selection strategy used in this thesis is inherited from  
 2460 the analyses in References [145, 149], thus, the information in this section is extracted  
 2461 from those documents unless other References are stated.

### 2462 6.5.1 Lepton reconstruction and identification

2463 Two types of leptons are defined in this analysis: *signal leptons* are those coming from  
 2464  $W, Z$  and  $\tau$  decays which usually are isolated from other particles; *background leptons*  
 2465 are defined as leptons produced in  $b$ -jet hadron decays, light-jets misidentification,  
 2466 and photon conversions.

2467 The process of reconstruction and identification of electron and muon candidates  
 2468 was described in chapter3, hence, the identification variables used in order to retain  
 2469 the highest possible efficiency for signal leptons while maximizing the rejection of  
 2470 background leptons are listed and described in the following sections <sup>2</sup>.

2471 The identification variables include not only observables related directly to the re-  
 2472 constructed leptons themselves, but also to the clustered energy deposits and charged  
 2473 particles in a cone around the lepton direction (jet-related variables); an initial loose  
 2474 preselection of leptons candidates is performed and then an MVA discriminator, re-  
 2475 ferred to as *lepton MVA* discriminator, is used to distinguish signal leptons from  
 2476 background leptons.

### 2477 Muons

2478 The Physics Objects Groups (POG) at CMS, are in charge of studying and defining  
 2479 the set of selection criteria applied on the course of reconstruction and identification  
 2480 of particles. These selection criteria are implemented in the CMS framework in the  
 2481 form of several object identification working points according to the strength of the  
 2482 requirements.

2483 The muon candidates are reconstructed by combining information from the tracker  
 2484 system and the muon detection system of CMS detector and the POG defined three

---

<sup>2</sup> the studies performed to optimize the identification are far from the scope of this thesis, therefore, only general descriptions are provided

2485 working points for muon identification *MuonID* [153];

- 2486     • *POG Loose Muon ID* is a particle identified as a muon by the PF event re-  
 2487         construction and also reconstructed either as a global-muon or as an arbitrated  
 2488         tracker-muon. This identification criteria is designed to be highly efficient for  
 2489         prompt muons and for muons from heavy and light quark decays; it can be com-  
 2490         plemented by applying impact parameter cuts in analyses with prompt muon  
 2491         signals.
- 2492     • *POG Medium Muon ID* is a Loose muon with additional track-quality and  
 2493         muon-quality (spatial matching between the individual measurements in the  
 2494         tracker and the muon system) requirements. This identification criteria is de-  
 2495         signed to be highly efficient in the separation of the muons coming from decay  
 2496         in flight of heavy quarks and muons coming from B meson decays as well as  
 2497         prompt muons. An additional category *MVA Prompt ID* is defined in this iden-  
 2498         tification criteria directed to discriminated muons from B mesons and prompt  
 2499         muons (from W,Z and  $\tau$  decays). The Medium ID provides the same fake rate as  
 2500         the Tight Muon ID but a higher efficiency on prompt and B-decays muons. [154]
- 2501     • *POG Tight Muon ID* is a global muon with additional muon-quality require-  
 2502         ments Tight Muon ID selects a subset of the PF muons.

2503         Only muons within the muon system acceptance  $|\eta| < 2.4$  and minimum  $p_T$  of 5  
 2504         GeV are considered.

## 2505     **Electrons**

2506         Electrons are reconstructed using information from the tracker and from the electro-  
 2507         magnetic calorimeter and identified by an MVA algorithm (*MVA eID* discriminant)

2508 using the shape of the calorimetric shower variables like the shape in  $\eta$  and  $\phi$ , the clus-  
 2509 ter circularity, widths along  $\eta$  and  $\phi$ ; track-cluster matching variables like  $E_{tot}/p_{in}$ ,  
 2510  $E_{Ele}/p_{out}$ ,  $\Delta\eta_{in}$ ,  $\Delta\eta_{out}$ ,  $\Delta\phi_{in}$ ,  $1/E - 1/p$ ; and track quality variables like  $\chi^2$  of the  
 2511 GSF tracks, the number of hits used by the GSF filter [155].

2512 A loose selection based on  $\eta$ -dependent cuts on this discriminant is used to prese-  
 2513 lect electron candidates, the full shape of the discriminant is used in the lepton MVA  
 2514 selection to separate signal leptons from background leptons (described in Section  
 2515 6.5.1).

2516 In order to reject electrons from photon conversions, electron candidates with  
 2517 missing hits in the pixel tracker layers or matched to a conversion secondary vertex  
 2518 are discarded. Electrons are selected for the analysis if they have  $p_T > 7$  GeV and  
 2519 are located within the tracker system acceptance region ( $|\eta| < 2.5$ ).

## 2520 Lepton vertexing and pile-up rejection

2521 The impact parameter in the transverse plane  $d_0$ , impact parameter along the  $z$ -  
 2522 axis  $d_z$ , and the impact parameter significance in the detector space  $SIP_{3D}$ , are  
 2523 considered to perform the identification and rejection of pile-up, misreconstructed  
 2524 tracks, and background leptons from b-hadron decays; pile-up and misreconstructed  
 2525 track mitigation is achieved by imposing loose cuts on the impact parameter variables.  
 2526 The full shape of the those variables is used in a lepton MVA classifier to achieve the  
 2527 best separation between the signal and the background leptons.

## 2528 Lepton isolation

2529 PF is able to recognize leptons from two different sources: on one side, leptons from  
 2530 the decays of heavy particles, such as W and Z bosons, which are normally isolated  
 2531 in space from the hadronic activity in the event; on the other side, leptons from the

2532 decays of hadrons and jets misidentified as leptons, which are not isolated as the  
 2533 former. For highly boosted systems, like the lepton and the  $b$ -jet generated in the  
 2534 semileptonic decay of a boosted top, the decay products tend to be more closer and  
 2535 sometimes they even overlap; thus, the PF standard definition of isolation in terms of  
 2536 the separation between the lepton candidates and other PF objects in the  $\eta$ - $\phi$  plane,

$$\Delta R = \sqrt{(\eta^l - \eta^i)^2 + (\phi^l - \phi^i)^2} < 0.3 \quad (6.1)$$

2537 which considers all the neutral, charged hadrons and photons in a cone around the  
 2538 leptons, is refocused to the local isolation of the leptons through the mini-isolation  
 2539  $I_{mini}$  [156] defined as the sum of particle flow candidates  $p_T$  within a cone around  
 2540 the lepton, corrected for the effects of pileup and divided by the lepton  $p_T$

$$I_{mini} = \frac{\sum_R p_T(h^\pm) - \max\left(0, \sum_R p_T(h^0) + p_T(\gamma) - \rho \mathcal{A}\left(\frac{R}{0.3}\right)^2\right)}{p_T(l)} \quad (6.2)$$

2541 where  $\rho$  is the pileup energy density,  $h^\pm, h^0, \gamma, l$ , represent the charged hadron, neutral  
 2542 hadrons, photons, and the lepton, respectively. The radius  $R$  of the cone depends on  
 2543 the  $p_T$  of the lepton according to

$$R = \frac{10\text{GeV}}{\min(\max(p_T(l), 50\text{GeV}), 200\text{GeV})}, \quad (6.3)$$

2544 The  $p_T$  dependence of the cone size allows for greater signal efficiency. Setting a  
 2545 cut on  $I_{mini}$  below a given threshold ensures that the lepton is locally isolated, even  
 2546 in boosted systems. The effect of pileup is mitigated using the so-called effective area  
 2547 correction  $\mathcal{A}$  listed in Table 6.3.

2548 A loose cut on  $I_{mini}$  is applied to pre-select the muon and electron candidates;

$ \eta $ range	$\mathcal{A}(e)$ neutral/charged	$A(\mu)$ neutral/charged
0.0 - 0.8	0.1607 / 0.0188	0.1322 / 0.0191
0.8 - 1.3	0.1579 / 0.0188	0.1137 / 0.0170
1.3 - 2.0	0.1120 / 0.0135	0.0883 / 0.0146
2.0 - 2.2	0.1228 / 0.0135	0.0865 / 0.0111
2.2 - 2.5	0.2156 / 0.0105	0.1214 / 0.0091

**Table 6.3:** Effective areas, for electrons and muons used to mitigate the effect of pileup by using the so-called effective area correction.

however, the full shape is used in the lepton MVA discriminator when performing the signal lepton selection.

### Jet-related variables

In order to reject misidentified leptons from  $b$ -jets, mostly coming from  $t\bar{t}$ +jets, Drell-Yan+jets, and  $W$ +jets events, the vertexing and isolation described in previous sections are complemented with additional variables related to the closest reconstructed jet to the lepton, i.e., the PF jets reconstructed<sup>3</sup> around the leptons with  $\Delta R = \sqrt{(\eta^l - \eta^{jet})^2 + (\phi^l - \phi^{jet})^2} < 0.5$ . The identification variables used in the lepton MVA discriminator are the ratio  $p_T^l/p_T^{jet}$ , the CSV b-tagging discriminator value of the jet, the number of charged tracks of the jet, and the relative  $p_T$  given by

$$p_T^{rel} = \frac{(\vec{p}_{jet} - \vec{p}_l) \cdot \vec{p}_l}{||\vec{p}_{jet} - \vec{p}_l||}. \quad (6.4)$$

### LeptonMVA discriminator

Electrons and muons passing the basic selection process described above are referred to as *loose leptons*. Additional discrimination between signal leptons and background leptons is crucial considering that the rate of  $t\bar{t}$  production is much larger than the signal, hence, an overwhelming background from  $t\bar{t}$  production. To maximally ex-

<sup>3</sup> charged hadrons from PU vertices are not removed prior to the jet clustering.

2564 exploit the available information in each event to that end, the dedicated lepton MVA  
 2565 discriminator, based on a boosted decision tree (BDT) algorithm, has been built so  
 2566 that all the identification variables can be used together.

2567 The lepton MVA discriminator training is performed using simulated signal Loose  
 2568 leptons from the  $t\bar{t}H$  MC sample and fake leptons from the  $t\bar{t}$  + jets MC sample,  
 2569 separately for muons and electrons. The input variables used include vertexing, iso-  
 2570 lation and jet-related variables, the  $p_T$  and  $\eta$  of the lepton, the electron MVA eID  
 2571 discriminator and the muon segment-compatibility variables. An additional require-  
 2572 ment known as *tight-charge* requirement, is imposed by comparing two independent  
 2573 measurement of the charge, one from the ECAL supercluster and the other from the  
 2574 tracker; thus, the consistency in the measurements of the electron charge is ensured  
 2575 so that events with a wrong electron charge assignment are rejected; this variable is  
 2576 particularly used in the  $2lss$  channel to suppress opposite-sign events for which the  
 2577 charge of one of the leptons has been mismeasured. The tight-charge requirement for  
 2578 muons is represented by the requirement of a consistently well measured track trans-  
 2579 verse momentum given by  $\Delta p_T/p_T < 0.2$ . Leptons are selected for the final analysis  
 2580 if they pass a given threshold of the BDT output, and are referred to as *tight leptons*  
 2581 in the following.

2582 The validation of the lepton MVA algorithm and the lepton identification variables  
 2583 is performed using data in various control regions; the details about that validation  
 2584 are not discussed here but can be found in Reference [149].

## 2585 Selection definitions

2586 Electron and muon object identification is defined in three different sets of selections  
 2587 criteria; the *Loose*, *Fakeable Object*, and *Tight* selection. These three levels of selection  
 2588 are designed to serve for event level vetoes, the fake rate estimation application region,

and the final signal selection, respectively. The  $p_T$  of fakeable objects is defined as  $0.85 \times p_T(\text{jet})$ , where the jet is the one associated to the lepton object. This mitigates the dependence of the fake rate on the momentum of the fakeable object and thereby improves the precision of the method.

Tables 6.4 and 6.5 list the full criteria for the different selections of muons and electrons.

Cut	Loose	Fakeable object	Tight
$ \eta  < 2.4$	✓	✓	✓
$p_T$	$> 5\text{GeV}$	$> 15\text{GeV}$	$> 15\text{GeV}$
$ d_{xy}  < 0.05$ (cm)	✓	✓	✓
$ d_z  < 0.1$ (cm)	✓	✓	✓
$\text{SIP}_{3D} < 8$	✓	✓	✓
$I_{\text{mini}} < 0.4$	✓	✓	✓
is Loose Muon	✓	✓	✓
jet CSV	–	$< 0.8484$	$< 0.8484$
is Medium Muon	–	–	✓
tight-charge	–	–	✓
lepMVA $> 0.90$	–	–	✓

**Table 6.4:** Requirements on each of the three muon selections. In the cases where the cut values change between the selections, those values are listed in the table. Otherwise, whether the cut is applied is indicated.

In addition to the previously defined requirements for jets, they are required to be separated from any lepton candidates passing the fakeable object selections by  $\Delta R > 0.4$ .

## 6.5.2 Lepton selection efficiency

Efficiencies of reconstruction and selecting loose leptons are measured both for muons and electrons using a tag and probe method on both data and MC, using  $Z \rightarrow \ell^+ \ell^-$  [157]. The scale factors are derived from the ratio of efficiencies  $\varepsilon_i(p_T, \eta)$  measured

Cut	Loose	Fakeable Object	Tight
$ \eta  < 2.5$	✓	✓	✓
$p_T$	$> 7\text{GeV}$	$> 15\text{GeV}$	$> 15\text{GeV}$
$ d_{xy}  < 0.05 \text{ (cm)}$	✓	✓	✓
$ d_z  < 0.1 \text{ (cm)}$	✓	✓	✓
$\text{SIP}_{3D} < 8$	✓	✓	✓
$I_{\text{mini}} < 0.4$	✓	✓	✓
MVA eID $> (0.0, 0.0, 0.7)$	✓	✓	✓
$\sigma_{in\eta} < (0.011, 0.011, 0.030)$	—	✓	✓
$\text{H/E} < (0.10, 0.10, 0.07)$	—	✓	✓
$\Delta\eta_{in} < (0.01, 0.01, 0.008)$	—	✓	✓
$\Delta\phi_{in} < (0.04, 0.04, 0.07)$	—	✓	✓
$-0.05 < 1/E - 1/p < (0.010, 0.010, 0.005)$	—	✓	✓
$p_T^{\text{ratio}}$	—	$> 0.5^\dagger / -$	—
jet CSV	—	$< 0.3^\dagger / < 0.8484$	$< 0.8484$
tight-charge	—	—	✓
conversion rejection	—	—	✓
Number of missing hits	$< 2$	$== 0$	$== 0$
lepton MVA $> 0.90$	—	—	✓

**Table 6.5:** Criteria for each of the three electron selections. In cases where the cut values change between selections, those values are listed in the table. Otherwise, whether the cut is applied is indicated. In some cases, the cut values change for different  $\eta$  ranges. These ranges are  $0 < |\eta| < 0.8$ ,  $0.8 < |\eta| < 1.479$ , and  $1.479 < |\eta| < 2.5$  and the respective cut values are given in the form (value<sub>1</sub>, value<sub>2</sub>, value<sub>3</sub>). For the two  $p_T^{\text{ratio}}$  and CSV rows, the cuts marked with a  $\dagger$  are applied to leptons that fail the lepton MVA cut, while the loose cut value is applied to those that pass the lepton MVA cut.

2602 for a given lepton in data/MC, according to

$$\rho(p_T, \eta) = \frac{\varepsilon_{\text{data}}(p_T, \eta)}{\varepsilon_{\text{MC}}(p_T, \eta)}. \quad (6.5)$$

2603 The scale factor for each event is used to correct the weight of the event in the  
 2604 full sample; therefore, the full simulation correction is given by the product of all  
 2605 the individual scale factors. The scale factors used in this thesis are inherited from  
 2606 Reference [149] which in turns inherited them from leptonic SUSY analyses using  
 2607 equivalent lepton selections.

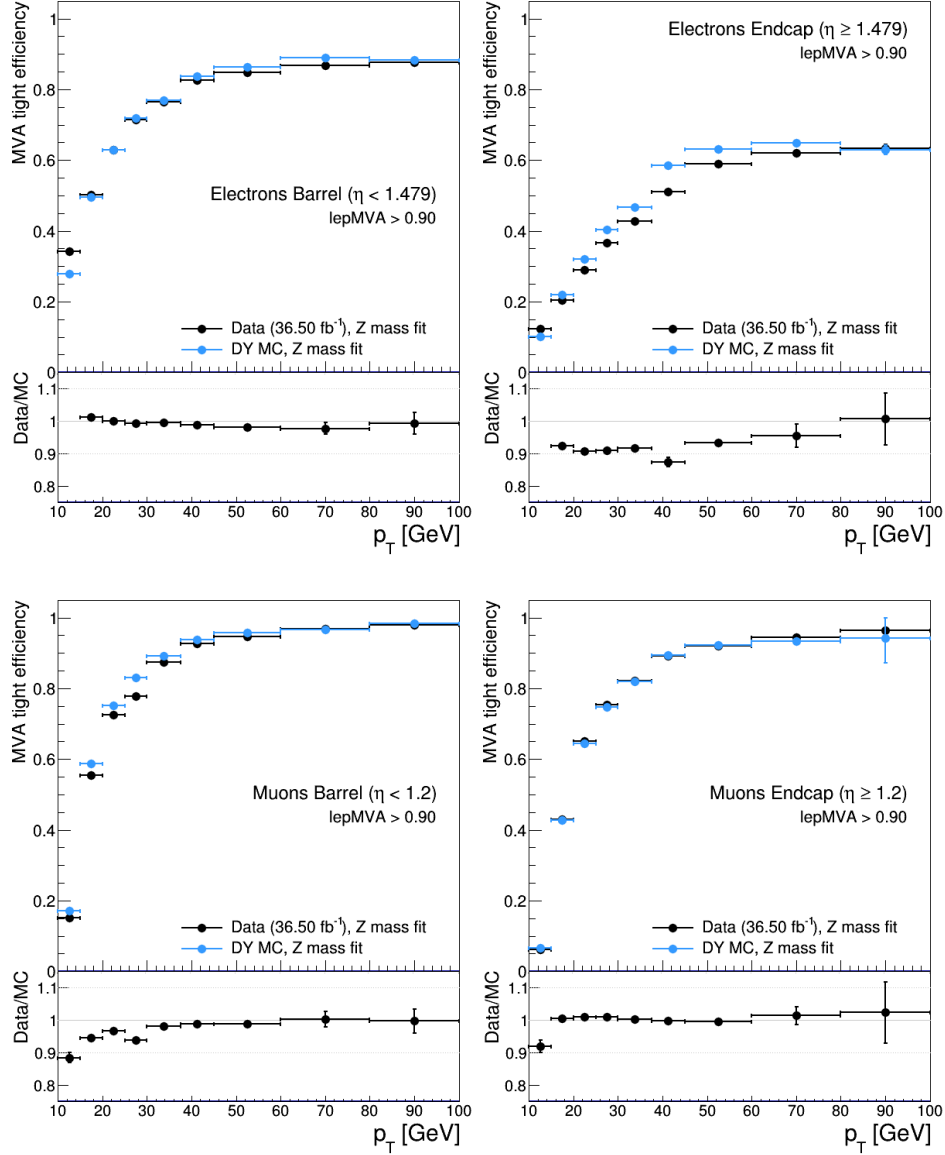


**Figure 6.8:** Tight vs loose selection efficiencies for electrons (top), and muons (bottom), for the  $2lss$  definition, i.e., including the tight-charge requirement.

2608        The efficiency of applying the tight selection as defined in Tables 6.4 and 6.5, on the  
 2609        loose leptons are determined by using a tag and probe method on a sample of Drell-  
 2610        Yan enriched events. Figures 6.8 and 6.9 show the efficiencies for the  $2lss$  channel and  
 2611         $3l$  channel respectively. Efficiencies in the  $2lss$  channel have been produced including  
 2612        the tight-charge requirement, while for the  $3l$  channel it is not included. Number

of passed and failed probes are determined from a fit to the invariant mass of the dilepton system. Simulation is corrected using these scale factors; note that they depends on  $\eta$  and  $p_T$ .

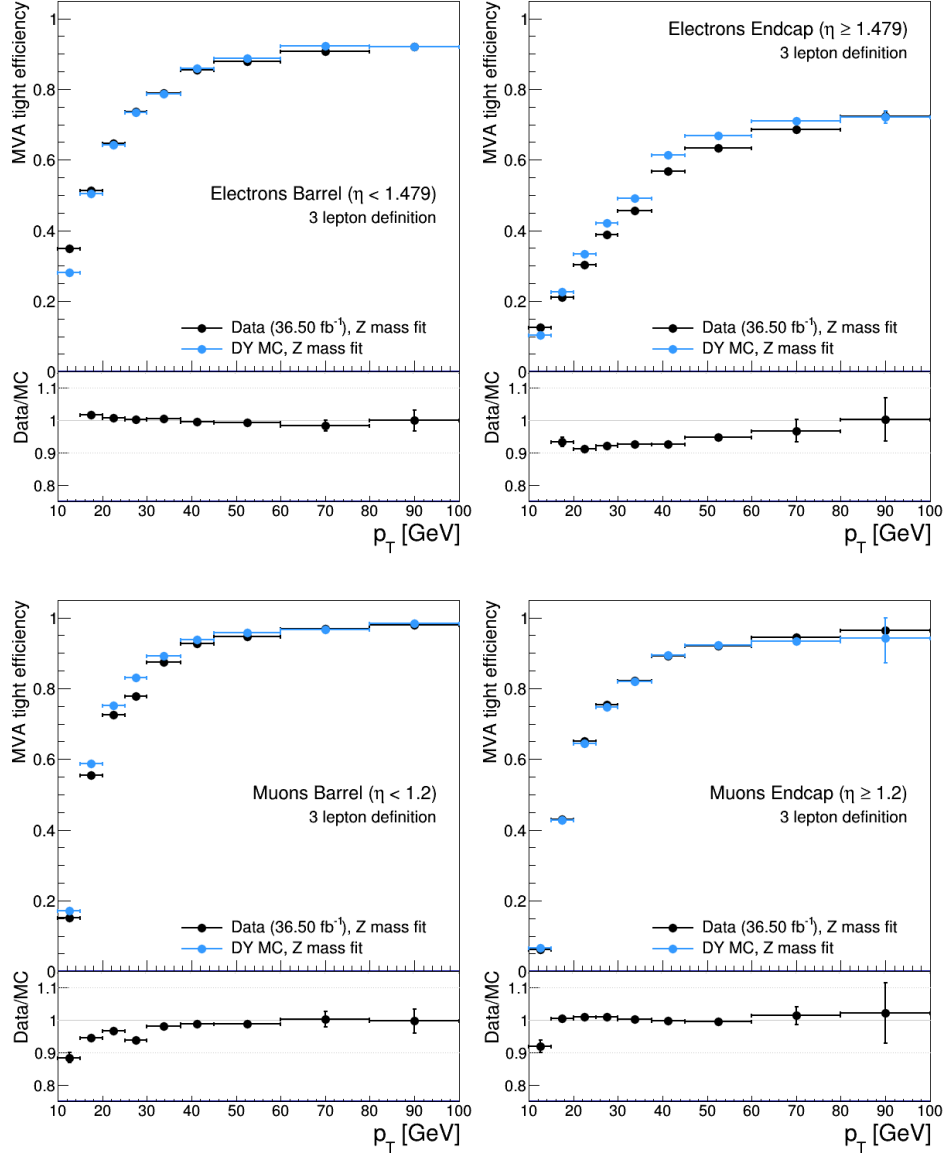


**Figure 6.9:** Tight vs loose selection efficiencies for electrons (top), and muons (bottom), for the  $3l$  channel not including the tight-charge requirement.

2616 **6.5.3 Jets and  $b$ -jet tagging**

2617 In this analysis, jets are reconstructed by clustering PF candidates using the anti- $k_t$   
 2618 algorithm with parameter distance  $\Delta R = 0.4$ ; those charged hadrons that are not  
 2619 consistent with the selected primary vertex are discarded from the clustering. The  
 2620 jet energy is then corrected for the varying response of the detector as a function  
 2621 of transverse momentum  $p_T$  and pseudorapidity  $\eta$ . Jets are selected for use in the  
 2622 analysis only if they have  $p_T > 25$  GeV and are separated from any selected leptons  
 2623 by  $\Delta R > 0.4$ .

2624 Jets coming from the primary vertex and jets coming from pile-up vertices are  
 2625 distinguished using a MVA discriminator based on the differences in the jet shapes,  
 2626 in the relative multiplicity of charged and neutral components, and in the different  
 2627 fraction of transverse momentum which is carried by the hardest components. Jet  
 2628 tracks are also required to be compatible with the primary vertex.

2629 Jets originated from the hadronization of a  $b$  quark are selected using a MVA  
 2630 likelihood discriminant which uses track-based lifetime information and reconstructed  
 2631 secondary vertices (CSV algorithm). Only jets within the CMS tracker acceptance  
 2632 ( $\eta < 2.4$ ) are identified with this tool. Data samples are used to measure the efficiency  
 2633 of the  $b$ -jet tagging and the probability to misidentify jets from light quarks or gluons;  
 2634 in both cases the measurements are parametrized as a function of the jet  $p_T$  and  $\eta$   
 2635 and later used to correct differences between the data and MC simulation in the  $b$   
 2636 tagging performance, by applying per-jet weights to the simulation, dependent on  
 2637 the jet  $p_T$ ,  $\eta$ ,  $b$  tagging discriminator, and flavor (from simulation truth) [151]. The  
 2638 per-event weight is taken as the product of the per-jet weights, including those of the  
 2639 jets associated to the leptons. The weights are derived on  $t\bar{t}$  and Z+jets events.

2640 Two working points are defined, based on the CSV algorithm output: ‘*loose*’ work-

ing point ( $\text{CSV} > 0.46$ ) with a  $b$  signal tagging efficiency of about 83% and a mistagging rate of about 8%; and *medium* working point ( $\text{CSV} > 0.80$ ) with  $b$ -tagging efficiency of about 69% and mistagging rate of order 1% [152]. Tagging of jets from charm quarks have efficiencies of about 40% and 18% for loose and medium working points respectively. Separate scale factors are applied to jets originating from bottom/charm quarks and from light quarks in simulated events to match the tagging efficiencies measured in the data.

#### 6.5.4 Missing Energy MET

As stated in Section 3.4.1.1, the MET vector is calculated as the negative of the vector sum of transverse momenta of all PF candidates in the event and its magnitude is referred to as  $E_T^{\text{miss}}$ . Due to pile-up interactions, the performance in determining MET is degraded; in order to correct for that, the energy from the selected jets and leptons that compose the event is assigned to the variable  $H_T^{\text{miss}}$ . It is calculated in the same way as  $E_T^{\text{miss}}$  and although it has worse resolution than  $E_T^{\text{miss}}$ , it is more robust in the sense that it does not rely on the soft part of the event. The event selection uses a linear discriminator based on the two variables given by

$$E_T^{\text{miss}} \text{LD} = 0.00397 * E_T^{\text{miss}} + 0.00265 * H_T^{\text{miss}} \quad (6.6)$$

taking advantage of the fact that the correlation between  $E_T^{\text{miss}}$  and  $H_T^{\text{miss}}$  is less for events with instrumental missing energy than for events with real missing energy. The working point  $E_T^{\text{miss}} \text{LD} > 0.2$  was chosen to ensure a good signal efficiency while keeping a good background rejection.

## 2661 6.6 Event selection

2662 Events are selected considering the features of the signal process and the decay sig-  
 2663 nature as described in Section 6.2. At the trigger level, events are selected to contain  
 2664 either one, two, or three leptons with minimal  $p_T$  thresholds:

- 2665 • single-lepton trigger → 24 GeV for muons and at 27 GeV for electrons
- 2666 • double-lepton triggers → leading and sub-leading leptons: 17 and 8 GeV for  
 2667 muons and 23 and 12 GeV for electrons.
- 2668 • three-lepton triggers → threshold on the third hardest lepton in the event: 5  
 2669 and 9 GeV for muons and electrons, respectively.

2670 The offline event selection level targets the specific topology of the  $tHq$  signal  
 2671 with  $H \rightarrow WW$  and  $t \rightarrow Wb \rightarrow l\nu b$ ; therefore, the resulting state is composed of three  
 2672 W bosons, one  $b$  quark, and a light spectator quark at high rapidity. The selection  
 2673 criteria for the two channels exploited in this analysis are summarized in Table 6.6.

Same-sign $\ell\ell$ channel	$\ell\ell\ell$ channel
have fired one of the corresponding trigger paths	
No loose leptons with $m_{\ell\ell} < 12\text{GeV}$	
One or more $b$ tagged jets $ \eta  < 2.4$	
One or more non-tagged jets: central → $p_T > 25\text{ GeV}$ , $\eta < 2.4$	
	forward → $p_T > 40\text{ GeV}$ , $\eta > 2.4$
	$E_T^{\text{miss}} \text{LD} > 0.2$
Exactly two tight same-sign leptons	Exactly three tight leptons
Lepton $p_T > 25/15\text{GeV}$	Lepton $p_T > 25/15/15\text{GeV}$
Electrons are triple-charge consistent.	No OSSF lepton pair with $ m_{\ell\ell} - m_Z  < 15\text{GeV}$
Muon $p_T$ resolution: $\Delta p_T/p_T < 0.2$ .	

**Table 6.6:** Summary of event selection.

2674 In the  $2lss$  channel, events with additional tight leptons are vetoed as well as those  
 2675 for which a loose lepton pair has an invariant mass below 12 GeV. A threshold in  $p_T$  of

2676 the leading and sub-leading leptons is also required. events where the two electrons  
2677 have invariant mass within 10 GeV of the Z boson mass (*Z-veto*) are discarded in  
2678 order to reject events from DY+jets production with charge misidentified electrons.

2679 In the  $3l$  lepton channel, leptons are required to have respectively  $p_T > 25\text{GeV}$ ,  $>$   
2680  $15\text{ GeV}$ , and  $> 15\text{ GeV}$ . Events with an opposite-sign, same-flavor lepton combina-  
2681 tion (OSSF) with invariant mass within 15 GeV of the Z boson mass are discarded in  
2682 order to reject events from  $WZ + \text{jets}$  production.

2683 The selection criteria in Table 6.6 represent a relatively loose selection that allows  
2684 to maintain a large signal efficiency while suppressing the main backgrounds. This  
2685 selection includes contributions from  $H \rightarrow \tau\tau$  and  $H \rightarrow ZZ$  as well. The events  
2686 obtained from the selection are then used to extract the signal contribution in a  
2687 second analysis step, using BDT discriminators against the main backgrounds of  
2688  $t\bar{t}W/t\bar{t}Z$  and non-prompt leptons from  $t\bar{t}$ . The shape of the discriminator variables  
2689 is then fit to the observed data distribution to estimate the signal and background  
2690 yields, simultaneously for all channels.

## 2691 6.7 Background modeling and predictions

2692 Irreducible backgrounds are reliably estimated from MC simulated events; there-  
 2693 fore, in this analysis all backgrounds involving prompt leptons are estimated in this  
 2694 way. Reducible backgrounds, are not well predicted by simulation, hence, they are  
 2695 estimated using data-driven methods; in the case of non-prompt leptons, a fake rate  
 2696 method is used.

2697 Drell-Yan contribution is reduced in the  $3l$  channel due to the requirement of an  
 2698 additional lepton, the jet counting and the Z-veto. Three boson contributions are  
 2699 reduced by rejecting events with extra leptons and by requiring forward jets or  $b$ -jets

2700 The  $2lss$  channel receives contribution from the associated production of two W  
 2701 bosons of equal charge and two light jets  $W^\pm W^\pm qq$  and from same-sign W boson  
 2702 pairs can also be produced in double parton scattering (DPS) processes, where each  
 2703 of the colliding protons gives two partons, resulting in two hard interactions.

2704 Backgrounds from  $t\bar{t}W$  and  $t\bar{t}Z$  processes are estimated using simulated events,  
 2705 corrected for data/MC differences and inefficiencies (trigger and lepton selection) in  
 2706 the same way as signal events. Their production cross sections are calculated at  
 2707 NLO order of QCD and EWK, considering theoretical uncertainties from unknown  
 2708 higher orders of 12% for  $t\bar{t}W$  and 10% for  $t\bar{t}Z$ . Additional uncertainties arise from the  
 2709 knowledge of PDFs and  $\hat{\text{S}}$  of about 4% each for  $t\bar{t}W$  and  $t\bar{t}Z$ .

### 2710 6.7.1 Diboson backgrounds

2711 Background contamination from diboson processes is strongly suppressed by imposing  
 2712 the Z-veto, vetoing additional leptons and requiring  $b$ -jets in the event. The diboson  
 2713 contribution is also estimated from simulated events; however, the overall normal-  
 2714 ization of this process is obtained from a dedicated control region. The motivation

behind that strategy is that even though the measured inclusive cross section for diboson processes (WZ,ZZ) is in good agreement with the NLO calculations [149], that agreement is perturbed when leptonic Z decays and hadronic jets in the final state are required; those requirements are precisely the ones that make the diboson production a background for the  $tHq$  signal. Thus, by using a dedicated control region dominated by WZ production<sup>4</sup>, the overall normalization is constrained.

The control region is defined by the presence of at least three leptons, of which one opposite-sign pair must be compatible with a Z boson decay, i.e., invert the Z-veto which makes the control region orthogonal to signal region; the b-jet tagging requirements is also inverted with respect to the signal region, i.e., require two not  $b$ -jets. A scale factor is extracted from the predicted distribution of WZ events in the control region, and the observed data, while keeping other processes fixed; this factor is used to scale the diboson prediction in the signal selection region. More details about the procedure used can be found in Reference [149] from where the scale factor is taken.

In order to test the usability of the diboson background scale factor in this analysis, a Z-enriched control region<sup>5</sup> was defined by inverting the Z-veto and requiring exactly three tight leptons with  $p_T > 25/15/15$  GeV, one or more jets passing the CSVv2 loose working point and less than four central jets. Figure 6.10 shows the distribution of three variables in the diboson control region; the good agreement between MC and data motivates the adoption of the diboson background scale factor.

. Their production cross sections are calculated at NLO of QCD and EWK, with theoretical uncertainties from unknown higher orders of 12% for  $t\bar{t}W$  and 10% for  $t\bar{t}Z$ . Further uncertainties arise from the knowledge of PDFs and  $\alpha_s$  of about 4% each for

---

<sup>4</sup> ZZ background is strongly reduced by the cut on MET.

<sup>5</sup> This control region is different to the one used to find the scale factor.

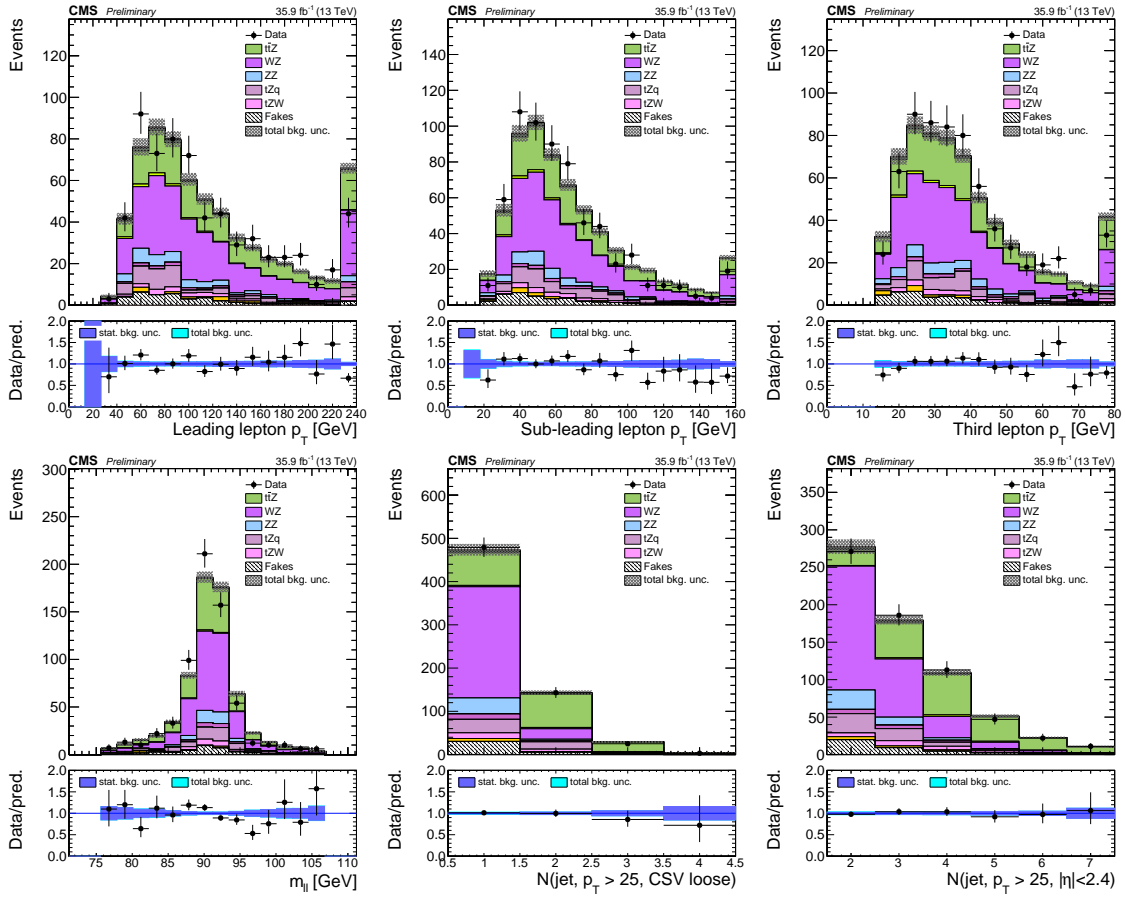


**Figure 6.10:** Kinematic distributions in the diboson control region.

2739  $t\bar{t}W$  and  $t\bar{t}Z$ .

2740 In the  $2lss$  channel case, additional background arises when the charge of a lepton  
 2741 in events with an originally opposite-sign pair is misidentified; usually this happens  
 2742 due to strongly asymmetric conversions of hard bremsstrahlung photons emitted from  
 2743 the initial lepton, therefore, it is more likely to happen for electrons than for muons.

2744 Additional identification criteria are applied for electrons with  $p_T$  greater than 30  
 2745 GeV to mimic the identification applied at trigger level in order to ensure consistency  
 2746 between the measurement region and application region of the fake-rate.

2747 where the contribution to the final selection is estimated by extrapolating from a  
 2748 sideband (or *application region*) with a looser lepton definition (the fakeable object

definitions in Tabs. 6.4 and 6.5) to the signal selection. The tight-to-loose ratios (or *fake rates*) are measured in several background dominated data events with dedicated triggers, subtracting the residual prompt lepton contribution using MC. Non-prompt leptons in our signal regions are predominantly produced in  $t\bar{t}$  events, with a much smaller contribution, from Drell–Yan production. The systematic uncertainty on the normalization of the non-prompt background estimation is on the order of 50%, and thereby one of the dominant limitations on the performance of multilepton analyses in general and this analysis in particular. It consists of several individual sources, such as the result of closure tests of the method using simulated events, limited statistics in the data control regions due to necessary prescaling of lepton triggers, and the uncertainty in the subtraction of residual prompt leptons from the control region.

The fake background where the leptons pass the looser selection are weighted according to how many of them fail the tight criteria. Events with a single failing lepton are weighted with the factor  $f/(1-f)$  for the estimate to the tight selection region, where  $f$  is the fake rate. Events with two failing leptons are given the negative weight  $-f_i f_j / (1-f_i)(1-f_j)$ , and for three leptons the weight is positive and equal to the product of  $f/(1-f)$  factor evaluated for each failing lepton.

Figures 6.11 show the distributions of some relevant kinematic variables, normalized to the cross section of the respective processes and to the integrated luminosity.

The modeling of reducible and irreducible backgrounds in this analysis uses the exact methods, analysis code, and ROOT trees used for the  $t\bar{t}H$  multilepton analysis. We give a brief description of the methods and refer to the documentation of that analysis in Refs. [145, 149] for any details.

Once the events are selected in agreement with the signal characteristics, the extraction of the signal contribution is performed using multivariate discriminators

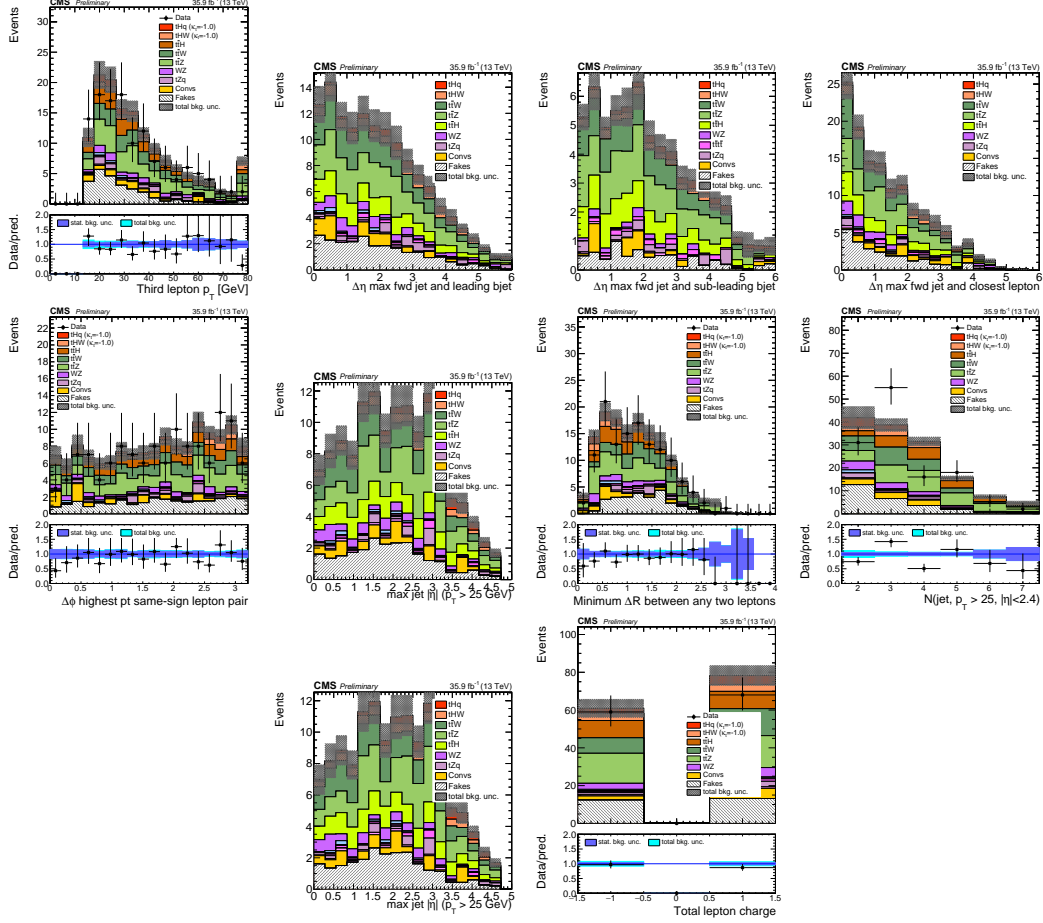


**Figure 6.11:** Distributions of input variables to the BDT for signal discrimination, three lepton channel, normalized to their cross section and to  $35.9\text{fb}^{-1}$ .

against the main backgrounds of  $t\bar{t}W/t\bar{t}Z$  and non-prompt leptons from  $t\bar{t}$ . The shape of the discriminator variables is then fit to the observed data distribution to estimate the signal and background yields, simultaneously for all channels.

A significant fraction of selected data events (about 50% in the dilepton channels, and about 80% in the trilepton channel) also passes the selection used in the dedicated search for  $tth$  in multilepton channels [17]. The expected and observed event yields of this selection are shown in Tab. 2. For the  $tH$  and  $t\bar{t}H$  processes, the largest contribution comes from Higgs decays to  $WW$  (about 75%), followed by  $\text{I}\bar{D}\bar{I}\bar{D}$  (about 20%) and  $ZZ$  (about 5%). Other Higgs production modes contribute negligible event

2784 yields ( $< 5\%$  of the  $tH + ttH$  yield).

2785 .

2786 .

2787 .

2788 .

2789 .

2790 .

2791 .

2792 .

2793 .

2794 . . .

2795 . Multivariate techniques are used to discriminate the signal from the dominant  
2796 backgrounds. The analysis yields a 95% confidence level (C.L.) upper limit on the  
2797 combined  $tH + ttH$  production cross section times branching ratio of 0.64 pb, with  
2798 an expected limit of 0.32 pb, for a scenario with  $kt = \pm 1.0$  and  $kV = 1.0$ . Values  
2799 of  $kt$  outside the range of  $\pm 1.25$  to  $\pm 1.60$  are excluded at 95% C.L., assuming  $kV$   
2800 = 1.0.

2801 Dont forget to mention previous constrains to ct check Reference ?? and Refer-  
2802 ences <https://link.springer.com/content/pdf/10.1007%2FJHEP01%282013%29088.pdf>  
2803 (paragraph after eq 2)

2804 **6.8 Signal discrimination**

2805 The production cross section for the signal processes  $tHq$ ,  $tHW$ , and  $t\bar{t}H$  is only  
 2806 about 600 fb (the enhancement provided by inverted couplings,  $\kappa_t = -1$  almost double  
 2807 it), resulting in a small signal to background ratio even for a tight selection. A  
 2808 multivariate method is hence employed to train a discriminator to separate  $tH$  signal  
 2809 events from the dominant background events ( $t\bar{t}$  and  $t\bar{t}V$ ).

2810 **6.8.1 MVA classifiers evaluation**

2811 Several MVA classifier algorithms were evaluated in order to determine the most  
 2812 appropriate method for this analysis<sup>6</sup>. The comparison is based on the performance  
 2813 of the classifiers, encoded in the plot of the background rejection as a function of the  
 2814 signal efficiency (ROC curve). The top row of Figure 6.12 shows the ROC curves  
 2815 for the several methods evaluated; two separated training were performed in the  $3l$   
 2816 channel: against  $t\bar{t}$  (right) and  $t\bar{t}V$  (left) processes.

2817 In both cases the gradient boosted decision tree  $BDTG$  ( $BDTA\_GRAD$  in the  
 2818 plot) classifier offers the best results, followed by the adaptive BDT classifier ( $BDTA$ );  
 2819 the several Fisher classifiers tested, which differ in their parameters and/or boosting  
 2820 method, they offer similar performance among them, while the k-Nearest Neighbour  
 2821 (kNN) classifier performance is below the rest of the classifiers. The corresponding  
 2822 ROC curves and in the  $2lss$  channel for trainings against  $t\bar{t}V$ (left) and  $t\bar{t}$  (right)  
 2823 processes are shown in the bottom row of Figure 6.12; the BDTG performance is  
 2824 similar to that in the  $3l$  channel.

---

<sup>6</sup> The choice of the tested algorithms was based on the experience from previous analyses and considering the expertise of the members of the  $tHq$  and  $t\bar{t}H$  analyses groups. Only the BDT classifier is described in this thesis and a detailed description of all available methods can be found in Reference [127]

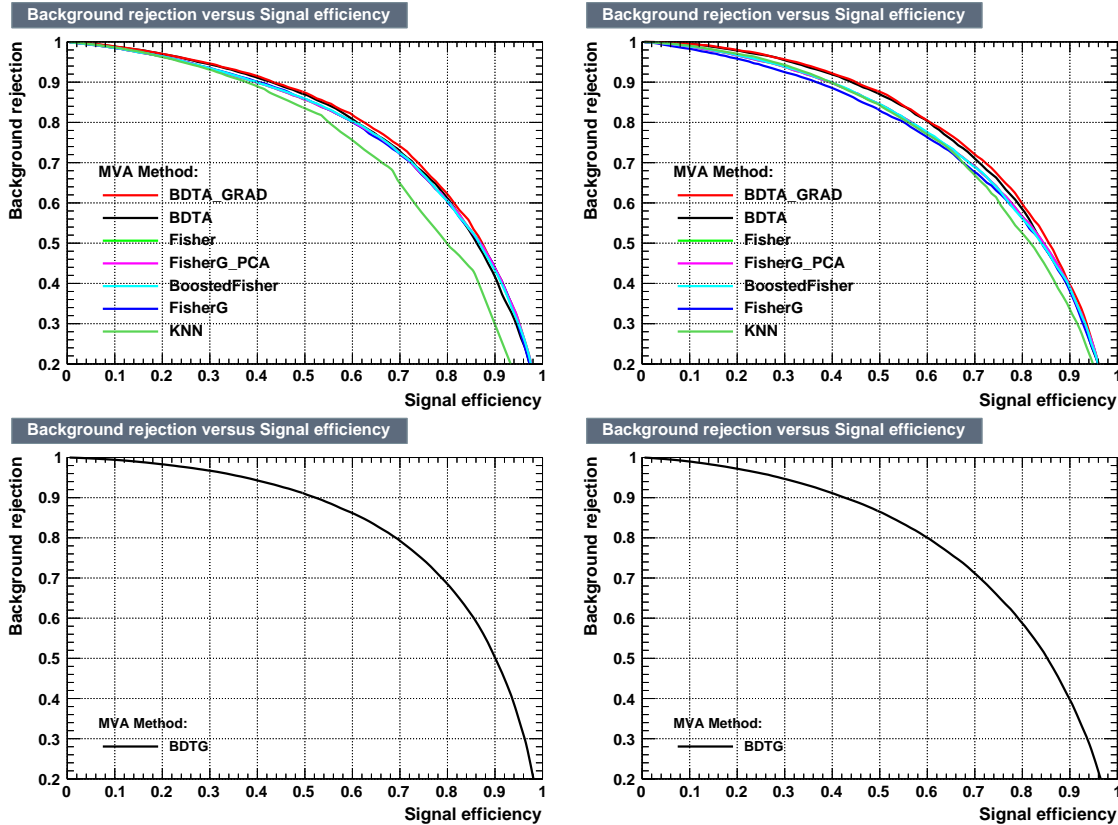


**Figure 6.12:** Top: Background rejection vs signal efficiency (ROC curves) for various MVA classifiers in the  $3l$  channel for training against  $t\bar{V}$  (left) and  $t\bar{t}$  (right). Bottom: background rejection vs signal efficiency (ROC curve) in the  $2lss$  channel for a single discriminator: BDTG, against  $t\bar{V}$  (left) and  $t\bar{t}$  (right).

## 2825 6.8.2 Discriminating variables

2826 The classifier chosen to separate the  $tHq$  signal from the main backgrounds is the  
 2827 BDTG classifier, trained on simulated signal and background events. The samples  
 2828 used in the training are the  $tHq$  sample in Table 6.2, the samples in the third section  
 2829 of table A.4 and the samples marked with an \* in the same table.

2830 As explained in Section 5.1.1, a set of discriminating variables are given as input to  
 2831 the BDTG which combines the individual discrimination power of each input variable  
 2832 to produce a discriminator with the maximum discrimination power. Table 6.7 lists  
 2833 the input variables used in the BDTG trainings for this analysis.

2834     The same set of input variables was used to produce the plots for MVA classifiers  
 2835    evaluation.

Variable name	Description
nJet25	Number of jets with $p_T > 25$ GeV, $ \eta  < 2.4$
nJetEta1	Number of jets with $ \eta  > 1.0$ , non-CSV-loose
MaxEtaJet25	Max. $ \eta $ of any (non-CSV-loose) jet with $p_T > 25$ GeV
detaFwdJetClosestLep	$\Delta\eta$ forward light jet and closest lepton
detaFwdJetBJet	$\Delta\eta$ forward light jet and hardest CSV loose jet
detaFwdJet2BJet	$\Delta\eta$ forward light jet and second hardest CSV loose jet
Lep3Pt/Lep2Pt	$p_T$ of the 3 <sup>rd</sup> lepton (2 <sup>nd</sup> for ss2l)
totCharge	Sum of lepton charges
minDRll	Min $\Delta R$ any two leptons
dphiHighestPtSSPair	$\Delta\phi$ of highest $p_T$ same-sign lepton pair

**Table 6.7:** BDTG input variables. First section lists variables related to jet multiplicities; second section lists variables related to forward jet activity, and third section lists variables related to lepton kinematics.

2836     Plots in Figure 6.13 shows the BDTG input variables distributions for the signal  
 2837    and background samples, in the 3*l* channels.

2838     All the input variables have some discrimination power, however, that power is  
 2839    bigger for some of them; for instance, the third lepton  $p_T$  plot (top left in Figure 6.13)  
 2840    shows some discrimination power against WZ and VVV backgrounds for which there  
 2841    is a peak around 30 GeV while  $tHq$  peak around 18 GeV; although the discrimination  
 2842    power does not cover all the backgrounds, it counts for the final discriminator. A  
 2843    similar situation can be seen in the plot for the number of jets (row three, column two);  
 2844     $t\bar{t}W$ ,  $t\bar{t}Z$  and  $t\bar{t}H$  processes tend to have more jets compared to the  $tHq$  process. The  
 2845    discrimination power is more evident in other plots like in the plot of the maximum  
 2846     $|\eta|$  of the jets in the event (row two, column three). The same or equivalent input  
 2847    variables are found to be performing well for both 3*l* and 2*lss* channels. Figure B.1  
 2848    shows the corresponding input variables distribution plots for the 2*lss* channel.

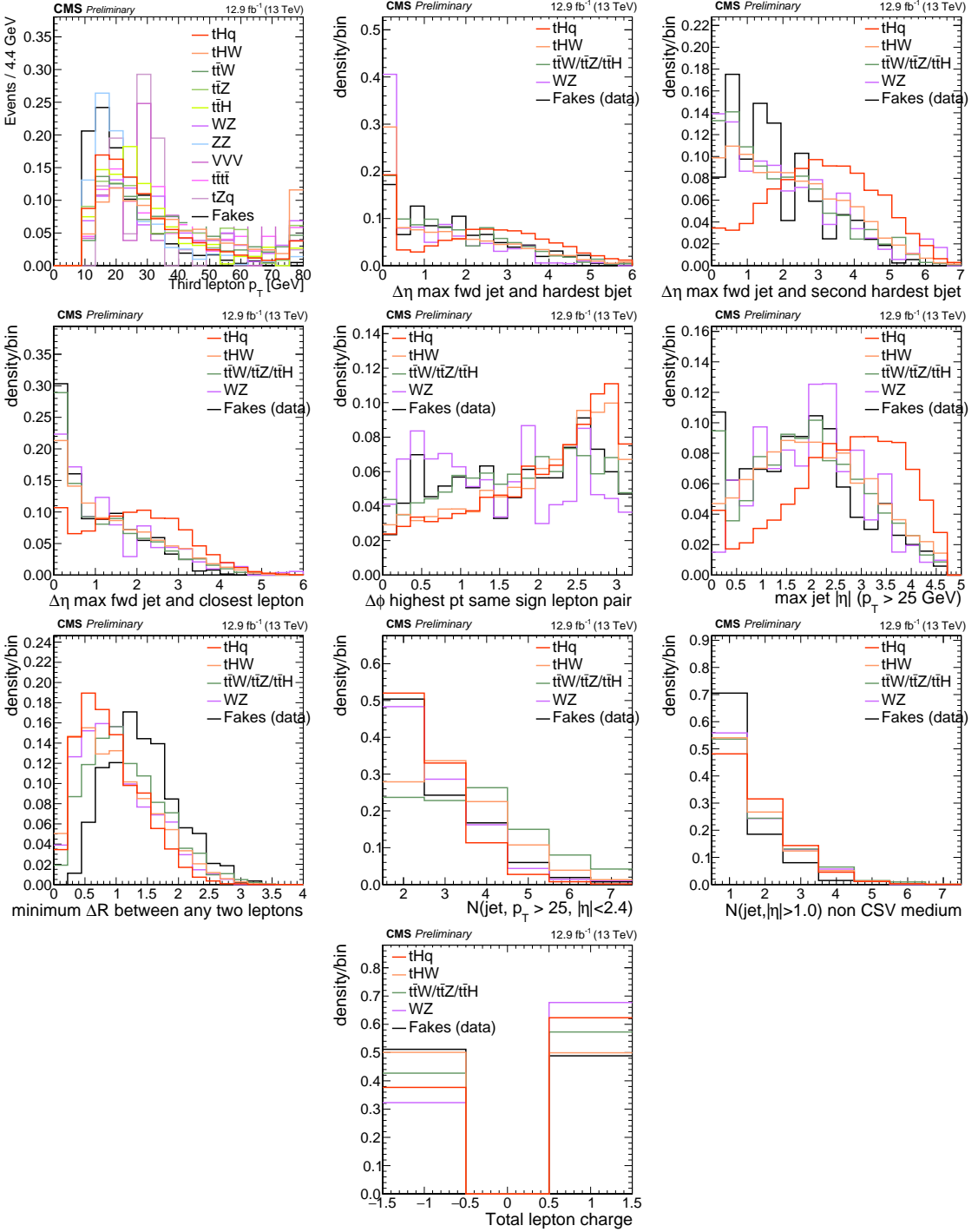


**Figure 6.13:** Distributions of the BDTG classifier input variables (not normalized) for signal discrimination in the  $3l$  channel.

2849 **Discrimination power from BDTG classifier**

2850 The Discrimination power of the input variables can also be evaluated from the BDTG  
 2851 training, exclusively for the training samples, i.e., dominant backgrounds ( $t\bar{t}$  and  $t\bar{t}V$ );  
 2852 the training samples are submitted to the selection cuts on Table 6.6.

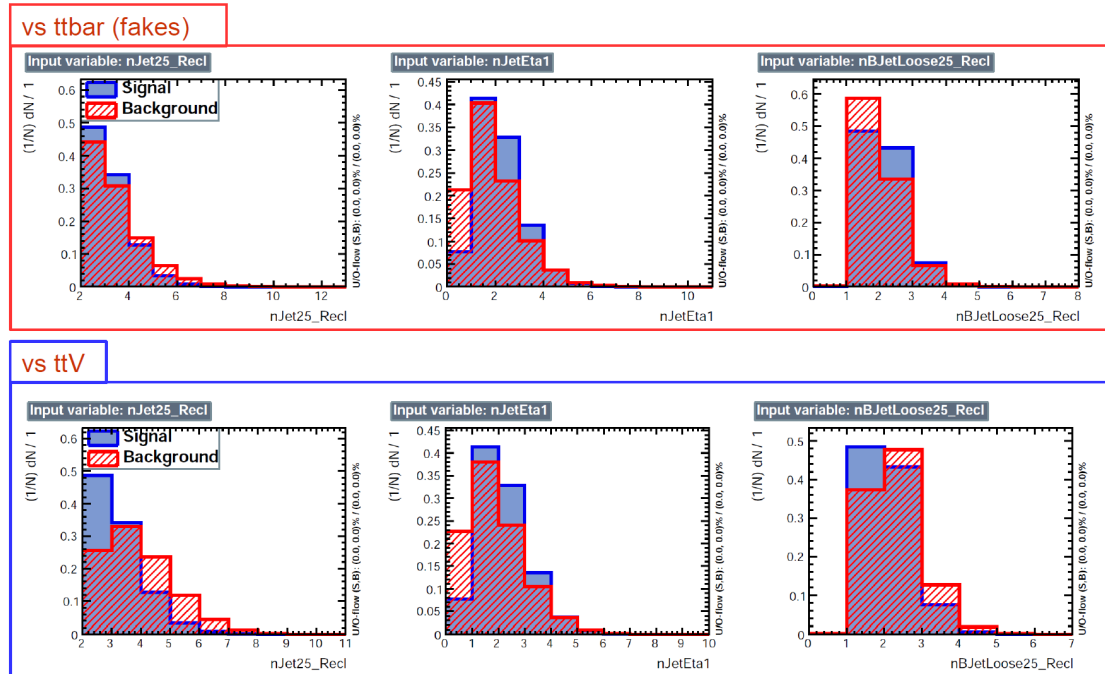


**Figure 6.14:** BDT input variables as seen by BDTG classifier for the  $3l$  channel,  $tHq$  signal(blue) discriminated against  $t\bar{t}V$  background (red).

2853 Figure 6.14 shows the comparison between input variables for the two trainings  
 2854 in the  $3l$  channel; it reveals that some variables show opposite behavior for the two  
 2855 background sources, which results in potentially screening the discrimination power  
 2856 if they were to be used in a single discriminant, i.e., if the training would join  $t\bar{t}$  and  
 2857  $t\bar{t}V$ . For some other variables the distributions are similar in both background cases.  
 2858 In contrast to the distributions in Figure 6.13 only the dominant backgrounds are  
 2859 included; however, the discrimination power agrees among plots.

Figures B.2, B.3, B.4, and B.5 show the input variables distributions for the  $2lss$  and  $3l$  channel as seen by the BDTG classifier.

## Input variables correlations

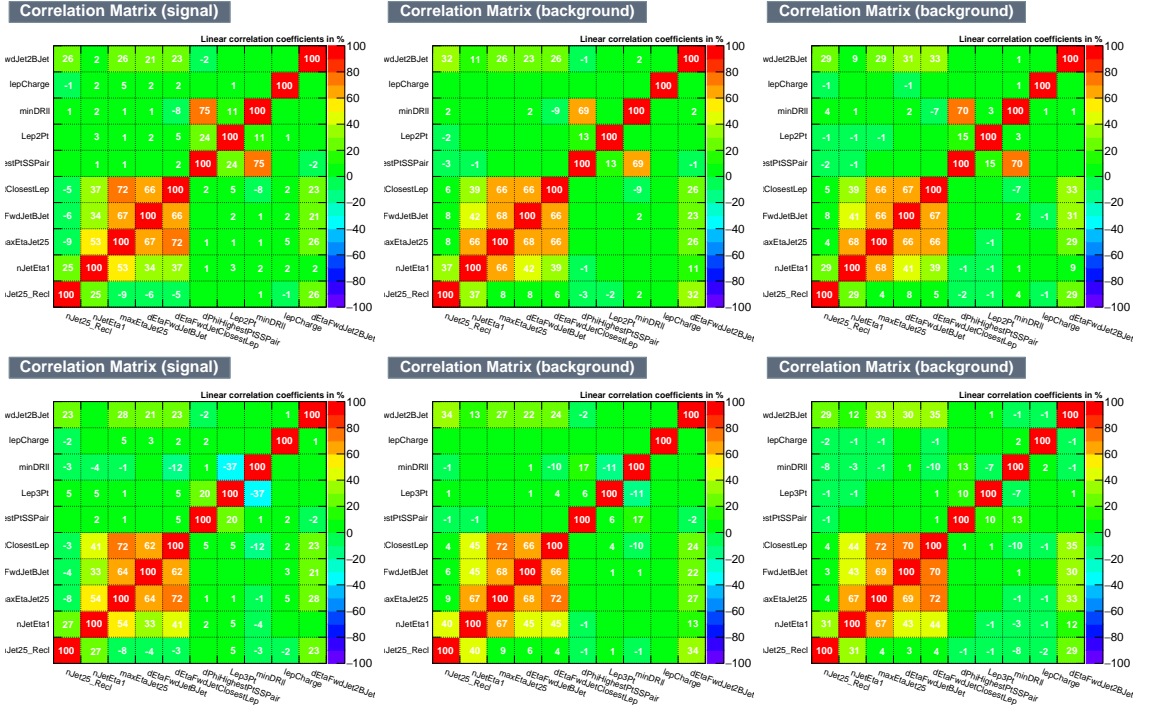


**Figure 6.15:** Signal (left),  $t\bar{t}$  background (middle), and  $t\bar{t}V$  background (right.) correlation matrices for the input variables in the BDTG classifier for the  $2lss$  (top) and  $3l$  (bottom) channels.

From Table 6.7, it is clear that the input variables are correlated to some extend. These correlations play an important role for some MVA methods like the Fisher discriminant method in which the first step consist of performing a linear transformation to an phase space where the correlations between variables are removed. In the case of BDT, correlations do not affect the performance. Figure 6.15 shows the linear correlation coefficients for signal and background for the two training cases (the signal values are identical by construction). As expected, strong correlations appears for variables related to the forward jet activity.

### 2871 6.8.3 BDTG classifiers response

2872 After the training stage, the BDTG classifier is tested to ensure its ability to discrim-  
 2873 inate between simulated signal and background events. The BDTG classifier output  
 2874 distributions for signal and backgrounds in the  $3l$  channel are shown in Figure 6.16.  
 2875 As expected, a good discrimination power is obtained using default discriminator  
 2876 parameter values; some overtraining is also visible.

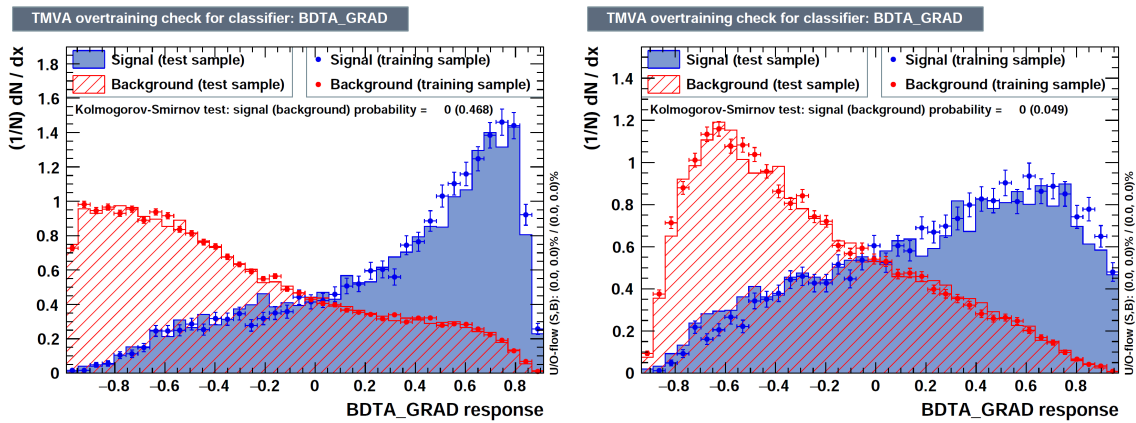


**Figure 6.16:** BDTG classifier output for trainings against  $t\bar{t}V$ (left) and  $t\bar{t}$  (right). Default BDTG parameters have been used.

2877 In order to explore further optimization in the BDTG performance, several changes  
 2878 from the default BDTG parameters were tested; Table 6.8 list the set of parameters  
 2879 found to be most discriminant with minimal overtraining as shown in Figure 6.17.

TMVA.Types.kBDT		
Option	Default	Used
NTrees	200	800
BoostType	AdaBoost	Grad
Shrinkage	1	0.1
nCuts	20	50
MaxDepth	3	

**Table 6.8:** Configuration used in the final BDTG training. Parameters not listed were not tested.

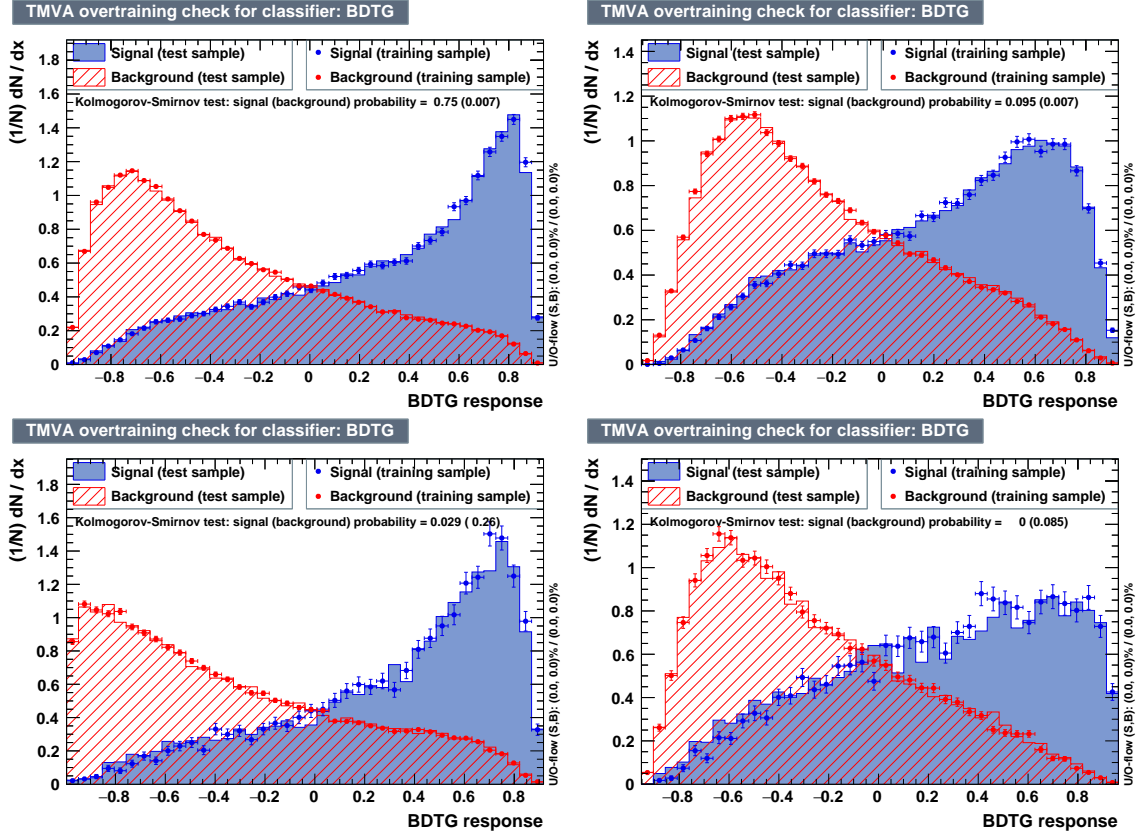


**Figure 6.17:** BDTG classifiers output for training against  $t\bar{t}V$ (left) and  $t\bar{t}$  (right) for  $2lss$  channel(top) and  $3l$  channel (bottom) .

2lss channel		3l channel	
Rank	$t\bar{t}$ training Variable	$t\bar{t}V$ training Variable	$t\bar{t}$ training Variable
1	minDRll	dEtaFwdJetBJet	dEtaFwdJetClosestLep
2	dEtaFwdJetClosestLep	Lep3Pt	minDRll
3	dEtaFwdJetBJet	maxEtaJet25	maxEtaJet25
4	dPhiHighestPtSSPair	dEtaFwdJet2BJet	dPhiHighestPtSSPair
5	Lep3Pt	dEtaFwdJetClosestLep	Lep2Pt
6	maxEtaJet25	minDRll	dEtaFwdJetClosestLep
7	dEtaFwdJet2BJet	dPhiHighestPtSSPair	dEtaFwdJet2BJet
8	nJetEta1	nJet25	nJetEta1
9	nJet25	nJetEta1	nJet25
10	lepCharge	lepCharge	lepCharge

**Table 6.9:** Input variables ranking for BDTG classifiers for the trainings in the  $3l$  channel and  $2lss$  channel. In both trainings the rankings show almost the same 5 variables in the first places.

2880        The ranking of the input variables by their importance in the classification process  
 2881    is shown in Table 6.9; for both trainings the rankings show almost the same 5 variables  
 2882    in the first places.

2883    **6.8.4 Additional discriminating variables**

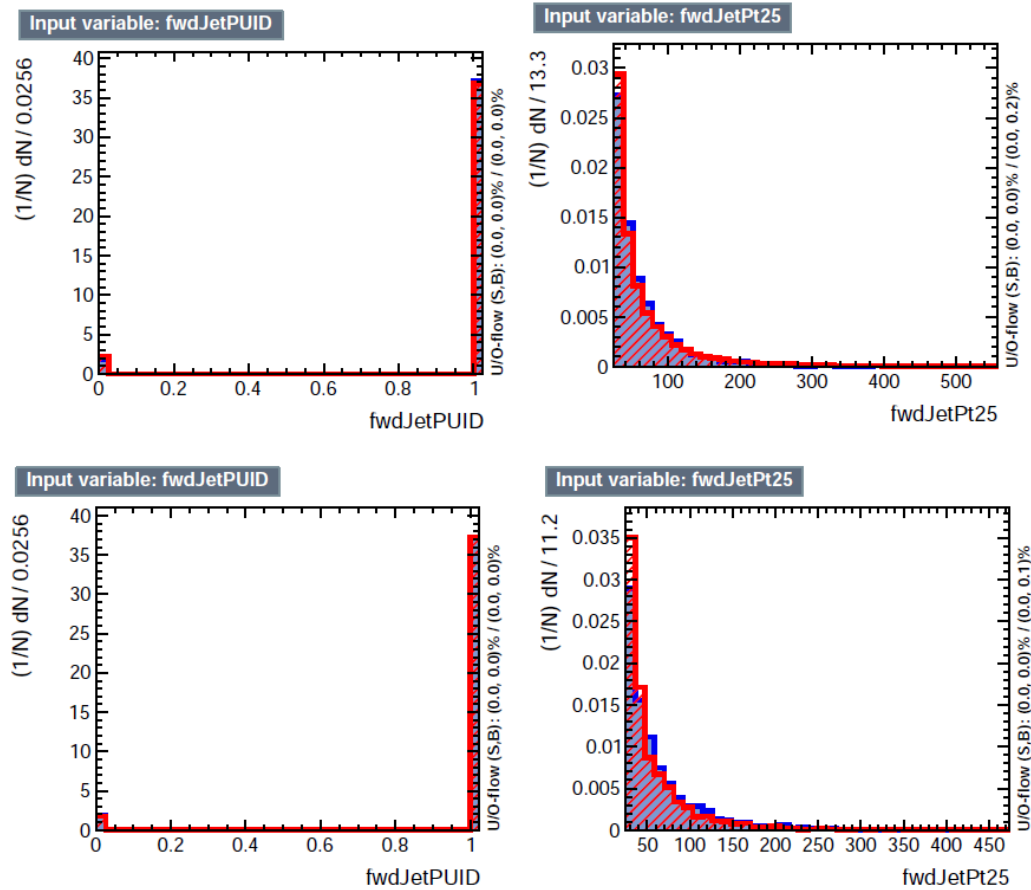


**Figure 6.18:** Additional discriminating variables distributions for  $t\bar{t}V$  training (top row) and  $t\bar{t}$  training (bottom row) in the  $3l$  channel. The origin of the jets in the forward jet identification distribution is tagged as 0 for *pileup jets* while *primary vertex jets* are tagged as 1.

2884        Given that the forward jet in background processes could be originated from  
 2885    pileup, two additional discriminating variables accounting for that were tested. These  
 2886    additional variables describe the forward jet momentum ( $fwdJetPt25$ ) and the forward

jet identification(fwdJetPUID); their distributions in the  $3l$  channel are shown in Figure 6.18. The forward jet identification distribution show that for both, signal and background, jets are mostly originated in the primary vertex.

The testing was performed by including in the BDTG input one variable at a time, so the discrimination power of each variable can be evaluated individually, and then both simultaneously. fwdJetPUID was ranked in the last place in importance (11) in both training ( $t\bar{t}V$  and  $t\bar{t}$ ) while fwdJetPt25 was ranked 3 in the  $t\bar{t}V$  training and 7 in the  $t\bar{t}$  training. When training using 12 variables, fwdJetPt25 was ranked 5 and 7 in the  $t\bar{t}V$  and  $t\bar{t}$  trainings respectively, while fwdJetPUID was ranked 12 in both cases.

	ROC-integral	
	$t\bar{t}V$	$t\bar{t}$
base 10 var	0.848	0.777
+ fwdJetPUID	0.849	0.777
+ fwdJetPt25	0.856	0.787
12 var	0.856	0.787

**Table 6.10:** ROC-integral for all the testing cases performed in the evaluation of the additional variables discriminating power. The improvement in the discrimination performance provided by the additional variables is about 1% .

The improvement in the discrimination performance provided by the additional variables is about 1%, so it was decided not to include them in the procedure. Table 6.10 show the ROC-integral for all the testing cases performed.

### 6.8.5 Signal extraction procedure

The two BDT classifiers introduced in the previous section, trained against the dominant  $t\bar{t}$  and  $t\bar{t}V$  backgrounds in each channel, are used to evaluate the limits in a fit to the classifier shape. Figure ?? shows the expected output distributions in a 2D plane of one training vs. the other. Each event is now classified into one of ten 2D-bins according to its position in the plane, see Fig. 6.20. The number of bins is chosen

2905 such that no bins are entirely empty for any process. The bin boundary positions  
 2906 have been studied and optimized with respect to the expected limit, see Sec. 6.8.6.

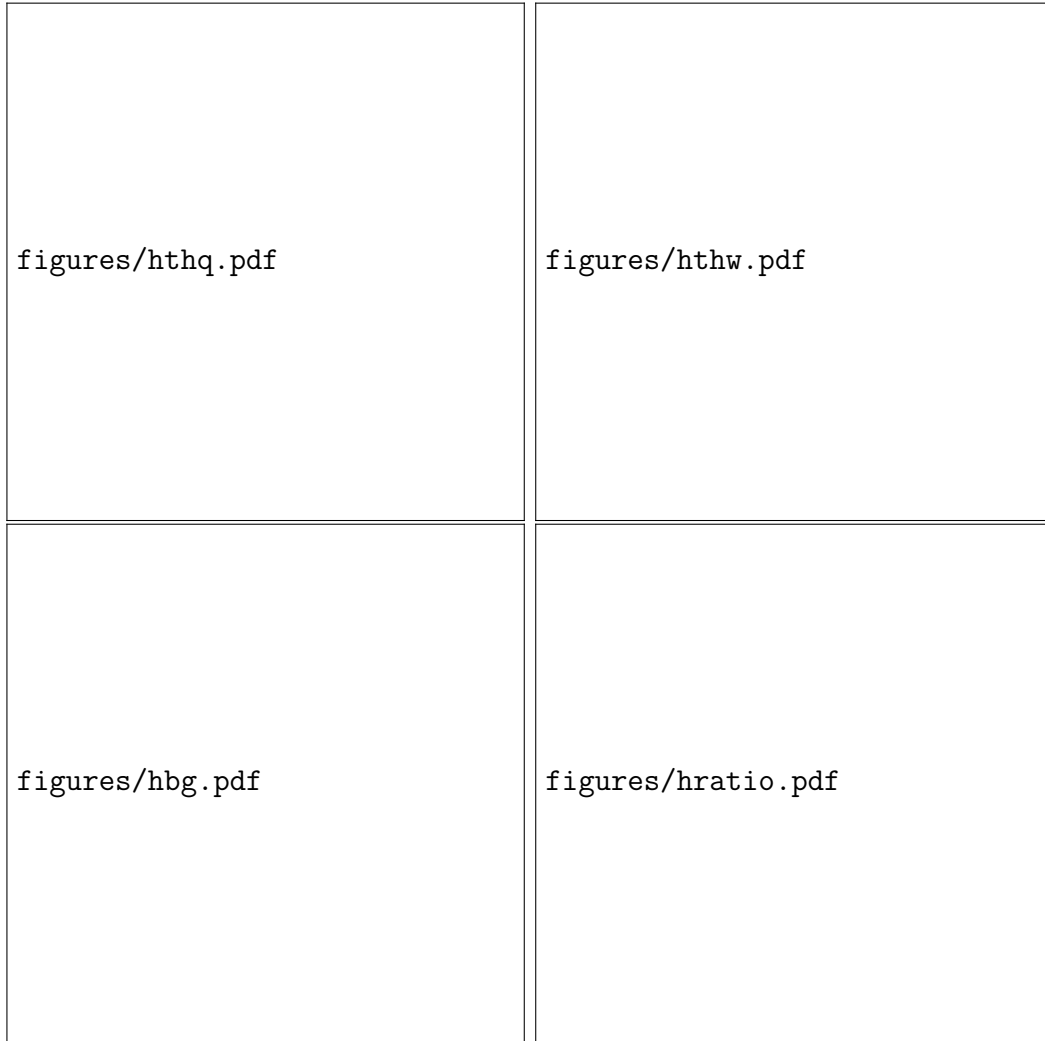


**Figure 6.19:** BDT classifier output planes (training vs  $t\bar{t}$  on x-axis and vs  $t\bar{t}V$  on y-axis) for the  $tHq$  and  $tHW$  signals (top row), and for the combined backgrounds (bottom left). Backgrounds are evaluated as in the final background prediction, i.e. these are not the samples used in the MVA training and this includes data-driven backgrounds. Bottom right shows the S/B ratio (combining  $tHq$  and  $tHW$ ) in the same plane. Three lepton channel only.

2907 From this event categorization, a 1D histogram of expected distribution is pro-  
 2908 duced for each signal and background process, and fit to the observed data (or the  
 2909 Asimov dataset for expected limits).



**Figure 6.20:** Binning overlaid on the S/B ratio map on the plane of classifier outputs.

### 2910 6.8.6 Binning and selection optimization

2911 Note that the numbers in this subsection are upper limits on the  $tHq + tHW$  cross  
 2912 sections only (without  $t\bar{t}H$ ), and are always evaluated at  $\kappa_t = -1.0$ ,  $\kappa_V = 1.0$ .  
 2913 The effect on the cross section limit of the choice of pre-selection cuts is evaluated

2914 by varying the most important cuts and re-calculating the limit (in the three lepton  
 2915 channel) in each case. Table 6.11 shows the several variations made, compared to a  
 2916 baseline corresponding to the selection reported in Tab. ??, but with only a loose CSV  
 2917 jet and a veto of  $\pm 10$ . The optimal limit is found when requiring a slightly tighter  
 2918 selection with respect to the baseline. This is the selection reported in Tab. ??.

2919 The obtained cross section limit also depends on the chosen binning in the 2D

Selection	Variation	Expected limit
Baseline	see Tab. ??	< 2.93
Loose CSV tags	$\geq 1 \rightarrow \geq 2$	< 3.81
Medium CSV tags	$\geq 0 \rightarrow \geq 1$	< 2.76
Light forward jet $\eta$	$\geq 0 \rightarrow \geq 1$	< 2.94
Light forward jet $\eta$	$\geq 0 \rightarrow \geq 1.5$	< 3.00
$> 30$		< 2.91
veto ( $ m_{\ell\ell} - m_j $ )	$> 10 \rightarrow > 15$	< 2.79
One medium CSV + 15 veto	combined	< 2.62

**Table 6.11:** Limit variation as a function of tighter cuts. The baseline selection corresponds to a looser selection as the one reported in Tab. ?? (which is the optimal selection determined here (last line)), where only a CSV-loose -tagged jet is required, and the veto is loosened to  $\pm 10$ .

2920 plane as the S/B ratio varies across the plane, hence several sizes and binning com-  
 2921 bination were tested in order to optimize the limit. Figure 6.21 show some of the  
 2922 binning combinations tested; in the default combination all the bins have the same  
 2923 size, while the best limit was found for a set of 10 bins.

2924 The bins borders and the resulting cross section limits are shown in Tab. 6.12:

Number of bins	Bin borders						Expected limit
	$x_1$	$x_2$	$x_3$	$y_1$	$y_2$	$y_3$	
16 (default)	-0.5	0.0	0.5	-0.5	0.0	0.5	< 2.91
16	-0.5	0.3	0.7	-0.5	0.3	0.7	< 2.83
10	-0.5	0.0	0.5	-0.5	0.0	0.5	< 2.93
10	-0.5	0.0	0.7	-0.5	0.0	0.7	< 2.86
10	-0.5	0.0	0.7	-0.5	0.0	0.5	< 2.84
10	-0.5	0.0	0.5	-0.5	0.0	0.7	< 2.87
<b>10</b>	<b>-0.5</b>	<b>0.4</b>	<b>0.7</b>	<b>-0.5</b>	<b>0.4</b>	<b>0.7</b>	<b>&lt; 2.81</b>

**Table 6.12:** Limit variation as a function of bin size in the three lepton channel. (In bold: the final bin borders used in the analysis.)

2925 Combining the optimization of binning and using the tighter pre-selection cuts,  
 2926 the expected limit in the three lepton channel alone reaches  $r < 2.59$ .

2927 For same-sign dilepton channel, other binning combinations were also tested. First  
 2928 the three lepton binning was used to estimate the expected limit then bin borders were



figures/bin\_scheme.pdf

**Figure 6.21:** Binning combination scheme.

2929 varied to obtain the best possible expected limit. The bin borders and the resulting  
2930 cross section limits for the same-sign dimuon channel are shown in Tab. 6.13:  
2931 The expected limit was found to be  $r < 1.69$  for optimized bin borders in 10 bins.

Number of bins	Bin borders						Expected limit
	$x_1$	$x_2$	$x_3$	$y_1$	$y_2$	$y_3$	
16	-0.5	0.4	0.7	-0.5	0.4	0.7	< 1.72
12	-0.5	0.4	0.7	-0.5	0.4	0.7	< 1.72
12	-0.3	0.4	0.7	-0.5	0.4	0.7	< 1.71
12	-0.3	0.3	0.7	-0.5	0.4	0.7	< 1.71
12	-0.3	0.3	0.7	-0.4	0.4	0.7	< 1.70
12	-0.3	0.3	0.7	-0.3	0.4	0.7	< 1.70
12	-0.3	0.3	0.7	-0.3	0.2	0.7	< 1.68
12	-0.3	0.3	0.7	-0.3	0.1	0.7	< 1.70
12	-0.3	0.3	0.7	-0.3	0.2	0.6	< 1.70
10	-0.5	0.4	0.7	-0.5	0.4	0.7	< 1.75
<b>10</b>	<b>-0.3</b>	<b>0.3</b>	<b>0.7</b>	<b>-0.3</b>	<b>0.2</b>	<b>0.6</b>	<b>&lt; 1.69</b>

**Table 6.13:** Limit variation as a function of bin size in the same-sign dimuon channel. (In bold: the final bin borders used in the analysis.)

### 2932 6.8.7 Other binning strategies

2933 Two further strategies of clustering regions in the 2D plane of  $BDT_{tt}$  vs  $BDT_{t\bar{t}V}$   
 2934 into bins were attempted, following studies done in the  $t\bar{t}H$  multilepton analysis (and  
 2935 documented in greater detail in [149]).

2936 **Clustering by S/B ratio** The 2D plane is clustered into a given number of bins  
 2937 corresponding to regions where S/B is within a certain range. The bin borders are  
 2938 determined such that the number of background events in each bin is approximately  
 2939 equal. (See Sec. 5.3 in v4 of Ref. [149] for more details.) The resulting regions for  
 2940 same-sign dilepton and three lepton events are shown in Fig. 6.22, with the expected  
 2941 distribution of signal and main backgrounds in Fig. 6.23.

2942 Using this technique, the resulting limits (for the  $\kappa_t = -1, \kappa_V = 1$  scenario) are  
 2943 about 20% worse than with the binnings described above:  $\mu^\pm\mu^\pm$  changed from 1.82  
 2944 to 2.15,  $\ell\ell\ell$  from 1.52 to 1.75.

2945  **$k$ -Means geometric clustering** A second clustering strategy employs a recur-  
 2946 sive application of the  $k$ -means algorithm (see Appendix D in v4 of Ref. [149]) to

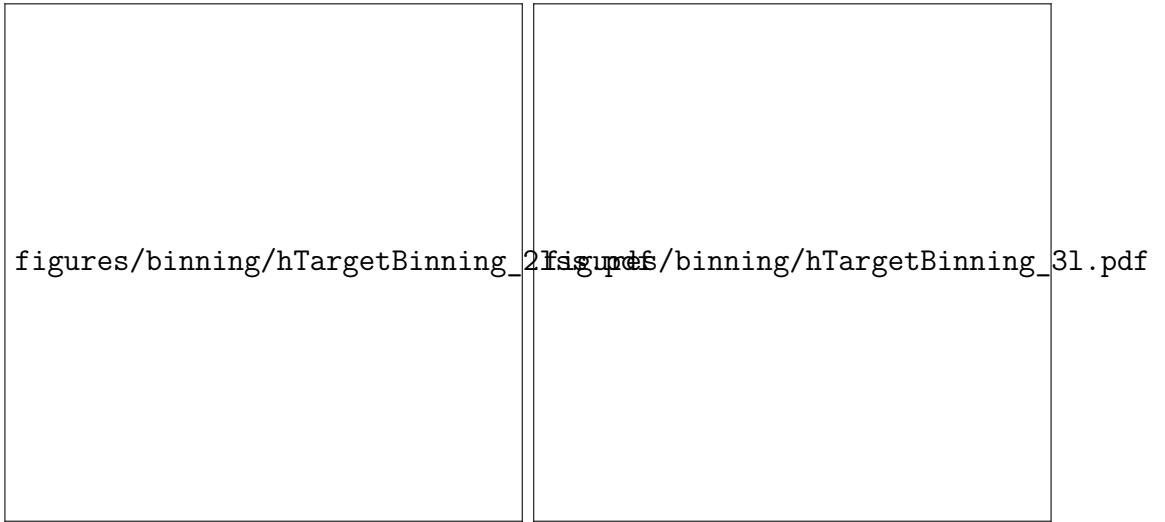


**Figure 6.22:** Binning by S/B regions for same-sign dilepton (left) and three leptons (right).



**Figure 6.23:** Final bins (corresponding to S/B regions in the 2D plane) for same-sign dilepton (left) and three leptons (right).

2947 separate the 2D plane into geometric regions. The resulting clustering (using the  
 2948  $t\bar{t}H$  multilepton code on  $tHq$  signal and  $t\bar{t}$  and  $t\bar{t}V$  background events) are shown in  
 2949 Fig. 6.24. The expected distribution of events for the signal and main background in  
 2950 these bins is shown in Fig. 6.25.

2951 Similarly to the S/B ratio binning, the limits using the  $k$ -means clustering are  
 2952 significantly worse than those of the bins described before. In the  $\mu^\pm\mu^\pm$  channel, the

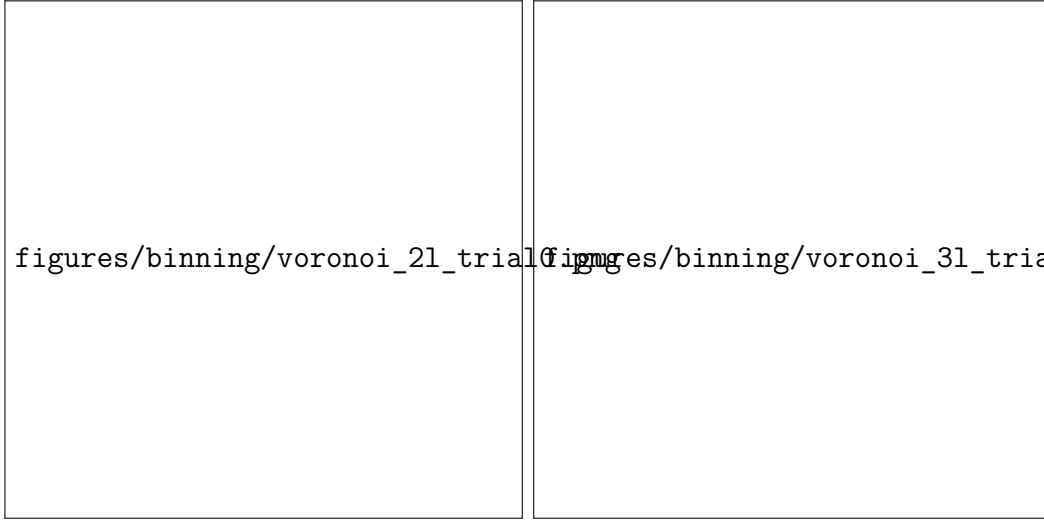


**Figure 6.24:** Binning into geometric regions using a  $k$ -means algorithm for same-sign dilepton (left) and three leptons (right).



**Figure 6.25:** Final bins using a  $k$ -means algorithm for same-sign dilepton (left) and three leptons (right). Note that the bin numbering here is such that signal-like bins are lower.

2953 limit deteriorates from 1.82 to 2.05, whereas in  $\ell\ell\ell$  it changes from 1.58 to 1.78.

### 2954 6.8.8 Signal model

2955 The goal of this analysis is to test the compatibility of points in the parameter space of  
 2956 Higgs-to-vector boson and Higgs-to-top quark couplings. The simulated  $tHq$ ,  $tHW$ ,

and  $t\bar{t}H$  signal events are used with event-by-event weights to reflect the impact of the couplings on kinematic distributions, and together with different predictions of the respective production cross sections and branching ratios, we can produce limits for different values of  $\kappa_V$  and  $\kappa_t$ . (See Tab. A.3 for the set of  $\kappa_t$  and  $\kappa_V$  values generated.) The slight shape-dependence of the BDT outputs as a function of the couplings is documented in App. ??.

Apart from the  $\kappa_t/\kappa_V$  interference of the  $tHq$  and  $tHW$  production cross sections, the cross section of  $t\bar{t}H$  scales as  $\kappa_t^2$ . Furthermore, the Higgs branching fractions to vector bosons depend on  $\kappa_V$ , and the overall Higgs decay width depend both on  $\kappa_t$  and  $\kappa_V$  when considering resolved top-quark loops in the  $\rightarrow \gamma\gamma$ ,  $\rightarrow \gamma$ , and  $\rightarrow$  decays. The relative contributions from  $\rightarrow WW$ ,  $\rightarrow ZZ$ , and  $\rightarrow \tau\tau$  changes with changing  $\kappa_V$ .

We hence set an upper limit on the combined cross section times branching ratio of  $tHq$ ,  $tHW$ , and  $t\bar{t}H$ .

If we assume a modifier for the Higgs-to-tau coupling ( $\kappa_\tau$ ) to be equal to  $\kappa_t$ , the relative fractions of  $WW$ ,  $ZZ$ , and  $\tau\tau$  in our selection will only depend on the ratio of  $\kappa_t/\kappa_V$ . Any limit set at any given value of  $\kappa_t/\kappa_V$  is thus valid for all values of  $\kappa_t$  and  $\kappa_V$  with that ratio, and could then be compared with theoretical predictions of cross sections at different values of either modifier. Rather than as a function of the  $\kappa_t/\kappa_V$  ratio, limits could (equivalently) be reported as a function of the relative strength of Higgs-top and Higgs-vector-boson couplings, multiplied by the relative sign. Such a parameter, further referred to as  $f_t$ , as defined in Eq. 6.7, spans the entire possible parameter space between  $-1.0$  and  $1.0$ , with the SM expectation at  $0.5$ . Absolute values of  $1.0$  or  $0.0$  would then correspond to purely Higgs-top and purely Higgs-V

2981    couplings, respectively.

$$f_t = \text{sign}(\kappa_t/\kappa_V) \times \frac{\kappa_t^2}{\kappa_t^2 + \kappa_V^2}. \quad (6.7)$$

2982    Table 6.14 shows the points in the  $\kappa_t/\kappa_V$  and  $f_t$  parameter space that are mapped  
2983    by the 51 individual  $\kappa_t$  and  $\kappa_V$  points.

2984    The overall higgs decay width (modified by both  $\kappa_t$  and  $\kappa_V$ ) becomes irrelevant  
2985    if limits are quoted as absolute cross sections rather than multiples of the expected  
2986    cross section (which depends on the overall Higgs decay width).

2987    The 1D histograms of events as categorized in regions of the 2D BDT plane is  
2988    then used in a maximum likelihood fit of signal and background shapes, where the  
2989     $tHq$ ,  $tHW$ , and  $t\bar{t}H$  signals are floating with a common signal strength modifier  $r$ ,  
2990    producing a 95% C.L. upper limit the observed cross section of  $tHq + tHW + t\bar{t}H$ .

2991    This is done separately for each point of  $\kappa_t$  and  $\kappa_V$ , where the cross sections and  
2992    branching fractions are scaled accordingly in each point. Limits at fixed values of  
2993     $\kappa_t/\kappa_V$  are by construction identical. Tables ??–?? and ??–?? in Appendix ?? show  
2994    the scalings of cross section times branching fraction, as well as branching fractions  
2995    alone for each of the Higgs decay modes and each of the signal components.

$f_t$	$\kappa_t/\kappa_V$	$\kappa_V = 0.5$	$\kappa_V = 1.0$	$\kappa_V = 1.5$
-0.973	-6.000	-3.00		
-0.941	-4.000	-2.00		
-0.900	-3.000	-1.50	-3.00	
-0.862	-2.500	-1.25		
-0.800	-2.000	-1.00	-2.00	-3.00
-0.692	-1.500	-0.75	-1.50	
-0.640	-1.333			-2.00
-0.610	-1.250		-1.25	
-0.500	-1.000	-0.50	-1.00	-1.50
-0.410	-0.833			-1.25
-0.360	-0.750		-0.75	
-0.308	-0.667			-1.00
-0.200	-0.500	-0.25	-0.50	-0.75
-0.100	-0.333			-0.50
-0.059	-0.250		-0.25	
-0.027	-0.167			-0.25
0.000	0.000	0.00	0.00	0.00
0.027	0.167			0.25
0.059	0.250		0.25	
0.100	0.333			0.50
0.200	0.500	0.25	0.50	0.75
0.308	0.667			1.00
0.360	0.750		0.75	
0.410	0.833			1.25
0.500	1.000	0.50	1.00	1.50
0.610	1.250		1.25	
0.640	1.333			2.00
0.692	1.500	0.75	1.50	
0.800	2.000	1.00	2.00	3.00
0.862	2.500	1.25		
0.900	3.000	1.50	3.00	
0.941	4.000	2.00		
0.973	6.000	3.00		

**Table 6.14:** The 33 distinct values of  $\kappa_t/\kappa_V$  and  $f_t$  as mapped by the 51  $\kappa_t$  and  $\kappa_V$  points.

<sup>2996</sup> **Appendix A**

<sup>2997</sup> **Datasets and triggers**

Dataset name
/JetHT/Run2016X-23Sep2016-vY/MINIAOD
/HTMHT/Run2016X-23Sep2016-vY/MINIAOD
/MET/Run2016X-23Sep2016-vY/MINIAOD
/SingleElectron/Run2016X-23Sep2016-vY/MINIAOD
/SingleMuon/Run2016X-23Sep2016-vY/MINIAOD
/SinglePhoton/Run2016X-23Sep2016-vY/MINIAOD
/DoubleEG/Run2016X-23Sep2016-vY/MINIAOD
/MuonEG/Run2016X-23Sep2016-vY/MINIAOD
/DoubleMuon/Run2016X-23Sep2016-vY/MINIAOD
/Tau/Run2016B-23Sep2016-v3/MINIAOD
/JetHT/Run2016H-PromptReco-v3/MINIAOD
/HTMHT/Run2016H-PromptReco-v3/MINIAOD
/MET/Run2016H-PromptReco-v3/MINIAOD
/SingleElectron/Run2016H-PromptReco-v3/MINIAOD
/SingleMuon/Run2016H-PromptReco-v3/MINIAOD
/SinglePhoton/Run2016H-PromptReco-v3/MINIAOD
/DoubleEG/Run2016H-PromptReco-v3/MINIAOD
/MuonEG/Run2016H-PromptReco-v3/MINIAOD
/DoubleMuon/Run2016H-PromptReco-v3/MINIAOD

**Table A.1:** Full 2016 dataset used in the analysis. In the first section of the table are listed the 23Sep2016 samples; in the Run2016X-23Sep-vY label, X:B-G tag the run while Y:1,3 tag the version of the data sample. Second section list the PromptReco version of the dataset.

Same-sign dilepton (==2 muons)
HLT_Mu17_TrkIsoVVL_Mu8_TrkIsoVVL_DZ_v*
HLT_Mu17_TrkIsoVVL_TkMu8_TrkIsoVVL_DZ_v*
HLT_IsoMu22_v*
HLT_IsoTkMu22_v*
HLT_IsoMu22_eta2p1_v*
HLT_IsoTkMu22_eta2p1_v*
HLT_IsoMu24_v*
HLT_IsoTkMu24_v*
Same-sign dilepton (==2 electrons)
HLT_Ele23_Ele12_CaloIdL_TrackIdL_IsoVL_DZ_v*
HLT_Ele27_eta2p1_WP Loose_Gsf_v*
HLT_Ele27_WPTight_Gsf_v*
HLT_Ele25_eta2p1_WPTight_Gsf_v*
Same-sign dilepton (==1 muon, ==1 electron)
HLT_Mu23_TrkIsoVVL_Ele8_CaloIdL_TrackIdL_IsoVL_v*
HLT_Mu8_TrkIsoVVL_Ele23_CaloIdL_TrackIdL_IsoVL_v*
HLT_Mu23_TrkIsoVVL_Ele8_CaloIdL_TrackIdL_IsoVL_DZ_v*
HLT_Mu8_TrkIsoVVL_Ele23_CaloIdL_TrackIdL_IsoVL_DZ_v*
HLT_IsoMu22_v*
HLT_IsoTkMu22_v*
HLT_IsoMu22_eta2p1_v*
HLT_IsoTkMu22_eta2p1_v*
HLT_IsoMu24_v*
HLT_IsoTkMu24_v*
HLT_Ele27_WPTight_Gsf_v*
HLT_Ele25_eta2p1_WPTight_Gsf_v*
HLT_Ele27_eta2p1_WP Loose_Gsf_v*
Three lepton
HLT_DiMu9_Ele9_CaloIdL_TrackIdL_v*
HLT_Mu8_DiEle12_CaloIdL_TrackIdL_v*
HLT_TripleMu_12_10_5_v*
HLT_Ele16_Ele12_Ele8_CaloIdL_TrackIdL_v*
HLT_Mu23_TrkIsoVVL_Ele8_CaloIdL_TrackIdL_IsoVL_v*
HLT_Mu23_TrkIsoVVL_Ele8_CaloIdL_TrackIdL_IsoVL_DZ_v*
HLT_Mu8_TrkIsoVVL_Ele23_CaloIdL_TrackIdL_IsoVL_v*
HLT_Mu8_TrkIsoVVL_Ele23_CaloIdL_TrackIdL_IsoVL_DZ_v*
HLT_Ele23_Ele12_CaloIdL_TrackIdL_IsoVL_DZ_v*
HLT_Mu17_TrkIsoVVL_Mu8_TrkIsoVVL_DZ_v*
HLT_Mu17_TrkIsoVVL_TkMu8_TrkIsoVVL_DZ_v*
HLT_IsoMu22_v*
HLT_IsoTkMu22_v*
HLT_IsoMu22_eta2p1_v*
HLT_IsoTkMu22_eta2p1_v*
HLT_IsoMu24_v*
HLT_IsoTkMu24_v*
HLT_Ele27_WPTight_Gsf_v*
HLT_Ele25_eta2p1_WPTight_Gsf_v*
HLT_Ele27_eta2p1_WP Loose_Gsf_v*

**Table A.2:** Table of high-level triggers considered in the analysis.

		<i>tHq</i>		<i>tHW</i>		
$\kappa_V$	$\kappa_t$	sum of weights	cross section [pb]	sum of weights	cross section [pb]	LHE weights
1.0	-3.0	35.700022	2.991	11.030445	0.6409	LHEweight_wgt[446]
1.0	-2.0	20.124298	1.706	5.967205	0.3458	LHEweight_wgt[447]
1.0	-1.5	14.043198	1.205	4.029093	0.2353	LHEweight_wgt[448]
1.0	-1.25	11.429338	0.9869	3.208415	0.1876	LHEweight_wgt[449]
1.0	-1.0		0.7927		0.1472	
1.0	-0.75	7.054998	0.6212	1.863811	0.1102	LHEweight_wgt[450]
1.0	-0.5	5.294518	0.4723	1.339886	0.07979	LHEweight_wgt[451]
1.0	-0.25	3.818499	0.3505	0.914880	0.05518	LHEweight_wgt[452]
1.0	0.0	2.627360	0.2482	0.588902	0.03881	LHEweight_wgt[453]
1.0	0.25	1.719841	0.1694	0.361621	0.02226	LHEweight_wgt[454]
1.0	0.5	1.097202	0.1133	0.233368	0.01444	LHEweight_wgt[455]
1.0	0.75	0.759024	0.08059	0.204034	0.01222	LHEweight_wgt[456]
1.0	1.0	0.705305	0.07096	0.273617	0.01561	LHEweight_wgt[457]
1.0	1.25	0.936047	0.0839	0.442119	0.02481	LHEweight_wgt[458]
1.0	1.5	1.451249	0.1199	0.709538	0.03935	LHEweight_wgt[459]
1.0	2.0	3.335034	0.2602	1.541132	0.08605	LHEweight_wgt[460]
1.0	3.0	10.516125	0.8210	4.391335	0.2465	LHEweight_wgt[461]
1.5	-3.0	45.281492	3.845	13.426212	0.7825	LHEweight_wgt[462]
1.5	-2.0	27.606715	2.371	7.809713	0.4574	LHEweight_wgt[463]
1.5	-1.5	20.476088	1.784	5.594971	0.3290	LHEweight_wgt[464]
1.5	-1.25	17.337465	1.518	4.635978	0.2749	LHEweight_wgt[465]
1.5	-1.0	14.483302	1.287	3.775902	0.2244	LHEweight_wgt[466]
1.5	-0.75	11.913599	1.067	3.014744	0.1799	LHEweight_wgt[467]
1.5	-0.5	9.628357	0.874	2.352505	0.1410	LHEweight_wgt[468]
1.5	-0.25	7.627574	0.702	1.789184	0.1081	LHEweight_wgt[469]
1.5	0.0	5.911882	0.5577	1.324946	0.08056	LHEweight_wgt[470]
1.5	0.25	4.479390	0.4365	0.959295	0.05893	LHEweight_wgt[471]
1.5	0.5	3.331988	0.3343	0.692727	0.04277	LHEweight_wgt[472]
1.5	0.75	2.469046	0.2558	0.525078	0.03263	LHEweight_wgt[473]
1.5	1.0	1.890565	0.2003	0.456347	0.02768	LHEweight_wgt[474]
1.5	1.25	1.596544	0.1689	0.486534	0.02864	LHEweight_wgt[475]
1.5	1.5	1.586983	0.1594	0.615638	0.03509	LHEweight_wgt[476]
1.5	2.0	2.421241	0.2105	1.170602	0.06515	LHEweight_wgt[477]
1.5	3.0	7.503280	0.5889	3.467546	0.1930	LHEweight_wgt[478]
0.5	-3.0	27.432685	2.260	8.929074	0.5136	LHEweight_wgt[479]
0.5	-2.0	13.956013	1.160	4.419093	0.2547	LHEweight_wgt[480]
0.5	-1.5	8.924438	0.7478	2.757611	0.1591	LHEweight_wgt[481]
0.5	-1.25	6.835341	0.5726	2.075247	0.1204	LHEweight_wgt[482]
0.5	-1.0	5.030704	0.4273	1.491801	0.08696	LHEweight_wgt[483]
0.5	-0.75	3.510528	0.2999	1.007273	0.05885	LHEweight_wgt[484]
0.5	-0.5	2.274811	0.1982	0.621663	0.03658	LHEweight_wgt[485]
0.5	-0.25	1.323555	0.1189	0.334972	0.01996	LHEweight_wgt[486]
0.5	0.0	0.656969	0.06223	0.147253	0.008986	LHEweight_wgt[487]
0.5	0.25	0.274423	0.02830	0.058342	0.003608	LHEweight_wgt[488]
0.5	0.5	0.176548	0.01778	0.068404	0.003902	LHEweight_wgt[489]
0.5	0.75	0.363132	0.03008	0.177385	0.009854	LHEweight_wgt[490]
0.5	1.0	0.834177	0.06550	0.385283	0.02145	LHEweight_wgt[491]
0.5	1.25	1.589682	0.1241	0.692099	0.03848	LHEweight_wgt[492]
0.5	1.5	2.629647	0.2047	1.097834	0.06136	LHEweight_wgt[493]
0.5	2.0	5.562958	0.4358	2.206057	0.1246	LHEweight_wgt[494]
0.5	3.0	14.843102	1.177	5.609519	0.3172	LHEweight_wgt[495]

**Table A.3:**  $\kappa_V$  and  $\kappa_t$  combinations generated for the two signal samples and their NLO cross sections. The *tHq* cross section is multiplied by the branching fraction of the enforced leptonic decay of the top quark (0.324) [150].

Sample	$\sigma$ [pb]	*
TTWJetsToLNu_TuneCUETP8M1_13TeV-amcatnloFXFX-madspin-pythia8	0.2043	*
TTZToLLNuNu_M-10_TuneCUETP8M1_13TeV-amcatnlo-pythia8	0.2529	*
/store/cmst3/group/susy/gpetrucc/13TeV/u/TTLL_m1to10_L0_NoMS_for76X/	0.0283	
WGToLNuG_TuneCUETP8M1_13TeV-madgraphMLM-pythia8	585.8	
ZGTo2LG_TuneCUETP8M1_13TeV-amcatnloFXFX-pythia8	131.3	
TGJets_TuneCUETP8M1_13TeV_amcatnlo_madspin_pythia8	2.967	
TGJets_TuneCUETP8M1_13TeV_amcatnlo_madspin_pythia8	2.967	
TTGJets_TuneCUETP8M1_13TeV-amcatnloFXFX-madspin-pythia8	3.697	
WpWpJJ_EWK-QCD_TuneCUETP8M1_13TeV-madgraph-pythia8	0.03711	
ZZZ_TuneCUETP8M1_13TeV-amcatnlo-pythia8	0.01398	
WWZ_TuneCUETP8M1_13TeV-amcatnlo-pythia8	0.1651	
WZZ_TuneCUETP8M1_13TeV-amcatnlo-pythia8	0.05565	
WW_DoubleScattering_13TeV-pythia8	1.64	
tZq_ll_4f_13TeV-amcatnlo-pythia8_TuneCUETP8M1	0.0758	
ST_tW1l_5f_L0_13TeV-MadGraph-pythia8	0.01123	
TTTT_TuneCUETP8M1_13TeV-amcatnlo-pythia8	0.009103	
WZTo3LNu_TuneCUETP8M1_13TeV-powheg-pythia8	4.4296	
ZZTo4L_13TeV_powheg_pythia8	1.256	
TTJets_SingleLeptFromTbar_TuneCUETP8M1_13TeV-madgraphMLM-pythia8	182.1754	*
TTJets_SingleLeptFromT_TuneCUETP8M1_13TeV-madgraphMLM-pythia8	182.1754	*
TTJets_DiLept_TuneCUETP8M1_13TeV-madgraphMLM-pythia8	87.3	*
DYJetsToLL_M-10to50_TuneCUETP8M1_13TeV-amcatnloFXFX-pythia8	18610	
DYJetsToLL_M-50_TuneCUETP8M1_13TeV-madgraphMLM-pythia8	6024	
WJetsToLNu_TuneCUETP8M1_13TeV-amcatnloFXFX-pythia8	61526.7	
ST_tW_top_5f_inclusiveDecays_13TeV-powheg-pythia8_TuneCUETP8M1	35.6	
ST_tW_antitop_5f_inclusiveDecays_13TeV-powheg-pythia8_TuneCUETP8M1	35.6	
ST_t-channel_4f_leptonDecays_13TeV-amcatnlo-pythia8_TuneCUETP8M1	70.3144	
ST_t-channel_antitop_4f_leptonDecays_13TeV-powheg-pythia8_TuneCUETP8M1	26.2278	
ST_s-channel_4f_leptonDecays_13TeV-amcatnlo-pythia8_TuneCUETP8M1	3.68064	
WWTo2L2Nu_13TeV-powheg	10.481	
ttWJets_13TeV_madgraphMLM	0.6105	
ttZJets_13TeV_madgraphMLM	0.5297/0.692	

**Table A.4:** List of background samples used in this analysis (CMSSW 80X). The first section of the table lists the samples used in simulation to extract the final yields and shapes; the second section lists the samples of the processes for which the yields are estimated from data. The MC simulation is used to design the data driven methods and in the derivation of the associated systematic uncertainties. The third section list the leading order  $t\bar{t}W$  and  $t\bar{t}Z$  samples, which in addition to the ones market with a \*, where used in the BDT training.

<sub>2998</sub> **Appendix B**

<sub>2999</sub> **BDTG aditional plots**

<sub>3000</sub> **B.1 BDTG input variables distributions for  $2lss$**

<sub>3001</sub> **channel**

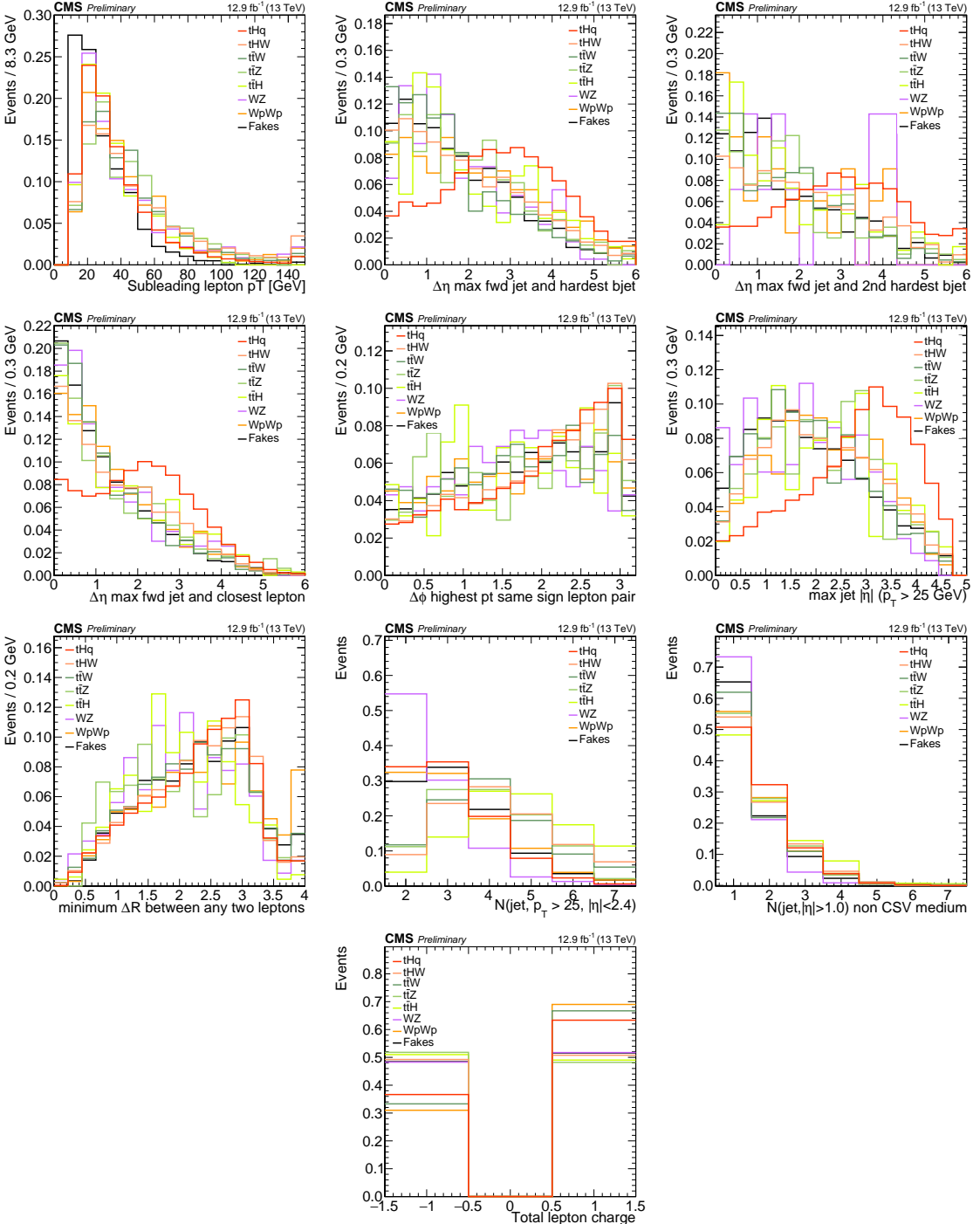


**Figure B.1:** Distributions of input variables to the BDT for signal discrimination, two lepton same sign channel.

3002    **B.2 Input variables distributions from BDTG**  
 3003    classifiers

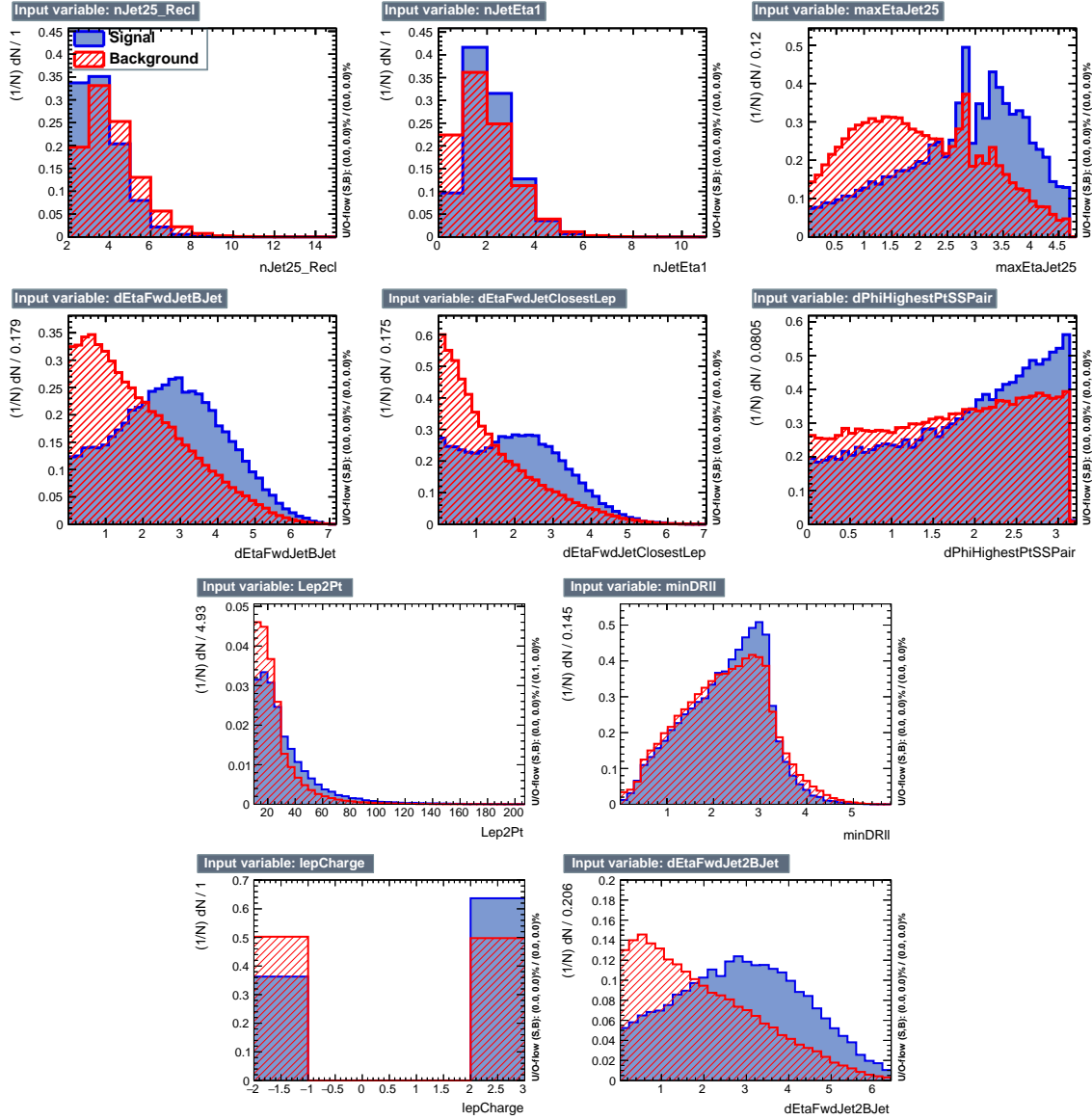


**Figure B.2:** BDT input variables as seen by BDTG classifier for the  $2lss$  channel,  $tHq$  signal (blue) discriminated against  $t\bar{t}$  background (red).

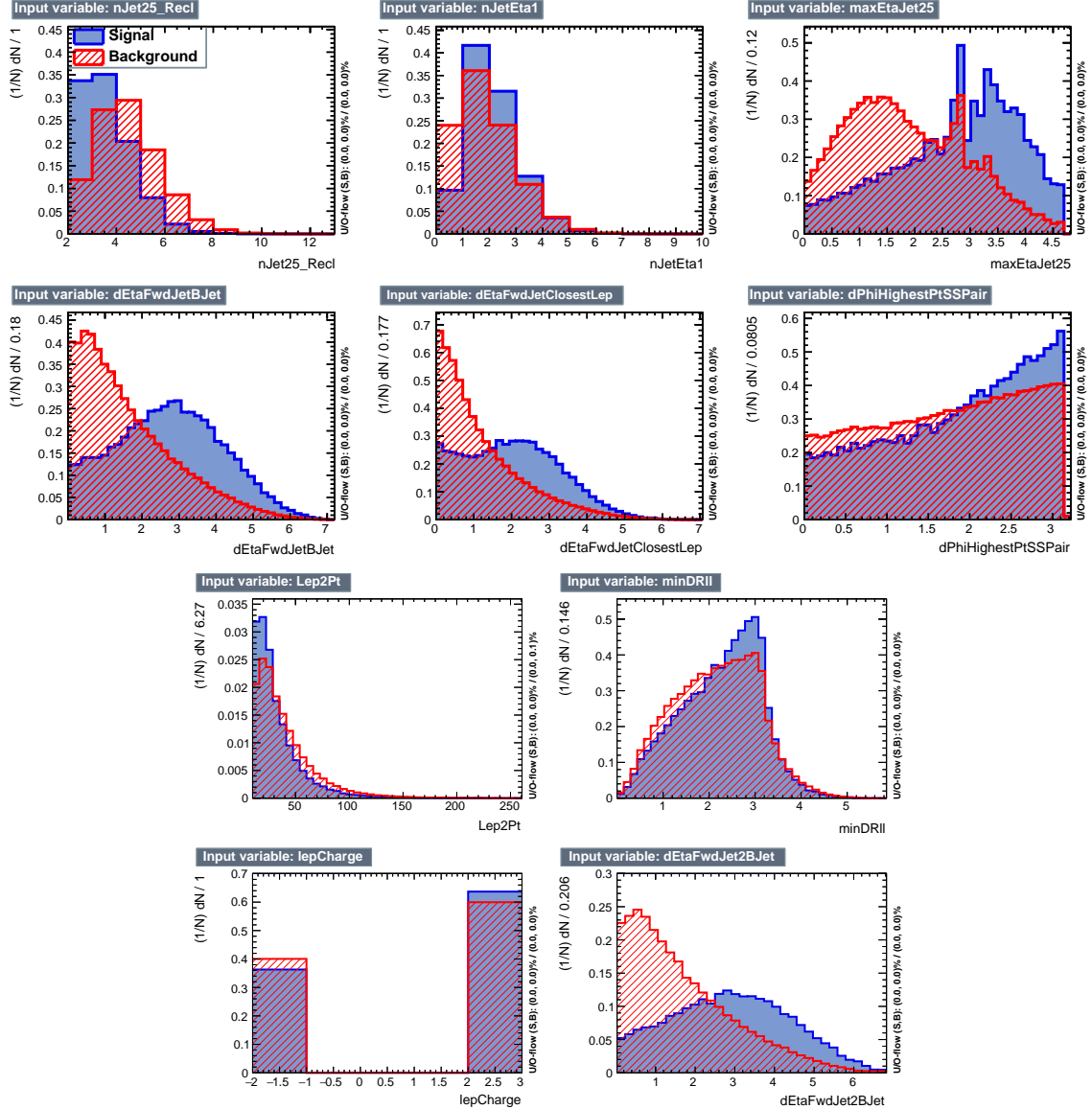


**Figure B.3:** BDT input variables as seen by BDTG classifier for the  $2lss$  channel,  $tHq$  signal(blue) discriminated against  $t\bar{t}V$  background (red).

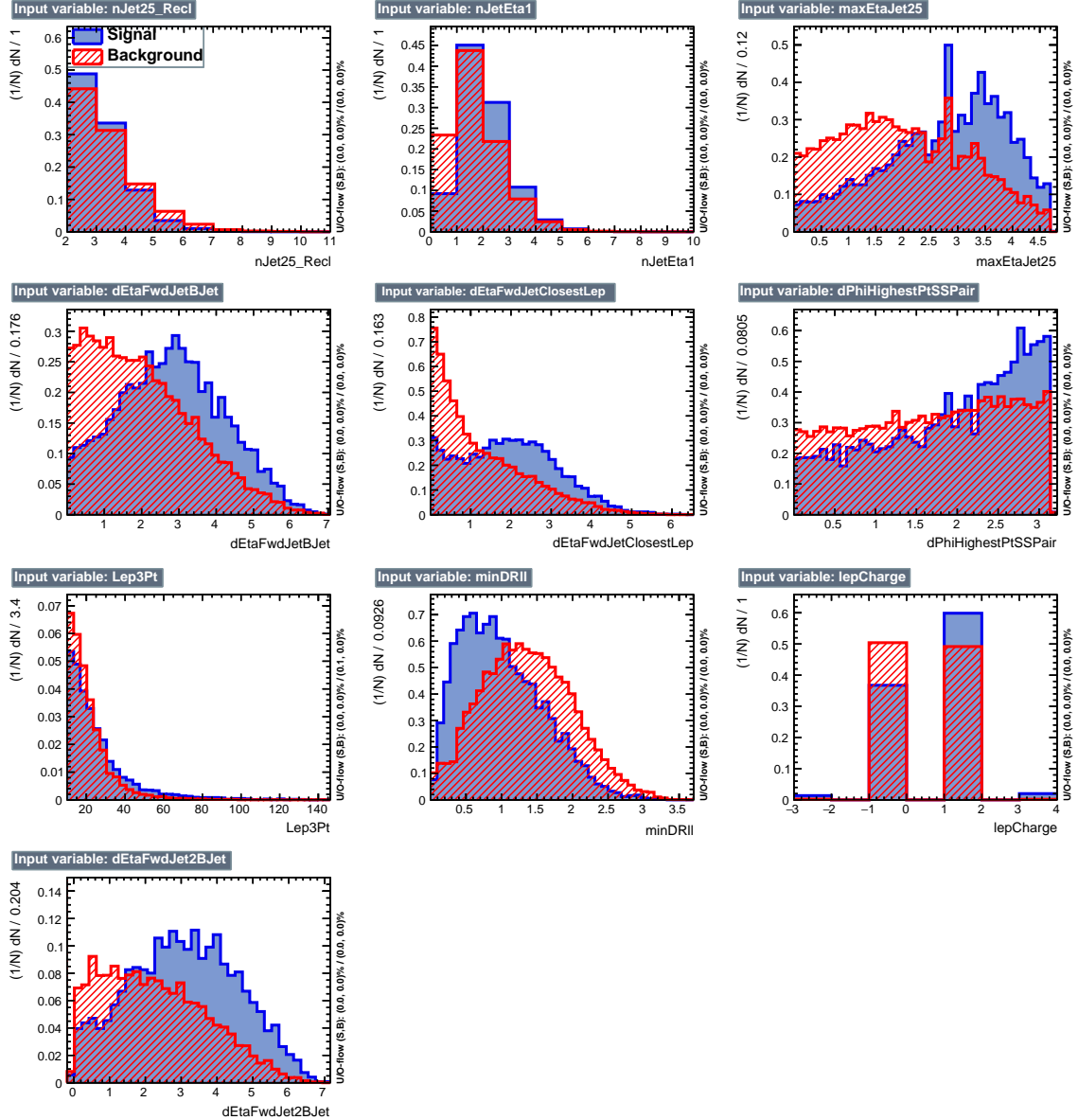


**Figure B.4:** BDT input variables as seen by BDTG classifier for the  $3l$  channel,  $tHq$  signal (blue) discriminated against  $t\bar{t}$  background (red).

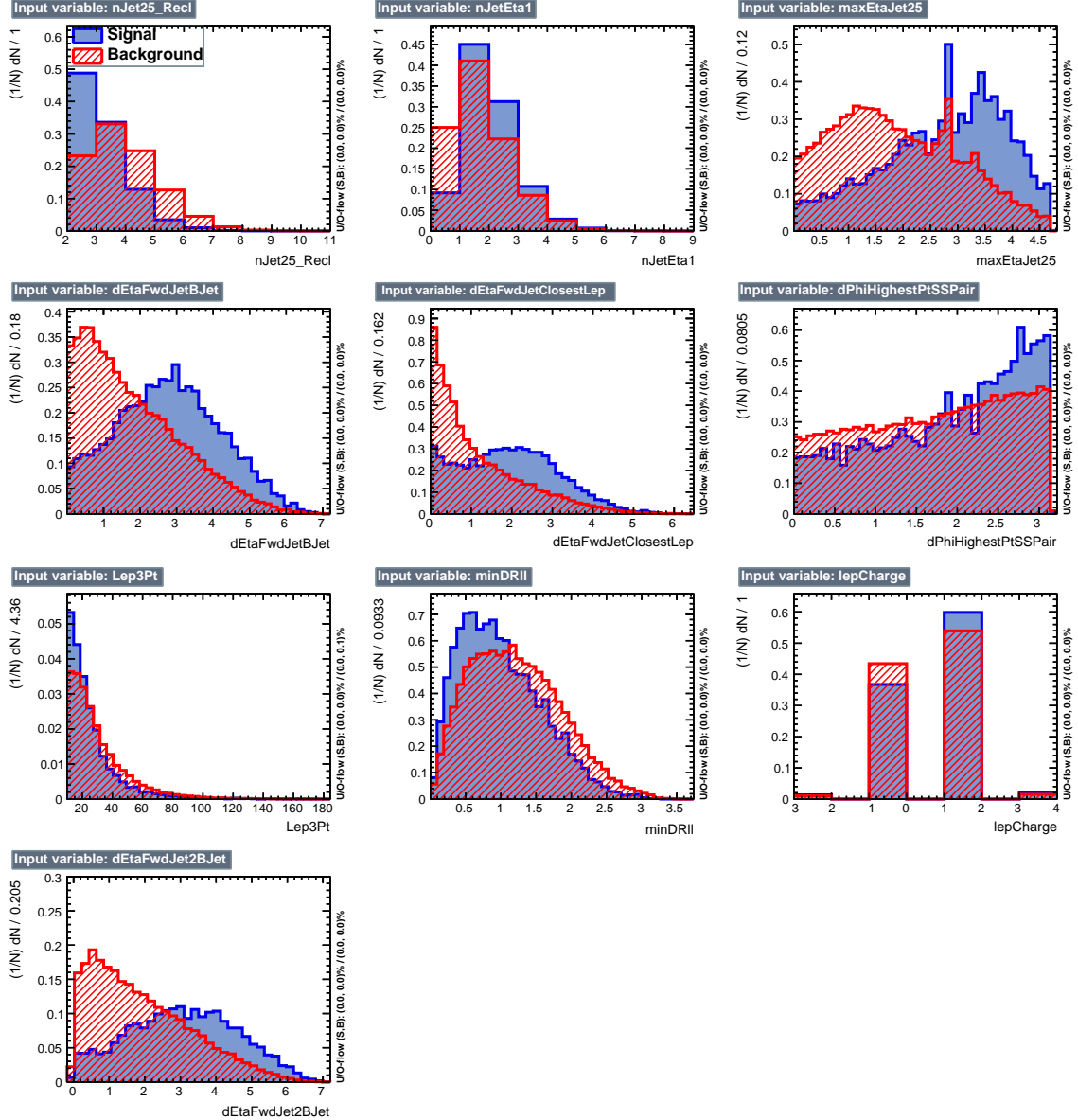


**Figure B.5:** BDT input variables as seen by BDTG classifier for the  $3l$  channel,  $tHq$  signal (blue) discriminated against  $t\bar{t}V$  background (red).

3004      **References**

- 3005 [1] J. Schwinger. "Quantum Electrodynamics. I. A Covariant Formulation". Physical Review. 74 (10): 1439-61, (1948). <https://doi.org/10.1103/PhysRev.74.1439>
- 3008 [2] R. P. Feynman. "Space-Time Approach to Quantum Electrodynamics". Physical Review. 76 (6): 769-89, (1949). <https://doi.org/10.1103/PhysRev.76.769>
- 3010 [3] S. Tomonaga. "On a Relativistically Invariant Formulation of the Quantum Theory of Wave Fields". Progress of Theoretical Physics. 1 (2): 27-42, (1946). <https://doi.org/10.1143/PTP.1.27>
- 3013 [4] D.J. Griffiths, "Introduction to electrodynamics". 4th ed. Pearson, (2013).
- 3014 [5] F. Mandl, G. Shaw. "Quantum field theory." Chichester, Wiley (2009).
- 3015 [6] F. Halzen, and A.D. Martin, "Quarks and leptons: An introductory course in modern particle physics". New York: Wiley, (1984) .
- 3017 [7] File: Standard\_Model\_of\_Elementary\_Particle\_dark.svg. (2017, June 12) Wikimedia Commons, the free media repository. Retrieved November 27, 2017 from <https://www.collegiate-advanced-electricity.com/single-post/2017/04/10/The-Standard-Model-of-Particle-Physics>.

- 3021 [8] E. Noether, "Invariante Variationsprobleme", Nachrichten von der Gesellschaft  
3022 der Wissenschaften zu Göttingen, mathematisch-physikalische Klasse, vol. 1918,  
3023 pp. 235-257, (1918).
- 3024 [9] C. Patrignani et al. (Particle Data Group), Chin. Phys. C, 40, 100001 (2016)  
3025 and 2017 update.
- 3026 [10] M. Goldhaber, L. Grodzins, A.W. Sunyar "Helicity of Neutrinos", Phys. Rev.  
3027 109, 1015 (1958).
- 3028 [11] Palanque-Delabrouille N et al. "Neutrino masses and cosmology with Lyman-  
3029 alpha forest power spectrum", JCAP 11 011 (2015).
- 3030 [12] M. Gell-Mann. "A Schematic Model of Baryons and Mesons". Physics Letters.  
3031 8 (3): 214-215 (1964).
- 3032 [13] G. Zweig. "An SU(3) Model for Strong Interaction Symmetry and its Breaking"  
3033 (PDF). CERN Report No.8182/TH.401 (1964).
- 3034 [14] G. Zweig. "An SU(3) Model for Strong Interaction Symmetry and its Breaking:  
3035 II" (PDF). CERN Report No.8419/TH.412(1964).
- 3036 [15] M. Gell-Mann. "The Interpretation of the New Particles as Displaced Charged  
3037 Multiplets". Il Nuovo Cimento 4: 848. (1956).
- 3038 [16] T. Nakano, K. Nishijima. "Charge Independence for V-particles". Progress of  
3039 Theoretical Physics 10 (5): 581-582. (1953).
- 3040 [17] N. Cabibbo, "Unitary symmetry and leptonic decays" Physical Review Letters,  
3041 vol. 10, no. 12, p. 531, (1963).

- 3042 [18] M.Kobayashi, T.Maskawa, “CP-violation in the renormalizable theory of weak  
3043 interaction,” Progress of Theoretical Physics, vol. 49, no. 2, pp. 652-657, (1973).
- 3044 [19] File: Weak Decay (flipped).svg. (2017, June 12). Wikimedia Com-  
3045 mons, the free media repository. Retrieved November 27, 2017  
3046 from [https://commons.wikimedia.org/w/index.php?title=File:  
3047 Weak\\_Decay\\_\(flipped\)\.svg&oldid=247498592](https://commons.wikimedia.org/w/index.php?title=File:Weak_Decay_(flipped)\.svg&oldid=247498592).
- 3048 [20] Georgia Tech University. Coupling Constants for the Fundamental Forces(2005).  
3049 Retrieved January 10, 2018, from [http://hyperphysics.phy-astr.gsu.edu/  
3050 hbase/Forces/couple.html#c2](http://hyperphysics.phy-astr.gsu.edu/hbase/Forces/couple.html#c2)
- 3051 [21] M. Strassler. (May 31, 2013).The Strengths of the Known Forces. Retrieved Jan-  
3052 uary 10, 2018, from [https://profmattstrassler.com/articles-and-posts/  
3053 particle-physics-basics/the-known-forces-of-nature/  
3054 the-strength-of-the-known-forces/](https://profmattstrassler.com/articles-and-posts/particle-physics-basics/the-known-forces-of-nature/the-strength-of-the-known-forces/)
- 3055 [22] S.L. Glashow. “Partial symmetries of weak interactions”, Nucl. Phys. 22 579-  
3056 588, (1961).
- 3057 [23] A. Salam, J.C. Ward. “Electromagnetic and weak interactions”, Physics Letters  
3058 13 168-171, (1964).
- 3059 [24] S. Weinberg, “A model of leptons”, Physical Review Letters, vol. 19, no. 21, p.  
3060 1264, (1967).
- 3061 [25] M. Peskin, D. Schroeder, “An introduction to quantum field theory”. Perseus  
3062 Books Publishing L.L.C., (1995).
- 3063 [26] A. Pich. “The Standard Model of Electroweak Interactions” <https://arxiv.org/abs/1201.0537>
- 3064

- 3065 [27] G. Arnison et al. (UA1 Collaboration), Phys. Lett. B 122, 103 (1983).
- 3066 [28] M. Banner et al. (UA2 Collaboration), Phys. Lett. B 122, 476 (1983).
- 3067 [29] G. Arnison et al. (UA1 Collaboration), Phys. Lett. B 126, 398 (1983).
- 3068 [30] P. Bagnaia et al. (UA2 Collaboration), Phys. Lett. B 129, 130 (1983).
- 3069 [31] F.Bellaiche. (2012, 2 September). “What’s this Higgs boson anyway?”. Retrieved  
3070 from: <https://www.quantum-bits.org/?p=233>
- 3071 [32] M. Endres et al. Nature 487, 454-458 (2012) doi:10.1038/nature11255
- 3072 [33] F. Englert, R. Brout. “Broken Symmetry and the Mass of Gauge  
3073 Vector Mesons”. Physical Review Letters. 13 (9): 321-23.(1964)  
3074 doi:10.1103/PhysRevLett.13.321
- 3075 [34] P.Higgs. “Broken Symmetries and the Masses of Gauge Bosons”. Physical Re-  
3076 view Letters. 13 (16): 508-509,(1964). doi:10.1103/PhysRevLett.13.508.
- 3077 [35] G.Guralnik, C.R. Hagen and T.W.B. Kibble. “Global Conservation Laws  
3078 and Massless Particles”. Physical Review Letters. 13 (20): 585-587, (1964).  
3079 doi:10.1103/PhysRevLett.13.585.
- 3080 [36] CMS collaboration. “Observation of a new boson at a mass of 125 GeV with  
3081 the CMS experiment at the LHC”. Physics Letters B. 716 (1): 30-61 (2012).  
3082 arXiv:1207.7235. doi:10.1016/j.physletb.2012.08.021
- 3083 [37] ATLAS collaboration. “Observation of a New Particle in the Search for the Stan-  
3084 dard Model Higgs Boson with the ATLAS Detector at the LHC”. Physics Letters  
3085 B. 716 (1): 1-29 (2012). arXiv:1207.7214. doi:10.1016/j.physletb.2012.08.020.

- 3086 [38] ATLAS collaboration; CMS collaboration (26 March 2015). “Combined Mea-  
3087 surement of the Higgs Boson Mass in pp Collisions at  $\sqrt{s}=7$  and 8 TeV with  
3088 the ATLAS and CMS Experiments”. Physical Review Letters. 114 (19): 191803.  
3089 arXiv:1503.07589. doi:10.1103/PhysRevLett.114.191803.
- 3090 [39] LHC InternationalMasterclasses“When protons collide”. Retrieved from [http://atlas.physicsmasterclasses.org/en/zpath\\_protoncollisions.htm](http://atlas.physicsmasterclasses.org/en/zpath_protoncollisions.htm)
- 3092 [40] CMS Collaboration, “SM Higgs Branching Ratios and Total Decay Widths (up-  
3093 date in CERN Report4 2016)”. <https://twiki.cern.ch/twiki/bin/view/LHCPhysics/CERNYellowReportPageBR>, last accessed on 17.12.2017.
- 3095 [41] R.Grant V. “Determination of Higgs branching ratios in  $H \rightarrow W^+W^- \rightarrow l\nu jj$   
3096 and  $H \rightarrow ZZ \rightarrow l^+l^- jj$  channels”. Physics Department, University of Ten-  
3097 nessee (Dated: October 31, 2012). Retrieved from <http://aesop.phys.utk.edu/ph611/2012/projects/Riley.pdf>
- 3099 [42] LHC Higgs Cross Section Working Group, Denner, A., Heinemeyer, S. et al.  
3100 “Standard model Higgs-boson branching ratios with uncertainties”. Eur. Phys.  
3101 J. C (2011) 71: 1753. <https://doi.org/10.1140/epjc/s10052-011-1753-8>
- 3102 [43] D. de Florian et al., LHC Higgs Cross Section Working Group,  
3103 CERNâš2017âš002-M, arXiv:1610.07922[hep-ph] (2016).
- 3104 [44] ATLAS and CMS Collaborations, “Measurements of the Higgs boson produc-  
3105 tion and decay rates and constraints on its couplings from a combined ATLAS  
3106 and CMS analysis of the LHC pp collision data at  $\sqrt{s} = 7$  and 8 TeV,” (2016).  
3107 CERN-EP-2016-100, ATLAS-HIGG-2015-07, CMS-HIG-15-002.

- 3108 [45] J. A. Aguilar-Saavedra, R. Benbrik, S. Heinemeyer, and M. Perez-Victoria,  
3109 “Handbook of vector-like quarks: Mixing and single production”, Phys. Rev. D  
3110 88 (2013) 094010, doi:10.1103/PhysRevD.88.094010, arXiv:1306.0572.
- 3111 [46] A. Greljo, J. F. Kamenik, and J. Kopp, “Disentangling flavor vio-  
3112 lation in the top-Higgs sector at the LHC”, JHEP 07 (2014) 046,  
3113 doi:10.1007/JHEP07(2014)046, arXiv:1404.1278.
- 3114 [47] F. Demartin, F. Maltoni, K. Mawatari, and M. Zaro, “Higgs production in  
3115 association with a single top quark at the LHC,” European Physical Journal C,  
3116 vol. 75, p. 267, (2015). doi:10.1140/epjc/s10052-015-3475-9, arXiv:1504.00611.
- 3117 [48] F. Demartin, B. Maier, F. Maltoni, K. Mawatari, and M. Zaro, “tWH associated  
3118 production at the LHC”, European Physical Journal C, vol. 77, p. 34, (2017).  
3119 arXiv:1607.05862
- 3120 [49] F. Maltoni, K. Paul, T. Stelzer, and S. Willenbrock, “Associated production  
3121 of Higgs and single top at hadron colliders”, Phys.Rev. D64 (2001) 094023,  
3122 [hep-ph/0106293].
- 3123 [50] S. Biswas, E. Gabrielli, F. Margaroli, and B. Mele, “Direct constraints on the  
3124 top-Higgs coupling from the 8 TeV LHC data,” Journal of High Energy Physics,  
3125 vol. 07, p. 073, (2013).
- 3126 [51] M. Farina, C. Grojean, F. Maltoni, E. Salvioni, and A. Thamm, “Lifting de-  
3127 generacies in Higgs couplings using single top production in association with a  
3128 Higgs boson,” Journal of High Energy Physics, vol. 05, p. 022, (2013).
- 3129 [52] T.M. Tait and C.-P. Yuan, “Single top quark production as a window to physics  
3130 beyond the standard model”, Phys. Rev. D 63 (2000) 014018 [hep-ph/0007298].

- 3131 [53] CMS Collaboration, “Modelling of the single top-quark production in associa-  
 3132 tion with the Higgs boson at 13 TeV.” <https://twiki.cern.ch/twiki/bin/viewauth/CMS/SingleTopHiggsGeneration13TeV>, last accessed on 16.01.2018.
- 3134 [54] CMS Collaboration, “SM Higgs production cross sections at  $\sqrt{s} =$   
 3135 13 TeV.” <https://twiki.cern.ch/twiki/bin/view/LHCPhysics/CERNYellowReportPageAt13TeV>, last accessed on 16.01.2018.
- 3137 [55] S. Dawson, The effective W approximation, Nucl. Phys. B 249 (1985) 42.
- 3138 [56] S. Biswas, E. Gabrielli and B. Mele, JHEP 1301 (2013) 088 [arXiv:1211.0499  
 3139 [hep-ph]].
- 3140 [57] LHC Higgs Cross Section Working Group, “Handbook of LHC Higgs Cross  
 3141 Sections: 4.Deciphering the Nature of the Higgs Sector”, arXiv:1610.07922.
- 3142 [58] J. Ellis, D. S. Hwang, K. Sakurai, and M. Takeuchi.“Disentangling Higgs-Top  
 3143 Couplings in Associated Production”, JHEP 1404 (2014) 004, [arXiv:1312.5736].
- 3144 [59] CMS Collaboration, V. Khachatryan et al., “Precise determination of the mass  
 3145 of the Higgs boson and tests of compatibility of its couplings with the standard  
 3146 model predictions using proton collisions at 7 and 8 TeV,” arXiv:1412.8662.
- 3147 [60] ATLAS Collaboration, G. Aad et al., “Updated coupling measurements of the  
 3148 Higgs boson with the ATLAS detector using up to  $25 \text{ fb}^{-1}$  of proton-proton  
 3149 collision data”, ATLAS-CONF-2014-009.
- 3150 [61] File:Cern-accelerator-complex.svg. Wikimedia Commons, the free media repos-  
 3151 itory. Retrieved January, 2018 from <https://commons.wikimedia.org/wiki/File:Cern-accelerator-complex.svg>

- 3153 [62] J.L. Caron , “Layout of the LEP tunnel including future LHC infrastructures.”,  
3154 (Nov, 1993). A C Collection. Legacy of AC. Pictures from 1992 to 2002. Re-  
3155 trieved from <https://cds.cern.ch/record/841542>
- 3156 [63] M. Vretenar, “The radio-frequency quadrupole”. CERN Yellow Report CERN-  
3157 2013-001, pp.207-223 DOI:10.5170/CERN-2013-001.207. arXiv:1303.6762
- 3158 [64] L.Evans. P. Bryant (editors). “LHC Machine”. JINST 3 S08001 (2008).
- 3159 [65] CERN Photographic Service.“Radio-frequency quadrupole, RFQ-1”, March  
3160 1983, CERN-AC-8303511. Retrieved from <https://cds.cern.ch/record/615852>.
- 3162 [66] CERN Photographic Service “Animation of CERN’s accelerator network”, 14  
3163 October 2013. DOI: 10.17181/cds.1610170 Retrieved from <https://videos.cern.ch/record/1610170>
- 3165 [67] C.Sutton. “Particle accelerator”.Encyclopedia Britannica. July 17,  
3166 2013. Retrieved from <https://www.britannica.com/technology/particle-accelerator>.
- 3168 [68] L.Guiraud. “Installation of LHC cavity in vacuum tank.”. July 27 2000. CERN-  
3169 AC-0007016. Retrieved from <https://cds.cern.ch/record/41567>.
- 3170 [69] J.L. Caron, “Magnetic field induced by the LHC dipole’s superconducting coils”.  
3171 March 1998. AC Collection. Legacy of AC. Pictures from 1992 to 2002. LHC-  
3172 PHO-1998-325. Retrieved from <https://cds.cern.ch/record/841511>.
- 3173 [70] AC Team. “Diagram of an LHC dipole magnet”. June 1999. CERN-DI-9906025  
3174 retrieved from <https://cds.cern.ch/record/40524>.

- 3175 [71] CMS Collaboration “Public CMS Luminosity Information”. [https://twiki.cern.ch/twiki/bin/view/CMSPublic/LumiPublicResults#2016\\\_\\\_proton\\_proton\\_13\\_TeV\\_collis](https://twiki.cern.ch/twiki/bin/view/CMSPublic/LumiPublicResults#2016\_\_proton_proton_13_TeV_collis), last accessed 24.01.2018
- 3176
- 3177
- 3178 [72] J.L Caron. “LHC Layout” AC Collection. Legacy of AC. Pictures from 1992  
3179 to 2002. September 1997, LHC-PHO-1997-060. Retrieved from <https://cds.cern.ch/record/841573>.
- 3180
- 3181 [73] J.A. Coarasa. “The CMS Online Cluster:Setup, Operation and Maintenance  
3182 of an Evolving Cluster”. ISGC 2012, 26 February - 2 March 2012, Academia  
3183 Sinica, Taipei, Taiwan.
- 3184 [74] CMS Collaboration. “The CMS experiment at the CERN LHC” JINST 3 S08004  
3185 (2008).
- 3186 [75] CMS Collaboration. “CMS detector drawings 2012” CMS-PHO-GEN-2012-002.  
3187 Retrieved from <http://cds.cern.ch/record/1433717>.
- 3188 [76] Davis, Siona Ruth. “Interactive Slice of the CMS detector”, Aug. 2016,  
3189 CMS-OUTREACH-2016-027, retrieved from <https://cds.cern.ch/record/2205172>
- 3190
- 3191 [77] R. Breedon. “View through the CMS detector during the cooldown of the  
3192 solenoid on February 2006. CMS Collection”, February 2006, CMS-PHO-  
3193 OREACH-2005-004, Retrieved from <https://cds.cern.ch/record/930094>.
- 3194 [78] Halyo, V. and LeGresley, P. and Lujan, P. “Massively Parallel Computing and  
3195 the Search for Jets and Black Holes at the LHC”, Nucl.Instrum.Meth. A744  
3196 (2014) 54-60, DOI: 10.1016/j.nima.2014.01.038”

- 3197 [79] A. Dominguez et. al. “CMS Technical Design Report for the Pixel Detector  
3198 Upgrade”, CERN-LHCC-2012-016. CMS-TDR-11.
- 3199 [80] CMS Collaboration. “Description and performance of track and primary-vertex  
3200 reconstruction with the CMS tracker,” Journal of Instrumentation, vol. 9, no.  
3201 10, p. P10009,(2014).
- 3202 [81] CMS Collaboration and M. Brice. “Images of the CMS Tracker Inner Bar-  
3203 rel”, November 2008, CMS-PHO-TRACKER-2008-002. Retrieved from <https://cds.cern.ch/record/1431467>.
- 3205 [82] M. Weber. “The CMS tracker”. 6th international conference on hyperons, charm  
3206 and beauty hadrons Chicago, June 28-July 3 2004.
- 3207 [83] CMS Collaboration. “Projected Performance of an Upgraded CMS Detector at  
3208 the LHC and HL-LHC: Contribution to the Snowmass Process”. Jul 26, 2013.  
3209 arXiv:1307.7135
- 3210 [84] L. Veillet. “End assembly of HB with EB rails and rotation inside SX ”,Jan-  
3211 uary 2002. CMS-PHO-HCAL-2002-002. Retrieved from <https://cds.cern.ch/record/42594>.
- 3213 [85] J. Puerta-Pelayo.“First DT+RPC chambers installation round in the UX5 cav-  
3214 ern.”. January 2007, CMS-PHO-OREACH-2007-001. Retrieved from <https://cds.cern.ch/record/1019185>
- 3216 [86] X. Cid Vidal and R. Cid Manzano. “CMS Global Muon Trigger” web site:  
3217 Taking a closer look at LHC. Retrieved from [https://www.lhc-closer.es/taking\\_a\\_closer\\_look\\_at\\_lhc/0.lhc\\_trigger](https://www.lhc-closer.es/taking_a_closer_look_at_lhc/0.lhc_trigger)

- 3219 [87] WLCG Project Office, “Documents & Reference - Tiers - Structure,”  
 3220 (2014). <http://wlcg.web.cern.ch/documents-reference> , last accessed on  
 3221 30.01.2018.
- 3222 [88] CMS Collaboration. “CMSSW Application Framework”, <https://twiki.cern.ch/twiki/bin/view/CMSPublic/WorkBookCMSSWFramework>,  
 3223 last accesses 06.02.2018
- 3225 [89] A. Buckleya, J. Butterworthb, S. Giesekec, et. al. “General-purpose event gen-  
 3226 erators for LHC physics”. arXiv:1101.2599v1 [hep-ph] 13 Jan 2011
- 3227 [90] A. Quadt. “Top Quark Physics at Hadron Colliders”. Advances in the Physics  
 3228 of Particles and Nuclei. Springer-Verlag Berlin Heidelberg. DOI: 10.1007/978-  
 3229 3-540-71060-8 (2007)
- 3230 [91] DurhamHep Data Project, “The Durham HepData Project - PDF Plotter.”  
 3231 <http://hepdata.cedar.ac.uk/pdf/pdf3.html> , last accessed on 02.02.2018.
- 3232 [92] G. Altarelli and G. Parisi. “ASYMPTOTIC FREEDOM IN PARTON LAN-  
 3233 GUAGE”, Nucl.Phys. B126:298 (1977).
- 3234 [93] Yu.L. Dokshitzer. Sov.Phys. JETP 46:641 (1977)
- 3235 [94] V.N. Gribov, L.N. Lipatov. “Deep inelastic e p scattering in perturbation the-  
 3236 ory”, Sov.J.Nucl.Phys. 15:438 (1972)
- 3237 [95] F. Maltoni, G. Ridolfi, and M. Ubiali, “b-initiated processes at the LHC: a  
 3238 reappraisal,” Journal of High Energy Physics, vol. 07, p. 022, (2012).
- 3239 [96] B. Andersson, G. Gustafson, G.Ingelman and T. Sjostrand, “Parton fragmen-  
 3240 tation and string dynamics”, Physics Reports, Vol. 97, No. 2-3, pp. 31-145,  
 3241 1983.

- 3242 [97] CMS Collaboration, “Event generator tunes obtained from underlying event  
3243 and multiparton scattering measurements;” European Physical Journal C, vol.  
3244 76, no. 3, p. 155, (2016).
- 3245 [98] J. Alwall et. al., “The automated computation of tree-level and next-to-leading  
3246 order differential cross sections, and their matching to parton shower simula-  
3247 tions,” Journal of High Energy Physics, vol. 07, p. 079, (2014).
- 3248 [99] T. Sjöstrand and P. Z. Skands, “Transverse-momentum-ordered showers and  
3249 interleaved multiple interactions,” European Physical Journal C, vol. 39, pp.  
3250 129–154, (2005).
- 3251 [100] S. Frixione, P. Nason, and C. Oleari, “Matching NLO QCD computations with  
3252 Parton Shower simulations: the POWHEG method,” Journal of High Energy  
3253 Physics, vol. 11, p. 070, (2007).
- 3254 [101] S. Agostinelli et al., “GEANT4: A Simulation toolkit,” Nuclear Instruments  
3255 and Methods in Physics, vol. A506, pp. 250–303, (2003).
- 3256 [102] J.Allison et.al.,“Recent developments in Geant4”, Nuclear Instruments and  
3257 Methods in Physics Research A 835 (2016) 186-225.
- 3258 [103] CMS Collaboration “Full Simulation Offline Guide”, <https://twiki.cern.ch/twiki/bin/view/CMSPublic/SWGuideSimulation>, last accessed 04.02.2018
- 3260 [104] A. Giammanco. “The Fast Simulation of the CMS Experiment” J. Phys.: Conf.  
3261 Ser. 513 022012 (2014)
- 3262 [105] A.M. Sirunyan et. al. “Particle-flow reconstruction and global event description  
3263 with the CMS detector”, JINST 12 P10003 (2017) <https://doi.org/10.1088/1748-0221/12/10/P10003>.

- 3265 [106] The CMS Collaboration. “ Description and performance of track and pri-  
3266 mary vertex reconstruction with the CMS tracker”. JINST 9 P10009 (2014).  
3267 doi:10.1088/1748-0221/9/10/P10009
- 3268 [107] J. Incandela. “Status of the CMS SM Higgs Search” July 4, 2012. Pdf slides.  
3269 Retrieved from [https://indico.cern.ch/event/197461/contributions/](https://indico.cern.ch/event/197461/contributions/1478917/attachments/290954/406673/CMS_4July2012_Final.pdf)  
3270 [1478917/attachments/290954/406673/CMS\\_4July2012\\_Final.pdf](https://indico.cern.ch/event/197461/contributions/1478917/attachments/290954/406673/CMS_4July2012_Final.pdf)
- 3271 [108] P. Billoir and S. Qian, “Simultaneous pattern recognition and track fitting by  
3272 the Kalman filtering method”, Nucl. Instrum. Meth. A 294 219. (1990).
- 3273 [109] W. Adam, R. Fruhwirth, A. Strandlie and T. Todorov, “Reconstruction of  
3274 electrons with the Gaussian sum filter in the CMS tracker at LHC”, eConf  
3275 C 0303241 (2003) TULT009 [physics/0306087].
- 3276 [110] K. Rose, “Deterministic Annealing for Clustering, Compression, Classification,  
3277 Regression and related Optimisation Problems”, Proc. IEEE 86 (1998) 2210.
- 3278 [111] R. Fruhwirth, W. Waltenberger and P. Vanlaer, “ Adaptive Vertex Fitting”,  
3279 CMS Note 2007-008 (2007).
- 3280 [112] CMS collaboration, “Performance of CMS muon reconstruction in pp collision  
3281 events at  $\sqrt{s} = 7 \text{ TeV}$ ”, JINST 7 P10002 2012, [arXiv:1206.4071].
- 3282 [113] Coco, Victor and Delsart, Pierre-Antoine and Rojo-Chacon, Juan and Soyez,  
3283 Gregory and Sander, Christian, “Jets and jet algorithms”, Proceedings,  
3284 HERA and the LHC Workshop Series on the implications of HERA for LHC  
3285 physics: 2006-2008, pag. 182-204. <http://inspirehep.net/record/866539/files/access.pdf>, (2009), doi:10.3204/DESY-PROC-2009-02/54

- 3287 [114] M. Cacciari, G. P. Salam, and G. Soyez, “The anti- $k_t$  jet clustering algorithm,”  
3288 Journal of High Energy Physics, vol. 04, p. 063, (2008).
- 3289 [115] S. Catani, Y. L. Dokshitzer, M. H. Seymour, and B. R. Webber, “Longitudi-  
3290 nally invariant  $K_t$  clustering algorithms for hadron hadron collisions”, Nuclear  
3291 Physics B, vol. 406, pp. 187–224, (1993).
- 3292 [116] Y.L. Dokshitzer, G.D. Leder, S.Moretti, and B.R. Webber, “Better jet clustering  
3293 algorithms,” Journal of High Energy Physics, vol. 08, p. 001, (1997).
- 3294 [117] B. Dorney. “Anatomy of a Jet in CMS”. Quantum Diaries. June  
3295 1st, 2011. Retrieved from [https://www.quantumdiaries.org/2011/06/01/  
3296 anatomy-of-a-jet-in-cms/](https://www.quantumdiaries.org/2011/06/01/anatomy-of-a-jet-in-cms/)
- 3297 [118] The CMS Collaboration.“Event Displays from the high-energy collisions at 7  
3298 TeV”, May 2010, CMS-PHO-EVENTS-2010-007, Retrieved from [https://cds.  
3299 cern.ch/record/1429614](https://cds.cern.ch/record/1429614).
- 3300 [119] The CMS collaboration. “Determination of jet energy calibration and transverse  
3301 momentum resolution in CMS”. JINST 6 P11002 (2011). [http://dx.doi.org/  
3302 10.1088/1748-0221/6/11/P11002](http://dx.doi.org/10.1088/1748-0221/6/11/P11002)
- 3303 [120] The CMS Collaboration, “Introduction to Jet Energy Corrections at  
3304 CMS.”. <https://twiki.cern.ch/twiki/bin/view/CMS/IntroToJEC>, last ac-  
3305 cessed 10.02.2018.
- 3306 [121] CMS Collaboration Collaboration. “Identification of b quark jets at the CMS  
3307 Experiment in the LHC Run 2”. Tech. rep. CMS-PAS-BTV-15-001. Geneva:  
3308 CERN, (2016). <https://cds.cern.ch/record/2138504>.

- 3309 [122] CMS Collaboration Collaboration. “Performance of missing energy reconstruction  
3310 in 13 TeV pp collision data using the CMS detector”. Tech. rep. CMS-PAS-  
3311 JME16-004. Geneva: CERN, 2016. <https://cds.cern.ch/record/2205284>.
- 3312 [123] CMS Collaboration, “New CMS results at Moriond (Electroweak) 2013”,  
3313 Retrieved from [http://cms.web.cern.ch/sites/cms.web.cern.ch/files/styles/large/public/field/image/HIG13004\\_Event01\\_0.png?itok=LAWZzPHR](http://cms.web.cern.ch/sites/cms.web.cern.ch/files/styles/large/public/field/image/HIG13004_Event01_0.png?itok=LAWZzPHR)
- 3316 [124] CMS Collaboration, “New CMS results at Moriond (Electroweak) 2013”,  
3317 Retrieved from [http://cms.web.cern.ch/sites/cms.web.cern.ch/files/styles/large/public/field/image/TOP12035\\_Event01.png?itok=uMdnSqzC](http://cms.web.cern.ch/sites/cms.web.cern.ch/files/styles/large/public/field/image/TOP12035_Event01.png?itok=uMdnSqzC)
- 3320 [125] K. Skovpen. “Event displays highlighting the main properties of heavy flavour  
3321 jets in the CMS Experiment”, Aug 2017, CMS-PHO-EVENTS-2017-006. Re-  
3322 trieval from <https://cds.cern.ch/record/2280025>.
- 3323 [126] G. Cowan. “Topics in statistical data analysis for high-energy physics”.  
3324 arXiv:1012.3589v1
- 3325 [127] A. Hoecker et al., “TMVA-Toolkit for multivariate data analysis”  
3326 arXiv:physics/0703039v5 (2009)
- 3327 [128] L. Lista. “Statistical Methods for Data Analysis in Particle Physics”, 2nd  
3328 ed. Springer International Publishing. (2017) <https://dx.doi.org/10.1007/978-3-319-62840-0>

- 3330 [129] I. Antcheva et al., “ROOT-A C++ framework for petabyte data storage, sta-  
 3331       tistical analysis and visualization ,” Computer Physics Communications, vol.  
 3332       182, no. 6, pp. 1384â€¢1385, (2011).
- 3333 [130] Y. Coadou. “Boosted decision trees”, ESIPAP, Archamps, 9 Febru-  
 3334       ary 2016. Lecture. Retrieved from [https://indico.cern.ch/event/472305/contributions/1982360/attachments/1224979/1792797/ESIPAP\\_MVA160208-BDT.pdf](https://indico.cern.ch/event/472305/contributions/1982360/attachments/1224979/1792797/ESIPAP_MVA160208-BDT.pdf)
- 3337 [131] J.H. Friedman. “Greedy function approximation: A gradient boosting ma-  
 3338       chine”. Ann. Statist. Volume 29, Number 5 (2001), 1189-1232. [https://projecteuclid.org/download/pdf\\_1/euclid-aos/1013203451](https://projecteuclid.org/download/pdf_1/euclid-aos/1013203451).
- 3340 [132] W. Verkerke and D. Kirkby, “The RooFit toolkit for data modeling,” arXiv  
 3341       preprint physics, (2003).
- 3342 [133] CMS Collaboration, “Documentation of the RooStats-based statistics  
 3343       tools for Higgs PAG”. <https://twiki.cern.ch/twiki/bin/view/CMS/SWGuideHiggsAnalysisCombinedLimit>, last accessed on 08.04.2018.
- 3345 [134] F. James, M. Roos, “MINUIT: Function minimization and error analysis”. Cern  
 3346       Computer Centre Program Library, Geneve Long Write-up No. D506, 1989
- 3347 [135] J. Neyman and E. S. Pearson, “On the problem of the most efficient tests of  
 3348       statistical hypotheses”. Springer-Verlag, (1992).
- 3349 [136] A.L. Read. “Modified frequentist analysis of search results (the  $CL_s$  method),”  
 3350       (2000). CERN-OPEN-2000-205.
- 3351 [137] C. Palmer. “Searches for a Light Higgs with CMS”, CMS-CR-2012-215. <https://cds.cern.ch/record/1560435>.

- 3353 [138] A. Wald, “Tests of statistical hypotheses concerning several parameters when  
 3354 the number of observations is large”, Transactions of the American Mathematical  
 3355 society, vol. 54, no. 3, pp. 426–482, (1943).
- 3356 [139] G. Cowan, K. Cranmer, E. Gross, and O. Vitells, “Asymptotic formulae for  
 3357 likelihood-based tests of new physics”, European Physical Journal C, vol. 71,  
 3358 p. 1554, (2011).
- 3359 [140] S. S. Wilks, “The Large-Sample Distribution of the Likelihood Ratio for Testing  
 3360 Composite Hypotheses”, Annals of Mathematical Statistics, vol. 9, pp. 60–62,  
 3361 (03, 1938).
- 3362 [141] B. Hespel, F. Maltoni, and E. Vryonidou, “Higgs and Z boson associated pro-  
 3363 duction via gluon fusion in the SM and the 2HDM”, JHEP 06 (2015) 065,  
 3364 [https://dx.doi.org/10.1007/JHEP06\(2015\)065](https://dx.doi.org/10.1007/JHEP06(2015)065), arXiv:1503.01656.
- 3365 [142] ATLAS Collaboration, “Measurements of Higgs boson pro-  
 3366 duction and couplings in diboson final states with the AT-  
 3367 LAS detector at the LHC”, Phys. Lett. B726 (2013) 88–119,  
 3368 doi:10.1016/j.physletb.2014.05.011, 10.1016/j.physletb.2013.08.010,  
 3369 arXiv:1307.1427. [Erratum: Phys. Lett.B734,406(2014)].
- 3370 [143] CMS Collaboration, “Search for the associated production of a Higgs boson  
 3371 with a single top quark in proton-proton collisions at  $\sqrt{s} = 8$  TeV”, JHEP 06  
 3372 (2016) 177, doi:10.1007/JHEP06(2016)177, arXiv:1509.08159.
- 3373 [144] B. Stieger, C. Jorda Lope et al., “Search for Associated Production of a Single  
 3374 Top Quark and a Higgs Boson in Leptonic Channels”, CMS Analysis Note CMS  
 3375 AN-14-140, 2014.

- 3376 [145] M. Peruzzi, C. Mueller, B. Stieger et al., “Search for ttH in multilepton final  
3377 states at  $\sqrt{s} = 13$  TeV”, CMS Analysis Note CMS AN-16-211, 2016.
- 3378 [146] CMS Collaboration, “Search for H to bbar in association with a single top quark  
3379 as a test of Higgs boson couplings at  $\sqrt{s} = 13$  TeV”, CMS Physics Analysis  
3380 Summary CMS-PAS-HIG-16-019, 2016.
- 3381 [147] CMS Collaboration, “Search for production of a Higgs boson and a single top  
3382 quark in multilepton final states in proton collisions at  $\sqrt{s} = 13$  TeV”, CMS  
3383 Physics Analysis Summary CMS-PAS-HIG-17-005, 2016.
- 3384 [148] CMS Collaboration, “PdmV2016Analysis,” (2016). <https://twiki.cern.ch/twiki/bin/viewauth/CMS/PdmV2016Analysis#DATA>, last accessed 11.04.2016.
- 3386 [149] M. Peruzzi, F. Romeo, B. Stieger et al., “Search for ttH in multilepton final1  
3387 states at  $\sqrt{s} = 13$  TeV”, CMS Analysis Note CMS AN-17-029, 2017.
- 3388 [150] B. Maier, “SingleTopHiggProduction13TeV”, February, 2016. <https://twiki.cern.ch/twiki/bin/viewauth/CMS/SingleTopHiggsGeneration13TeV>.
- 3390 [151] B. WG, “BtagRecommendation80XReReco”, February, 2017. <https://twiki.cern.ch/twiki/bin/view/CMS/BtagRecommendation80XReReco>.
- 3392 [152] CMS Collaboration, “Identification of b quark jets at the CMS Experiment  
3393 in the LHC Run 2”, CMS Physics Analysis Summary CMS-PAS-BTV-15-001,  
3394 2016.
- 3395 [153] CMS Collaboration, “Baseline muon selections for Run-II.” <https://twiki.cern.ch/twiki/bin/view/CMSPublic/SWGuideMuonIdRun2>, last accessed on  
3396 24.02.2018.

- 3398 [154] G. Petrucciani and C. Botta, “Two step prompt muon identification”, January,  
3399 2015. [https://indico.cern.ch/event/368007/contribution/2/material/  
3400 slides/0.pdf](https://indico.cern.ch/event/368007/contribution/2/material/slides/0.pdf).
- 3401 [155] H. Brun and C. Ochando, “Updated Results on MVA eID with 13 TeV samples”,  
3402 October, 2014. [https://indico.cern.ch/event/298249/contribution/3/  
3403 material/slides/0.pdf](https://indico.cern.ch/event/298249/contribution/3/material/slides/0.pdf).
- 3404 [156] K. Rehermann and B. Tweedie, “Efficient Identification of Boosted Semileptonic  
3405 Top Quarks at the LHC”, JHEP 03 (2011) 059, [https://dx.doi:10.1007/  
3406 JHEP03\(2011\)059](https://dx.doi.org/10.1007/JHEP03(2011)059), arXiv:1007.2221.
- 3407 [157] CMS Collaboration. “Tag and Probe”, [https://twiki.cern.ch/twiki/bin/  
3408 view/CMS/TagAndProbe](https://twiki.cern.ch/twiki/bin/view/CMS/TagAndProbe), last accessed on 02.03.2018.